

Effects of Facility Backpressure on the Performance and Plume of a Hall Thruster

by

Mitchell Louis Ronald Walker

A dissertation submitted in partial fulfillment
of the requirements for the degree of
Doctor of Philosophy
(Aerospace Engineering)
in The University of Michigan
2005

Doctoral Committee:

Professor Alec D. Gallimore, Chair

Professor Iain D. Boyd

Professor Ronald M. Gilgenbach

Frank S. Gulczinski, United States Air Force Research Laboratory

Few things are impossible to diligence and skill. Great works are performed not by strength, but perseverance.
Samuel Johnson

© Mitchell Louis Ronald Walker II

All Rights Reserved
2005

ACKNOWLEDGEMENTS

How does a person say “thank you” when there are so many people to thank? This thesis is the result of several years of, challenging, but extremely rewarding work. It would not have been possible without the help of a great number of people. I consider myself “lucky” to have had the chance to work with such talented colleagues.

First off, I would like to give a genuine Thank You to my advisor, Professor Alec Gallimore. He provides a great working environment and gives students freedom and direction. The graduate students work on projects of true importance to the space community, which increases the quality of the work. Under his direction, the Plasmadynamics and Electric Propulsion Laboratory has become the premier University electric propulsion laboratory in the country, and arguably the world. Thank you for your help and direction.

I am also grateful for the contributions of the other members of my committee, Professor Iain Boyd, Professor Ron Gilgenbach, and Dr. Frank Gulczinski of the Air Force Research Laboratory. Their experience, insight, and enthusiasm have greatly shaped this work as well as me. I would also like to thank the administrative staff of the Aerospace Engineering department: Margaret, Denise, Debbie, Suzanne, Sharon, Cindy, Michelle, Tom, Dave, Chris, Eric, and Terry who have assisted me in my years here.

I would like to thank the many government agencies and private companies that helped make this work possible. I would like to thank Robert Jankvosky at NASA Glenn

Research Center for his assistance in calibrating the ionization gauges and loaning a hollow cathode and NASA GRC Faraday probe (Probe C). In addition, I would like to thank Dr. Colleen Marrese at JPL for loaning PEPL the nude Faraday probes (Probe A). I would like to thank Massimo Saverdi at Centrospazio/ALTA for donating a Faraday probe (Probe D) to PEPL. Robert Thomas's assistance with the construction of the Ionization Gauge Position System and the experimental equipment for the P5 cluster is greatly appreciated. I would like to thank Torsten Stindl at the University of Stuttgart for his assistance with the Langmuir probe work. I would also like to thank Dr. Mitat Birkan at the Air Force Office of Scientific Research, the Michigan Space Grant Consortium, and the National Science Foundation for their financial support.

I look forward to seeing the products of the younger generation of PEPL personnel: Allen, Josh, Jesse, Robbie, Kristina, Dan, Sonca, Bryan, and Tom. I appreciated the talks with my contemporaries Dan and Brian. I would also like to acknowledge the guidance of the older hands: Tim, Pete, and Rich. Special thanks to Dr. James Haas for making the P5 cluster dream a reality through Air Force support. It has been a pleasure working with all of you.

On a personal level I would like to thank my family for their support during my time at the University of Michigan. Most importantly I would like to thank my parents for their unwavering support of my endeavors. Finally, I would like to thank my wife for her support and patience.

Mitchell Walker
November 23, 2004

PREFACE

This research focuses on understanding the relationship between facility background pressure and Hall effect thruster performance and plume characteristics. Due to the wide range of facilities used in Hall thruster testing, it is difficult for researchers to make adequate comparisons between data sets because of both dissimilar instrumentation and backpressures. Thus, tools are needed that allow researchers to obtain relevant plume and performance data for a variety of chambers and backpressures. This research is divided into three parts. The first is the development of a technique for calibrating a vacuum chamber in terms of pressure. The second is an investigation of facility effects, i. e., how does elevated facility backpressure affect thruster performance, plume plasma parameters, and plume diagnostics. The third portion of this research is an investigation of the performance and plume characteristics of a cluster of UM/AFRL P5 5 kW Hall thrusters operated over a wide range of facility backpressures.

This work begins with the development of a technique for calibrating a vacuum chamber in terms of pressure to account for elevated backpressures while testing Hall thrusters. A neutral gas background pressure map of the Large Vacuum Test Facility is created at a series of cold anode flow rates and one hot anode flow rate at two P5 Hall thruster operating conditions. These data show that a cold flow pressure map can be used to approximate the neutral background pressure in the chamber with the thruster in operation. In the process, the sticking coefficient of xenon on to a cryosurface is

experimentally determined. The data are used to calibrate a numerical model that accurately predicts facility backpressure within a vacuum chamber of specified geometry. The numerical model includes facility geometry and pumping surface location.

This activity leads to the facility effects investigation, which is the second portion of this work. The plume of each cluster element is individually characterized at three vacuum facility operating pressures and two anode flow rates to study the effect of facility backpressure on plume parameters, plume diagnostics, and thruster performance. The plasma potential, electron number density, and electron temperature are measured with a single Langmuir probe. The plume ion current density profile is characterized with five different Faraday probe designs. The ionization and acceleration processes are studied with a parallel-plate electrostatic energy analyzer, a retarding potential analyzer, and an ExB probe. In addition, the performance of each thruster is characterized at the conditions stated above with a null-type inverted pendulum thrust stand.

Analysis of the plume and performance data, collected over the range of backpressures, provides insight into facility effects. The use of five Faraday probe designs shows that a magnetically-filtered Faraday probe possesses the ability to remove the effects of charge exchange ions that normally affect the wings of the ion current density traces. As shown previously, an increase in facility backpressure leads to an increase in the width of the ion energy distribution function, but it does not shift the peak voltage to which the ions are accelerated. Due to the elevated pressures present at the ExB probe entrance during P5 operation, it is not possible to accurately measure the percentage of multiply-charged particles in the thruster plume. The measured thrust increases with increasing facility backpressure. The variation of the facility backpressure

did not lead to a clear technique to correct the performance of the Hall thruster operating at elevated backpressure. This work shows that Randolph's ingestion explanation does not adequately account for the elevated discharge current and thrust measured at elevated facility backpressures.

The third portion of this work is an investigation that aims to develop a fundamental understanding of how multi-kW clustered Hall thrusters operate and how one can use single-engine ground-based data to predict the performance, plume interaction, and operation as a function of the cluster element centerline separation distance. This investigation also provides insight on how facility effects influence monolithic and cluster performance characteristics as well as plume diagnostics by characterizing the cluster plume at the elevated operating pressures created by the cluster. The plasma parameters are measured in the plume of the Hall thruster cluster with the same diagnostics used on the individual cluster elements. Measurements of the plasma parameters collected with the diagnostics centered on a single thruster element and on the cluster centerline show that no significant interaction occurs between the cluster elements. Comparison of the performance characteristics of the cluster and the monolithic thruster at conditions of nearly equal operating pressure shows that for a 5.25 mg/s anode flow rate, the cluster thrust is simply the addition of the thrust of the two monolithic thrusters. In addition, the anode efficiency and specific impulse are approximately equal to that of the monolithic thruster. However, these trends do not hold at the 10.46 mg/s anode flow rate for conditions of equal operating pressure, which may be due to elevated facility backpressure.

To further understand the feasibility of clustering Hall thrusters on spacecraft, a study of thruster centerline spacing and cathode-to-thruster separation distance is performed. The results of this study show that the two thruster elements with a centerline separation distance of 2+ m can share a single cathode with no negative effects on the operation of the individual thrusters. The study establishes that a Hall thruster-to-cathode centerline separation distance of 1.3 m does not negatively affect the performance of the thruster, and reliable restarts are possible in this configuration. Variation of the thruster centerline separation distance shows that the gas flow of one thruster does not directly affect the performance of the adjacent thruster.

These are the first experiments to take a holistic approach to understanding facility effects. In addition, this is the first study to investigate cluster performance, cathode sharing as a function of thruster separation distance, and distant cathode placement. These data will aid spacecraft designers in incorporating Hall thrusters into space propulsion systems.

TABLE OF CONTENTS

ACKNOWLEDGEMENTS	ii
PREFACE	iv
LIST OF FIGURES	xi
LIST OF TABLES	xxii
NOMENCLATURE	xxiii
CHAPTER 1 INTRODUCTION	1
1.1 Electric Propulsion Overview	1
1.1.1 Electrothermal Propulsion	4
1.1.2 Electromagnetic Propulsion	5
1.1.3 Electrostatic Propulsion	7
1.2 Hall Effect Thruster Overview	8
1.2.1 Hall Thruster Physics	8
1.3 Motivation	11
1.3.1 Summary of Facility Effects	14
1.3.2 Summary of Clustered Hall Thrusters for High-Power Missions	17
1.4 Contribution of Research	18
CHAPTER 2 EXPERIMENTAL APPARATUS.....	24
2.1 Hall Thruster	24
2.1.1 AFRL/UM P5 Cluster	24
2.1.2 NASA-173Mv1	28
2.2 Vacuum Facilities	29
2.2.1 Plasmadynamics and Electric Propulsion Laboratory (PEPL)	29
2.2.2 Vacuum Facility 12: NASA Glenn Research Center	30
2.3 Ionization Gauge	32
2.3.1 Introduction	32
2.3.2 Principle and Limitations of Ionization Gauges	34
2.3.3 Ionization Gauge calibration	37
2.4 Ionization Gauge Positioning System	38
2.4.1 LVTF Ionization Gauge Positioning System	38
2.4.2 VF-12 Ionization Gauge Positioning System	41
2.5 Langmuir Probe	43
2.6 Faraday Probes	47
2.6.1 Data Acquisition	49
2.6.2 Probe A Jet Propulsion Laboratory (JPL)	51
2.6.3 Probe B (MFFP)	53
2.6.4 Probe C (NASA Glenn Research Center)	54
2.6.5 Probe D (Centrosazio/ALTA)	56
2.6.6 Probe E (AFRL)	58
2.7 Retarding Potential Analyzer	61
2.8 Parallel-Plate Electrostatic Energy Analyzer	64

2.9	ExB Probe.....	70
2.10	NASA Glenn Research Center Null-Type Inverted Pendulum Thrust Stand	77
2.11	Summary.....	79
CHAPTER 3 NEUTRAL DENSITY MAP.....		80
3.1	Cold Flow Neutral Density Map.....	80
3.2	Numerical Tool Development.....	81
3.2.1	Cold Flow Model Comparison	81
3.2.2	Results and Discussion	82
3.3	Hot Flow Neutral Density Map.....	88
3.3.1	Hot Flow Pressure Map Procedure	88
3.3.2	Ionization Gauge Operation.....	89
3.3.3	Ionization Gauge Error	92
3.3.4	Hot Flow Neutral Density Map Results.....	94
3.3.5	Hot Flow Neutral Density Map Discussion	102
3.4	Vacuum Facility Calibration.....	104
3.5	Cluster Pressure Map.....	104
3.5.1	Cluster Pressure Map Procedure.....	105
3.5.2	Results	105
3.5.3	Discussion.....	107
3.6	Conclusions.....	108
CHAPTER 4 FACILITY EFFECTS AND SINGLE THRUSTER CHARACTERIZATION.....		110
4.1	Probe Data	111
4.1.1	Discharge Current Characteristics	114
4.1.2	Plasma Potential and Floating Potential	118
4.1.3	Electron Number Density and Electron Temperature.....	122
4.1.4	Ion Current Density	126
4.1.5	Ion Energy Spectra	136
4.1.6	Ion Species Fractions.....	141
4.1.7	Performance.....	145
4.1.8	Facility Effects.....	153
4.2	Conclusions.....	155
CHAPTER 5 CLUSTER CHARACTERIZATION.....		156
5.1	Probe Data	157
5.1.1	Discharge Current Characteristics	159
5.1.2	Plasma Potential and Floating Potential	163
5.1.3	Electron Number Density and Electron Temperature.....	169
5.1.4	Ion Current Density	176
5.1.5	Ion Energy Spectra	183
5.1.6	Ion Species Fractions.....	188
5.1.7	Performance.....	192
5.1.8	Predicting Cluster Performance and Plume Characteristics.....	203
5.2	Conclusions.....	205
CHAPTER 6 CATHODE SHARING		206
6.1	Plume data as a function of cluster spacing	206
6.2	Cluster Displacement Results	207
6.2.1	Separate Cathodes.....	208
6.2.2	Sharing the Cathode of an Adjacent Thruster.....	213
6.2.3	Sharing a Centered Cathode	218
6.2.4	Operation from a displaced Cathode.....	222
6.3	Conclusions.....	227
CHAPTER 7 CONCLUSIONS.....		229

7.1	Calibration of a Vacuum Facility with a Numerical Tool.....	229
7.2	Corrections for Facility Effects.....	230
7.3	Prediction of Cluster Performance.....	232
7.4	Cathode Sharing.....	233
7.5	Facility Design.....	234
7.6	Suggestions for Future Work.....	235
7.6.1	Validation of Numerical Tool.....	235
7.6.2	Faraday Probe Design Recommendations.....	236
7.6.3	Energy Spectra and Species Fractions measurements in the Cluster Plume.....	236
7.6.4	Validation of Cluster Performance Predictions.....	236
7.6.5	Cluster Spacing.....	237
REFERENCES		238

LIST OF FIGURES

Figure 1-1: Comparison of the Mass ratios of an EP and chemical system for the JIMO mission.	3
Figure 1-2: Schematic of a Hall thruster.	9
Figure 2-1: UM/AFRL 2x1 5 kW P5 Hall Thruster Cluster.	27
Figure 2-2: Electrical schematic of power electronics used to run the P5 Hall thruster. .	27
Figure 2-3: NASA-173Mv1 Hall thruster.	28
Figure 2-4: Schematic of the LVTF.	30
Figure 2-5: Schematic of VF-12.....	32
Figure 2-6: Internal schematic of an ionization gauge.....	35
Figure 2-7: Schematic of the Varian 571 BA Ionization Gauge connected to the neutralizer.....	37
Figure 2-8: Schematic of the IGPS mounted in the LVTF.	40
Figure 2-9: LVTF half-plane (looking down) with the IGPS and a 25 cm by 25 cm square grid. Each open circle denotes the location of a data point.	41
Figure 2-10: VF-12 half-plane (looking down) with the IGPS and a 25 cm by 25 cm grid. Each open circle denotes the location of a data point.	42
Figure 2-11: Typical Langmuir probe characteristic in a Hall thruster plume.....	44
Figure 2-12 Effect of varying the probe bias at several angular positions. (300 V, 4.41 A thruster operation with 140,000 l/s pumping speed).....	50
Figure 2-13: Schematic of Probe A. The collector is isolated from the guard ring with ceramic standoffs.....	52
Figure 2-14 Electrical schematic of the Faraday Probe A setup.....	52
Figure 2-15: Schematic of Magnetically Filtered Faraday Probe. The collector is isolated from the guard ring with ceramic standoffs. (Guard ring not shown).....	54

Figure 2-16: Solid model of the magnetic filter. Particles enter along the z-axis, directed into the page. (L = 5.85 cm, D = 2.54 cm).....	54
Figure 2-17: Schematic of Probe C. The collector is isolated from the guard ring with ceramic standoffs.....	55
Figure 2-18: Electrical schematic of the Faraday Probe C setup.....	56
Figure 2-19: Schematic of Probe D.....	57
Figure 2-20: Electrical schematic of Faraday Probe D.....	58
Figure 2-21: Schematic of Probe E/RPA. Note: Grid 3 is removed when used as Probe E.....	60
Figure 2-22: Electrical schematic of Faraday probe E.....	61
Figure 2-23: Raw RPA data, smoothed data, and the resulting ion energy per unit charge distribution.....	64
Figure 2-24: Schematic of parallel-plate electrostatic energy analyzer operation.....	65
Figure 2-25: Photo of the parallel-plate electrostatic energy analyzer.....	67
Figure 2-26: Two ESA traces collected on the centerline of the P5-A operating at 300 V, 5 A. The traces show that the ESA has good repeatability.....	70
Figure 2-27: Schematic of an ExB probe.....	71
Figure 2-28: Electrical Schematic of the ExB Probe.....	74
Figure 2-29: Sample ExB data taken on the centerline of the P5-A operating at 300 V, 5 A, which shows the peaks due to various charge species.....	75
Figure 2-30: Picture of the NASA-457 Null-type Inverted Pendulum Thrust Stand.....	79
Figure 3-1: Comparisons of simulated and measured pressure distribution within the LVTF for cold flow operation of the NASA-173Mv1 Hall thruster at 10.46 mg/s flow rate and 240,000 l/s pumping along the thruster centerline.....	84
Figure 3-2: Comparisons of simulated and measured pressure distribution within the LVTF for cold flow operation of the NASA-173Mv1 Hall thruster at 10.46 mg/s and 140,000 l/s.....	85
Figure 3-3: Comparisons of simulated and measured pressure distribution within the LVTF for cold flow operation of the NASA-173Mv1 Hall thruster at 5.25 mg/s flow rate and 140,000 l/s.....	86
Figure 3-4: Outer Screen Bias Voltage Study.....	92

Figure 3-5: Raw cold flow data axial profile for a nominal pumping speed of 240,000 l/s.	95
Figure 3-6: Raw hot flow data axial profile for a nominal pumping speed of 240,000 l/s.	96
Figure 3-7: Corrected cold flow data axial profile for a nominal pumping speed of 140,000 l/s.	96
Figure 3-8: Corrected cold flow data axial profile for a nominal pumping speed of 240,000 l/s.	97
Figure 3-9: Corrected hot flow data axial profile for a nominal pumping speed of 240,000 l/s.	97
Figure 3-10: Cold flow pressure map of the LVTF with an anode flow rate of 5.25 mg/s and a cathode flow rate of 0.92 mg/s, at a nominal pumping speed of 140,000 l/s and operating pressure of 6.9×10^{-4} Pa (5.2×10^{-6} Torr), corrected for xenon.	98
Figure 3-11: Hot flow pressure map of the LVTF with an anode flow rate of 5.25 mg/s and a cathode flow rate of 0.92 mg/s, at a nominal pumping speed of 140,000 l/s and operating pressure of 7.2×10^{-4} Pa (5.4×10^{-6} Torr), corrected for xenon. (300 V, 4.88 A thruster operation)	98
Figure 3-12: Hot flow pressure map of the LVTF with an anode flow rate of 5.25 mg/s and a cathode flow rate of 0.92 mg/s, at a nominal pumping speed of 140,000 l/s and operating pressure of 7.6×10^{-4} Pa (5.7×10^{-6} Torr), corrected for xenon. (500 V, 5.30 A thruster operation)	99
Figure 3-13: Cold flow pressure map of the LVTF with an anode flow rate of 5.25 mg/s and a cathode flow rate of 0.92 mg/s, at a nominal pumping speed of 240,000 l/s and operating pressure of 4.5×10^{-4} Pa (3.4×10^{-6} Torr), corrected for xenon.	99
Figure 3-14: Hot flow pressure map of the LVTF with an anode flow rate of 5.25 mg/s and a cathode flow rate of 0.92 mg/s, at a nominal pumping speed of 240,000 l/s and operating pressure of 4.7×10^{-4} Pa (3.5×10^{-6} Torr), corrected for xenon. (300 V, 4.80 A thruster operation)	100
Figure 3-15: Hot flow pressure map of the LVTF with an anode flow rate of 5.25 mg/s and a cathode flow rate of 0.92 mg/s, at a nominal pumping speed of 240,000 l/s and operating pressure of 4.5×10^{-4} Pa (3.4×10^{-6} Torr), corrected for xenon. (500 V, 5.22 A thruster operation)	100
Figure 3-16: Hot flow pressure map of the LVTF with an anode flow rate of 10.46 mg/s and a cathode flow rate of 0.60 mg/s, at a nominal pumping speed of 240,000 l/s and operating pressure of 7.6×10^{-4} Pa (5.7×10^{-6} Torr), corrected for xenon. (300 V, 11.1 A thruster operation)	101

Figure 3-17: Cold flow pressure map of VF-12 with an anode flow rate of 5.25 mg/s and a cathode flow rate of 0.60 mg/s, at a nominal pumping speed of 282,000 l/s and operating pressure of 4.0×10^{-4} Pa (3.0×10^{-6} Torr), corrected for xenon.....	102
Figure 3-18: Hot flow pressure map of the cluster in the LVTF with an anode flow rate of 5.25 mg/s and a cathode flow rate of 0.92 mg/s, at a nominal pumping speed of 240,000 l/s and operating pressure of 4.9×10^{-4} Pa (3.7×10^{-6} Torr), corrected for xenon. (300 V, 5.12 A thruster operation)	106
Figure 3-19: Cold flow pressure map of the cluster in the LVTF with an anode flow rates of 10.46 mg/s and cathode flow rate of 0.92 mg/s, at a nominal pumping speed of 240,000 l/s and operating pressure of 6.9×10^{-4} Pa (5.1×10^{-6} Torr), corrected for xenon.	106
Figure 3-20: Hot flow pressure map of the cluster in the LVTF with an anode flow rate of 10.46 mg/s and a cathode flow rate of 0.92 mg/s, at a nominal pumping speed of 240,000 l/s and operating pressure of 6.9×10^{-4} Pa (5.1×10^{-6} Torr), corrected for xenon. (500 V, 11.8 A thruster operation)	107
Figure 4-1: Diagram of the 1 m arc on which data are collected with respect to a single thruster. This diagram looks down on thruster with the thruster centerline parallel to the facility centerline.....	113
Figure 4-2: Discharge current characteristics of P5-A operating at 300 V, 5.25 mg/s as a function of backpressure.	116
Figure 4-3: Discharge current characteristics of P5-B operating at 500 V, 5.25 mg/s as a function of backpressure.	116
Figure 4-4: Discharge current characteristics of P5-A operating at 300 V, 10.46 mg/s as a function of backpressure.	117
Figure 4-5: Discharge current characteristics of P5-B operating at 500 V, 10.46 mg/s as a function of backpressure.	117
Figure 4-6: Traces of the P5-A floating potential and plasma potential as a function of angle at 300 V, 5.25 mg/s as a function of facility backpressure.....	119
Figure 4-7: Traces of the P5-B floating potential and plasma potential as a function of angle at 300 V, 5.25 mg/s as a function of facility backpressure.....	120
Figure 4-8: Traces of the P5-A floating potential and plasma potential as a function of angle at 500 V, 5.25 mg/s as a function of facility backpressure.....	120
Figure 4-9: Traces of the P5-A floating potential and plasma potential as a function of angle at 300 V, 10.46 mg/s as a function of facility backpressure.....	121

Figure 4-10: Traces of the P5-A floating potential and plasma potential as a function of angle at 500 V, 10.46 mg/s as a function of facility backpressure.....	121
Figure 4-11: Traces of the P5-A electron temperature and electron number density as a function of angle at 300 V, 5.25 mg/s as a function of facility backpressure.	124
Figure 4-12: Traces of the P5-B electron temperature and electron number density as a function of angle at 300 V, 5.25 mg/s as a function of facility backpressure.	124
Figure 4-13: Traces of the P5-A electron temperature and electron number density as a function of angle at 500 V, 5.25 mg/s as a function of facility backpressure.	125
Figure 4-14: Traces of the P5-A electron temperature and electron number density as a function of angle at 300 V, 10.46 mg/s as a function of facility backpressure... ..	125
Figure 4-15: Traces of the P5-A electron temperature and electron number density as a function of angle at 500 V, 10.46 mg/s as a function of facility backpressure... ..	126
Figure 4-16: Ion current density versus position for Probe A at 3 backpressures. (P5-A: 300 V, 5.25 mg/s).....	132
Figure 4-17: Ion current density versus position for Probe A at 3 backpressures. (P5-A: 500 V, 5.25 mg/s).....	132
Figure 4-18: Ion current density versus position for 5 Faraday probe designs at a backpressure of 3.5×10^{-6} Torr-Xe. (P5-A: 300 V, 4.92 A).	133
Figure 4-19: Ion current density versus position for 5 Faraday probes at a backpressure of 3.5×10^{-6} Torr-Xe. (P5-B: 300 V, 4.98 A)	133
Figure 4-20: Ion current density versus position for Probe B at 3 backpressures. (P5-A: 300 V, 5.25 mg/s).....	134
Figure 4-21: Ion current density versus position for Probe B at 3 backpressures. (P5-A: 500 V, 5.25 mg/s).....	134
Figure 4-22: Ion current density versus position for Probe B at 3 backpressures (P5-A: 300 V, 10.46 mg/s).....	135
Figure 4-23: Ion current density versus position for Probe B at 3 backpressures. (P5-A: 500 V, 10.46 mg/s).....	135
Figure 4-24: RPA traces of P5-A as a function of angle at an operating pressure of 3.5×10^{-6} Torr-Xe. (500 V, 5.34 A).....	138
Figure 4-25: RPA traces of P5-B as a function of angle at an operating pressure of 5.3×10^{-6} Torr-Xe. (500 V, 5.12 A).....	139

Figure 4-26: ESA traces of P5-A for angles of -5° to -30° at an operating pressure of 5.3×10^{-6} Torr-Xe. (500 V, 5.38 A).....	139
Figure 4-27: ESA traces of P5-A for angles of -45° to -70° at an operating pressure of 5.3×10^{-6} Torr-Xe. (500 V, 5.38 A).....	140
Figure 4-28: ESA traces of P5-A on centerline for 3 backpressures. (300 V, 5.25 mg/s).....	140
Figure 4-29: ESA traces of P5-A on centerline for 3 backpressures. (500 V, 5.25 mg/s).....	141
Figure 4-30: ExB traces of the P5-A operating at 300 V, 4.92 A at 0° , 5° , and 10° at a backpressure of 3.5×10^{-6} Torr-Xe. Note that the current is measured with a Faraday probe. Thus, the peak magnitudes cannot be directly related to the ion species without considering the amount of charge each species carries.	144
Figure 4-31: ExB traces of the P5-A operating at 300 V, 4.92 A at 15° , 20° , and 35° at a backpressure of 3.5×10^{-6} Torr-Xe. Note that the current is measured with a Faraday probe. Thus, the peak magnitudes cannot be directly related to the ion species without considering the amount of charge each species carries.	144
Figure 4-32: ExB traces of the P5-A operating at 300 V, 5.25 mg/s on thruster centerline at facility backpressures of 9.1×10^{-6} , 5.3×10^{-6} , and 3.5×10^{-6} Torr-Xe. Note that the current is measured with a Faraday probe. Thus, the peak magnitudes cannot be directly related to the ion species without considering the amount of charge each species carries.	145
Figure 4-33: The P5-A thrust measurements at anode flow rates of 5.25 mg/s and 10.46 mg/s as a function of discharge voltage at nominal pumping speeds of 70 kl/s, 140 kl/s, and 240 kl/s.....	146
Figure 4-34: The P5-B thrust measurements at anode flow rates of 5.25 mg/s and 10.46 mg/s as a function of discharge voltage at nominal pumping speeds of 70 kl/s, 140 kl/s, and 240 kl/s.....	147
Figure 4-35: The P5-A anode efficiency versus discharge voltage.	148
Figure 4-36: The P5-A anode specific impulse versus discharge voltage.	149
Figure 4-37: Percent difference in measured thrust of the P5-A at nominal pumping speeds of 140 kl/s and 240 kl/s for an anode flow rate of 5.25 mg/s.	152
Figure 4-38: Percent difference in the measured thrust of the P5-A at nominal pumping speeds of 140 kl/s and 240 kl/s for an anode flow rate of 10.46 mg/s.	153
Figure 5-1: Configuration 1: Diagram of the cluster with the 1 m arc of data collection centered on P5-A.....	158

Figure 5-2: Configuration 2: Diagram of the cluster with the 1 m arc of data collection centered on the cluster.....	159
Figure 5-3: Cluster discharge current with the P5-A operating at 300 V, 5.14 A and the P5-B operating at 300 V, 4.96 A. The measurements are taken at a nominal pumping speed of 240 kl/s: 7.2×10^{-4} Pa (5.4×10^{-6} Torr).....	161
Figure 5-4: Cluster discharge current with the P5-A operating at 300 V, 5.76 A and the P5-B operating at 300 V, 5.68 A. The measurements are taken at a nominal pumping speed of 70 kl/s: 3.7×10^{-3} Pa (2.8×10^{-5} Torr).....	162
Figure 5-5: Discharge current of the monolithic P5-A (300 V, 5.34 A) at a backpressure of 9.1×10^{-6} Torr-Xe and the clustered P5-A (300 V, 5.24 A) at a backpressure of 8.6×10^{-6} Torr-Xe.....	162
Figure 5-6: Traces of the floating potential and plasma potential as a function of angle in Configuration 1. The cluster operating condition is 300 V, 5.25 mg/s at 3 backpressures.	166
Figure 5-7: Traces of the floating potential and plasma potential as a function of angle in Configuration 1. The cluster operating condition is 500 V, 5.25 mg/s at a backpressure of 5.4×10^{-6} Torr-Xe.	166
Figure 5-8: Traces of floating potential and plasma potential as a function of angle in Configuration 1. The cluster operating condition is 300 V, 10.46 mg/s at 3 backpressures.	167
Figure 5-9: Traces of the floating potential and plasma potential as a function of angle in Configuration 1. The cluster operating condition is 500 V, 10.46 mg/s at a backpressure of 8.9×10^{-6} Torr-Xe.	167
Figure 5-10: Traces of the floating potential and plasma potential as a function of angle in Configuration 2. The cluster operating condition is 300 V, 10.46 mg/s at 3 backpressures.	168
Figure 5-11: Traces of the floating potential and plasma potential as a function of angle in Configuration 2. The cluster operating condition is 500 V, 5.25 mg/s at 2 backpressures.	168
Figure 5-12: Traces of the floating potential and plasma potential as a function of angle in Configuration 2. The cluster operating condition is 300 V, 10.46 mg/s at 3 backpressures.	169
Figure 5-13: Traces of the electron number density and temperature as a function of angle in Configuration 1. The cluster operating condition is 300 V, 5.25 mg/s at 3 backpressures.	172

Figure 5-14: Traces of the electron number density and temperature as a function of angle in Configuration 1. The cluster operating condition is 500 V, 5.25 mg/s at 5.4×10^{-6} Torr-Xe.....	173
Figure 5-15: Traces of the electron number density and temperature as a function of angle in Configuration 1. The cluster operating condition is 300 V, 10.46 mg/s at 5.4×10^{-6} Torr-Xe.....	173
Figure 5-16: Traces of the electron number density and temperature as a function of angle in Configuration 1. The cluster operating condition is 500 V, 10.46 mg/s at 8.9×10^{-6} Torr-Xe.....	174
Figure 5-17: Traces of the electron number density and temperature as a function of angle in Configuration 2. The cluster operating condition is 300 V, 5.25 mg/s at 3 operating pressures.....	174
Figure 5-18: Traces of the electron number density and temperature as a function of angle in Configuration 2. The cluster operating condition is 500 V, 5.25 mg/s at 5.4×10^{-6} Torr-Xe.....	175
Figure 5-19: Traces of the electron number density and temperature as a function of angle in Configuration 2. The cluster operating condition is 300 V, 10.46 mg/s at 3 operating pressures.....	175
Figure 5-20: The cluster ion current density as a function of angle in Configuration 1. The cluster operating condition is 300 V, 5.25 mg/s at a backpressure of 8.9×10^{-6} Torr-Xe.....	179
Figure 5-21: The cluster ion current density as a function of angle in Configuration 2. The cluster operating condition is 300 V, 5.14 A at a backpressure of 8.9×10^{-6} Torr-Xe.....	179
Figure 5-22: The cluster ion current density as a function of angle in Configuration 1. The monolithic thruster and cluster operating condition is 300 V, 5.25 mg/s....	180
Figure 5-23: The cluster ion current density as a function of angle in Configuration 1. The cluster and monolithic thruster operating condition is 300 V, 10.46 mg/s..	180
Figure 5-24: The cluster ion current density as a function of angle in Configuration 1. The cluster and monolithic thruster operating condition is 500 V, 5.25 mg/s...	181
Figure 5-25: The cluster ion current density as a function of angle in Configuration 2. The cluster operating condition is 300 V, 5.25 mg/s at 3 backpressures.	181
Figure 5-26: The cluster ion current density as a function of angle in Configuration 2. The cluster operating condition is 300 V, 10.46 mg/s at 3 backpressures.	182

Figure 5-27: The cluster ion current density as a function of angle in Configuration 2. The cluster operating condition is 500 V, 5.25 mg/s at 3 backpressures.	182
Figure 5-28: RPA traces of the cluster in Configuration 2 for backpressures of 8.9×10^{-6} Torr-Xe with the cluster elements operating at 300 V, 10.46 mg/s. (0° to 15°)	185
Figure 5-29: RPA traces of the cluster in Configuration 2 for backpressures of 8.9×10^{-6} Torr-Xe with the cluster elements operating at 300 V, 10.46 mg/s. (20° to 45°)	186
Figure 5-30: RPA traces of the cluster in Configuration 2 for backpressures of 8.9×10^{-6} Torr-Xe with the cluster elements operating at 300 V, 10.46 mg/s. (50° to 90°)	186
Figure 5-31: RPA traces of the cluster in Configuration 2 for backpressures of 8.6×10^{-6} Torr-Xe and 5.4×10^{-6} Torr-Xe with the cluster elements operating at 500 V, 5.25 mg/s.	187
Figure 5-32: RPA traces of the cluster in Configuration 2 for backpressures of 1.3×10^{-5} Torr-Xe and 8.9×10^{-6} Torr-Xe with the cluster elements operating at 300 V, 10.46 mg/s.	187
Figure 5-33: ExB traces of the cluster in Configuration 2 for backpressures of 8.9×10^{-6} Torr-Xe and with the cluster elements operating at 300 V, 10.46 mg/s.	190
Figure 5-34: ExB traces of the cluster in Configuration 2 for backpressures of 5.4×10^{-6} Torr-Xe with the cluster elements operating at 300 V, 5.25 mg/s.	190
Figure 5-35: ExB traces of the cluster in Configuration 2 for backpressures of 8.6×10^{-6} Torr-Xe with the cluster elements operating at 300 V, 5.25 mg/s.	191
Figure 5-36: ExB traces of the cluster in Configuration 2 for backpressures of 8.6×10^{-6} Torr-Xe and with the cluster elements operating at 500 V, 5.25 mg/s.	191
Figure 5-37: ExB traces of the cluster in Configuration 2 for backpressures of 8.9×10^{-6} Torr-Xe and with the cluster elements operating at 500 V, 5.25 mg/s.	192
Figure 5-38: Cluster thrust measurements at anode flow rates of 5.25 mg/s and 10.46 mg/s as a function of discharge voltage at nominal pumping speeds of 70, 140, and 240 kl/s.	193
Figure 5-39: Cluster thrust measurements in comparison to the addition of the monolithic thrust for an anode flow rate of 5.25 mg/s at nominal pumping speeds of 70, 140, and 240 kl/s.	198
Figure 5-40: Cluster thrust measurements in comparison to the addition of the monolithic thrust at an anode flow rate of 10.46 mg/s at nominal pumping speeds of 70, 140, and 240 kl/s.	199

Figure 5-41: Percent difference between measured cluster thrust and the addition of the measured monolithic thrust at anode flow rates of 5.25 mg/s and 10.46 mg/s at nominal pumping speeds of 70, 140, and 240 kl/s.....	199
Figure 5-42: Cluster anode efficiency versus discharge voltage at nominal pumping speeds of 70, 140, and 240 kl/s.	200
Figure 5-43: Cluster anode specific impulse versus discharge voltage at nominal pumping speeds of 70 kl/s, 140 kl/s, and 240 kl/s.....	200
Figure 5-44: Thrust versus discharge voltage for the sum of the P5-A and P5-B at a nominal pumping speed of 70 kl/s, and the thrust of the cluster at nominal pumping speed of 140 kl/s.	201
Figure 5-45: Specific impulse versus discharge voltage for the sum of the P5-A at a nominal pumping speed of 70 kl/s and the cluster at a nominal pumping speed of 140 kl/s.....	201
Figure 5-46: Anode efficiency versus discharge voltage for the sum of the P5-A at a nominal pumping speed of 70 kl/s, and the cluster at a nominal pumping speed of 140 kl/s.....	202
Figure 6-1: Diagram of the shared cathode circuit.....	208
Figure 6-2: Diagram of the separate cathodes on the cluster.	209
Figure 6-3: Discharge current as a function of thruster centerline distance for anode flow rates of 5.25 mg/s at a backpressure of 5.4×10^{-6} Torr-Xe.....	211
Figure 6-4: Discharge current as a function of thruster centerline distance for anode flow rates of 10.46 mg/s at a backpressure of 8.9×10^{-6} Torr-Xe.....	211
Figure 6-5: Cathode-to-ground voltage as a function of thruster centerline distance for an anode flow rate of 5.25 mg/s at a backpressure of 5.4×10^{-6} Torr-Xe.....	212
Figure 6-6: Cathode-to-ground voltage as a function of thruster centerline distance for an anode flow rate of 10.46 mg/s at a backpressure of 8.9×10^{-6} Torr-Xe.....	212
Figure 6-7: Sharing Cathode A - Discharge current as a function of thruster centerline distance 5.25 mg/s at a backpressure of 5.4×10^{-6} Torr-Xe.....	214
Figure 6-8: Sharing Cathode A - Discharge current as a function of thruster centerline distance 10.46 mg/s at a backpressure of 8.9×10^{-6} Torr-Xe.....	215
Figure 6-9 Sharing Cathode A – Cathode-to-ground voltage as a function of thruster centerline distance 5.25 mg/s at a backpressure of 5.4×10^{-6} Torr-Xe.....	215

Figure 6-10: Sharing Cathode A - Cathode-to-ground voltage as a function of thruster centerline distance 10.46 mg/s at a backpressure of 8.9×10^{-6} Torr-Xe.....	216
Figure 6-11: Sharing Cathode B - Discharge current as a function of thruster centerline distance 5.25 mg/s at a backpressure of 5.4×10^{-6} Torr-Xe.....	216
Figure 6-12: Sharing Cathode B - Discharge current as a function of thruster centerline distance 10.46 mg/s at a backpressure of 8.9×10^{-6} Torr-Xe.....	217
Figure 6-13: Sharing Cathode B - Cathode-to-ground voltage as a function of thruster centerline distance 5.25 mg/s at a backpressure of 5.4×10^{-6} Torr-Xe.....	217
Figure 6-14: Sharing Cathode B - Cathode-to-ground voltage as a function of thruster centerline distance 10.46 mg/s at a backpressure of 8.9×10^{-6} Torr-Xe.....	218
Figure 6-15: Diagram of cluster sharing a single cathode.	220
Figure 6-16: Sharing a Centered Cathode - Discharge current as a function of thruster centerline distance at an anode flow rate of 5.25 mg/s at a backpressure of 5.4×10^{-6} Torr-Xe.	220
Figure 6-17: Sharing a Centered Cathode - Discharge current as a function of thruster centerline distance at an anode flow rate of 10.46 mg/s.	221
Figure 6-18: Sharing a Centered Cathode - Cathode-to-ground voltage as a function of thruster centerline distance at an anode flow rate of 5.25 mg/s.....	221
Figure 6-19: Sharing a Centered Cathode - Cathode-to-ground voltage as a function of thruster centerline distance at an anode flow rate of 10.46 mg/s.....	222
Figure 6-20: Diagram of the cathode displacement setup.....	223
Figure 6-21: Discharge current versus thruster-to-centerline separation distance for a nominal pumping speed of 240 kl/s.	225
Figure 6-22: Cathode-to-ground floating voltage versus thruster-to-centerline separation distance for a nominal pumping speed of 240 kl/s.....	226
Figure 6-23: Thrust versus thruster-to-centerline separation distance for the 5.25 mg/s anode flow rate at a nominal pumping speed of 240 kl/s.....	226
Figure 6-24: Thrust versus thruster-to-centerline separation distance for the 10.46 mg/s anode flow rate at a nominal pumping speed of 240 kl/s.....	227

LIST OF TABLES

Table 2-1: 173Mv1 Cold Flow operating conditions in VF-12.	31
Table 2-2: Dimensions of Probe A.....	52
Table 2-3: Dimensions of Probe C.....	55
Table 2-4: Dimensions of Probe D.....	57
Table 2-5: Probe D component bias voltages.....	57
Table 2-6: Dimensions of Probe E (AFRL).	60
Table 2-7: Probe E component bias voltages.....	60
Table 2-8: Geometric properties of the ExB probe used for this study.....	73
Table 3-1: Nominal pumping speeds and corresponding LVTF operating pressures for each anode flow rate and thruster condition investigated.	89
Table 3-2: Ionization gauge correction constants for each pumping speed.	94
Table 4-1: P5-A Operating conditions	112
Table 4-2: P5-B Operating conditions	113
Table 4-3: Ion Beam current, ratio of discharge current to beam current, and 90% divergence half-angle for each backpressure.	130
Table 4-4: Ion species fraction on the centerline of P5-A for 3 facility backpressures (300 V, 5.25 mg/s) in comparison to ion species fractions measured by Gulczinski on the P5 operating at 300 V, 5.3 A.....	143
Table 5-1: Cluster operating conditions.....	158

NOMENCLATURE

Constants

e	Electron charge	[1.6×10^{-19} C]
ϵ_0	Permittivity of free space	[8.854×10^{-12} F/m]
g_e	Earth's gravitational constant	[9.81 m/s ²]
k_b	Boltzmann's constant	[1.38×10^{-23} J/K]
m_e	Electron mass	[9.11×10^{-31} kg]
m_p	Proton mass	[1.67×10^{-27} kg]
μ_0	Permeability of free space	[$4\pi \times 10^{-7}$ N/A ²]

Variables

A_c	Collector area	[m ²]
A_{exit}	Thruster exit plane area	[m ²]
a_1	Collimator entrance orifice diameter	[m]
a_2	Collimator exit orifice diameter	[m]
a_3	Drift tube entrance diameter	[m]
a_4	ExB collector diameter	[m]
\mathbf{B}, \vec{B}	Magnetic field vector	[T]
B	Scalar magnetic field strength	[T]
d	Plate separation (in both ESA and ExB probes)	[m]

\mathbf{E}, \vec{E}	Electric field vector	[V/m]
E	Scalar electric field strength	[V/m]
$f_i(v)$	Ion velocity distribution function	[-]
$f(V)$	Ion energy per charge distribution function	[-]
\mathbf{F}, \vec{F}	Force vector	[N]
I^+	Collector current	[A]
I_B	Ion beam current	[A]
I_d	Discharge current	[A]
I^e	Emission current	[A]
I_i	Ion Beam current	[A]
$I_{i,sat}$	Ion saturation current	[A]
I_j	Current due to species j	[A]
I_p	Probe current	[A]
I_r^+	Independent residual current	[A]
I_{sp}	Specific impulse	[sec]
$i(\theta)$	Ion current density	[A/m ²]
\mathbf{j}, \vec{j}	Current density vector	[A/m ²]
j	Current density scalar	[A/m ²]
K_{45}	ESA spectrometer constant	[-]
m_{final}	Final spacecraft mass (after maneuver)	[kg]
m_i	Ion mass	[kg]
$m_{initial}$	Initial spacecraft mass (before maneuver)	[kg]
m_{prop}	Propellant mass load	[kg]

\dot{m}	Propellant mass flow rate	[kg/sec]
\dot{m}_{anode}	Propellant mass flow rate through the anode	[kg/sec]
\dot{m}_{in}	Rate of background gas ingestion into engine	[kg/sec]
n_e	Electron number density	[m ⁻³]
n_i	Ion number density	[m ⁻³]
n_j	Number density of ions with charge multiple j	[m ⁻³]
n_n	Neutral number density	[m ⁻³]
P	Pressure	[Torr, Pa]
P_c	Corrected pressure	[Torr, Pa]
P_B	Background pressure	[Torr, Pa]
P_i	Indicated pressure	[Torr]
p_e	Electron pressure	[Torr]
P_t	Thrust power	[watts]
P_{in}	Input power	[watts]
q	Electric charge	[C]
q_i	Ion charge state (1, 2, 3, ...)	[-]
q_{eff}	Effective charge state	[-]
$r_{L,e}$	Electron Larmor radius (gyroradius)	[m]
$r_{L,i}$	Ion Larmor radius (gyroradius)	[m]
r_p	Probe electrode radius	[m]
R	Resolution	[-]
S'	Gauge sensitivity	[-]
T	Thrust	[N]

T_e	Electron Temperature	[K] or [eV]
T_i	Ion temperature	[K] or [eV]
T_n	Neutral temperature	[K]
u_o	Drift Velocity	[m/s]
\bar{u}_e	Exhaust velocity	[m/s]
V	Voltage	[V]
V_b	Beam voltage	[V]
V_{cg}	Cathode-to-ground voltage	[V]
V_D	Discharge voltage	[V]
V_{grid}	Repelling grid voltage	[V]
V_{ExB}	Voltage between electrodes of ExB probe	[V]
V_R	ESA ion repeller plate voltage	[V]
v_{crit}	Critical velocity	[m/s]
v_{ExB}	ExB drift speed	[m/s]
v_i	Ion velocity	[m/s]
$v_{th,e}$	Electron thermal speed	[m/s]
$v_{th,i}$	Ion thermal speed	[m/s]
Δv	Velocity Increment	[m/s]
W	Characteristic discharge channel dimension	[m]
w	Slit width	[m]
x	Distance	[m]
Z_c	Length of inlet collimator	[m]
Z_f	Distance between collimators	[m]

Z_M	Length of exit collimator	[m]
α_j	Fraction of ions with charge multiple j	[-]
∇	Gradient operator	[m ⁻¹]
γ	Secondary electron yield	[-]
Φ	Particle flux	[particles/m ² -s]
ϕ	Plasma potential	[V]
η_t	Total efficiency	[-]
λ_D	Debye length	[m]
Λ	Plasma parameter	[-]
ν	Total electron collision frequency	[s ⁻¹]
Ω_j	Current fraction due to species j	[-]
σ_{CEX}	Charge exchange collision cross section	[m ²]

CHAPTER 1

INTRODUCTION

1.1 Electric Propulsion Overview

The benefits of electric propulsion (EP) become more attractive as mission velocity increments, Δv and the amount of available in-space power increase. The roots of modern EP go back to the seminal work performed in the 1960s.^{1, 2, 3} This work was aimed at developing more efficient propulsion systems for the future exploration of space.

The goal of a rocket propulsion system is to deliver the maximum payload to a given destination as efficiently as possible. The amount of energy required to deliver a payload is related directly to the velocity increment required for the mission. The rocket equation, shown in Eqn. 1-1, relates the ratio of the initial mass, $m_{initial}$ and the final mass, m_{final} of the rocket for a thrust period to the average exhaust velocity, \bar{u}_e and required Δv . The initial mass is composed of the final mass of the rocket plus the mass of the propellant, as shown in Eqn. 1-2

$$\frac{m_{final}}{m_{initial}} = 1 - e^{-\Delta V / g I_{sp}} \quad \text{Eqn. 1-1}$$

$$m_{initial} = m_{final} + m_{prop} \quad \text{Eqn. 1-2}$$

For a chemical rocket, the amount of energy that can be released from the propellant is limited to the energy stored in the chemical bonds of the propellant

molecules. Thus, \bar{u}_e of chemical rockets has a fixed maximum value dependent on the propellant used. For a chemical rocket, we see that the amount of propellant required for a given mission increases exponentially with increasing Δv . This means that the mission will lose payload mass or the cost of the mission must increase because more propellant is required.

In an electric propulsion device, electrical energy accelerates the particles to high velocities to generate thrust. EP offers a significant advantage over chemical rockets because the exhaust velocity is not limited by the amount of energy that is released from the chemical bonds that hold molecules together. Therefore, an exponential decrease in mass ratio can be realized through an increase in propellant exhaust velocity for a mission of given Δv . Clearly, the advantages of electric propulsion are best suited to missions with large Δv .

The main attractions of EP devices are their ability to achieve specific impulses far above those of chemical rockets and their efficient use of propellant.³ EP devices are ideal for deep space and station-keeping missions, which require high specific impulse. Specific impulse is a measure of the amount of thrust a propulsion device makes per unit mass flow of propellant. Eqn. 1-3 shows that the specific impulse (I_{sp}) is equivalent to the thrust, T divided by the product of the propellant mass flow rate, \dot{m} and the acceleration due to gravity at the earth's surface, g_e . I_{sp} is also equivalent to the average exhaust velocity of the propellant divided by g_e .

$$I_{sp} \equiv \frac{T}{\dot{m}g_e} = \frac{\bar{u}_e}{g_e} \quad \text{Eqn. 1-3}$$

In spite of the fact that EP systems have large exhaust velocities, they do not have large thrust levels because of the limited spacecraft power available. However, this makes EP systems very attractive for missions such as orbit-transfer, station-keeping of satellites, and deep space missions, which require large Δv and high specific impulses. Figure 1-1 illustrates this point for the Jupiter Icy Moons Orbiter (JIMO), a mission designed to explore three moons of Jupiter.⁴ Figure 1-1 shows a plot of the mass ratios using the mission Δv of 50 km/s for the JIMO mission powered by EP and chemical rockets systems. The EP system increases the amount of delivered payload mass from 0.002% to 29%. This analysis does not account for the added mass of the power processing unit needed for the EP system nor losses associated with long “burn” times of EP systems. Nevertheless, the result is clear; EP systems enable space missions that could never take place with chemical propulsion alone.

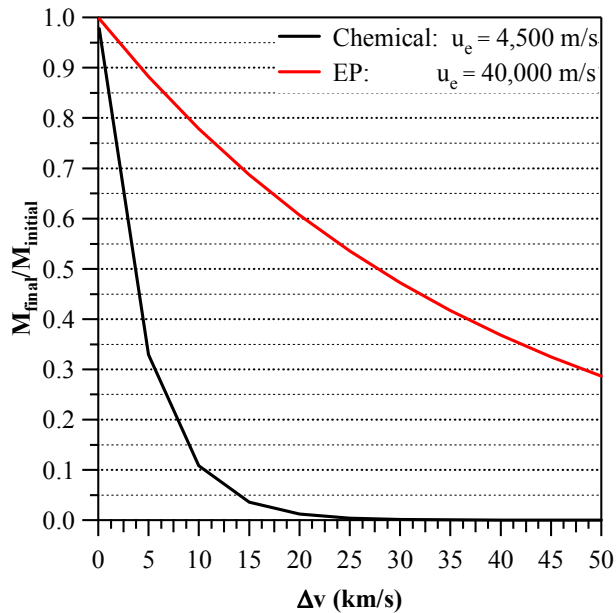


Figure 1-1: Comparison of the Mass ratios of an EP and chemical system for the JIMO mission.

For a spacecraft of fixed launch mass, the increase in the ratio of $m_{final}/m_{initial}$ may also be used to reduce the amount of required propellant mass. This mass savings can be used to add more scientific equipment to the spacecraft. To reduce cost, the saving in propellant mass may allow a smaller, less expensive launch vehicle to be used. Keeping all other parameters constant and applying the high I_{sp} of an EP system increases the capability of the spacecraft. The high I_{sp} of EP systems increases the life of orbiting satellites by allowing more station-keeping maneuvers for a given amount of propellant. To achieve these benefits, the type of electric propulsion system selected must take into account the mission requirements.

Electric propulsion is characterized into three distinct divisions. Each of these divisions will be discussed in more detail in the following sections.

1.1.1 Electrothermal Propulsion

Electrothermal propulsion devices use electrical energy supplied by the spacecraft to heat the propellant and expand it out of a nozzle to create thrust. This type of propulsion is most closely related to the chemical rocket engine. The addition of thermal heat is accomplished in two ways.

The first approach is the use of an electrical resistor to transfer the electrical energy to thermal energy in the propellant. The heated gas is then expanded out of a diverging nozzle to create thrust. This device is known as a resistojet. Resistojets have been used for stationkeeping on communication satellites for more than 20 years. The resistojets used on commercial spacecraft typically have specific impulses of 300 s or more for thrust efficiencies above 50%, at input power levels of 400-800 W.⁵

The second approach to electrothermal propulsion uses an electrical arc established between an anode and cathode located in the throat of the nozzle. The arc adds thermal energy to the propellant before it is expanded out of a diverging nozzle to create thrust. Devices of this type are categorized as arcjets. These devices operate on a wide range of propellants that are compatible with all current storage systems.⁶ Arcjets have been developed for a multitude of applications ranging from stationkeeping of moderate-sized spacecraft (500 W, hydrazine) to a piloted mission to Mars (100 kW, hydrogen).⁷ Specific impulses range from approximately 500-600 s on hydrazine to approximately 2,000 s on hydrogen.^{8,9,10}

1.1.2 Electromagnetic Propulsion

Electromagnetic propulsion devices use the interaction of applied electric and magnetic fields to accelerate ions out of the device. These devices use a potential applied between the anode and cathode to ionize the propellant gas. A current flows through the ionized propellant that interacts with self-generated and/or externally-applied magnetic fields through the Lorentz force, which accelerates the plasma downstream.¹¹ Eqn. 1-4 shows the force produced by the interaction of the current and magnetic field.

$$\vec{F} = \vec{j} \times \vec{B} \quad \text{Eqn. 1-4}$$

This division of electric propulsion consists of magnetoplasmadynamic (MPD) thrusters, pulse-inductive thrusters (PITs), and pulsed plasma thrusters (PPTs). Electromagnetic devices do not accelerate the propellant with an electric field, and thus have high power densities because they are not “space-charge” limited.

The MPD thruster uses an annular anode with a concentric central cathode to drive current through the flowing propellant stream. The propellant is ionized by a high-

current arc created between the anode and cathode. The azimuthal magnetic field generated by the current returning to the cathode (self-field) or supplied by external means (applied field) interacts with radial discharge current flowing through the plasma to produce an axial electromagnetic body force (Lorentz Force), which accelerates the propellant to produce thrust. The thrust is augmented by the conversion of propellant enthalpy to directed kinetic energy. These engines are not “space-charge” limited in propellant throughput and thus achieve large exhaust velocities (5–100 km/s) at high thrust densities.¹²

A pulsed inductive thruster (PIT) uses a fast gas valve to inject a few milligrams of propellant over a flat induction coil. Once the gas has been injected, a bank of high-voltage, high-energy storage capacitors is discharged, providing a large azimuthal current pulse to the coil. The time-varying electromagnetic field caused by the current pulse ionizes the propellant gas and causes the ionized gas to accelerate away from the coil, which produces thrust.¹³

In a pulsed plasma thruster (PPT), electrical power is used to ablate, ionize, and electromagnetically accelerate atoms and molecules from a block of solid propellant material, typically a solid bar of TeflonTM. A negator spring feeds the Teflon into the discharge area. The power processing unit (PPU) uses power from the spacecraft to charge a capacitor. Once the capacitor is charged, a spark igniter is fired to create an initial conducting path for the primary discharge. During the discharge, current flowing between the electrodes ablates layers of the Teflon bar. The ablated products are ionized and then accelerated by the electromagnetic Lorentz force to a velocity of 10 - 20 km/sec,

which produces thrust. PPTs have a specific impulse on the order of 1000 - 2000s and thrust efficiencies of approximately 10%.¹⁴

1.1.3 Electrostatic Propulsion

The last division of EP is electrostatic propulsion. Electrostatic propulsion devices use large electric fields to accelerate the ionized propellant to generate thrust. Eqn. 1-5 shows the electrostatic force on a particle of charge, q placed in an electric field, \vec{E} . This division of devices includes Hall thrusters, gridded ion engines, colloid thrusters, and field effect electric propulsion (FEEP). Hall thrusters are the focus of this work and will be discussed in detail in the following section.

$$\vec{F} = q\vec{E} \qquad \text{Eqn. 1-5}$$

Of the electrostatic devices, the gridded ion engine currently has the most flight time on western spacecraft. The gridded ion engine injects propellant both through a discharge cathode and through a ring of injectors. The discharge cathode emits electrons that are accelerated by the electric field established between the positively biased discharge chamber walls and the negatively biased cathode. To enhance the ionization efficiency, the electrons are then trapped in a “ring-cusp” magnetic field to increase their residence time in the discharge chamber. The electrons ionize propellant distributed from the positively biased anode walls by striking the gas atoms, knocking away one or more of the electrons orbiting an atom's nucleus. The ions drift downstream to the rear of the discharge chamber where they encounter an area of strong electric field created across a set of dished grids. The ions are accelerated out of the ion engine by the electric field, which produces thrust. An external cathode (neutralizer) positioned downstream of the accelerator grid keeps the spacecraft electrically neutral with respect to its environment

by emitting one electron for every positively charged ion that leaves the thruster. Ion thrusters have specific impulses of 1,000-10,000 seconds with efficiencies approaching 80%.²

Currently, colloid thrusters and FEEP have not been realized on a large scale. Thus, they will not be discussed in this dissertation. Further information on colloid thrusters and FEEP can be found in References 15 and 16, respectively.

1.2 Hall Effect Thruster Overview

1.2.1 Hall Thruster Physics

Hall effect thrusters (HETs) are electrostatic electric propulsion devices. The Hall thruster uses a radial magnetic field to decrease the axial electron mobility, creating an axial electric field. A schematic of the magnetic layer type is shown in Figure 1-2. The most common Hall thruster design uses an annular discharge chamber. However, successful operation has been achieved with racetrack and linear configurations.^{17, 18, 19, 20}

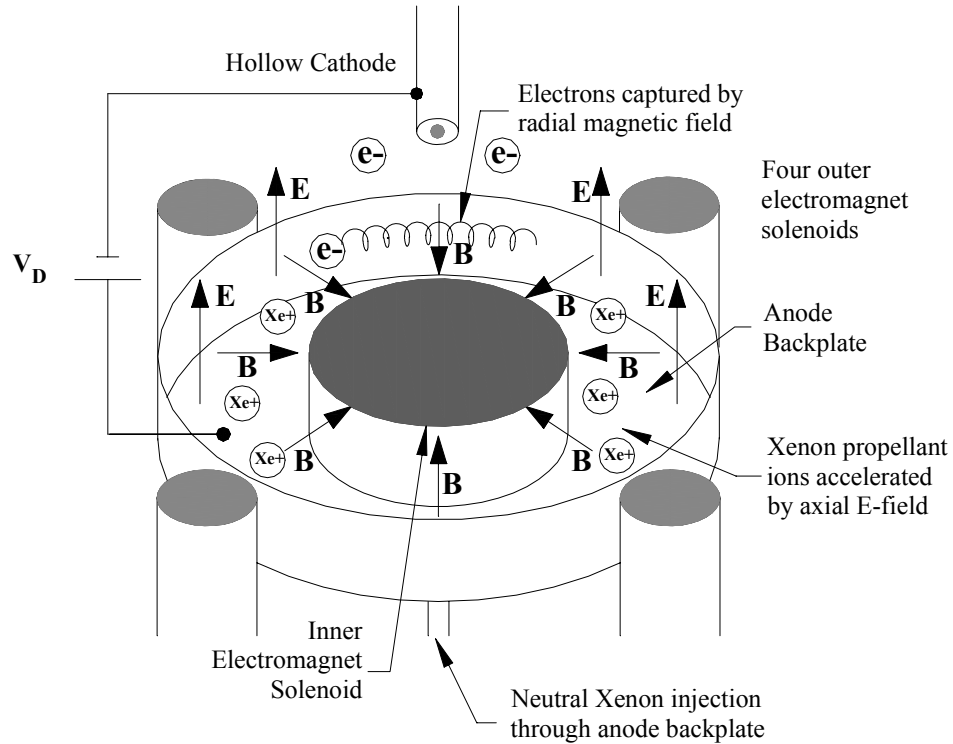


Figure 1-2: Schematic of a Hall thruster.

During HET operation, plasma is sustained within an annular discharge chamber by an axial electric field established between an external hollow cathode and the anode located at the rear. A hollow cathode emits electrons into the region immediately in front of the discharge chamber. The positively-biased anode located at the rear of the discharge chamber, which also serves as a propellant distributor, attracts electrons. On the way to the anode the electrons encounter a radially directed magnetic field that is generated by electromagnetic coils and guided by ferromagnetic inner and outer pole pieces. The strength of the magnetic field is strong enough to yield an electron gyroradius, $r_{L,e}$ considerably smaller than the characteristic width of the discharge channel, W . In addition, the magnetic field strength is chosen such that it has little effect on the much more massive ions. Eqn. 1-6 shows the necessary conditions.

$$r_{L,\beta} = \frac{m_i v_{th,e}}{eB} \ll W \ll r_{L,i} = \frac{m_i v_{th,i}}{eB} \quad \text{Eqn. 1-6}$$

The cyclotron motion generated by the radial magnetic field prevents electrons from traveling toward the anode unless they collide with the wall or another particle. This configuration allows strong electric fields to be formed in the plasma that are orthogonal to the applied magnetic field. The gradient in the nearly orthogonal electric field causes an azimuthal flow of electrons in the $\mathbf{E} \times \mathbf{B}$ direction at a speed of v_{ExB} , defined in Eqn. 1-7. This component of electron motion normal to the electric field is called the Hall current. The annular discharge chamber allows a complete closed path for the Hall current, thus the device is also known as a closed-drift thruster. In spite of the suppressed axial motion of the electrons caused by the radial magnetic field, electrons do slowly diffuse toward the anode. The increase in electron residence time increases the ionization efficiency.

$$v_{ExB} = \frac{E}{B} \quad \text{Eqn. 1-7}$$

Xenon (or another noble gas or bismuth) diffuses toward the discharge channel exit plane. Most xenon atoms are ionized by collisions with the Hall current electrons before reaching the exit. The magnetic field has little effect on the ion motion and the large electric field efficiently accelerates the ions downstream. The thrust is the reaction force to the downstream acceleration of ions. The force is imparted to the thruster through the magnetic field surfaces created by the Hall current. The magnetic field surfaces, to first-order, are equipotential to the magnetic field lines of the thruster. The electron-ion pairs, along with additional electrons emitted from the hollow cathode to neutralize the beam, insure that the plasma meets the quasineutrality condition shown in

Eqn. 1-8. The quasineutral plasma created by the Hall thruster prevents the space-charge effect from limiting the current density. The space-charge effect occurs when a net build-up of charge alters the local electric field, thus restricting the charged particle motion in that region. Therefore, Hall thrusters are able to achieve much higher current densities than gridded ion engines.

$$n_e \approx n_i \quad \text{Eqn. 1-8}$$

At first glance, it appears that the thruster should be operated at the maximum possible discharge voltage to maximize the specific impulse of the device. However, the efficiency of the device does not increase monotonically with voltage due to the inefficiencies of the ionization process. The thruster efficiency is defined as the ratio of the jet power, P_t to the supplied electrical energy, P_{in} as shown in Eqn. 1-9.

$$\eta_t = \frac{P_t}{P_{in}} = \frac{1/2 T \cdot \bar{u}_e}{V_D I_D} \quad \text{Eqn. 1-9}$$

The mass of the required power supply scales with the required applied power, and thus the specific impulse of the Hall thruster at a constant thrust level. Therefore, the efficiency of the device is very important if the mass of the propulsion system is to be minimized. For optimum propulsion system performance, the EP thruster should not be operated at maximum I_{sp} , but at maximum efficiency to reduce the mass of the PPU.

1.3 Motivation

Initial development of Hall thrusters began independently in the US and in the former Soviet Union in the 1960s.^{1, 21, 22} At that time, the American researchers expected to develop high-power, light weight power supplies and thus they attempted to operate the thruster in the 5,000 to 10,000 second range.² The researchers soon found that the

acceleration mechanism became unacceptably inefficient at the discharge voltages required for these specific impulses. Thus, the researchers opted to develop the gridded ion engine to reach their specific impulse goals. However, development of the HET continued in the Soviet Union.

Following the dissolution of the former Soviet Union, much of the Russian technology has become available to Western scientists. US development of the HET technology over the last decade has turned it into one of the main EP systems considered for future space missions.

There are several configurations for closed drift thrusters (CDTs), which can be divided into two distinct types. The first type is the anode layer thruster, commonly referred to as a thruster with an anode layer (TAL). The second type is the magnetic layer thruster, commonly referred to as the stationary plasma thruster (SPT). The primary difference between the two is that the anode layer thruster has a metal discharge chamber and the magnetic layer type has a ceramic discharge chamber.³ Most closed drift thrusters are single-stage, but work has been done on two-stage thrusters.²³ Under the direction of Morozov the SPT matured, while in a competing group, Zharinov brought the TAL to a high level of flight readiness.³ Since 1972, the Soviet Union and Russia have flown more than 100 HETs in space; most of these have been SPTs.

Its combination of high specific impulse, efficiency, and thrust density has increased the popularity of HETs for use as spacecraft propulsion. Currently, the widespread use of HETs is hindered somewhat by the limited understanding of plume interaction with the spacecraft.

As the availability of in-space power increases, the trend in HET development is growing proportionally towards high-power engines. In the last ten years, the HET community has seen the completion of flight qualification to Western standards of the SPT-100 (1.35 kW),^{24, 25} on-going activities for qualifying the SPT-140 (4.5 kW),^{26, 27} BPT-4000 (3 and 4.5 kW),²⁸ and a 1000 hour test of the T-220 (10 kW).^{29, 30} The latest trends at government laboratories sponsoring HET research are towards monolithic power levels of 20-150 kW.³¹

The USAF has recently identified the high-power 20 kW CDT propulsion system as the baseline approach for a variety of missions.³² The Air Force Research Laboratory (AFRL) has performed extensive testing on a cluster of four 200 W HETs,³³ with the eventual goal of testing high-power clusters. The USAF is increasing spacecraft bus power through advanced solar array designs.

NASA has recently announced Project Prometheus³⁴, which strives to develop high-power nuclear reactors and electric propulsion systems.³⁴ The NASA Glenn Research Center (GRC) has recently tested a nominally 50 kW engine and was awarded a multimillion dollar contract to develop a 150 kW HET.

Next generation communication satellites are becoming both larger and more powerful. Recent satellite designs suggests that electric propulsion systems will have to double or triple in power from the current 3-5 kW systems within the next decade to satisfy commercial spacecraft needs. The ability of high-power HETs to perform orbit-raising as well as stationkeeping maneuvers may eliminate the need for chemical rockets on satellites and deep space probes. This means that vacuum systems will have to be

modified to handle the added propellant flow rates demanded by these higher-power thrusters.

1.3.1 Summary of Facility Effects

The limited understanding of plume interaction with the spacecraft has hindered the industry-wide use of HETs. The plume contains high-speed ions that can erode sensitive spacecraft surfaces, and contamination products created by thruster discharge channel erosion can coat solar cell optics, thus reducing their performance. The parasitic facility effects present in ground tests create additional plume components such as slow propellant ions and neutral atoms.³⁵ Ions and neutrals present in the HET plume interact through the process of resonant charge exchange (CEX) collisions.

Accounting for CEX ions is not the only obstacle to using ground tests for in-space performance prediction. The wide range of facilities used in HET testing makes it difficult for researchers to compare data sets, given dissimilar probe designs and elevated background pressures in facilities with modest pumping speeds and varying geometries.³⁶ As mentioned in the previous section, in spite of facility effects, there is a trend toward high-power Hall thruster propulsion systems.

There are several advantages inherent to going to larger thrusters. The geometric increase in thruster size causes the thruster to be inherently more efficient due to plasma scaling within the discharge chamber.³⁷ Furthermore, as size increases the radial magnetic field is more uniform and the reduction in wall losses increases performance. The lifetime improves with thruster size because the reduced plasma density results in fewer sputtering wall collisions, thus extending insulator life.

However, large thrusters have their own technical issues for ground testing. Many national electric propulsion test facilities, while physically large enough to test 50 kW thrusters, possess pumping speeds that are at least an order of magnitude too low to ameliorate facility pressure effects for plume/contamination studies, and life testing. The reason for this is that as thruster power and/or I_{sp} are increased, the internal discharge chamber pressure tends to decrease to maintain efficient operation.

Thruster mass flow rate, and hence facility background pressure, increase proportionately with power for fixed thruster voltage. So as the power of the CDT increases, its internal pressure decreases because ion-neutral collision mean free path must be greater than the ion acceleration length. Yet, the background chamber pressure increases. This poses an issue not only for measuring high-power CDT performance and plume/contamination characteristics, but also for assessing engine life.³⁶

If the tank pressure is too high, the background gas can artificially modify the exhaust plume as well as alter the operation of the CDT itself.^{36, 38} Thruster operation may be influenced by entrainment and/or ingestion of the background chamber atoms. This effect artificially increases the propellant mass flow rate of the engine, resulting in performance and operation changes consistent with the increased number of propellant particles. Furthermore, plume diagnostic experiments can be affected. A large partial pressure of background gas molecules can affect ion current density and energy distribution measurements by artificially increasing the local charge density through charge exchange collisions.³⁹

NASA and the USAF both require high-power Hall thruster systems for future missions. The AFRL, NASA GRC, and laboratories in Europe have recently upgraded

their pumping systems in anticipation of higher-powered thrusters. It is clear that testing 50-kW-class CDTs in current or near-term test facilities is of concern given the fact that a large increase in pumping speed would still be necessary to satisfy pressure requirements. Vacuum facilities capable of testing 100-plus-kW CDTs are unlikely to be available in sufficient numbers by the time these engines are needed. Thus, modular, high-power CDT propulsion systems will undoubtedly be required both for USAF and NASA missions in the future to make ground testing feasible.

Several investigations are underway to model thruster performance and the interactions between Hall thruster plumes and spacecraft numerically.^{27, 40} The results of these models are highly dependent on the boundary conditions used. For simulations of laboratory experiments, one of the most important auxiliary inputs required by these codes is the background pressure of a laboratory vacuum chamber.⁴⁰ To provide high-fidelity data to the models that simulate the interaction between the Hall thruster plume and spacecraft, we must first correct the experimental performance and plume data for facility effects.

The goal of this research is to understand facility effects introduced by elevated backpressures. This investigation has included the characterization of the performance of the P5 HET (5 kW) at different pumping speeds,⁴¹ an evaluation of the ability of a collimated Faraday probe to filter out CEX ions while measuring the ion current density at elevated background pressures,^{42, 43, 44} and a pressure map of the Large Vacuum Test Facility (LVTF) and NASA GRC's Vacuum Facility 12 (VF-12) in conjunction with a computational facility model using the direct simulation Monte Carlo method (DSMC) to characterize chamber backpressure of the former.⁴⁵

1.3.2 Summary of Clustered Hall Thrusters for High-Power Missions

In response to the issue of national facility pumping limitations, the USAF has started to explore clustering as a way of reaching its high-power EP goal; i.e., the use of smaller Hall thrusters in a propulsion array.³³ In theory, clustering allows ground-based testing of a single, lower-power cluster element to predict the characteristics of the cluster. In general, a cluster of thrusters will have a lower total efficiency and higher dry mass than a monolithic device of equal power. Yet, a cluster provides propulsion system redundancy and the ability to vary the system power while allowing the thrusters in use to operate at their peak efficiency.

Currently, there is no fundamental basis for predicting:

- cluster performance
- interaction between cluster elements
- cluster lifetime
- spacecraft integration problems

from single-engine ground-based test data from a 1-plus-kW Hall thruster.

For example, plume divergence not only detracts from engine performance, but also may cause damage to the spacecraft due to sputtering. This issue may be even more pronounced when the engines are arranged in a cluster, since the plume of one engine will interact with the plume of another.

This portion of the research develops a Hall thruster cluster test capability, using the University of Michigan LVTF.^{46, 47, 48} A 2x1 cluster of UM/AFRL P5, 5 kW Hall thrusters has been constructed at the AFRL. This cluster facilitates the investigation of

high-power Hall thruster operation and provides insight on how chamber effects influence monolithic and cluster characteristics.

This study measures the thrust and plume characteristics of each of the P5 Hall thrusters over the range of 300 - 600 V at 5.25 mg/s and 10.46 mg/s. The two thrusters are then operated simultaneously and the thrust of the cluster is measured over the same thruster operating conditions. In addition, the effect of facility backpressure on Hall thruster performance is quantified. Furthermore, Hall thruster cluster configurations are investigated.

1.4 Contribution of Research

The aim of this thesis is to investigate and characterize the effect of facility backpressure on Hall thruster cluster performance and plume characteristics. The hypothesis is that below a critical pressure, which depends on thruster mass flow rate, backpressure induced facility effects are negligible. As thrusters increase in size, current vacuum facilities will not be able to maintain operating pressures below the critical pressure. There are three possible solution paths to overcome facility effects in Hall thruster testing. The first is to develop new facilities and/or test in space. The second is to develop tools that correct plume and performance for facility effects. The third is to cluster small Hall thrusters together (which can be characterized at pressures where facility effects are negligible) to create high-power EP systems. The thesis investigates the last two of these possibilities.

The experimental investigation is composed of three major components. Facility effects are caused by the backpressure present in the vacuum facility so first we use the cold and hot flow pressure map investigation to understand the distribution of

neutral background gas in a vacuum facility with an operating Hall thruster. An ionization gauge position system is constructed to map the LVTF. This system moves five ionization gauges throughout the chamber to create a neutral density map of two vacuum facilities with a Hall thruster in operation. The cold flow* neutral density maps were used in conjunction with a DSMC code to determine the sticking coefficient of xenon onto a cryosurface. This work was the first measurement of the xenon-to-cryosurface sticking coefficient. The hot flow neutral density map data obtained were then compared to the results generated by the DSMC model, which allowed for verification of the model. The model is a tool that can accurately calibrate a vacuum facility in terms of pressure.

The second portion of this work is the facility effects investigation. This portion of the investigation tests the hypothesis by performing plume and performance measurement over a wide range of pressures. The plume of each cluster element is individually characterized at three vacuum facility operating pressures and two anode flow rates to study the effect of facility backpressure on plume parameters. A single Langmuir probe measures the plasma potential, electron number density, and electron temperature. The plume ion current density profile is characterized with five different Faraday probe designs. The ionization and acceleration processes are studied with a parallel-plate electrostatic energy analyzer, a retarding potential analyzer, and an ExB probe. In addition, the performance of each thruster is characterized at the conditions stated above with a null-type inverted pendulum thrust stand.

* Throughout the text, we use the phrase “cold flow” to denote xenon flowing through the thruster anode and cathode without a plasma discharge and “hot flow” to denote xenon flowing through the anode and cathode of an operating thruster.

A summary of the second portion of this work includes the following:

- The use of five Faraday probe designs shows that a magnetically-filtered Faraday probe possesses the ability to remove the effects of charge exchange ions that normally affect the wings of the ion current density traces.
- An increase in facility backpressure leads to an increase in the width of the ion energy distribution function, but it does not shift the location of the ion energy distribution maximum.
- Due to the elevated pressures present at the ExB probe entrance during P5 operation, it is not possible to accurately measure the percentage of multiply-charged particles in the thruster plume.
- Randolph's ingestion explanation does not adequately account for the elevated discharge current measured at elevated facility backpressures.³⁸
- The measured thrust increases with increasing facility backpressure.
- The variation of the facility backpressure does not lead to a clear technique to correct the performance of the Hall thruster operating at elevated backpressure.

The third portion of this work is an investigation to develop a fundamental understanding of how multi-kW clustered Hall thrusters operate and how one can use single-engine, ground-based data to predict the performance, plume interaction, and operation as a function of the cluster element centerline separation distance. A cluster of laboratory-model 5 kW Hall thrusters using Moscow Aviation Institute (MAI) hollow

cathodes were constructed for two primary reasons. Firstly, it allowed investigation of the performance, plume characteristics, and diagnostic operation at a range of facility operating pressures. Secondly, it allowed for the investigation of how Hall thruster clusters interact. The plasma parameters are measured in the plume of the Hall thruster cluster with the same diagnostics on the single cluster element. Measurements collected with the diagnostics centered on a single thruster element and on the cluster centerline show that no significant interaction occurs between the cluster elements. Comparison of the performance characteristics of the cluster and the monolithic thruster at conditions of nearly equal operating pressure shows that for a 5.25 mg/s anode flow rate the cluster thrust is simply the addition of the thrust of the two monolithic thrusters. In addition, the anode efficiency and specific impulse are approximately equal to that of the monolithic thruster. However, these trends do not hold at the 10.46 mg/s anode flow rate for conditions of equal operating pressure, which may be due to elevated facility backpressure.

To further understand the feasibility of clustering Hall thrusters on spacecraft, a study of thruster centerline spacing and cathode-to-thruster separation distance is performed. The results of this study show that the cluster thruster elements with a centerline separation distance of 2+ m can share a single cathode without coupling their ionization and acceleration processes. The study establishes that a Hall thruster to cathode centerline separation distance of 1.3 m does not negatively affect the performance of the thruster and reliable restarts are possible in this configuration. Variation of the thruster centerline separation distance shows that the gas flow of one thruster does not directly affect the performance of the adjacent thruster.

Currently, the only studies performed on facility effects are those of Randolph,³⁸ Manzella,⁴⁹ and a study at the University of Michigan's Plasmadynamics and Electric Propulsion Laboratory (PEPL) by Hofer and Peterson.⁴¹ In Russia, Semenkin has also noted the importance of facility effects and a need for EP testing standardization.³⁶ The work done by Randolph is based on free molecular diffusion controlling neutral gas ingestion into the discharge channel. The work makes gross assumptions about the ingestion area and does not explain the ionization process of the ingested gas. Manzella also studied facility effects, but he only looked at the plume characteristics with a nude Faraday probe, which as this Thesis shows is prone to facility backpressure effects. He also bled xenon into the facility with no support of why he chose the injection location other than convenience. Hofer and Peterson looked at how facility backpressure affects the performance of a Hall thruster. Unfortunately, the error in their thrust measurements was too large to discern facility effects. This thesis takes a holistic look at facility effects.

As discussed earlier, the concept of HET clustering has become of interest as in-space power has increased. The only work published at this time has been performed by Beal in conjunction with the AFRL, and the USAF European Office of Aerospace Research and Development (EOARD).^{33, 46, 47, 50} Beal characterized the basic plume properties, cross-talk, phenomena among cluster elements, the ion energy spectra downstream of the thrusters, and cluster sensitivity to cathode placement. Beal used a 2x2 cluster of Busek model BHT-200-X3 Hall thrusters, each of which operates at a nominal power of 200 watts. EOARD conducted tests at the Russian Central Research Institute of Machine Building (TSNIIMASH).^{51, 52} The EOARD sponsored cluster work used three D-55 TALs to demonstrate that multiple thrusters can share a single cathode

and operate from one common power supply with no noticeable increase in discharge current oscillations and no sign of “cross-talk” between the thrusters.

Building on the work discussed above, this thesis research investigates the performance and plume characteristics of a cluster of Hall thrusters versus a single monolithic element over a wide range of operating pressures. A criterion is validated for thruster element spacing to ensure that the elements do not interact adversely. In addition, several configurations for cathode sharing are investigated while varying the separation distance between the thruster centerlines. Finally, the performance of a thruster is measured as the cathode is moved away from the thruster centerline.

CHAPTER 2

EXPERIMENTAL APPARATUS

To characterize the effect of backpressure and clustering on the plume characteristics and performance of a Hall thruster, we measure the neutral number density, electron temperature, electron number density, ion current density, ion energy per unit charge distribution, multiple charge fractions, and performance. The diagnostics used for this purpose include 5 ionization gauges, a Langmuir probe, 5 Faraday probes of various design, a retarding potential analyzer, a parallel-plate electrostatic energy analyzer, an ExB probe, and a null-type inverted pendulum thrust stand. This chapter describes each piece of experimental hardware and the diagnostics used to perform this research. The text documents the physics governing the operation of each diagnostic and the electrical configurations used during each experiment. Geometric schematics of each of the diagnostics are provided as well as pictures of the actual device. Representative plots of data taken with several of the diagnostics show device repeatability and resolution. We also discuss the limitations and measurement error of each diagnostic.

2.1 Hall Thruster

2.1.1 AFRL/UM P5 Cluster

For this investigation, all experiments performed at PEPL use the AFRL/UM P5 2x1 cluster, laboratory-model Hall thrusters, shown in Figure 2-1. The P5 has a mean

diameter of 148 mm, a channel width of 25 mm, a channel depth of 38 mm, and a nominal power rating of 5 kW. Moscow Aviation Institute (MAI) laboratory-model cathodes are located at the 12 o'clock position on each of the thrusters. The cathode orifice is located approximately 30 mm downstream from the outer front pole piece and the cathode body is oriented at angle of 45° below horizontal. For all cases, the cathode flow rate is set at 0.92 mg/s. Haas provides a more detailed description of the P5 in Reference 53.

Each of the P5 Hall thrusters is powered by a separate set of power supplies and operates from its own cathode. The thruster electrical connections enter the chamber through two separate feedthrough ports. Each thruster discharge supply is connected to a filter consisting of a 1.3 Ω resistor in series with the discharge current and a 95 μF capacitor in parallel. The filter damps out thruster discharge oscillations. Discharge current oscillations are measured with a F.W. Bell IHA-25 Hall probe connected to a Tektronix TDS 3034B oscilloscope. Figure 2-2 shows an electrical schematic of the P5 Hall thruster electrical circuit.

High-purity (99.9995% pure) xenon propellant is supplied to the Hall thrusters from compressed gas bottles through stainless-steel feed lines. MKS 1179JA mass flow controllers with full scales of 20 and 200 sccm meter the cathode and anode propellant flows, respectively. The flow controllers are calibrated with a custom apparatus that measures gas pressure and temperature as a function of time in an evacuated chamber of known volume. The mass flow controllers have an accuracy of $\pm 1\%$ full scale.

One of the most important criteria for Hall thruster clustering is the spacing of the array elements. To minimize structural mass and the physical envelope of the cluster,

the elements of the cluster should be as close as possible without adversely affecting their performance. In large part, the magnetic field inside the Hall thruster channel governs the performance of the Hall thruster.⁵⁴ The cluster elements are spaced 40 cm apart (centerline-to-centerline), to ensure that the magnetic field within the discharge chamber and the external radial field are unaffected by the adjacent element of the cluster array at the maximum magnetic field strength of the monolithic thruster. The maximum magnetic field operating condition has an inner coil current of 8.53 A and a outer coil current of 2.05 A. The radial spacing of 40 cm is selected by measuring the radial magnetic field of one thruster and then of the cluster while increasing centerline spacing. The differences in the radial component of the magnetic field between these two configurations are found to be negligible (less than 5%) with a centerline spacing of 40 cm. The magnetic field is measured 6 mm upstream of the thruster exit plane with a standard Hall probe mounted on a linear motion table to provide linear axial position with an accuracy of ± 1 mm. The error in the magnetic field strength measurement is $\pm 5\%$.

The voltage potentials within the plume plasma are also considered for thruster element spacing. The varying magnitude of the plume plasma potential is not large enough to create an electric field sufficient to cause a substantial deviation in the trajectory of high-speed ions created in the discharge channel. Therefore plume interaction should not be large enough to affect the performance of the individual elements. However, plume interaction may affect the plume characteristics by changing the trajectories of the slow CEX ions.⁴⁷ This effect is investigated in Chapter 5.



Figure 2-1: UM/AFRL 2x1 5 kW P5 Hall Thruster Cluster.

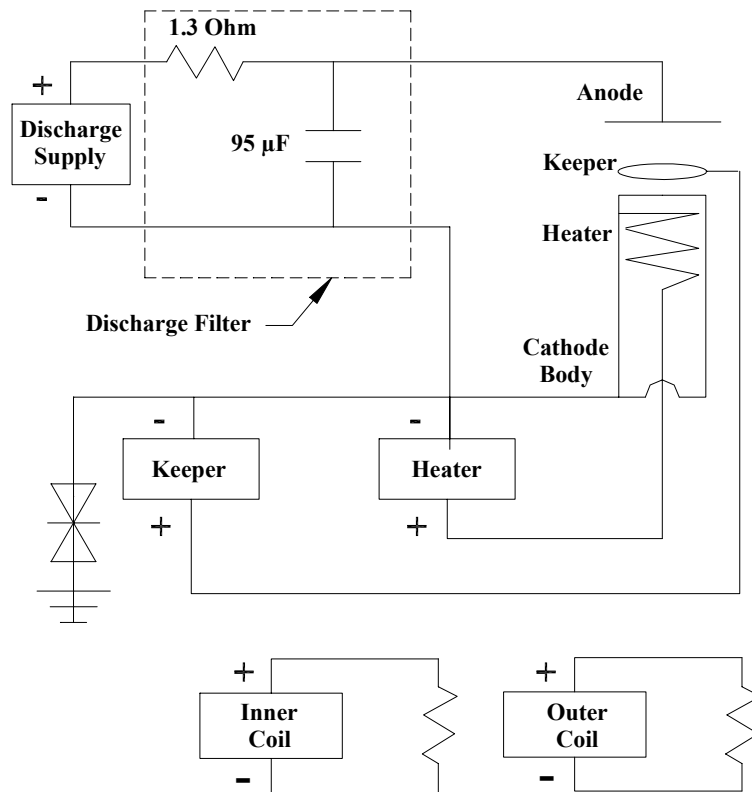


Figure 2-2: Electrical schematic of power electronics used to run the P5 Hall thruster.

2.1.2 NASA-173Mv1

The pressure map experiments in VF-12 at NASA GRC are performed on the NASA-173Mv1, which is shown in Figure 2-3. The 173Mv1 has a mean diameter of 148 mm, a channel width of 25 mm, a channel depth of 38 mm, and has a nominal power rating of 5 kW. The 173Mv1 and the P5 have identical discharge chamber dimensions, but different magnetic field profiles. A laboratory-model cathode is located at the 12 o'clock position on the thruster. The cathode orifice is located approximately 30 mm downstream from the outer front pole piece. For all cases, the cathode flow rate is set at 0.60 mg/s. The discharge chamber is constructed of M-grade boron nitride. The 173Mv1 uses the same electrical circuit show in Figure 2-2 minus the discharge filter. Hofer provides a more detailed description of the 173Mv1 in Reference 23.



Figure 2-3: NASA-173Mv1 Hall thruster.

2.2 Vacuum Facilities

2.2.1 Plasmadynamics and Electric Propulsion Laboratory (PEPL)

The P5 experiments are conducted in the Large Vacuum Test Facility (LVTF). The LVTF is a stainless steel-clad vacuum chamber that has a diameter of 6 m and a length of 9 m. The thruster is mounted at Station 1, as indicated in Figure 2-4. At this position, the thruster is medially located along the radial axis of the tank, and the plume is allowed to expand freely approximately 7 meters along the centerline axis. The facility is equipped with seven CVI TM-1200 re-entrant cryopumps, each of which is surrounded by a LN₂ baffle. With seven pumps operating, the pumping speed of the facility is 500,000 l/s on air, and 240,000 l/s on xenon.

Two hot-cathode ionization gauges monitor chamber pressure, as indicated in Figure 2-4. The first gauge is a Varian model 571 gauge with a HPS model 919 Hot Cathode Controller. The second is a Varian model UHV-24 nude gauge with a Varian UHV senTorr Vacuum Gauge Controller. Pressure measurements from both gauges are corrected for xenon using the known base pressure on air and a correction factor of 2.87 for xenon according to the following equation.⁵⁵

$$P_c = \frac{P_i - P_b}{2.87} + P_b, \quad \text{Eqn. 2-1}$$

where P_c is the corrected pressure on xenon, P_b is the base pressure, and P_i is the indicated pressure when xenon is flowing into the vacuum chamber. For the experiments reported here, the LVTF is operated with two, four, and seven cryopumps. The nude gauge reading is used to measure operating pressure. A previous study has shown that

the nude ion gauge reading is the most accurate estimate of the LVTF background pressure.⁴⁵

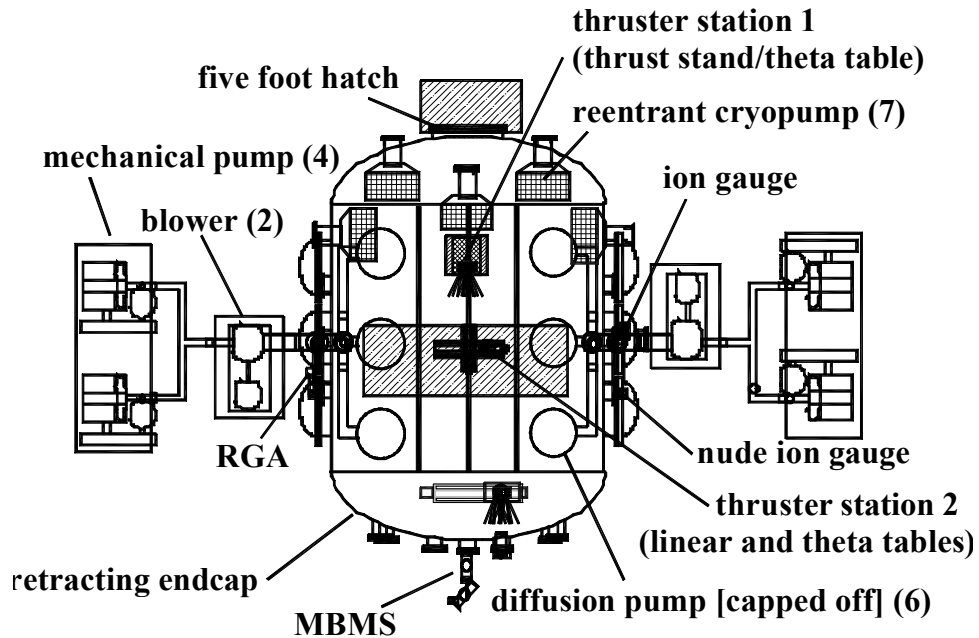


Figure 2-4: Schematic of the LVTF.

2.2.2 Vacuum Facility 12: NASA Glenn Research Center

Experiments at NASA GRC are conducted in Vacuum Facility 12 (VF-12). The NASA-173Mv1 is mounted on the chamber centerline with the exit plane 1.25 m downstream of the rear door, as indicated in Figure 2-5. VF-12 is 3 m in diameter and 9 m long and is equipped with a liquid helium cryopanel surface with a pumping speed in excess of 1,000,000 liters per second on air and 282,000 l/s on xenon. A 1000 l/s (air) turbo pump, located on top of the chamber, evacuates non-condensable gases. Table 2-1 presents the average anode and cathode flow rates, pumping speed, and resulting operating pressures in VF-12 for the conditions investigated.

Anode Flow (mg/s)	Cathode Flow (mg/s)	Nominal Pumping Speed (l/s)	Main Pressure (Torr-Xe)
5.25	0.60	282,000	3.0E-06
10.46	0.60	282,000	5.0E-06
14.09	0.60	282,000	6.7E-06

Table 2-1: 173Mv1 Cold Flow operating conditions in VF-12.

Chamber pressure is monitored by two hot-cathode ionization gauges, as indicated in Figure 2-5. The corrected main gauge reading is reported as the facility background pressure. The turbo ionization gauge, located near the turbo pump, is not considered when reporting the facility pressure. All pressure measurements from the main gauge are corrected for xenon using the known base pressure on air and a correction factor of 2.87 for xenon according Eqn. 2-1.

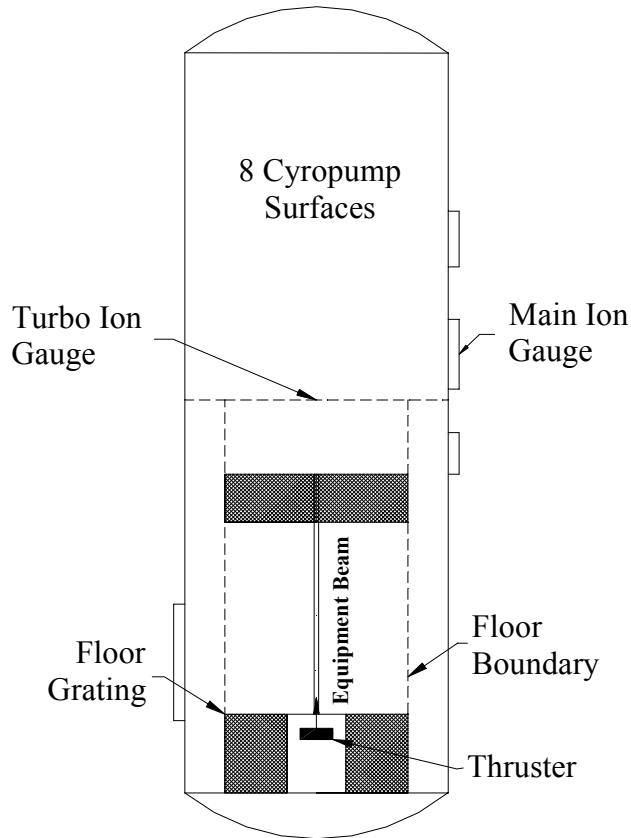


Figure 2-5: Schematic of VF-12.

2.3 Ionization Gauge

A set of hot-cathode ionization gauges measures the pressure over a large area of the LVTF. The pressure maps are later used to create a technique for calibrating a vacuum facility in terms of pressure. The pressure map data are then used to validate a numerical simulation of a Hall thruster plume expansion in the LVTF as well as to determine the xenon-to-cryosurface sticking coefficient of the cryopumps.

2.3.1 Introduction

“Pressure” is a measurement of great importance in scientific investigations that require a vacuum environment. Electric propulsion requires the creation of the space

environment in a ground-based vacuum facility as well as knowing the pressure of the background gas in the facility. Although the true quantity of interest is the gas number density, it can be related back to the force-per-unit-area (pressure) that we are familiar with at higher pressures. As the pressure is reduced, it becomes increasingly difficult to measure the pressure with conventional mechanical gauges. The problem is that mechanical gauges lose their sensitivity as the pressure decreases. In addition, their application is further hampered by cost and/or response time. In the high and ultrahigh vacuum region (where the particle density is extremely small) it is only possible to detect the minute forces that result from the direct transfer of momentum or energy in specialized laboratory situations. Even a capacitance manometer cannot detect pressures lower than 10^{-4} Pa (10^{-6} Torr).⁵⁶ The principle used for the measurement of pressures lower than 10^{-3} Pa is the ionization of gas molecules, and the collection of the ions and their subsequent amplification by sensitive and stable circuitry. Because of the limitations of the mechanical gauge, the ionization gauge is clearly the most widely used vacuum gauge below 10^{-1} Pa.

The Bayert-Alpert (BA) hot-cathode ionization gauge measures pressure over the range of 10^{-2} Pa (10^{-4} Torr) to 10^{-10} Pa (10^{-12} Torr) with an accuracy of $\pm 30\%$ as reported by Varian.⁵⁷ Estimates of the pressure for the experiment are 10^{-3} Pa (10^{-5} Torr) to 10^{-6} Pa (10^{-8} Torr), based on previous experimental data taken by the LVTF wall gauges. Because of its accuracy over the anticipated range of pressures, the BA gauge is selected to measure the chamber pressure field. For this investigation, Varian 571 BA type-standard range ionization gauge tubes are used to measure the chamber pressure field because of their rugged construction, low cost, and long life.

2.3.2 Principle and Limitations of Ionization Gauges

In a hot-cathode ionization gauge, a heated cathode emits a current of electrons, which is accelerated through a voltage between the cathode and a grid. For the Varian BA 571 ionization gauge, the grid is at +150 VDC with respect to ground and the cathode filament is at +30 VDC with respect to ground. The energetic electrons collide with and ionize the background gas that enters the gauge. The ions are attracted to a collector which is connected to the facility ground. Figure 2-6 shows an internal schematic of an ionization gauge. The number of positive ions formed is actually proportional to the number density, not the pressure; the ion gauge is not a true pressure-measuring instrument, but rather a particle-density gauge. The collected positive ion current is proportional to pressure, provided that all other parameters, including temperature, are held constant. The pressure in the gauge, P , can be related to the emission current, I^e , and collector current, I^+ , by

$$P = \frac{I^+ - I_r^+}{I^e S'} \quad \text{Eqn. 2-2}$$

where S' is the gauge sensitivity, and I_r^+ is a pressure independent residual current. It is assumed that pumping conductance losses caused by the tube on the ionization gauge are small. Thus, the background number density within the ionization gauge is equivalent to the background number density in the vacuum facility.

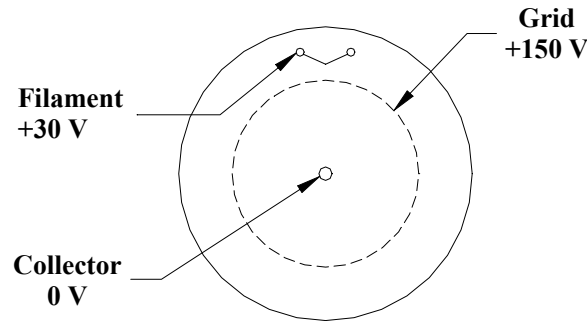


Figure 2-6: Internal schematic of an ionization gauge.

The inverted triode geometry, commonly known as the BA configuration, has the cathode outside the grid and the collector is a fine wire along the axis of the grid. Electrostatic forces maintain a high ion collection efficiency, while the small geometric cross section of the collector results in residual currents three or more orders of magnitude small than those of older conventional triode gauges.

The lower pressure limit of an ionization gauge is determined by the pressure at which the ionized particle current is equal to a residual or background current. The residual current is primarily due to photoelectrons ejected from the collector by soft x-rays generated by collisions of electrons with the grid. The x-ray limit pressure of the Varian BA 571 ionization gauge is 2×10^{-10} Torr- N_2 . A secondary contribution is due to electron-stimulated desorption of ions from the grid.

Eqn. 2-2 and the mechanical simplicity of the ion gauge give the impression that ion gauges are simple, theoretically predictable devices. Unfortunately, the performance of an ion gauge depends on a number of factors that are difficult to model and quantitatively evaluate: electrode geometry, electrical parameters, surface and bulk properties of electrode material, emission characteristic of filaments, space and surface charges, to name a few of the more obvious. Further information on ionization gauge operation can be found in Tilford,⁵⁸ Lafferty,⁵⁹ and Readhead.⁶⁰

In this investigation hot and cold pressure maps are performed in the LVTF. Thus, the BA gauges need a neutralizer to ensure that the plasma does not affect the pressure measurements. To make the hot and cold flow experiments identical in setup, the neutralizers are also used during the cold flow experiment. The neutralizer design prevents plume ions from having a direct line of sight to the ionization gauge filament. The neutralizer contains two 72 mesh screens (0.5 mm by 0.5 mm and 1.0-mm-thick) that are floating to ensure neutralization of any ions that travel inside the orifice that are not neutralized by the grounded walls of the neutralizer body. Figure 2-7 shows the Varian 571 BA ionization gauge and the neutralizer along with their orientation with respect to the anode flow direction.

The screen grid openings are sized to ensure that the sheaths merge at all locations within the exhaust plume. A grid opening larger than a few Debye lengths will not allow the sheaths to merge. Therefore, repulsion of beam ions will not occur near the grid opening centerline, which allows beam ions to travel into the ionization gauge and be collected by the filament. The Debye length is calculated with data previously taken in the P5 plume using a Langmuir probe. The electron number density, n_e , and electron temperature, T_e , are approximately $7.5 \times 10^{10} \text{ cm}^{-3}$ and 1.6 eV at a location 1 m downstream of the P5 exit plane.⁵³ This yields a Debye length of 0.034 mm. The screen opening is 0.5 mm by 0.5 mm, which requires a sheath thickness of approximately 7 Debye lengths for the sheaths to merge. Away from the thruster centerline and exit plane, the Debye length increases due to the decrease in electron number density. A longer Debye length ensures that the sheaths have merged, which makes it less likely for

ions to enter the gauge. Thus, the ion filter is more effective the farther the gauge is from the thruster exit plane and from thruster centerline.

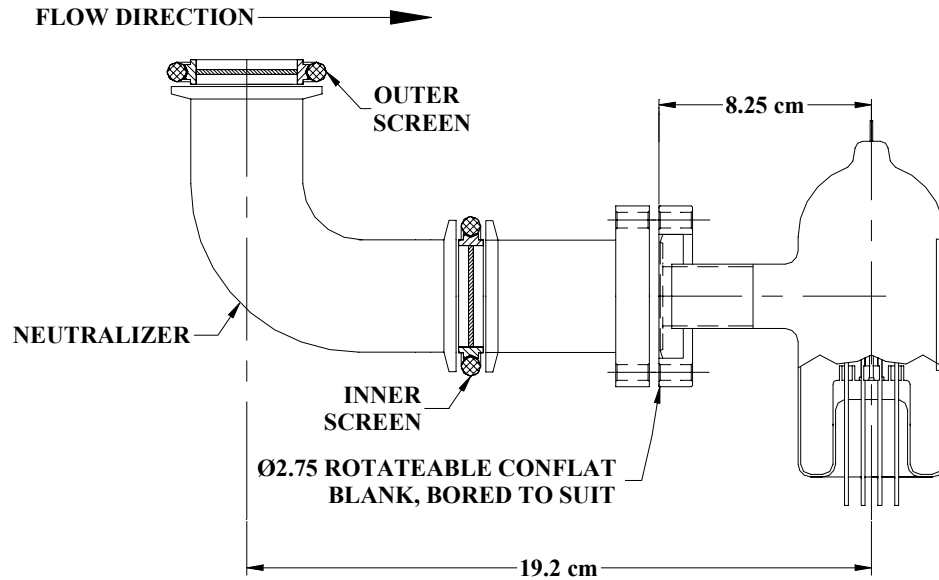


Figure 2-7: Schematic of the Varian 571 BA Ionization Gauge connected to the neutralizer.

2.3.3 Ionization Gauge calibration

Calibration of the five ionization gauge systems is performed by the Helium Leak Testing Incorporated Calibration Laboratory in Northridge, CA[†]. Two of the BA gauges are controlled by separate Varian senTorr gauge controllers. The remaining three BA gauges are controlled by a Varian Multi-Gauge controller. Each system is comprised of a BA gauge, the actual internal and external cables used in the LVTF, a Varian 10-wire vacuum chamber instrumentation feedthrough, and a Varian BA circuit board mounted in either the senTorr or Multi-Gauge controller. Each system is calibrated with xenon as a

[†] <http://www.heliumleaktesting.com/general/study.htm>

one-piece unit using a National Institute of Standards and Technology traceable Leybold-Heraeus Viscovac VM211 spinning rotor viscosity gauge.

2.4 Ionization Gauge Positioning System

The Ionization Gauge Positioning System (IGPS) allows the pressure measurements to be taken throughout the majority of a chamber with a single evacuation cycle. The following sections describe the systems used in the LVTF and VF-12.

2.4.1 LVTF Ionization Gauge Positioning System

The pressure maps are performed with a rake consisting of five calibrated BA hot-cathode ionization gauges. To generate the two-dimensional pressure map inside the LVTF, the ionization gauges are mounted to a custom built, two-axis positioning stage. This crossed-stage positioning system is composed of a 1.8-m-long linear stage in the radial direction, mounted on a 0.9-m-long linear stage in the axial direction. Both stages have an absolute linear position accuracy of 0.15 mm. The IGPS mounts to the positioning stage and carries the five BA gauges used to survey the chamber. Figure 2-8 shows a schematic of the IGPS mounted within the LVTF. The locations mapped by the IGPS cover an area with a minimum distance from the thruster of 0.5 m, encompassing the typical 1 m distance at which plume properties are measured. Pressures at locations closer than 0.5 m to the exit plane exceed the shut-down limit of the ionization gauge controller.

The 5 Varian 571 BA type standard range ionization gauge tubes measure the chamber pressure field in the LVTF. To operate the BA gauges on the IGPS, a custom set of cables are constructed. These cables pass through the chamber wall on five, 10-

wire instrumentation feedthroughs. The overall cable lengths from controller to BA gauge are between 15 and 23 m, depending on the location of the particular gauge. To verify the operation of each line after the setup is complete, a sealed-glass ionization gauge is operated with a senTorr controller. This test confirms the operation of the equipment while the facility is at atmosphere to avoid unnecessary evacuation cycles of the vacuum chamber. Varian reports that the reference ionization tube is sealed-off at less than 6.7×10^{-4} Pa (5.0×10^{-6} Torr). Each of the five ionization gauge systems measure pressures below the maximum pressure reported by the vendor. The maximum spread in measured pressure is 35%, which is the standard uncertainty of BA gauges. The five BA gauges mounted to the IGPS all measure base pressures within 45% percent of the pressure reported on the nude gauge used to monitor facility background pressure. This agreement confirms that the ionization gauges mounted on the IGPS are operating properly at vacuum.

Given the symmetric pump configuration, we assume that chamber pressure is horizontally symmetric about the chamber centerline in the LVTF. This assumption reduces the number of spatial positions that are mapped. All pressure map data presented are only from one side of the chamber. In a previous experiment we created a cold flow pressure map of the LVTF with the same ionization gauges and neutralizers used in the experiments presented in this thesis. The results of that study show that the neutralizer conductance does not noticeably affect the time response of the internal ionization gauges.⁴⁵

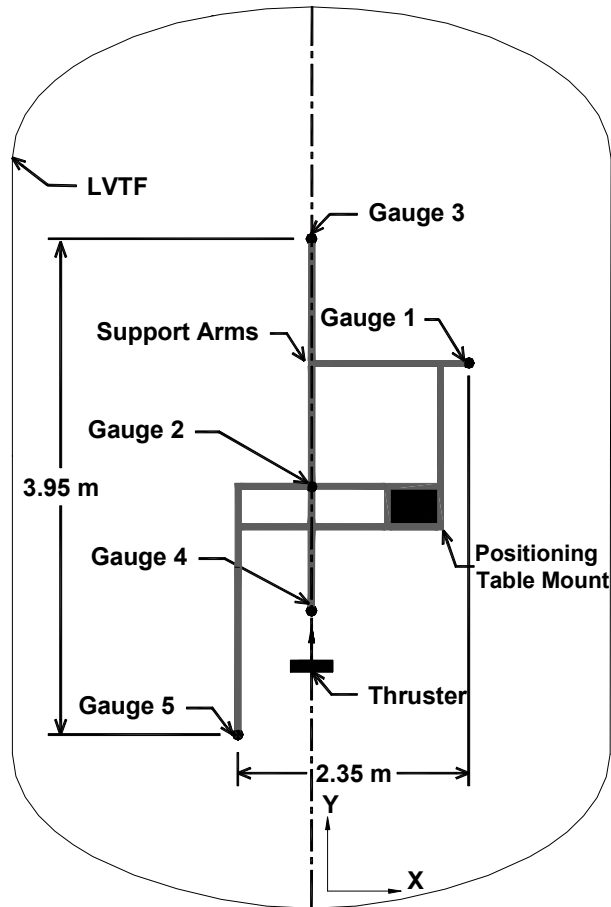


Figure 2-8: Schematic of the IGPS mounted in the LVTF.

Figure 2-8 displays the IGPS mounted in the LVTF and Figure 2-9 shows the 25 cm by 25 cm square grid on which data points are taken. The solid circles indicate the position of each of the five probes when the IGPS is in the initial position. Gauge 1 is positioned on the opposite side of the chamber centerline so any possible wake effects generated by the gauges do not interfere with downstream probes. Figure 2-9 also shows the coordinate system used for this experiment. The coordinate system origin is located at the discharge chamber exit plane on the thruster centerline. The cluster pressure maps discussed in Chapter 5 only use gauges 2 and 4 of this system.

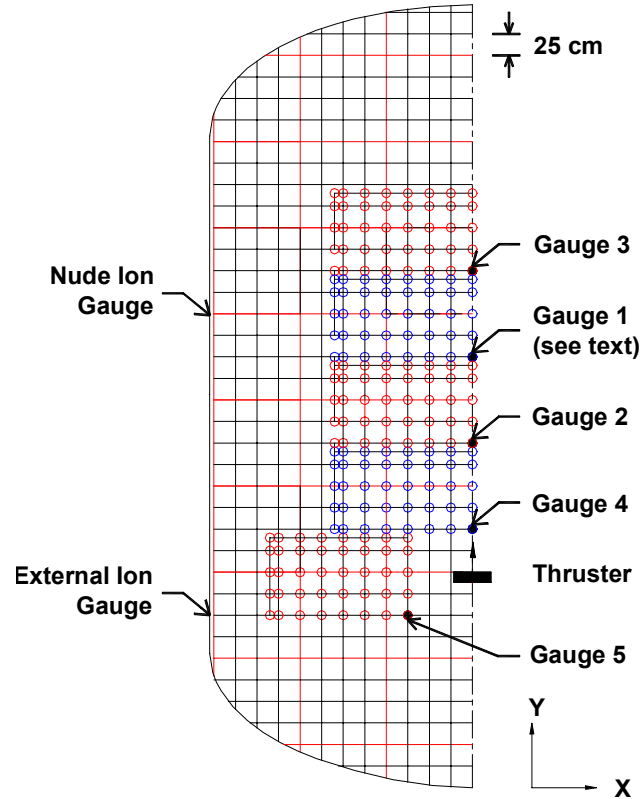


Figure 2-9: LVTF half-plane (looking down) with the IGPS and a 25 cm by 25 cm square grid. Each open circle denotes the location of a data point.

2.4.2 VF-12 Ionization Gauge Positioning System

To generate the two-dimensional mapping inside VF-12, the ionization gauges are mounted to a Parker Daedal two-axis positioning system. The positioning system consists of a 0.6-m-long linear stage in the radial direction mounted on a 0.9-m-long axial stage; both have an absolute linear position accuracy of 0.1 mm. A LabView “Virtual Instrument” (VI) controls the motion of the two linear position tables, which in turn move the IGPS that carries the five BA gauges used to survey the chamber. Figure 2-9 shows a schematic of the IGPS mounted within VF-12. The IGPS allowed the pressure measurements to be taken throughout the majority of the chamber with a single

evacuation cycle of VF-12. As in the LVTF, the region mapped by the IGPS covers an area with a minimum distance from the thruster of 0.5 m, encompassing the typical 1 m distance at which plume properties are measured.

Figure 2-10 displays the 25 cm by 25 cm grid in VF-12 on which data points were taken. The solid circles indicate the position of each of the five probes when the IGPS is in the initial position. Figure 2-10 also shows the coordinate system used for this experiment. The coordinate system origin is located at the discharge chamber exit plane on the thruster centerline, where negative X is to the left and positive Y is up the page.

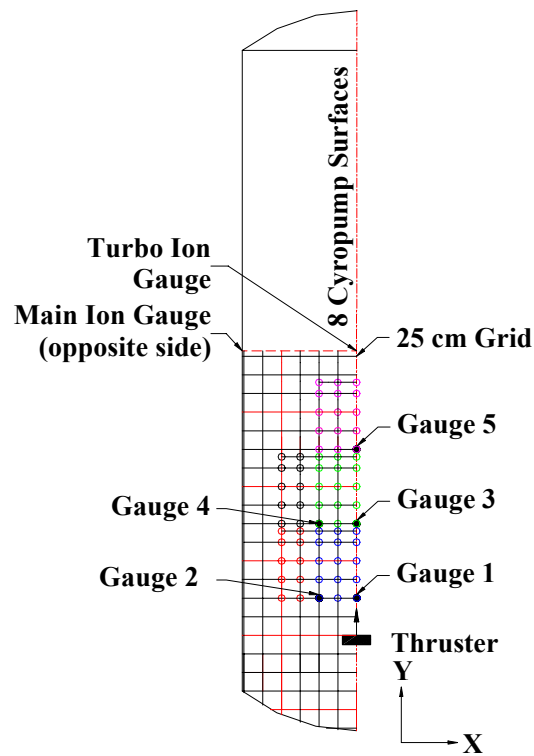


Figure 2-10: VF-12 half-plane (looking down) with the IGPS and a 25 cm by 25 cm grid. Each open circle denotes the location of a data point.

2.5 Langmuir Probe

Langmuir probes are simple electrostatic devices used to measure plasma parameters. Langmuir probes provide one of the best means for making spatially resolved measurements of electron temperature, electron number density, and plasma potential in plasmas. While the basic probe theory in an ideal plasma is quite simple to implement, the plasma characteristics in the plume of the Hall thruster create significant difficulties in collecting and interpreting probe data. Therefore, great care must be taken in choosing the shape, size, and orientation of the probe due to the presence of streaming ions, high plasma potentials and potential gradients, and large radial magnetic fields.^{61, 62} Fortunately, many of these effects can be made negligible with proper consideration.

Langmuir probes are generally classified according to two parameters: the number and the shape of the electrodes. Planar, cylindrical, and spherical probes with one to four electrodes have been used in a wide range of plasmas and the theory of their operation is extensive. Spherical probes are immediately rejected for this experiment because of the difficulty in their construction, particularly of sizes small enough to provide good spatial resolution in the plume. Both planar and cylindrical probes are easily constructed at very small sizes and can be configured as single, double or triple probes. A single-cylindrical Langmuir probe is used for this investigation.

Information is derived from the Langmuir probe by understanding that the current collected by the biased probe is composed of both ions and electrons. To first order, the ion flux to the probe can be considered nearly constant because the low bias voltages weakly affects the more massive ions. The electrons are strongly affected by the bias voltage; thus, the current collected by the probe can be separated into the 3 regions

shown in Figure 2-11. At voltages significantly below the local plasma potential, the electrons are repelled and the collected current is due completely to the collected ion flux. This is known as the ion saturation region, as labeled in Figure 2-11. At higher potentials with respect to ground (but still below plasma potential) the slower electrons do not reach the probe, but the faster electrons are able to overcome the bias potential and reach the probe. At potentials greater than the plasma potential, essentially all of the electrons that reach the edge of the thin sheath around the probe are collected and the current density reaches a plateau. This plateau is referred to as the electron saturation current. As seen in Figure 2-11 the collected current in the electron saturation region tends to continually increase with bias voltage because of sheath expansion.⁶³

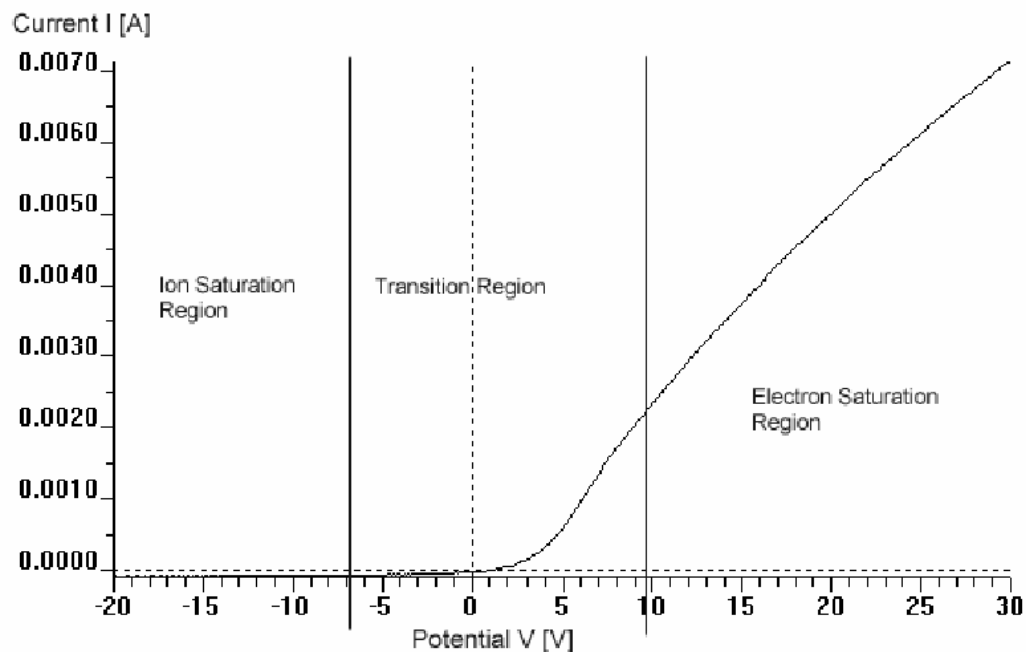


Figure 2-11: Typical Langmuir probe characteristic in a Hall thruster plume.

The interpretation of the current trace depends on the ratio of the probe radius to the local Debye length and the environment in which the probe is immersed. All Langmuir probe measurements are made 1 m downstream of the thruster exit plane (where the plasma is unmagnetized) with a single Langmuir probe constructed of 0.1 mm diameter x 7.5 mm long tungsten.

The plasma density and electron number density can be calculated for a Maxwellian electron velocity distribution using thin-sheath theory, (where the sheath thickness is much smaller than the probe radius). The local electron temperature, T_e can be calculated from the exponential increase in collected current in the electron retarding region using Eqn. 2-3.

$$\frac{k_b T_e}{e} = \left(\frac{d \ln(I_p)}{dV} \right)^{-1} \quad \text{Eqn. 2-3}$$

The electron number density shown in Eqn. 2-5 is derived using the calculated electron temperature, the Bohm sheath criterion shown in Eqn. 2-4, and the standard assumption of quasineutrality shown Eqn. 1-8.

$$u_o > \left(\frac{KT_e}{m_i} \right)^{1/2} \quad \text{Eqn. 2-4}$$

$$n_e = \frac{I_{i,sat} \exp\left(\frac{1}{2}\right) \left(\frac{m_i}{k_b T_e} \right)^{1/2}}{e A_p} \quad \text{Eqn. 2-5}$$

Langmuir probe measurements in a Hall thruster plume are far more complex than the linear case modeled by the above equations, particularly because the plasma is flowing. The expansion of the non-neutral sheath causes the collected ion current to increase with decreasing probe bias voltage. Thus, curve fits are applied to the collected

current traces to approximate the ion saturation current, which introduces error into the results. Furthermore, it is non-trivial to determine the plasma potential from the “knee” in the collected current because the “knee” is not distinct. Finally, the probe perturbs the plasma, since it must collect current from the plasma in order to function. Depending on the conditions, the probe may cause a large perturbation in the local plasma, which introduces significant error into the results. For standard Langmuir probe theory, Hutchinson indicates that the electron temperature and ion number density measurements have an uncertainty of 20% and 50%, respectively.⁶⁴

A commercial system built by Hiden is used to operate the Langmuir probe in this study. The Hiden software applies Orbital-Motion-Limited (OML)^{61, 65} and thin-sheath theory⁶² to the resultant Langmuir probe traces to determine several plasma parameters. The use of OML theory for analysis of the data is valid because the probe radius (0.1 mm) is much smaller than the calculated sheath thickness (0.5 mm to 0.9 mm, 5 to 10 Debye lengths). In addition, a collisionless sheath may be assumed since the sheath thickness is much smaller than the electron mean free path (which is approximately 1 m). The Langmuir probe current (1-5 mA) is small with respect to the total discharge current (4.86 A), so the probe represents a minor perturbation to the plasma. Therefore, the measurements are expected to be valid.

The Langmuir probe bias voltage and current measurements are controlled by the Hiden Langmuir probe system.⁶⁶ The Hiden software, ESPion, records the data and calculates the plasma characteristics. By sweeping the Langmuir probe bias from -25 V to 30 V, the probe current is measured through the ion saturation region, the electron energy distribution region, and the electron saturation region. Each Langmuir probe trace

contains 1100 points and 10 sweeps are obtained at each position. The Langmuir probe is cleaned by the 200+ eV ions that collide with it during the ion collection portion of the voltage sweep.

2.6 Faraday Probes

Faraday probes measure the ion current density profile in the Hall thruster plume. In its simplest form, the Faraday probe consists of a planar metallic disc biased to a sufficiently negative potential to repel all electrons. Thus, the probe current is only caused by ions impacting on the probe surface. As seen in Figure 2-12, it operates in the ion saturation region.

A shortcoming of nude Faraday probes is that the measured ion current density depends partly on the facility size and operating pressure, which makes comparisons between ion current density data collected in different facilities non-trivial. Facility effects due to elevated operating pressures are driven by CEX collisions of directed plume ions with the random background population of neutrals. In resonant CEX collisions, a “fast moving” ion exchanges an electron with a “slow moving” neutral. Because the process does not involve momentum transfer, the resulting products are a fast neutral moving with the original ion velocity and a slow ion moving in a random direction. The nude Faraday probe is unable to differentiate between ions created in the discharge chamber and slow CEX ions, which leads to artificially high ion current density measurements at large angles off axis ($> 60^\circ$). This leads to an over-prediction of the beam divergence angle and the integrated total beam current.

The ion current density measured by a Faraday probe 1 m downstream of the exit plane is subject to several sources of error. First, the probe is a physical disturbance

to the local plasma, but the dimensions of all of the probes used are much larger than the local Debye length and the electron mean free path is large compared to the probe dimensions. Thus, the disturbance to the plasma should be small, as discussed in the previous section on Langmuir probes. Second, secondary electron emission (SEE) from the probe surface causes error in the measured ion current. The probe collector surface material effects are discussed in the following sections, as is the expected error caused by SEE. Third, sheath edge effects on the negatively-biased collector surfaces can increase the effective collection area of the probe, thus leading to error in the calculated ion current density. Each of the Faraday probe designs includes a negatively biased “guard ring” designed to create a flat, uniform sheath over the collector surface, minimizing the error caused by edge effects. The last two sources of error are due to physical alignment of the probes and the electronic measurement of the current. Misalignment of the probe causes a reduction in the effective probe area. This error creates uncertainty in the calculation of ion current density. The probes are aligned with a laser and an electronic level to within ± 0.2 degrees. The electronic measurements of the current have an error of 2%.

In response to the shortcomings of nude Faraday probes, this study evaluates the performance of five distinct Faraday probe designs (Probes A, B, C, D, E) in an attempt to determine which design most accurately measures the ion current density independent of facility backpressure. The following sections describe the five designs used and their electrical configurations.

2.6.1 Data Acquisition

The thruster and cluster are mounted with the exhaust beam aligned parallel to the chamber axis, such that the thruster and cluster centerline is referenced as zero degrees. The probes are positioned $(19.50 \pm 0.25)^\circ$ apart on an overhead, rotating arm that is attached to a rotary table with a repeatability of 12 arc-sec. The probes are aligned to the center of the cluster element or the cluster exit plane and placed (100.9 ± 0.1) cm downstream of the thruster. A scan of the thruster plume from -100 to 100 degrees, in 1° increments, takes approximately 6 minutes. Typical collector currents range from 0.2 to 3.4 mA.

Probe data are acquired using an Agilent HP34970A 22-bit, 20-channel data acquisition system. In the following discussion, all data reported are with the collector and guard ring of Probes A, B, C, D and, E biased to 20 V below facility ground by a single power supply. Figure 2-12 shows that prior use of Probes A and C at PEPL indicates that a bias voltage of 20 V below facility ground is sufficient for the collector to enter ion saturation without substantial sheath growth.^{67, 68} Similar studies performed on Probes D and E confirm the validity of the collector and guard ring bias voltage used, but are not shown. A 99.6Ω current shunt is placed in the biasing line connected to each collector. Probe current is measured with this shunt resistor. The ion current density is calculated by dividing the current by the collector surface area.

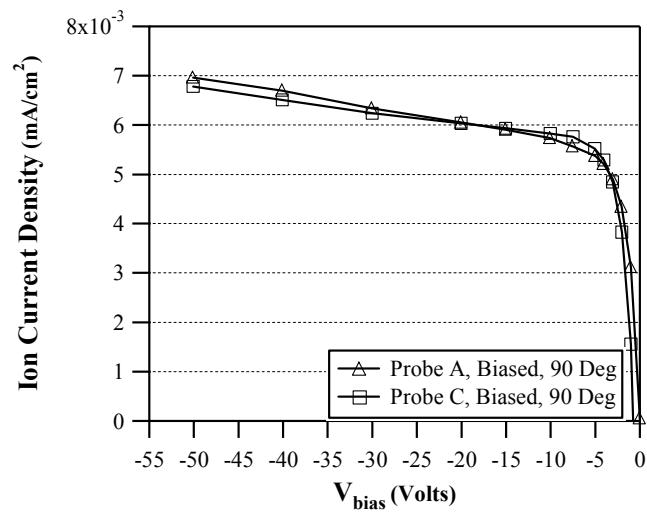
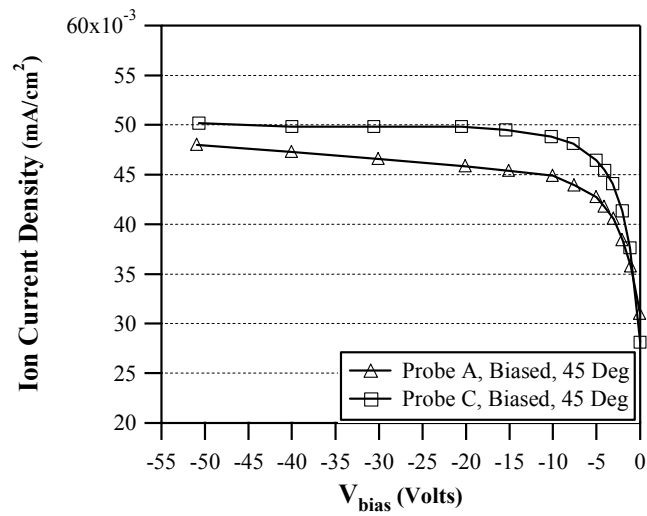
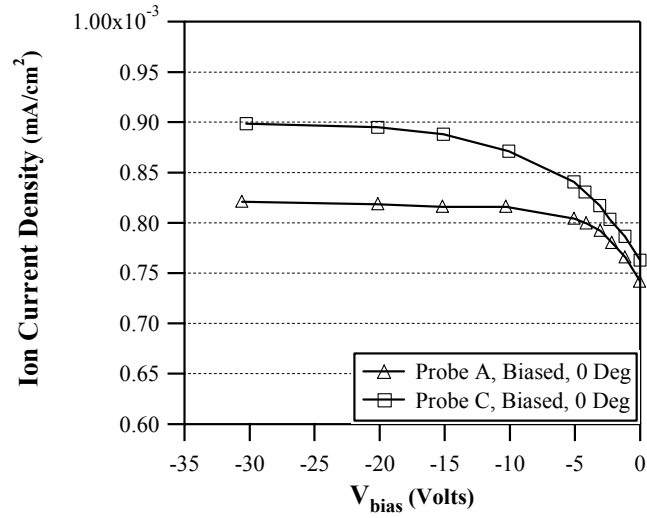


Figure 2-12 Effect of varying the probe bias at several angular positions. (300 V, 4.41 A thruster operation with 140,000 l/s pumping speed)

2.6.2 Probe A Jet Propulsion Laboratory (JPL)

Probe A is a nude Faraday probe provided by JPL. Nude means that the probe does not have a filter upstream of the collector. Figure 2-13 shows a schematic of Probe A, which consists of a collection electrode enclosed within a guard ring. The collection electrode is aluminum, spray-coated with tungsten to minimize secondary electron emission (SEE). The collector and guard ring of Probe A are designed to be biased to the same negative potential below facility ground; this minimizes edge effects around the collector by creating a flat, uniform sheath over the collection area. The guard ring spacing is compared to the plasma Debye length to qualitatively verify the collector sheath profile of nude Faraday probe. Haas presents measurements of typical P5 plume parameters.⁶⁹ From the measured electron temperature, T_e , and the electron number density, n_e , the Debye length, λ_d , is calculated using Eqn. 2-6, and the probe sheath, t_s , is approximately 1.5–3.0 mm (the sheath thickness is 5-10 Debye lengths). The guard ring gap of the nude Faraday probe is 0.4 mm, which is smaller than the sheath thickness and should result in a smooth sheath surface over the collector. Table 2-2 summarizes the relevant dimensions and component bias voltages. Figure 2-14 shows the electrical schematic used for Probe A.

$$\lambda_d = \left(\frac{\epsilon_o T_e}{e^2 n_e} \right)^{1/2} \quad \text{Eqn. 2-6}$$

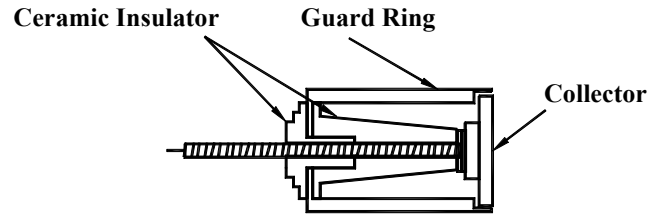


Figure 2-13: Schematic of Probe A. The collector is isolated from the guard ring with ceramic standoffs.

Part Name	Dimension (cm)	Bias Voltage (V)
Probe Collector		-20
Outer Diameter	2.31	
Gap Thickness	0.23	
Probe Guard Ring		-20
Outer Diameter	2.54	
Thickness	0.07	

Table 2-2: Dimensions of Probe A.

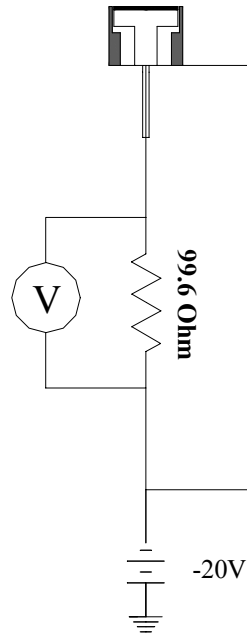


Figure 2-14 Electrical schematic of the Faraday Probe A setup.

2.6.3 Probe B (MFFP)

Probe B is composed of a nude Faraday probe, identical to Probe A, positioned behind a “C” bracket that creates a magnetic field in front of the probe. This setup is referred to as the magnetically-filtered Faraday probe (MFFP). Figure 2-15 shows a schematic of the MFFP looking in towards the collector. The magnetic field is designed to filter CEX ions away from the probe collector. Probe A is positioned behind the filter to collect ions that pass through the magnetic field. A graphite faceplate is attached to the front of the filter and two aluminum side panels are also attached. The faceplate has a 2.54 cm (1 in.) diameter hole machined directly upstream of the probe to allow ions to enter. The distance from the faceplate hole to the probe is 5.85 cm. The other faces of the probe are physical shields to prevent stray ions from being collected by the probe. The faceplate and sideplates are electrically floated. The magnetic filter contains a cylindrical solenoid connected to two iron plates to form a “C” shape. Permanent samarium cobalt magnets connected to the iron plates provide a “baseline” magnetic field. The solenoid can operate between ± 5 A, with +5 A increasing the flux density and -5 A reducing it. This yields an ion energy filtration range of approximately 8 – 30 eV when the solenoid current is varied from -5 to +5 A. Figure 2-16 shows the trajectory paths for filtered and unfiltered ions. Rovey describes the probe in more detail in Reference 70.

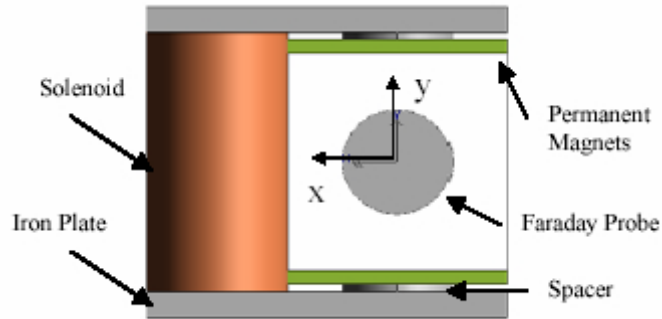


Figure 2-15: Schematic of Magnetically Filtered Faraday Probe. The collector is isolated from the guard ring with ceramic standoffs. (Guard ring not shown)

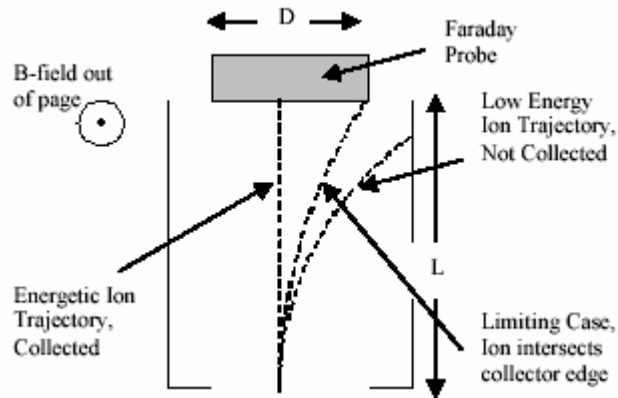


Figure 2-16: Solid model of the magnetic filter. Particles enter along the z-axis, directed into the page. ($L = 5.85$ cm, $D = 2.54$ cm)

2.6.4 Probe C (NASA Glenn Research Center)

Probe C is a nude Faraday probe designed by NASA GRC. Figure 2-17 shows a schematic of Probe C, which consists of a 1.94 cm diameter collection electrode enclosed within a guard ring. The collector and guard ring are constructed of stainless steel and are not spray-coated with tungsten, like Probe A, to reduce SEE. The collector surface and guard ring are mounted to a ceramic electrical insulator. As with Probe A, the collector and guard ring of Probe C are biased to the same potential below facility ground to minimize sheath edge effects. Table 2-3 summarizes the relevant dimensions

and component bias voltages of Probe C. Figure 2-18 shows the electrical schematic for Probe C. The results of prior use of this probe are located in Reference 67.

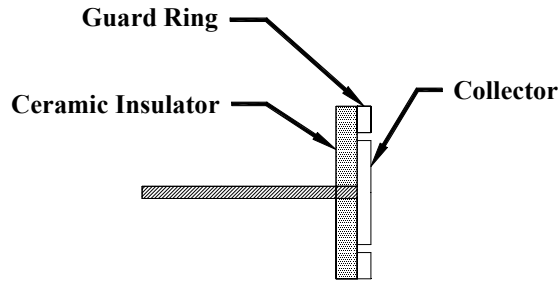


Figure 2-17: Schematic of Probe C. The collector is isolated from the guard ring with ceramic standoffs.

Part Name	Dimension (cm)	Bias Voltage (V)
Probe Collector		-20
Outer Diameter	1.941	
Gap Thickness	0.279	
Probe Guard Ring		-20
Outer Diameter	3.185	
Thickness	0.483	

Table 2-3: Dimensions of Probe C

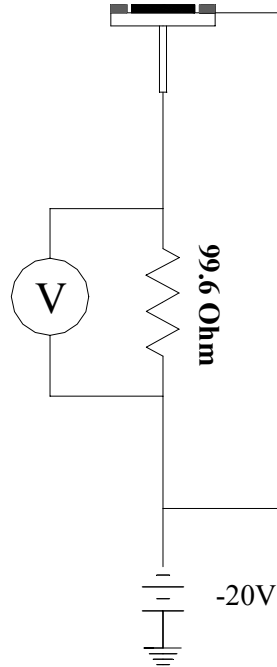


Figure 2-18: Electrical schematic of the Faraday Probe C setup.

2.6.5 Probe D (Centrosazio/ALTA)

Faraday Probe D was donated to PEPL from Centrosazio/ALTA for facility effects work. Figure 2-19 shows a schematic of Probe D. The collimator diameter and spacing from the collector ensure that a uniform sheath is created across the collector face. The probe collector is made from molybdenum. The outer shield-spacer is made from stainless steel and molybdenum, and the inner insulators are constructed of Teflon. Tables 2-6 and 2-7 list the relevant dimensions and bias voltage of each component, respectively. Figure 2-20 shows the electrical schematic used for Probe D.

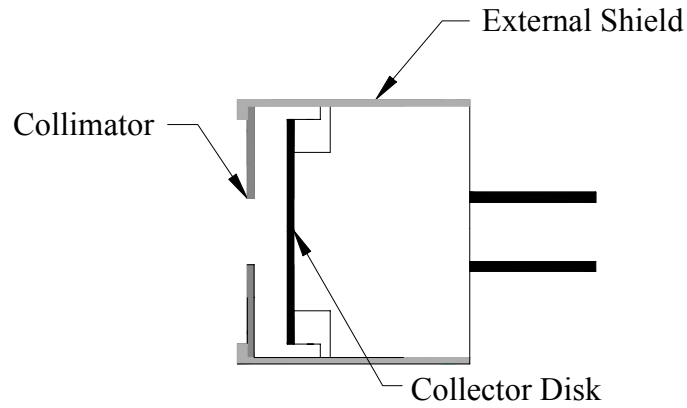


Figure 2-19: Schematic of Probe D.

Part Name	Dimension (cm)
Collimation hole diameter	1.0
External shield diameter	4.0
Collimator angular resolution	0.6° @ 100.0 m
Probe length	3.5
Collector Area	0.5

Table 2-4: Dimensions of Probe D.

Part Name	Bias (V)
Probe Collector	-20
External diameter	-20

Table 2-5: Probe D component bias voltages.

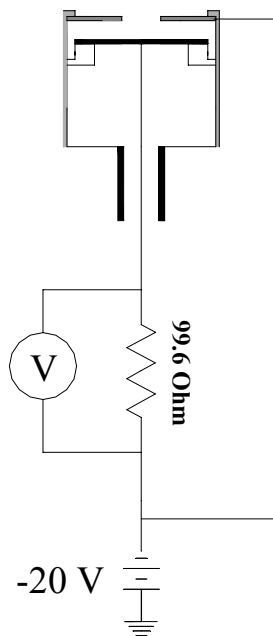


Figure 2-20: Electrical schematic of Faraday Probe D.

2.6.6 Probe E (AFRL)

Probe E is a gridded Faraday probe designed by the AFRL. Gridded Faraday probes are designed to repel all CEX ions away from the collector, thus allowing the true ion current density to be measured at elevated facility backpressures. This device is identical to the retarding potential analyzer (RPA) described in the next section, but with the center electrodes removed. Figure 2-21 shows a schematic of Probe E in the RPA configuration. To use the RPA as a gridded Faraday probe, Grid 1 floats to minimize perturbations to the plasma, Grid 3 is removed, and the outer body is held at ground potential. Grid 2 is biased 30 V above ground to repel CEX ions and the copper collector is biased 20 V below ground to repel electrons. Therefore, only high-energy ions originating from the discharge channel reach the probe collector. The secondary electron emission coefficient of copper is less than 0.1 for ion impact energies up to 1 keV.^{71, 72}

The SEE coefficient of copper is an order of magnitude larger than the SEE coefficient of tungsten impacted by singly-charged xenon and may lead to a small overestimate in the measurement of the ion current density. This error is discussed in more detail in the next section, which describes the RPA.

The outer body of the probe is constructed of 316 stainless steel (SS) tubing. A phenolic sleeve placed inside the body provides electrical isolation of the grids. All grids are identical and are cut from photochemically-machined 316 SS sheet with a thickness of 0.127 mm (0.005"). The grid openings are 0.2794 mm (0.011") in diameter with a total open area fraction of 38%. The grids are spaced with machined Macor washers. A stainless steel wire electrode, spot-welded to each grid, provides an electrical connection. The wires are routed along the inner face of the phenolic sleeve and out the back of the probe body. Structural contact between the washers and grids is maintained by a spring placed behind the collector and the rear cover. Table 2-6 and Table 2-7 list the relevant dimensions and component bias voltages, respectively. Figure 2-22 shows the electrical schematic used for Probe E.

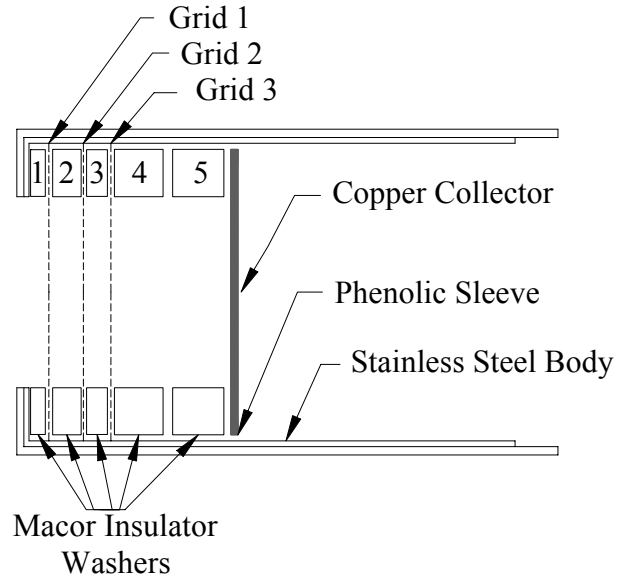


Figure 2-21: Schematic of Probe E/RPA. Note: Grid 3 is removed when used as Probe E.

Washer	Inner Diameter (mm)	Thickness (mm)
1	18.54	1.067
2	21.54	3.353
3	21.54	1.727
4	21.16	6.553
5	21.23	6.533

Table 2-6: Dimensions of Probe E (AFRL).

Part Name	Bias (V)
Grid 1	Floating
Grid 2	30
Grid 3	N/A
Collector	-20

Table 2-7: Probe E component bias voltages

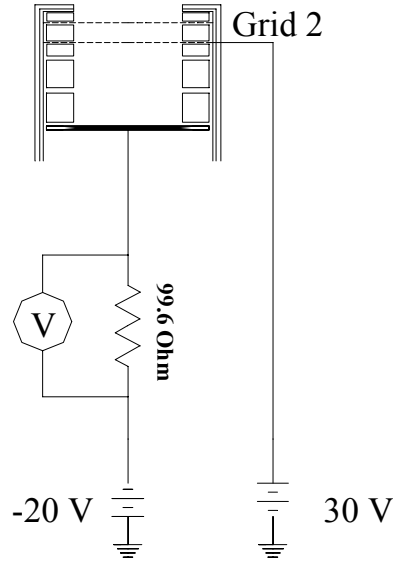


Figure 2-22: Electrical schematic of Faraday probe E.

2.7 Retarding Potential Analyzer

A retarding potential analyzer (RPA) is one diagnostic used to measure the ion energy per unit charge distribution in the Hall thruster plume. By positively biasing Grid 3 in the gridded Faraday probe (Figure 2-21), ions below a critical velocity, v_{crit} as defined in Eqn. 2-8, are repelled away from the collector of the diagnostic. Since the ions are not collected, the current measured by the collector is shown in Eqn. 2-7, where $f(v)$ is the ion velocity distribution function and j is the charge state of the species.

$$I_{coll} = A_c e \sum_j n_j q_j \int_{V_{grid}}^{\infty} v f(v) dv \quad \text{Eqn. 2-7}$$

Eqn. 2-8 yields v_{crit} as a function of the grid bias voltage.

$$v_{crit} = \sqrt{\frac{2q_j e V_{grid}}{m_i}} \quad \text{Eqn. 2-8}$$

The critical velocity below which ions are rejected depends on both the mass and charge state of the sampled ions. The Hall thruster plume is comprised of ions of nearly identical mass, which is dependent on the propellant. However, approximately 10% of the plume contains multiply-charged ions.⁷³ For simplicity, we define an equivalent ion voltage, which is the ion kinetic energy per unit charge. Using this definition and substituting variables allows the collected current to be written as a function of the retarding grid potential and the ion voltage as shown in Eqn. 2-9, where the effective charge state, q_{eff} , is defined in Eqn. 2-10. Differentiating Eqn. 2-9 yields Eqn. 2-11, which shows that the ion voltage distribution is directly proportional to the derivative of the collected current with respect to the retarding grid voltage. The RPA is only capable of measuring the energy distribution per charge because a singly-charged ion traveling with a given kinetic energy is indistinguishable from a doubly-charged ion possessing twice that kinetic energy.

$$I_{\text{coll}} = A_c \frac{n_e e^2 q_{\text{eff}}^2}{m_i} \int_{V_{\text{grid}}}^{\infty} v f(v) dv \quad \text{Eqn. 2-9}$$

$$q_{\text{eff}}^2 = \frac{\sum_j (n_j q_j^2)}{\sum_j n_j} \quad \text{Eqn. 2-10}$$

$$\left. \frac{dI}{dV} \right|_{V=V_{\text{grid}}} = -A_c \frac{n_e q_{\text{eff}}^2 e^2}{m_i} f(V) \quad \text{Eqn. 2-11}$$

The RPA used in this experiment is based on the multi-gridded energy analyzer described by Hutchinson.⁶⁴ A physical description of the probe is given in the previous section that describes Probe D. During operation, Grid 1 floats providing a non-perturbing interface between the probe and the plasma, while a laboratory power supply

biases the second grid 30 volts below ground to repel electrons. A Keithley model 2410 sourcemeter sweeps Grid 3 from 0 to 750 volts relative to ground. The resulting current to the collector is measured by a Keithley model 486 picoammeter, and the entire data acquisition routine is controlled by a computer running LabView software.

One neglected factor in the present implementation of this diagnostic is SEE from the copper collector. In theory, the variable SEE yield for the collector material as a function of ion impact energy could cause an overestimate of the fraction of ions at the energies for which the SEE yield of copper is high. Fortunately, for impact energies below 1 keV, the SEE yield of copper is less than 0.1 electrons per ion.⁷¹ The potential source of error due to SEE is thought to be negligible because of previous, unpublished tests with this instrument, which used an electron suppression grid upstream of the collector (between washer 4 and 5 in Figure 2-22). This grid is biased below ground, reflecting the secondary electrons back to the collector. A series of tests with and without the suppression grid in place show no noticeable changes in the measured data.⁵⁰ In this investigation, the suppression grid is not installed in order to maximize the open area fraction of the grid system and to ensure an adequate signal to noise ratio.

Eleven-point box smoothing of the raw RPA data reduces numerical noise in the numerical differentiation routine needed to obtain the ion energy distribution per charge. Figure 2-23 shows a sample of the smoothed data along with the raw data and the resulting ion energy distribution per charge. At each angle from the plume centerline, multiple traces are collected to verify the repeatability of the measured distribution. The trace shown in Figure 2-23 is taken 1.0 m downstream on the centerline of the P5-A Hall

thruster operating at 300 V and 5.46 A at an operating pressure of 1.9×10^{-6} Torr-Xe. RPA construction details can be found in References 33 and 50.

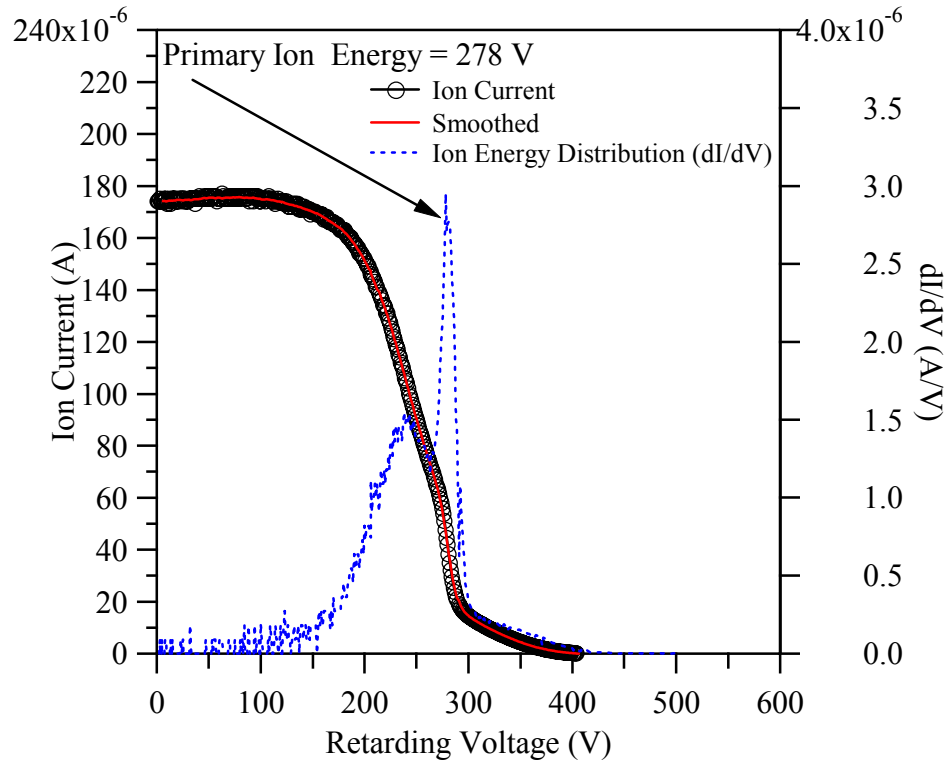


Figure 2-23: Raw RPA data, smoothed data, and the resulting ion energy per unit charge distribution.

2.8 Parallel-Plate Electrostatic Energy Analyzer

A 45-degree, parallel-plate electrostatic energy analyzer measures the ion energy distribution function throughout the Hall thruster plume.⁷⁴ This section describes the ESA used in this research.

The 45-degree, parallel-plate ESA is a well-known method in charged particle beam physics research for filtering particle energies.^{75, 76} Figure 2-24 shows a schematic of the ESA. The ESA uses a sampling slit to admit a beam of plume ions with velocity v_i

into the device. The beam then passes through the second skimmer slit located at the rear of the entrance box. The analyzer uses a constant electric field created by two parallel plates separated by a distance, d . The lower plate is electrically grounded while the upper plate is biased to a positive potential, V_r , to reflect ions admitted through a slit of width w in the grounded baseplate. The applied electric field, \vec{E} , forces ions of a selected initial energy to charge ratio, E_i/q_i , through a trajectory that passes through a second slit a distance L from the first slit. At this point, the ions are collected by a detector as shown in Figure 2-24. Since only ions of a specific energy to charge ratio are collected, the ESA acts as an energy-per-charge filter for a given ion species. The output current of the detector as a function of electric field strength between the plates is proportional to the ion energy distribution per unit charge.

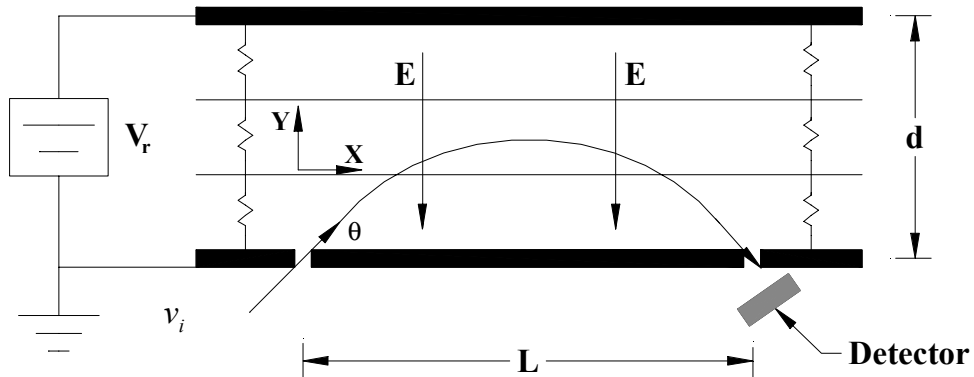


Figure 2-24: Schematic of parallel-plate electrostatic energy analyzer operation.

Within the ESA, ions experience a constant acceleration caused by the electric field magnitude, V_r/d . The E-field is oriented at an angle of θ to the initial direction of ion travel. The E-field accelerates the ions in the negative y-direction. By integrating Eqn. 2-12 and Eqn. 2-13 twice, removing the time variable, and then applying the

physical boundary conditions, the ion trajectory as a function θ , Eqn. 2-14, is derived.

The spatial coordinates are measured from the inlet slit.

$$m_i \frac{d^2 x}{dt^2} = 0 \quad \text{Eqn. 2-12}$$

$$m_i \frac{d^2 y}{dt^2} = -\frac{q_i e V_r}{d} \quad \text{Eqn. 2-13}$$

$$y = x \tan(\theta) - \frac{q_i e V_r x^2}{2m_i v_i^2 d \cos^2(\theta)} \quad \text{Eqn. 2-14}$$

For the specific case of a 45° ion injection angle, ions exiting the second slit ($x=L$, $y=0$) are related to the voltage of the repelling plate by Eqn. 2-15 where the spectrometer constant, K_{45} equals $L/2d$. Thus, the collector current measured as a function of the applied plate voltage is proportional to the ion energy per charge distribution. Note that this result is independent of the ion mass.

$$V_i = \frac{L}{2d} V_R = K_{45} V_R \quad \text{Eqn. 2-15}$$

The above analysis assumes a point source of ions entering the electric field region within the ESA. The resolution of the device, R for a finite slit width, w for the 45-degree analyzer is given by Eqn. 2-16.⁷⁶ The resolution of the ESA used is 0.6%. Hofer lists the resolution of past parallel-plate analyzers used to measure the ion energy distribution of Hall thrusters in Reference 77.

$$R \equiv \frac{\Delta E_i}{E_i} = \frac{w}{L} \sin \theta = \frac{\sqrt{2} w}{2L} \quad \text{Eqn. 2-16}$$

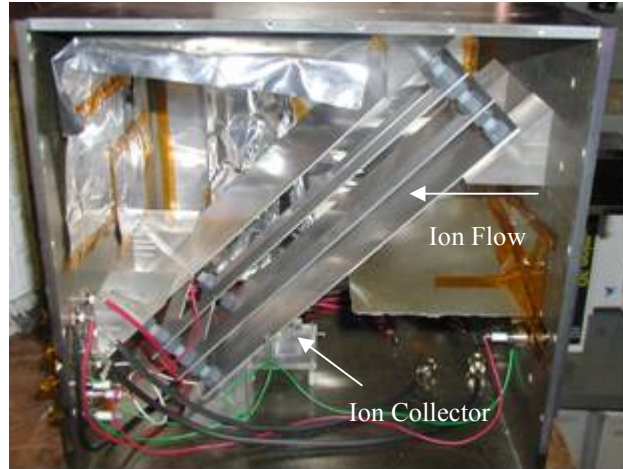


Figure 2-25: Photo of the parallel-plate electrostatic energy analyzer.

The resulting current to the detector can be expressed as the sum of the currents associated with ions of various charge states as given by Eqn. 2-17. The current due to each component can, in turn, be written as shown in Eqn. 2-18, where q_i is the charge multiple of each ionic species. Summing the components of Eqn. 2-18, explicitly calculating the factors involving charge state raised to the $3/2$ power, and combining constants into a single factor, k , allows the current to be written according to Eqn. 2-19, where we have introduced the charge state fractions, α_j defined by Eqn. 2-20. Finally, we note that the ion density, $n_i(V_i)$ is just the ion energy per charge distribution, as shown in Eqn. 2-21. By assuming that the term in square brackets in Eqn. 2-19 is constant at a given location, the ion voltage distribution can be expressed directly as a function of the collected current and the ion voltage as in Eqn. 2-22. Note that Eqn. 2-22 implicitly assumes that the charge state fractions are independent of the ion voltage. In situations where the fractions change significantly as a function of voltage, the energy per charge distribution would need to be modified by the bracketed term in Eqn. 2-19 where the charge state fractions would be specified at each value of ion voltage.

$$I_C = \sum_j I_j \quad \text{Eqn. 2-17}$$

$$I_j = A_c n_j(V_i) v_j q_j e = A_c n_j(V_i) q_j^{3/2} e^{3/2} \sqrt{\frac{2V_i}{m_i}} \quad \text{Eqn. 2-18}$$

$$I_C = k \sqrt{V_i} n_i(V_i) [\alpha_1 + 2.83\alpha_2 + 5.20\alpha_3 + \dots] \quad \text{Eqn. 2-19}$$

$$\alpha_j \equiv \frac{n_j}{\sum_k n_k} \quad \text{Eqn. 2-20}$$

$$n_i(V_i) = \int_{v_i}^{\infty} q_i f_i(v) dv \quad \text{Eqn. 2-21}$$

$$f(V_i) \propto \frac{I_C}{\sqrt{V_i}} \quad \text{Eqn. 2-22}$$

Several researchers have constructed ESAs of varying size to study electric propulsion devices both at PEPL^{77, 78} and the Aerospace Corporation.⁷⁶ The instrument used for this work was designed and constructed by Beal.⁵⁰ The instrument is a derivative of a similar design used successfully by Pollard to study a Hall thruster plume.²⁸ The main body of the ESA consists of a cube constructed of the dielectric mica material measuring approximately 300 mm (12") in each dimension. Use of a dielectric material reduces the disturbance to the plasma plume caused by the more common grounded devices. The inner surface of the box is covered in aluminum foil, which is electrically grounded to the chamber to prevent charge accumulation within the instrument. To maintain a low pressure within the mica box, slots are machined into the side panels. Grounded aluminum baffles placed at the vent hole entrances stop ions from entering, but allow neutrals to escape. A nude Faraday probe (Probe A) is used as a current detector to measure the impacting ion current. The collector is spray-coated with

tungsten to minimize the secondary electron emission. The SEE yield of tungsten due to impacting xenon ions is low (<0.04 electrons per ion for Xe^+) and nearly constant over the energy range of interest to the present study; and thus, the energy per unit charge distribution should not be skewed when collecting high-energy ions.⁷⁹

The parallel plates are held in position and electrically isolated by nylon rods that are threaded into plexiglas blocks bolted to the mica box. The parallel plates, constructed of 1.588 mm (0.0625") thick aluminum, are separated by a distance of d equals 76.2 mm (3.0"). The rectangular slits in the base plate measure 1.5 x 15 mm (0.06" x 0.6") and are 152.4 mm (6.0") apart. To reduce the adverse effects of fringing electric fields, two field correction plates are placed between the main plates at one-inch intervals and biased by 2 M Ω resistor strings.

During data collection, a LabView VI sweeps the repelling plate voltage, V_R , from 0 up to as high as 1000 volts using a Keithley 2410 sourcemeter. A Keithley model 486 picoammeter measures the ion current collected at the detector. Both the plate voltage and the collected current are recorded by a computer running LabView software. Several ESA traces recorded at each data point verify the repeatability of the collected data. Figure 2-26 shows two sets of data collected on centerline of the P5-A thruster, which show the repeatability of the device and the Hall thruster. The measured ion voltage distribution can be affected by the plasma potential at the sampling aperture. As plasma potential increases, the measured spectra shifts to higher voltages.⁸⁰ In this work, the ESA is positioned 1.0 or 1.5 meters downstream of the thruster exit plane (depending on operating condition), where the measured plasma potential is low enough (< 10 volts) that the effect on the ion energy per unit charge distribution should be negligible.

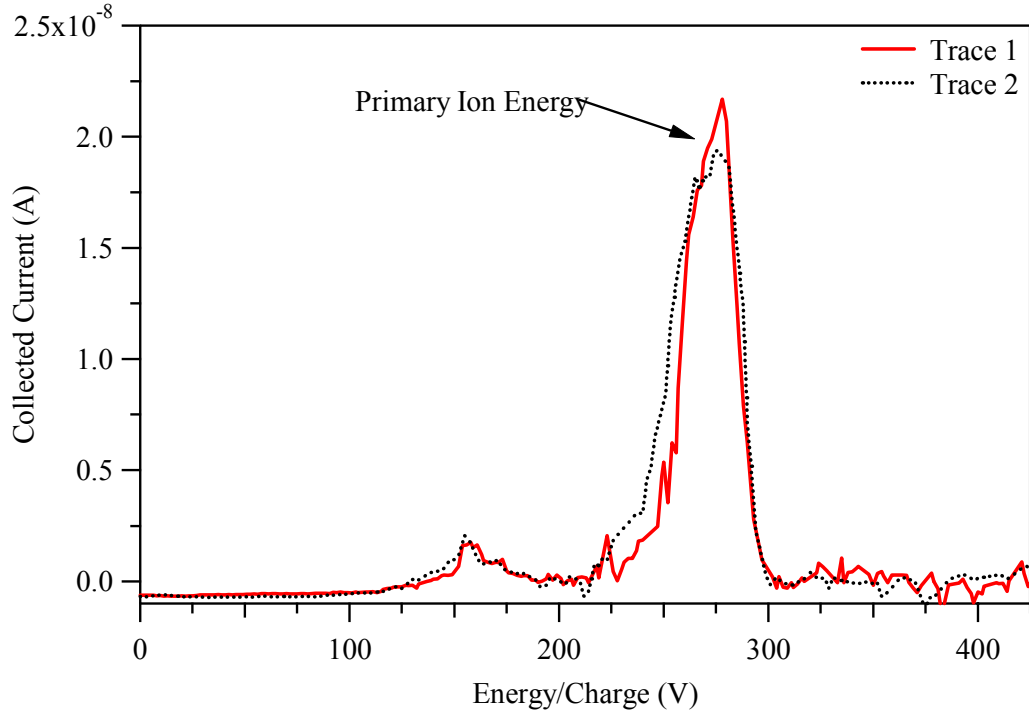


Figure 2-26: Two ESA traces collected on the centerline of the P5-A operating at 300 V, 5 A. The traces show that the ESA has good repeatability.

2.9 ExB Probe

As pointed out in the previous section, the ESA is unable to distinguish amongst ions of different charge. The ExB probe, also commonly referred to as a Wien filter, is designed to measure the charge state fractions in the plasma plume.^{81, 56} This device uses the Lorentz Force, given by Eqn. 2-23, on a moving ion caused by electric and magnetic fields. The ExB probe creates crossed electric and magnetic fields that are mutually perpendicular to the initial ion velocity vector, \vec{v}_i as depicted in Figure 2-27. In this system, only ions for which the Lorentz force vanishes are able to pass through the crossed field region and reach the collector. The velocity of the collected ion, v_{coll} , is thus related to the electric and magnetic field magnitudes by Eqn. 1-7.

$$\vec{F} = q_i e (\vec{E} + \vec{v}_i \times \vec{B})$$

Eqn. 2-23

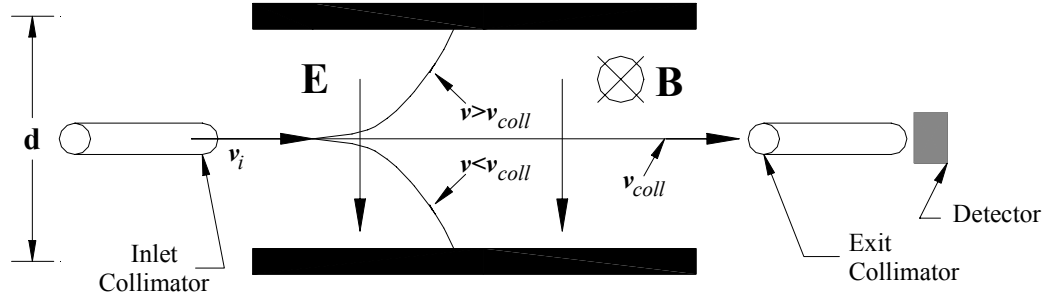


Figure 2-27: Schematic of an ExB probe.

The ExB probe is purely a velocity filter. Thus, the collection criterion is independent of ion mass and charge state, as shown in Eqn. 1-7. The charge state is determined by using the relationship between ion velocity, v_i and voltage, V_i given by Eqn. 2-24. Eqn. 1-7 written for the collected particles is combined with Eqn. 2-24 to yield an equation that relates the voltage and charge state of an ion to the probe voltage at which it will be detected. Eqn. 2-25 shows this relationship, where the magnitude of the electric field has been substituted with the voltage between the electrodes for the ExB probe, V_{ExB} , divided by the electrode separation distance, d . The ion voltage distribution in a Hall thruster plume is normally on the order of 20 to 30 volts wide. Thus, multiply-charged ions appear as distinct populations centered on a probe voltage of approximately $(q_i)^{1/2}$ times the probe voltage at which singly-charged ions are detected.

$$v_i = \sqrt{\frac{2q_i e V_i}{m_i}}$$

Eqn. 2-24

$$V_{ExB} = Bd \sqrt{\frac{2q_i e V_i}{m_i}}$$

Eqn. 2-25

The ExB probe used in this study was originally designed and built by Kim.⁸¹ Four ceramic permanent magnets create the magnetic field within this device. The resultant magnetic field strength in the crossed-field region averages to 0.162 Tesla and has an axial variation of less than 10%.⁸¹ The electric field is created by applying a voltage between the two 27.9 x 3.8 cm rectangular aluminum electrodes, separated by a distance of 1.90 cm. The configuration used in this investigation differs from Kim's in that the inlet and exit drift tube diameters have been increased to increase the magnitude of the collected signal and the size of the imaged thruster area. This change reduces the probe resolution, which is characterized by the degree to which the theoretical collection voltage of an ion can vary from the applied one, but still reach the collector. The resolution is give by w in Eqn. 2-26 and implies that ions with $V_{ExB} \pm w$ will be detected at a probe voltage of V_{ExB} .⁸¹ The geometric properties used in Eqn. 2-26 are defined in Table 2-8 and the values used for the measurements described in this dissertation are included as well. The probe geometry listed in Table 2-8 results in an acceptance cone half angle of approximately 3.1 degrees and a probe resolution (in voltage) of approximately 3% for 300 volt ions and 6% for 600 volt ions. The equation below is used to calculate the resolution of the ExB probe.⁸¹

$$w \leq \frac{V_i d}{Z_f} \left(\frac{a_1 + a_2}{Z_c} + \frac{a_3 + a_4}{Z_M} \right) \quad \text{Eqn. 2-26}$$

Parameter	Symbol	Value (mm)
Diameter of Inlet Collimator Entrance	a_1	6.5
Diameter of Inlet Collimator Exit	a_2	10.0
Diameter of Collector Collimator Entrance	a_3	8.7
Diameter of Collector Collimator Exit	a_4	8.7
Length of Inlet Collimator	Z_c	152.4
Distance Between Collimators	Z_f	254.0
Length of Exit Collimator	Z_M	152.4
Distance Between Electrodes	d	190

Table 2-8: Geometric properties of the ExB probe used for this study.

For this investigation, the negative electrode is grounded and the positive electrode is biased positive by a Keithley model 2410 sourcemeter. Figure 2-28 shows the circuit used. Ions that successfully traverse the crossed electric and magnetic fields are collected by a tungsten plate (Probe A), which has a SEE coefficient of γ_j . A Keithley model 486 picoammeter records the current to the plate, which can be written as

$$I_j = A_c q_j e n_j u_j (1 + \gamma_j) = A_c q_j e n_j (1 + \gamma_j) \sqrt{\frac{2e q_j V_j}{m_j}}. \quad \text{Eqn. 2-27}$$

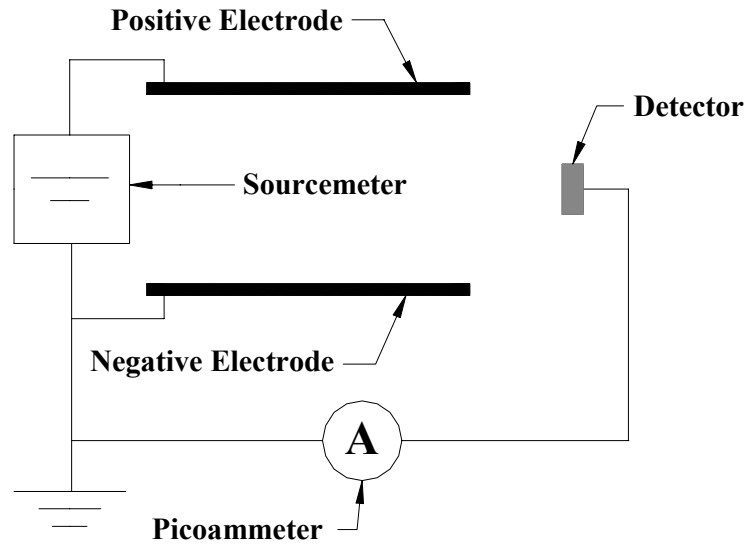


Figure 2-28: Electrical Schematic of the ExB Probe.

The current due to each charge state, I_j , is equal to the area under the corresponding peak depicted in the sample ExB probe trace shown in Figure 2-29. It is challenging to determine the area under each curve because of the overlap between the peaks. For example, the population visible between about 75 and 125 volts in the sample data of Figure 2-29 is likely to contain contributions from both singly-charged and doubly-charged ions.

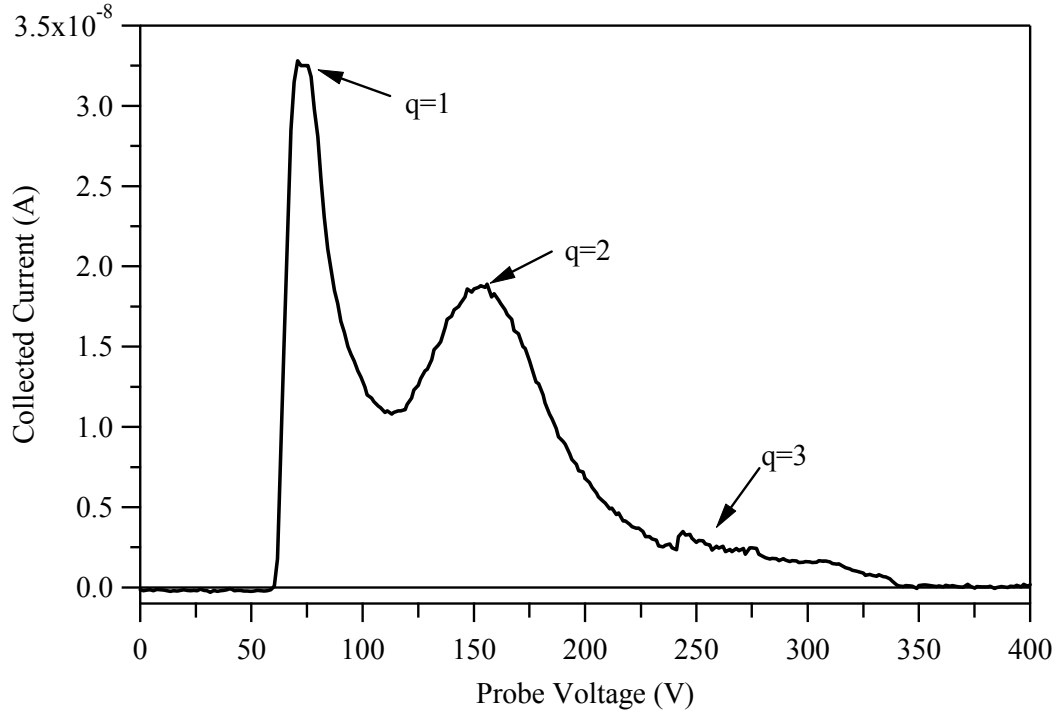


Figure 2-29: Sample ExB data taken on the centerline of the P5-A operating at 300 V, 5 A, which shows the peaks due to various charge species.

As explained by Beal, the ExB peak overlaps will not allow us to estimate each species contribution to the collected current.⁵⁰ To avoid inaccuracies inherent in estimating charge fraction from the area under the current traces, Beal assumes that the current due to each species is proportional to the product of the peak height and the half width at half the maximum value (HWHM). Following the derivation from Hofer, *et al*,⁸² the measured current due to each species is then related to the corresponding current fraction through Eqn. 2-28.⁵⁰ Substituting the expression in Eqn. 2-27 and the definition of the species fraction given by Eqn. 2-29, the measured current fractions can be related to the species fraction s by Eqn. 2-30. Evaluating Eqn. 2-30 for each species and applying the normalization condition stated in Eqn. 2-31 yields the charge state fractions.

$$\Omega_j = \frac{I_j}{\sum_j I_j} \quad \text{Eqn. 2-28}$$

$$\alpha_j = \frac{n_j}{\sum_k n_k} \quad \text{Eqn. 2-29}$$

$$\alpha_j = \frac{\Omega_j \sum_j \left[q_j^{3/2} \alpha_j (1 + \gamma_j) \right]}{q_j^{3/2} (1 + \gamma_j)} \quad \text{Eqn. 2-30}$$

$$\sum_j \alpha_j = 1 \quad \text{Eqn. 2-31}$$

Unfortunately, the operating pressure in the immediate vicinity of the ExB probe entrance is too high to allow multiply-charged ions to be detected for much of the operating condition text matrix of this investigation. The same phenomenon is observed by Kim in the plume of the SPT-100. Thus, charge fractions are not calculated at all conditions.

The derivation of Eqn. 2-30 requires an important assumption. It assumes that the $(V_j)^{1/2}$ term is constant for all charge states, which appears as the use of a single ion voltage, V_j , rather than a separate V_j for each species in Eqn. 2-27. This is valid if all ions, regardless of charge state, are created at the same location in the thruster discharge chamber, accelerated through the same potential drop, and reach the probe without having a CEX collision. For an unknown fraction of ions, this scenario is not the correct one.

For example, consider two ions, one with charge $q_i = 1$ and the other with $q_i = 2$, formed at the same location in the discharge chamber. Upon exiting the thruster, these ions have the same energy to charge ratio, J_j , and their velocities differ by a factor of $2^{1/2}$, as shown above. If the doubly-charge ion undergoes a CEX collision and becomes singly-charged, it reaches the probe with its original velocity. Because the ExB probe acts purely as a velocity filter, the ion is “counted” as a doubly-charged ion. So, the charge state fractions derived from ExB probe data are more closely related to the charge states of ions as they are accelerated through the electrostatic potential drop in the Hall thruster rather than the local species fractions that exist at the entrance to the probe. The distinction is probably not important for the diagnosis of a single thruster, since ExB probes have been used successfully for this purpose in the past.^{81, 82} However, for a cluster, any changes in charge state that occur as a result of the plumes interactions cannot be detected by this instrument. Nevertheless, the instrument can detect changes in the charge state that occur in the discharge channel due to multiple thruster interactions.

2.10 NASA Glenn Research Center Null-Type Inverted Pendulum Thrust Stand

The thrust of the monolithic and clustered Hall thruster is measured with a high-power null-type inverted pendulum type thrust stand based on the NASA GRC design, the industry standard. Figure 2-30 shows an image of the thrust stand. The springs of this stand are unusually stiff to accommodate the weight of multiple high-power thrusters. The null-type thrust stand holds the thruster at a set position at all thrust levels, which reduces error in the thrust by eliminating changes in the elevation of the thrust

vector. The designer reports the error of the thrust stand to be no better than $\pm 1\%$ of the full-scale calibration. The uncertainty of the thrust measurements in this experiment, determined by examination of the hysteresis and drift, is ± 1 mN.

In-situ thruster/thrust-stand leveling is performed by a remotely-controlled geared DC motor coupled to a jackscrew. A remotely-controlled geared DC motor driven pulley system provides in-situ thrust stand calibration by loading and off-loading small weights to simulate thrust. A linear curve-fit of null-coil voltage versus thrust is used for performance measurements. Soon after the thruster is turned off, a post-test calibration is performed.

To maintain thermal equilibrium within the thrust stand at Hall thruster operating conditions of 50+ kW, the stand is actively cooled by a VWR International 1172 refrigerated recirculating chiller. The thrust stand cooling consists of two and one-half parallel cooling circuits that travel through the structure and outer radiation shroud.

The thrust stand is calibrated in-situ by loading the apparatus with calibrated weights, before and after each test point. Current is passed through each set of thruster magnetic coils, and magnetic tares are found to be negligible. Xenon is passed through both of the cathodes and the cold flow tares are also found to be negligible. This is expected because the cathode centerlines are inclined approximately 45° below the horizontal.



Figure 2-30: Picture of the NASA-457 Null-type Inverted Pendulum Thrust Stand.

2.11 Summary

This chapter presents a detailed description of each diagnostic. The performance of each of the diagnostics is validated by the results of previous experiments. In addition, the theoretical limitations of the data analyses are discussed. These physical diagnostics give the capability to thoroughly characterize the performance and plume characteristics of Hall thrusters.

CHAPTER 3

NEUTRAL DENSITY MAP

The facility effects investigated in this thesis are caused by the neutral background pressure present in the facility. Thus, the first logical step towards understanding facility effects is to create a technique to fully characterize the background pressure in the facility for a given flow rate and facility pumping speed. This backpressure leads to a technique for calibrating a vacuum chamber in terms of pressure, which is a stepping stone into the facility effects portion of this work.

The pressure map investigation consists of 3 parts. The first study maps the cold flow pressure in two facilities to demonstrate the technique and determines the sticking coefficient of xenon on a cryosurface. The second study performs successive cold and hot flow pressure maps on the facility to show that a cold flow neutral density map is equivalent to a hot flow pressure map. The final study creates cold and hot flow pressure maps downstream of the P5 Hall thruster cluster.

3.1 Cold Flow Neutral Density Map

The goal of the pressure map study is to develop a technique to calibrate a vacuum chamber in terms of pressure to account for elevated backpressures while testing Hall thrusters. The neutral gas background pressure of the LVTF is mapped for a series of cold anode flow rates corresponding to Hall thruster operation conditions of 1.5, 3.0,

and 9.0 kW, all at 300 V and one hot anode flow rate at two P5 Hall thruster operating conditions.

Section 3.1 discusses the results of the neutral density background pressure maps, which are used to validate the models and experimentally verify the assumed sticking coefficient (the probability that a xenon atom incident on a cryogenic pumping panel actually sticks to the panel). The computational model employs a direct simulation Monte Carlo method (DSMC) that includes the chamber walls and cryopumps. The results of the cold flow model are discussed in the next section.

3.2 Numerical Tool Development

3.2.1 Cold Flow Model Comparison

Computational analyses of Hall thruster plumes are regularly performed using a hybrid DSMC-PIC formulation.^{41, 83, 84} The DSMC method⁸⁵ models the collisions of the heavy particles (ions and atoms). The Particle-In-Cell (PIC) method⁸⁶ models the transport of the ions in electric fields. A *hybrid* approach is used in which the electrons are modeled using a fluid description. The DSMC code used in the present analysis has been previously validated for cold xenon flows.⁸⁷ In the present study, we apply an existing axially-symmetric DSMC-PIC code developed specifically for Hall thruster plumes.⁸⁴ Atom-atom collisions employ the Variable Hard Sphere (VHS) model,⁸⁵ and isotropic scattering is assumed.

In the model, the LVTF is represented as a cylinder 9 m long and 6 m in diameter. In these cold-flow simulations, the PIC steps are of course not applied. The walls of the chamber are modeled assuming fully diffuse reflection at a temperature of

300 K. The LVTF is equipped with seven cryopumps that are grouped into two sets: four end pumps with a total pumping area of 4.15 m^2 , and three top pumps with a total pumping area of 3.11 m^2 . In the simulations, the total area of each of these two sets is represented by a single pumping surface located in the vicinity of the actual pumps. The temperature of the pumping surfaces is assumed to be 15 K, which is representative of the actual cryosurface temperature. There are no data for the sticking coefficient of xenon on cryogenic panels; however, data for other noble gases indicate a range of 0.6 to 0.8.⁸⁸ These are values for a flux of gas onto bare cryosurfaces. Since the pumps installed in the LVTF are surrounded by liquid-nitrogen-cooled, louvered shrouds, the effective sticking coefficient may be significantly lower than that achieved on a bare cryosurface. Simulations are therefore performed with values of 0.2, 0.4, 0.6, 0.8, and 1.0 to study the sensitivity of the results to this unknown parameter. The DSMC-PIC computations employ a grid of 91 by 61 uniform, rectangular cells. At steady state, the computations typically employ 200,000 particles and the total run time for each case is on the order of four hours.

3.2.2 Results and Discussion

The results of the experimental and numerical work are presented for several cold flow conditions of the Hall thruster in which the plasma is not ignited. These flows therefore simply consist of neutral xenon atoms, which will yield comparable backpressures for future pressure maps with the P5 in hot-flow mode. Figure 2-9 shows the half plane and the 25 cm by 25 cm grid on which pressure data are collected.

The simulation results are compared directly with experimental measurements of pressure for a number of conditions in which the mass flow rate and pumping speed

are varied. The highest values of the pressure map data in Figure 3-1, Figure 3-2, and Figure 3-3 are one order of magnitude below the upper limit of the BA ionization gauge. This is because the IGPS is positioned to allow the BA gauge to reach its upper limit of 10^{-2} Pa (10^{-4} Torr), 0.5 m downstream of the thruster exit plane for an anode mass flow rate of 14.09 mg/s.

Simulation results are presented in Figure 3-1 for a mass flow rate of 10.46 mg/s and a total pumping speed of 240,000 l/s (all seven pumps operating). Both the experiment and simulation include a 0.92 mg/s flow of xenon through the cathode to mimic hot-flow operation. Note that the ion gauges cannot be used within 50 cm of the thruster. Figure 3-1 shows the data comparison along the thruster centerline for the five different values of the sticking coefficient. Clearly, very good agreement is obtained between the simulations and the measurements. The simulation results are sensitive to the sticking coefficient, although the profiles obtained with a value of 0.4 show acceptable agreement with the measured data.

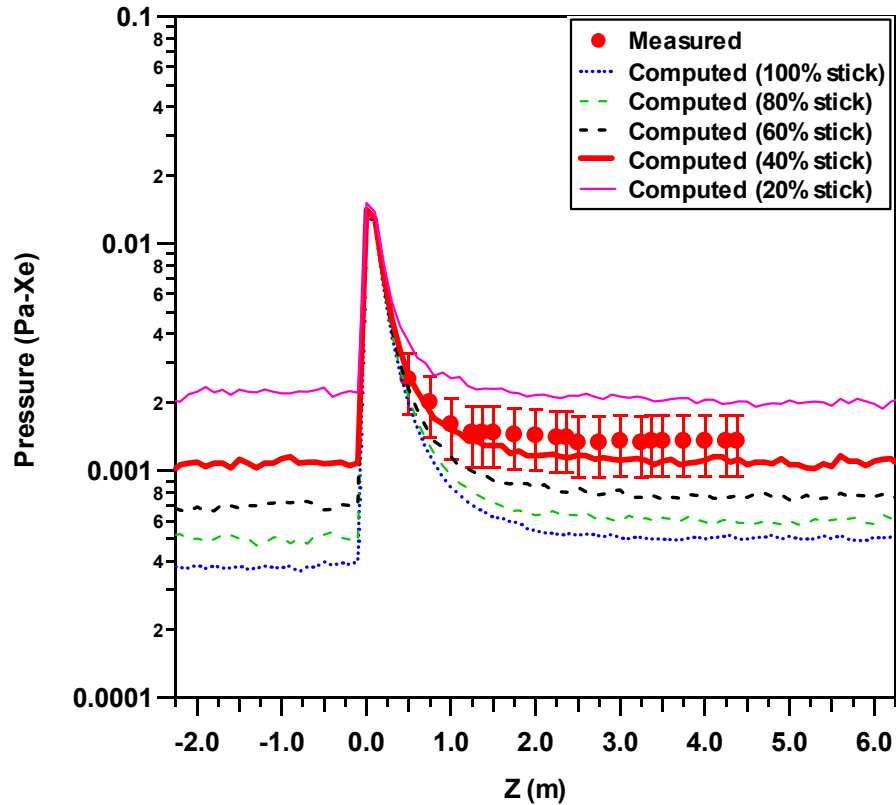


Figure 3-1: Comparisons of simulated and measured pressure distribution within the LVTF for cold flow operation of the NASA-173Mv1 Hall thruster at 10.46 mg/s flow rate and 240,000 l/s pumping along the thruster centerline.

To investigate the generality of the performance of the simulations, two additional cases are simulated. The first retains the flow rate of 10.46 mg/s and considers the lower pumping rate of 140,000 l/s by turning off the three side pumps in the simulation. These results are shown in Figure 3-2. In Figure 3-3, the results are shown for a flow rate of 5.25 mg/s (again with 0.92 mg/s flowing through the cathode) with a total pumping of 140,000 l/s. In both Figure 3-2 and Figure 3-3, acceptable agreement is obtained between simulation and experiment for a sticking coefficient of approximately 0.4.

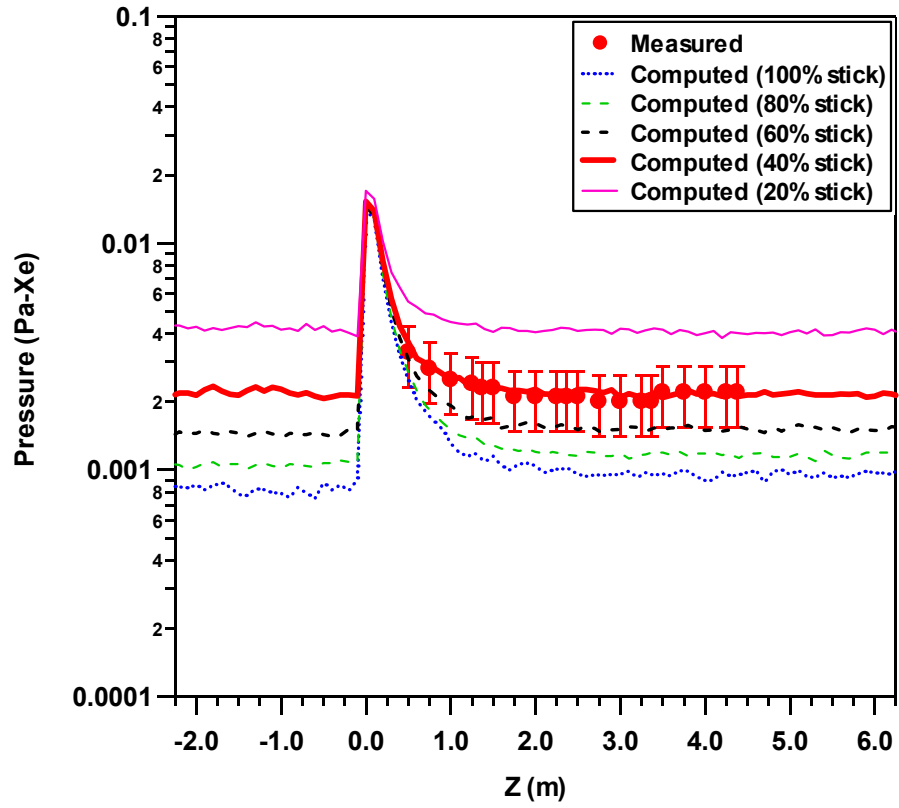


Figure 3-2: Comparisons of simulated and measured pressure distribution within the LVTF for cold flow operation of the NASA-173Mv1 Hall thruster at 10.46 mg/s and 140,000 l/s.

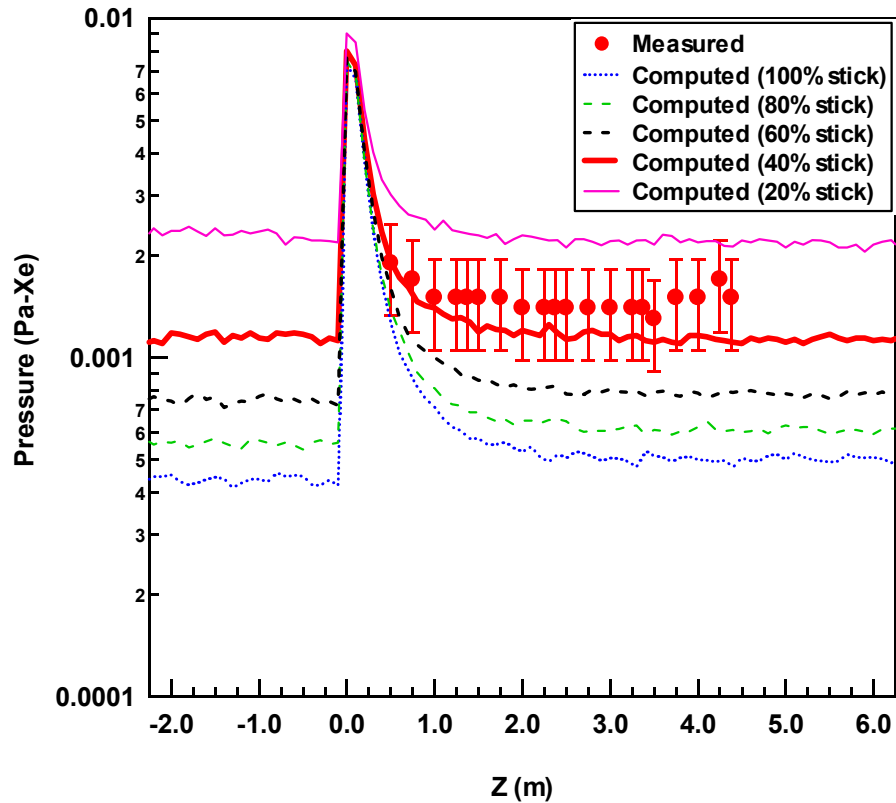


Figure 3-3: Comparisons of simulated and measured pressure distribution within the LVTF for cold flow operation of the NASA-173Mv1 Hall thruster at 5.25 mg/s flow rate and 140,000 l/s.

The cryosurface sticking coefficient is a function of the cryosurface wall properties, the species of the particle colliding with the surface, and the energy of the colliding particle. There is a concern that the sticking coefficient varies significantly with the composition and thickness of the ice formation on the cryosurface rendering the sticking coefficient predictions useless. The two most prevalent issues are the thickness of the initial water-ice layer created from the facility humidity level and the thickness of the xenon-ice layer on the cryosurface. A liquid nitrogen (70 K) flow through the cryopump shroud precedes the activation of the cryopump compressors. The liquid nitrogen-chilled shroud is the first surface inside the vacuum chamber to decrease to 273 K and remains the coldest surface for nearly 2 hours. A large percentage of the water

present in the vacuum chamber, after the mechanical pumps stop, freezes to the liquid nitrogen shroud because the majority of the water molecules make at least one collision with the shroud before reaching the cryosurface. Therefore, the sticking coefficient, which is a function of the composition of the initial layer of ice on the cryosurface, is not significantly affected by the relative humidity in the facility at the time of evacuation.

Past data show that once a thin xenon-ice surface is present on the cryosurface the pumping speed/sticking coefficient of the surface is nearly constant over a wide range of condensed xenon thicknesses on the cryosurface.⁸⁹ For a xenon flow rate of 5.25 mg/s, the cryopumps within the LVTF reach this condition in approximately five minutes. Before collecting pressure map data in the LVTF, a 5.25 mg/s flow rate is condensed on the cryosurfaces for 30 minutes. Therefore, the sticking coefficient remains nearly constant for the duration of the pressure map experiment.

Relevant predictions about the hot flow may be made with the cold flow data despite the large difference in temperature and velocity of the exit plane particles between the two conditions. The energy of the particle colliding with the cryosurface affects the sticking coefficient. The neutrals emanating from the hot anode and the high-speed ions created in the discharge chamber make at least one collision with the 300 K vacuum chamber wall before reaching the cryosurface. A particle collision with the wall accomplishes two things: first, the vacuum chamber wall neutralizes the ion; and second, the inelastic wall collision absorbs energy transferred to the neutrals and ions in the discharge chamber. When the neutral particles reach the liquid nitrogen-chilled shroud surrounding the cryosurface, they are more similar in kinetic make-up to the particles present in the cold flow experiment than those at the thruster exit plane. Moreover, a

large percentage of the particles will then strike the 70 K louvered liquid nitrogen shroud before reaching the cryosurface. Thus, the particles that collide with the cryosurface during the hot flow and cold flow experiments are of nearly the same kinetic makeup. This means that sticking coefficients determined during the cold flow experiment should be valid for simulations of the facility backpressure with the Hall thruster in operation.

3.3 Hot Flow Neutral Density Map

The objective of the experiments presented in this section is to demonstrate a technique for making neutral density pressure maps with hot flow in a vacuum facility. Successive cold flow and hot flow neutral density background pressure maps of the LVTF are performed. Cold anode flow rates of 5.25, 10.46, and 14.09 mg/s are investigated. Hot anode (i.e., discharge on) flow rates of 5.25 mg/s and 10.46 mg/s for discharge voltages of 300 V and 500 V are investigated. These conditions correspond to P5 Hall thruster operating conditions ranging from 1.5 to 5.0 kW. The maps are collected at nominal xenon pumping speeds of 140,000 and 240,000 l/s.

3.3.1 Hot Flow Pressure Map Procedure

Table 3-1 shows the LVTF operating pressure for each flow rate at the nominal xenon pumping speeds of 140,000 l/s and 240,000 l/s. A previous study shows that the nude gauge reading is a much better estimate of the true chamber pressure than the average of the nude and external gauge.⁴⁵ The chamber pressures listed in Table 3-1 are from the nude gauge and are corrected for xenon.

Discharge Voltage (V)	Discharge Current (A)	Anode Flow (mg/s)	Cathode Flow (mg/s)	Nominal Pumping Speed (l/s)	Chamber Pressure (nude) (Torr-Xe)	Chamber Pressure (nude) (Pa-Xe)
300	4.88	5.25	0.92	140,000	5.7E-06	7.6E-04
500	5.30	5.25	0.92	140,000	5.7E-06	7.6E-04
-	-	5.25	0.92	140,000	5.7E-06	7.6E-04
-	-	10.46	0.92	140,000	8.4E-06	1.1E-03
-	-	14.09	0.92	140,000	1.1E-05	1.5E-03
300	4.80	5.25	0.92	240,000	3.5E-06	4.7E-04
500	5.22	5.25	0.92	240,000	3.4E-06	4.5E-04
-	-	5.25	0.92	240,000	3.4E-06	4.5E-04
-	-	10.46	0.92	240,000	5.2E-06	6.9E-04
-	-	14.09	0.92	240,000	6.6E-06	8.8E-04

Table 3-1: Nominal pumping speeds and corresponding LVTF operating pressures for each anode flow rate and thruster condition investigated.

3.3.2 Ionization Gauge Operation

Pressure maps of the chamber are taken with xenon gas flowing through the anode and cathode both with and without the thruster discharge. During hot flow pressure maps, the BA ionization gauges are immersed in plasma. The outer screen of the neutralizer, located in the horizontal plane of the chamber centerline, is in direct contact with the plasma for the hot flow pressure maps. To avoid disturbing the ionization gauge pressure measurements, the outer screen is electrically isolated from the rest of the neutralizer, so that the screen floats. A bias voltage study on the outer screen, presented later in this section, validates this configuration. In addition, an identical inner screen is placed near the entrance of the ionization gauges. The inner screen is also electrically isolated from the neutralizer structure.

To characterize the effect of charged particles on the pressure measurements, outer and inner screen bias voltage studies are performed using the P5 in the LVTF. The

outer and inner screens are electrically isolated from the neutralizer; a biasing wire is connected to each screen so that they can be floated, grounded, or biased to a particular voltage. This configuration allows the screens to repel or attract the charged particle species. The biasing wires connect to a power supply outside of the chamber and current shunts measure the current collected or emitted in each electrical configuration.

First, we investigate the effects of biasing, grounding, and floating the outer and inner screens on the measured pressure. This investigation confirms that there is no capacitive coupling between the screens and the ionization gauge. This study is performed separately on the inner and outer screens of ionization gauge 2. The results show that, with no flow through the thruster, the measured pressure is unaffected by floating, grounding, and biasing the inner and outer screens.

Next, an outer screen bias voltage study is performed with the P5 operating at 300 V and 5.4 A. For this study, the gauge 2 pressure is monitored at a position 1.5 m downstream of the thruster exit plane and on the thruster centerline. The gauge pressure and current collected are recorded for each of the electrical configurations.

Figure 3-4 shows the results of the outer screen bias voltage study. Note that the ionization gauge collects ions to determine the pressure. Initially, the outer screen is floated with no perceptible effect on the pressure measurement. In the floating configuration, gauge 2 measures 4.1×10^{-3} Pa (3.1×10^{-5} Torr) and the outer screen collects 0.2 mA.

Next, the outer screen is biased from -20 V to 50 V in 5 V increments. At increasingly negative bias voltages, the indicated pressure increases slightly. This may

be a result of attracting additional ions into the gauge, which increases the current the gauge filament collects.

In the grounded configuration, the indicated pressure is not perceptibly affected. As the bias voltage becomes increasingly positive, the indicated pressure begins to rise and a large current is collected by the outer screen. The positively biased screen attracts a large number of electrons to the neutralizer resulting in the increased ionization of neutrals within the gauge. The gauge filament then collects the additional ions, increasing the indicated pressure. This study confirms that floating the outer screen for the hot flow pressure map does not affect the performance of the ionization gauges.

The effects on the measured pressure of biasing, grounding, and floating the inner screen are investigated with the P5 operating at 300 V and 4.88 A in the LVTF. In addition, to detect the existence of charged particles within the neutralizer near the entrance to the ionization gauge, an inner screen bias voltage study is performed. For this study, gauges 1 through 5 are monitored in their initial positions as shown in Figure 2-9. The gauge pressure and current collected are recorded with the inner screen biased to +20 V, -20 V, grounded, and floating. The indicated pressure of each gauge does not change with the electrical configuration. The inner screens of ionization gauges 1, 3, and 5 collected no current for any of the electrical configurations. The inner screen of gauge 4 collected a maximum of 10^{-3} mA when biased to +20 V. The inner screen of gauge 2 collects a maximum of 10^{-4} mA when biased to +20 V. The current caused by charged particles entering the neutralizer is far below the 4 mA emission current of the ionization gauges. Thus, the measured fraction of charged particles entering the ionization gauge during hot flow operation is not large enough to affect the indicated pressure.

The thruster is cycled off and on to observe its effect on the pressure indicated by the ionization gauges. If the ionization gauges truly measure the neutral background pressure, then the neutral pressure measured within 1 m of the thruster exit plane will be higher during cold flow than it would be with the thruster on. This is because during thruster operation, approximately 80% of the neutral propellant is ionized and accelerated downstream, reducing the neutral density immediately downstream of the thruster. However, at locations beyond 1.5 m downstream of the thruster exit plane, the plume expands to the chamber background pressure and the neutral density should not vary with the thruster off or on. The thruster is cycled 5 times at a power setting of 300 V and 4.88 A. A. No appreciable change in indicated pressure is observed 1.5 m downstream of the exit plane.

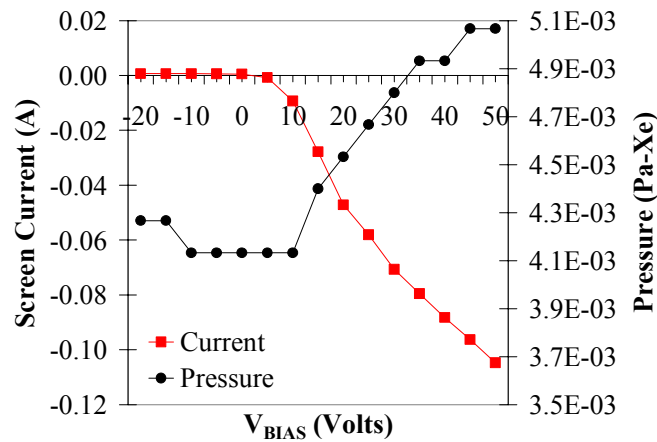


Figure 3-4: Outer Screen Bias Voltage Study

3.3.3 Ionization Gauge Error

Figures 3-5 and 3-6 present representative raw cold and hot flow data taken along the chamber centerline. There are noticeable discontinuities in the pressure when transitioning between the interrogation areas swept by each ionization gauge. Over the

range of motion of each ionization gauge, the pressure changes smoothly. The large gradients between ionization gauges are caused by the limited accuracy of the ionization gauge design. No two ionization gauges manufactured indicate the same pressure, even when exposed to the same atmosphere simultaneously.

Using the axial pressure profiles presented later in this section, the raw data are corrected. The raw data of gauge 2 are all shifted by a constant value, so that the furthest downstream centerline pressure taken by gauge 4 is approximately equal to the most upstream centerline point taken by gauge 2. The same procedure is used to correct the data of gauge 1 to gauge 2 and the data of gauge 3 to gauge 1. Thus, individual correction constants are developed for ionization gauges 1, 2, and 3. Analysis of the radial profiles shows that the offset between ionization gauge 4 and 5 is on the order of 10^{-5} Pa (10^{-7} Torr). Therefore, a correction constant is not developed for ionization gauge 5.

The correction constants derived from the cold flow data are applied to the hot flow data at both 300 V and 500 V for gauges 1, 2, and 3. Because of the unstable behavior of gauge 5 at hot flow operating conditions, those data are not included in the hot flow analysis. For the hot flow data, an additional correction factor is then needed for gauge 4. The raw data of gauge 4 are all shifted by a constant value so that the most downstream centerline point taken by gauge 4 is approximately equal to the most upstream centerline corrected point taken by gauge 2.

The chamber was vented to atmosphere between the 140,000 l/s and 240,000 l/s pressure maps to permit repair of the radial positioning table. The ionization gauges were exposed to atmosphere; thus, one set of correction constants were developed for the

140,000 l/s data set and another set for the 240,000 l/s data set. Table 3-2 shows the correction constants for these data. Figures 3-7 through 3-9 present the corrected cold and hot flow data taken along the chamber centerline.

Gauge 1 Δ (Pa-Xe)	Gauge 2 Δ (Pa-Xe)	Gauge 3 Δ (Pa-Xe)	Gauge 4 Δ (Pa-Xe)	Nominal Pumping Speed (l/s)	Flow Condition
+2.7E-04	+1.3E-04	-3.2E-04	-	140,000	Cold
+2.7E-04	+1.3E-04	-3.2E-04	1.3E-04	140,000	Hot
+2.4E-04	+1.3E-04	-2.5E-04	-	240,000	Cold
+2.4E-04	+1.3E-04	-2.5E-04	1.5E-04	240,000	Hot

Table 3-2: Ionization gauge correction constants for each pumping speed.

3.3.4 Hot Flow Neutral Density Map Results

Table 3-1 presents the operating conditions and facility background pressures investigated in this test. The chamber pressure is mapped at cold anode flow rates of 5.25, 10.46, and 14.09 mg/s for nominal facility pumping speeds of 140,000 and 240,000 l/s. In addition, the chamber pressure is mapped at P5 thruster operating conditions of 300 V and 500 V with flow rates of 5.25 mg/s and 10.46 mg/s at nominal facility pumping speeds of 140,000 and 240,000 l/s.

Figures 3-10 through 3-16 present the cold and hot flow pressure map data recorded in the LVTF. Figure 3-17 presents a cold flow pressure map of VF-12. We are unable to acquire data for the hot flow pressure maps with ionization gauge 5 because the gauge 5 pressure in the interrogation area is above the maximum allowable pressure of the controller. While it is possible to override the shutdown pressure of the ionization

controller, operating the ionization gauge at “high” pressure may damage the unit. Therefore, the automatic shutdown pressure limits are left operational for these experiments.

Hot flow data for ionization gauge 3 are only available for the 140,000 l/s pumping condition. The controller for ionization gauge 3 registers an electrical connection failure during thruster discharge for the 240,000 l/s pumping condition. The gauge resumes normal operation when the discharge is extinguished. Inspection of the electrical connections did not locate the problem.

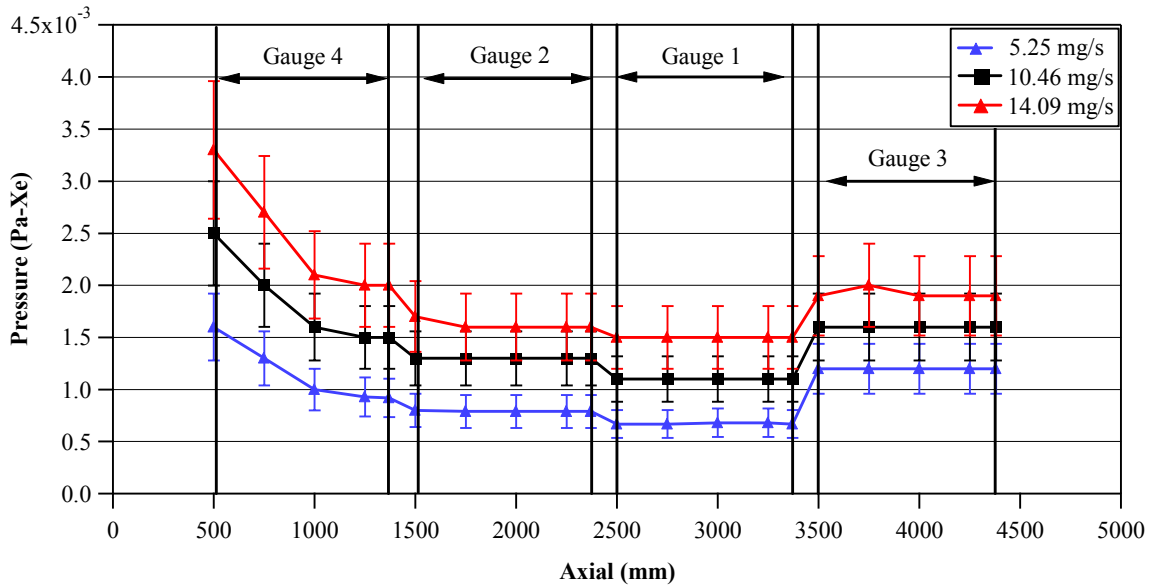


Figure 3-5: Raw cold flow data axial profile for a nominal pumping speed of 240,000 l/s.

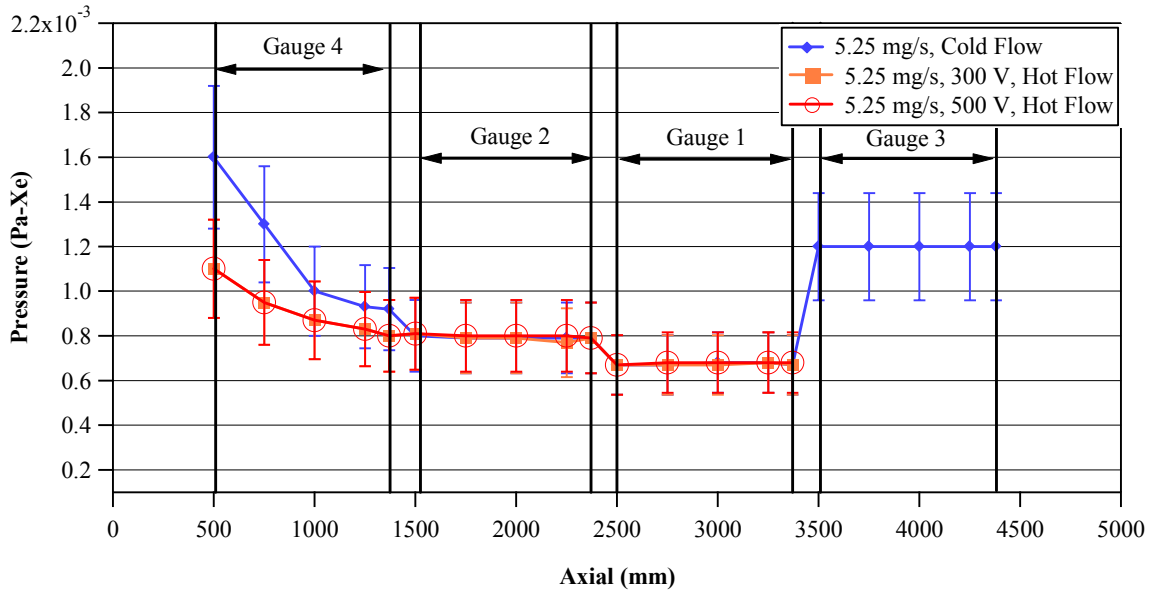


Figure 3-6: Raw hot flow data axial profile for a nominal pumping speed of 240,000 l/s.

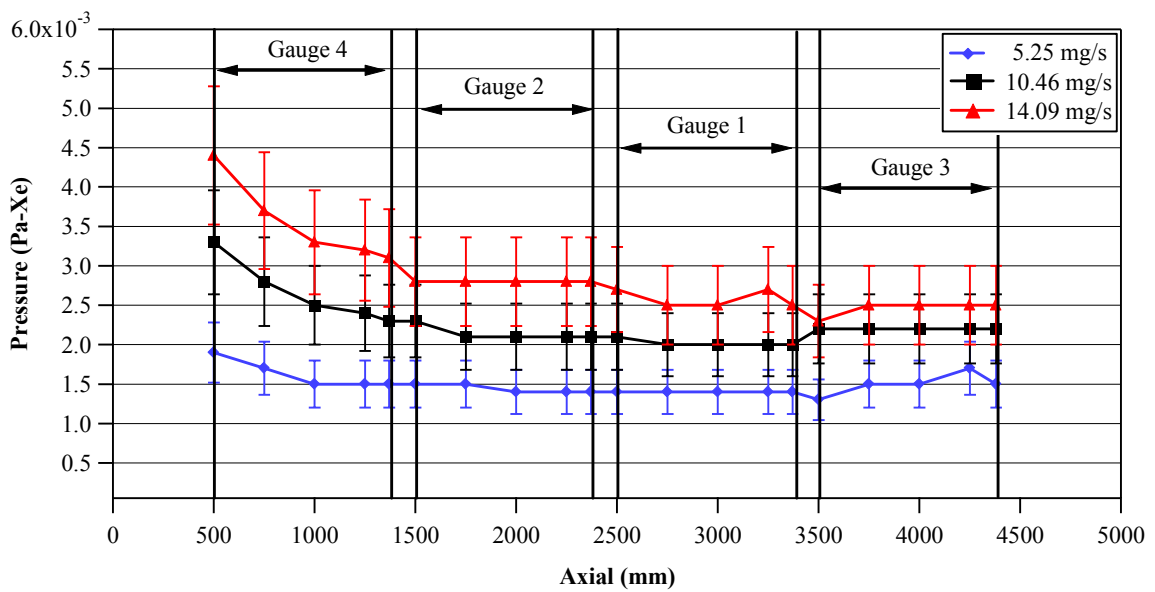


Figure 3-7: Corrected cold flow data axial profile for a nominal pumping speed of 140,000 l/s.

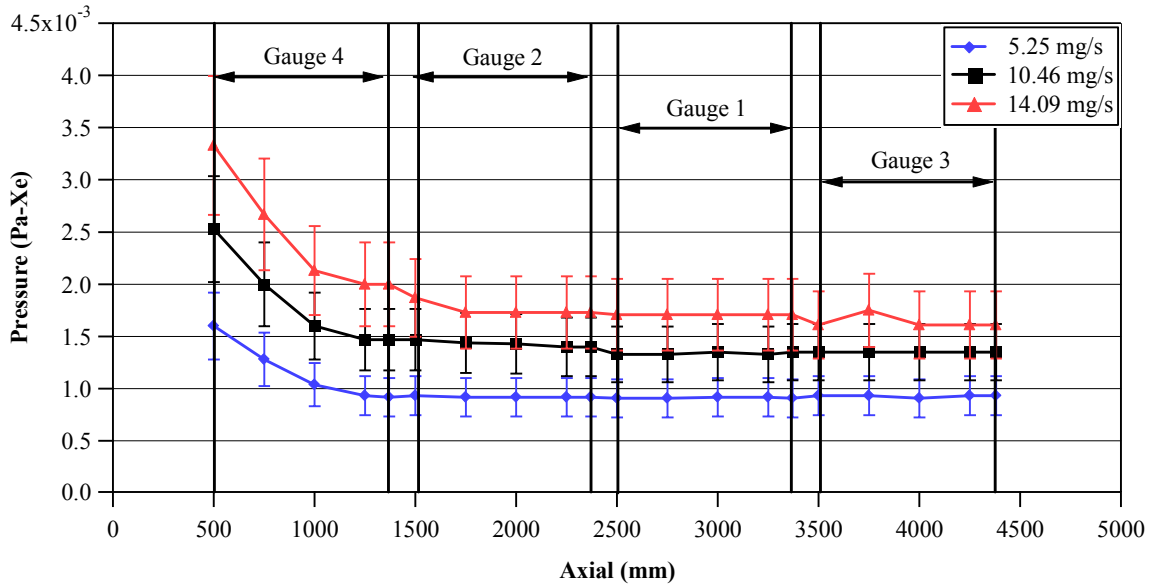


Figure 3-8: Corrected cold flow data axial profile for a nominal pumping speed of 240,000 l/s.

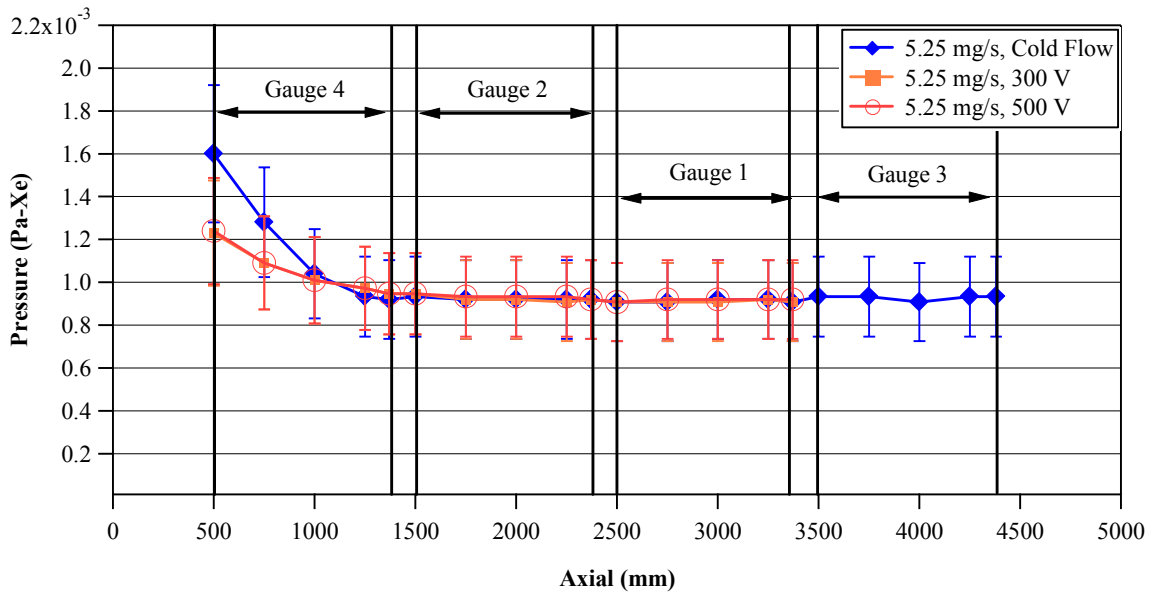


Figure 3-9: Corrected hot flow data axial profile for a nominal pumping speed of 240,000 l/s.

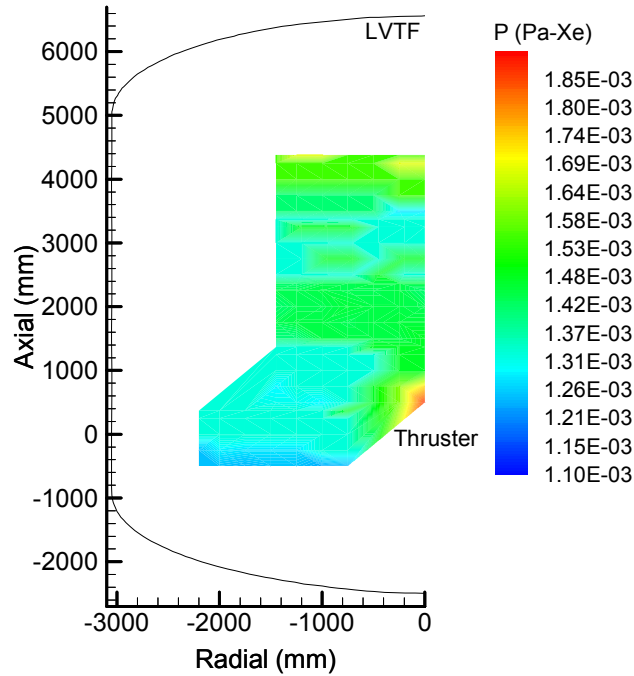


Figure 3-10: Cold flow pressure map of the LVTF with an anode flow rate of 5.25 mg/s and a cathode flow rate of 0.92 mg/s, at a nominal pumping speed of 140,000 l/s and operating pressure of 6.9×10^{-4} Pa (5.2×10^{-6} Torr), corrected for xenon.

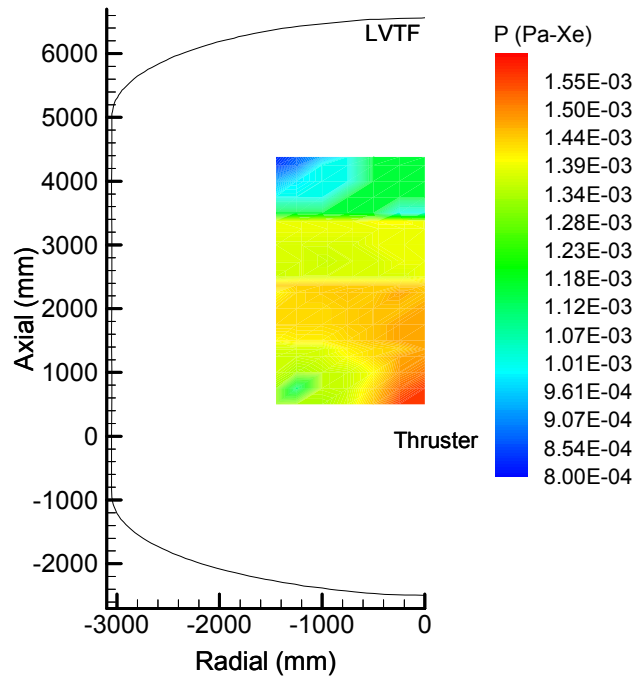


Figure 3-11: Hot flow pressure map of the LVTF with an anode flow rate of 5.25 mg/s and a cathode flow rate of 0.92 mg/s, at a nominal pumping speed of 140,000 l/s and operating pressure of 7.2×10^{-4} Pa (5.4×10^{-6} Torr), corrected for xenon. (300 V, 4.88 A thruster operation)

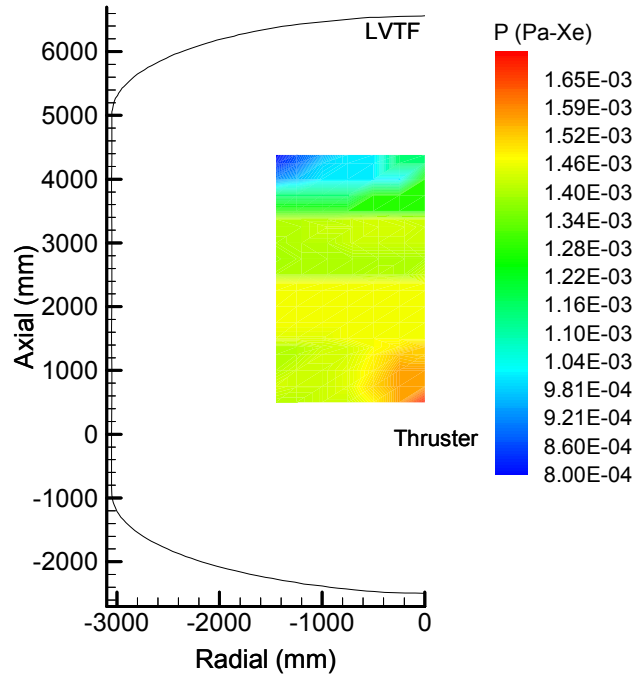


Figure 3-12: Hot flow pressure map of the LVTF with an anode flow rate of 5.25 mg/s and a cathode flow rate of 0.92 mg/s, at a nominal pumping speed of 140,000 l/s and operating pressure of 7.6×10^{-4} Pa (5.7×10^{-6} Torr), corrected for xenon. (500 V, 5.30 A thruster operation)

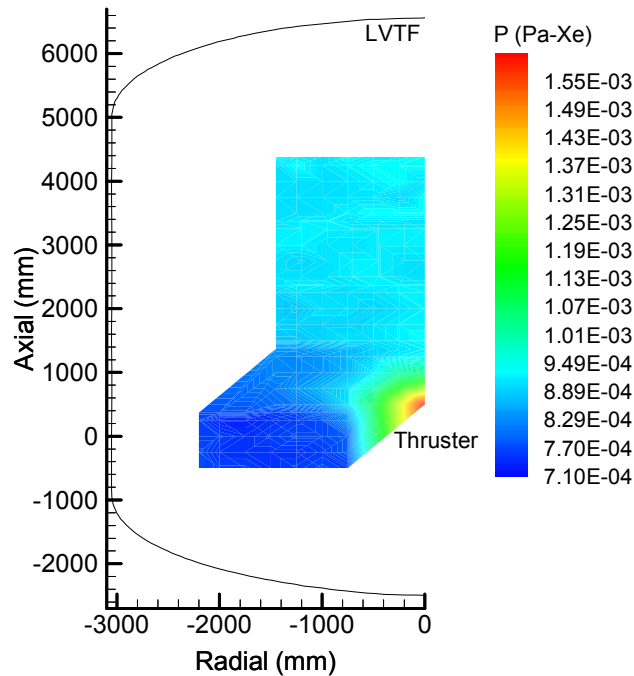


Figure 3-13: Cold flow pressure map of the LVTF with an anode flow rate of 5.25 mg/s and a cathode flow rate of 0.92 mg/s, at a nominal pumping speed of 240,000 l/s and operating pressure of 4.5×10^{-4} Pa (3.4×10^{-6} Torr), corrected for xenon.

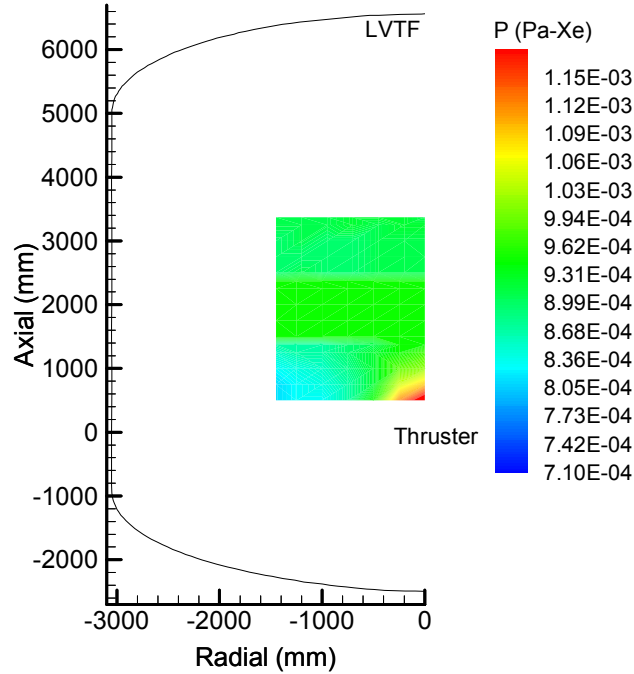


Figure 3-14: Hot flow pressure map of the LVTF with an anode flow rate of 5.25 mg/s and a cathode flow rate of 0.92 mg/s, at a nominal pumping speed of 240,000 l/s and operating pressure of 4.7×10^{-4} Pa (3.5×10^{-6} Torr), corrected for xenon. (300 V, 4.80 A thruster operation)

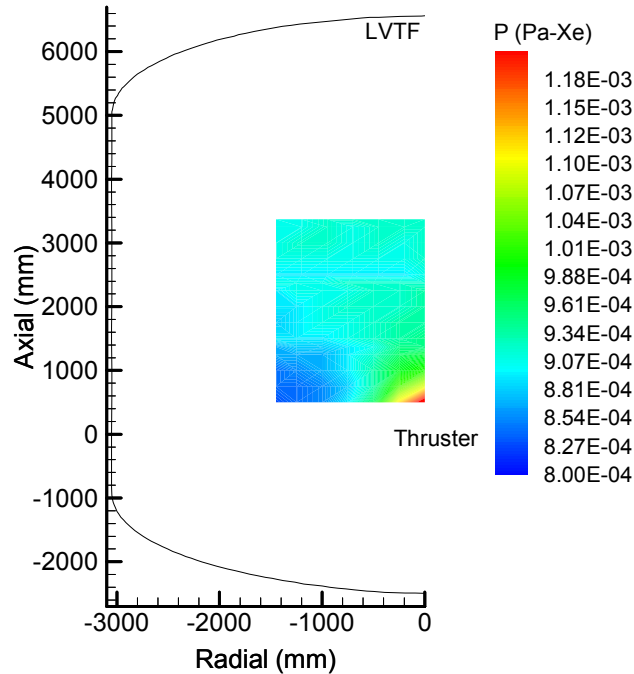


Figure 3-15: Hot flow pressure map of the LVTF with an anode flow rate of 5.25 mg/s and a cathode flow rate of 0.92 mg/s, at a nominal pumping speed of 240,000 l/s and operating pressure of 4.5×10^{-4} Pa (3.4×10^{-6} Torr), corrected for xenon. (500 V, 5.22 A thruster operation)

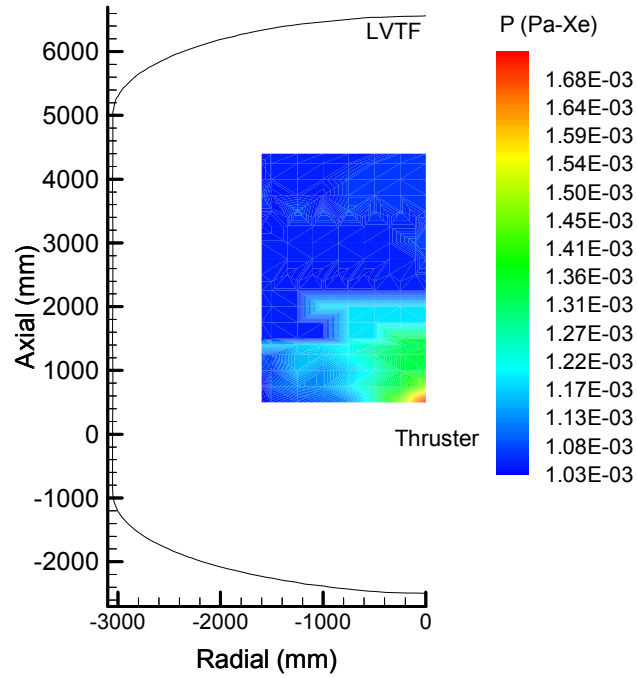


Figure 3-16: Hot flow pressure map of the LVTF with an anode flow rate of 10.46 mg/s and a cathode flow rate of 0.60 mg/s, at a nominal pumping speed of 240,000 l/s and operating pressure of 7.6×10^{-4} Pa (5.7×10^{-6} Torr), corrected for xenon. (300 V, 11.1 A thruster operation)

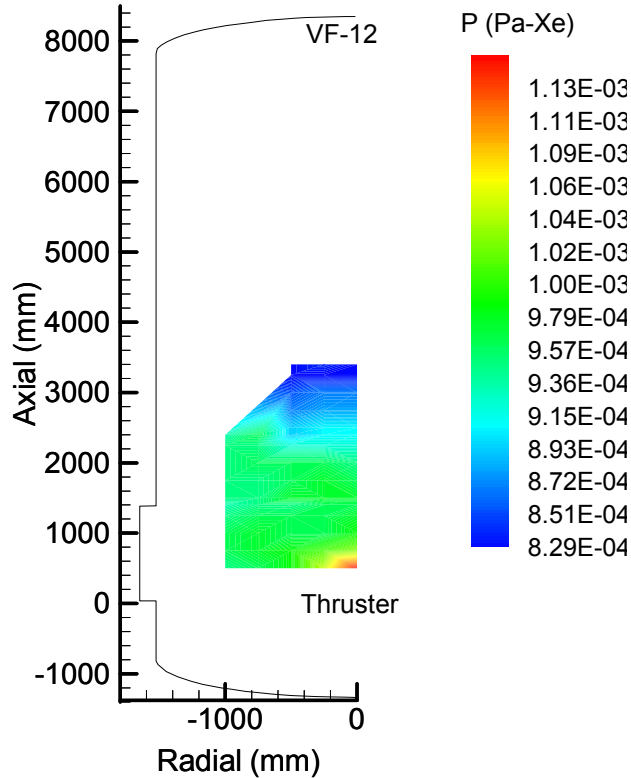


Figure 3-17: Cold flow pressure map of VF-12 with an anode flow rate of 5.25 mg/s and a cathode flow rate of 0.60 mg/s, at a nominal pumping speed of 282,000 l/s and operating pressure of 4.0×10^{-4} Pa (3.0×10^{-6} Torr), corrected for xenon.

3.3.5 Hot Flow Neutral Density Map Discussion

Analysis of the cold and hot flow axial pressure profiles on the chamber centerline shows that for all flow rates the plume pressure decreases from a maximum at the thruster exit plane to a minimum slightly higher than the facility background pressure approximately 2 m downstream of the exit plane. As the flow rate increases, the pressure gradient in the plume increases, but the length of the plume expansion to the chamber background pressure remains constant. Increasing the pumping speed lowers the magnitude of the pressure, while the behavior of the axial pressure profile remains unaffected. The previous two trends are apparent in Figures 3-7 and 3-8. The background pressure decreases continually in the radial direction. The trends shown in

Figures 3-10 through 3-16 suggest that the background pressure will drop to the facility background pressure near the chamber walls. Previous analysis shows that the nude ionization gauge reading is a much better estimate of the true LVTF operating pressure than the external ionization gauge.⁴⁵

The IGPS is used to map the neutral background pressure in Vacuum Facility 12 (VF-12) at NASA Glenn Research Center. The LVTF and VF-12 differ in physical geometry; i.e. the LVTF has a 3 m larger diameter than VF-12. Figure 3-17 shows a cold flow background pressure map in VF-12 with the NASA-173Mv1 at a flow rate of 5.25 mg/s and operating pressure of 4.0×10^{-4} Pa (3.0×10^{-6} Torr).⁹⁰ The background pressure trends in the LVTF are similar to those observed in VF-12.

Figure 3-9 shows that the axial pressure profiles of the LVTF for hot and cold flow are very close for identical flow rates and pumping speeds. The pressure maps in Figures 3-10 through 3-12 and Figures 3-13 through 3-15 show this trend for the 140,000 l/s and 240,000 l/s condition, respectively. Figure 3-16 shows a 300 V hot flow pressure map of the LVTF at an anode flow rate of 10.46 mg/s and a pumping speed of 240,000 l/s. The 10.46 mg/s cold flow pressure map taken at 240,000 l/s is not shown, but is very similar to the 300 V, 10.46 mg/s hot flow pressure map. Thus, measuring the neutral background pressure of the chamber with a cold flow is equivalent to taking the same measurement with a hot flow.

The fact that the 300 V hot flow, 500 V hot flow, and 5.25 mg/s cold flow axial pressure profiles and background pressures are nearly the same implies that a particle collision with the facility wall reduces the energy of the accelerated plume ion to that of a cold flow particle. We also see that the axial pressure profiles and background pressure

are nearly the same for the 10.46 mg/s cold and hot flow conditions. Therefore, the cryosurface sticking coefficient is unaffected by the hot flow present with the thruster operating.

3.4 Vacuum Facility Calibration

The above experiments demonstrate that the measured pressure field in a vacuum facility caused by cold flow from the Hall thruster anode and cathode is equivalent to the pressure field at a hot flow condition. This simplifies pressure determination in a vacuum facility containing a Hall thruster plume. With these data we have the ability to calibrate any vacuum facility in terms of pressure.

The measured facility operating pressure at several cold flow rates is used to calibrate a direct simulation Monte Carlo (DSMC) model of the operating facility.⁹⁰ The numerical model then makes accurate predictions of the vacuum facility backpressure for a given propellant flow rate. Simulations of the facility using this numerical model show where to place an ionization gauge on the facility to monitor the backpressure. The simulation results also show any gradients between the wall-mounted ionization gauge and the actual backpressure to which the plume expands. Thus, from a measurement of the pressure on the facility wall, the true operating pressure at the centerline of the facility can be determined.

3.5 Cluster Pressure Map

The final portion of this work is a pressure map of the P5 Hall thruster cluster plume. The cluster plume expansion cannot be modeled with an axially-symmetric code.

Thus, an experimental pressure map of the cluster plume provides excellent data with which to validate the 3-dimensional model.

3.5.1 Cluster Pressure Map Procedure

The same experimental procedure and experimental setup are used for the cluster experiment as in the single thruster experiment. For the cluster pressure map, data are only collected with ionization gauges 2 and 4. Previous pressure maps show that these gauges sample the region in which the majority of the plume expansion occurs.

The cluster pressure maps are collected at cluster cold and hot flow rates of 5.25 and 10.46 mg/s, with 0.92 mg/s flowing through each cathode. The mappings are only performed at a pumping speed of 240,000 l/s, so that the plume pressure does not exceed the upper limit of the ionization gauges. The cluster elements are placed at the same axial position as the single element. The centerline of P5-A is positioned 20 cm to the left of chamber centerline, and P5-B is positioned to 20 cm to the right of the chamber centerline.

3.5.2 Results

Figure 3-18 shows a hot flow pressure map of the cluster plume, with each element operating at 300 V and 5.12 A. Figure 3-19 shows a cold flow pressure map of the cluster plume with a flow rate of 10.46 mg/s through each thruster element. Figure 3-20 shows a hot flow pressure map of the cluster plume, with each element operating at 500 V and 11.8 A. The regions mapped capture the majority of the plume expansion from the cluster.

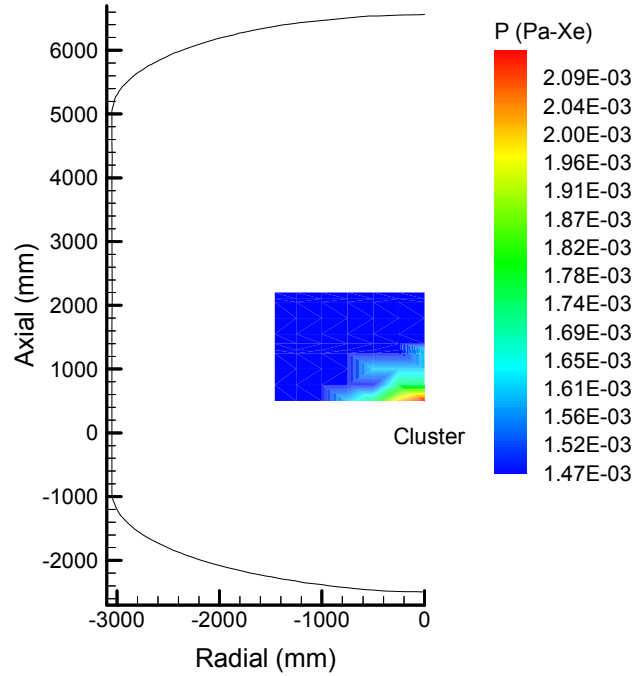


Figure 3-18: Hot flow pressure map of the cluster in the LVTF with an anode flow rate of 5.25 mg/s and a cathode flow rate of 0.92 mg/s, at a nominal pumping speed of 240,000 l/s and operating pressure of 4.9×10^{-4} Pa (3.7×10^{-6} Torr), corrected for xenon. (300 V, 5.12 A thruster operation)

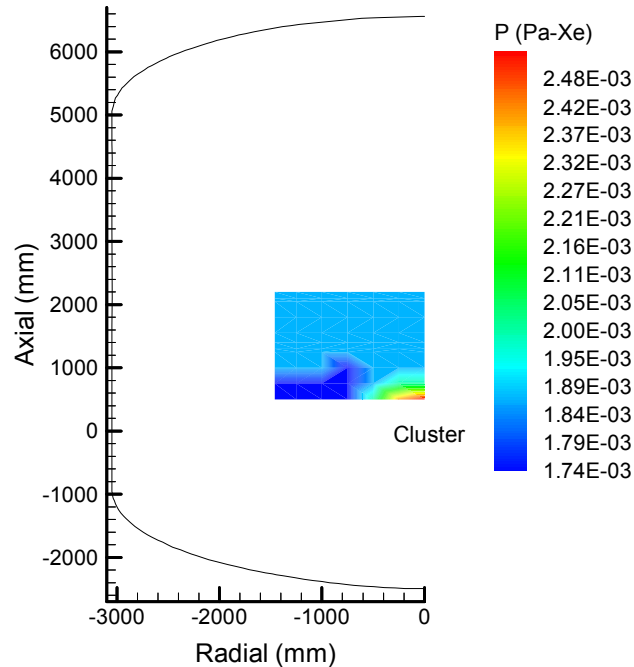


Figure 3-19: Cold flow pressure map of the cluster in the LVTF with an anode flow rates of 10.46 mg/s and cathode flow rate of 0.92 mg/s, at a nominal pumping speed of 240,000 l/s and operating pressure of 6.9×10^{-4} Pa (5.1×10^{-6} Torr), corrected for xenon.

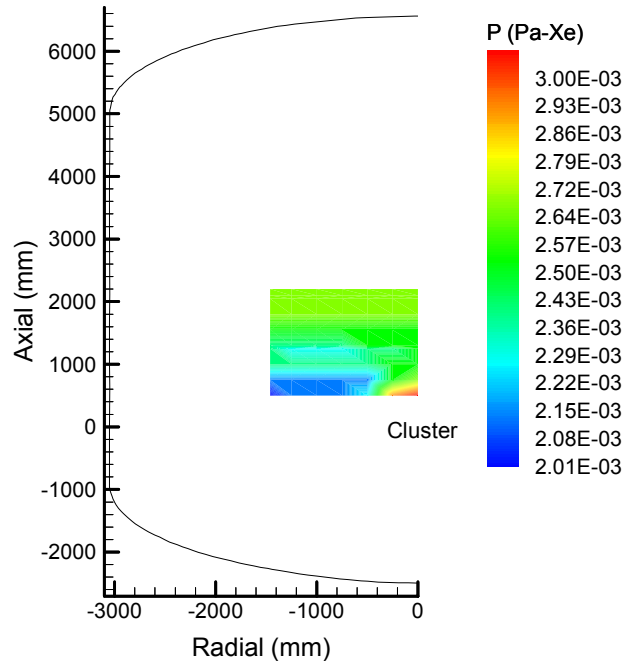


Figure 3-20: Hot flow pressure map of the cluster in the LVTF with an anode flow rate of 10.46 mg/s and a cathode flow rate of 0.92 mg/s, at a nominal pumping speed of 240,000 l/s and operating pressure of 6.9×10^{-4} Pa (5.1×10^{-6} Torr), corrected for xenon. (500 V, 11.8 A thruster operation)

3.5.3 Discussion

The ionization gauges do not clearly capture the double plume structure of the cluster. This is because the 25 cm x 25 cm grid on which the data are taken does not have the resolution to resolve these details. Analyses show that the cold and hot flow profiles on chamber centerline are very similar to the profiles seen in the previous pressure maps of the monolithic plume expansions.

The cluster pressure maps are noticeably higher than the facility operating pressure measured with the nude ionization gauge located on the chamber wall. The interrogation area of the ionization gauges is small. Thus, the pressure is not measured far enough away from the cluster plume expansion to see that the pressure relaxes to the nude gauge values.

The cluster plume expansion is not axially symmetric about the chamber centerline. Therefore, the previous numerical model is not capable of modeling the expansion into the facility. These data provide an excellent case with which to validate Boyd's 3-dimensional numerical model of an operating Hall thruster plume expansion into a vacuum chamber.

3.6 Conclusions

This chapter creates a technique for calibrating a vacuum chamber in terms of pressure through a series of studies. The first study in this chapter maps the cold flow pressure in two facilities. The experimental results are used to validate a numerical model of the LVTF with a cold flow thruster. While the simulation results are found to be sensitive to the sticking coefficient, very good agreement is obtained between the simulation and experimental data using sticking coefficient values in the range of 0.3 to 0.4.

The second study performs successive cold and hot flow pressure maps on the LVTF. Comparison of axial pressure profiles on the LVTF centerline shows that a cold flow neutral density background map accurately characterizes the neutral density in an operating Hall thruster plume. In addition, analysis shows that the nude ionization gauge reading is a much better estimate of the true LVTF operating pressure than the external ionization gauge. Furthermore, the plume pressure decreases from a maximum at the thruster exit plane to the facility backpressure at approximately 2 m downstream of the exit plane, independent of flow rate and facility background pressure. This technique permits validation of neutral background pressure simulations with the thruster in operation.

Finally, the cluster plume pressure map validates that the pressure map technique is capable of measuring the background pressure at very high facility backpressures. Unfortunately, the pressure maps do not show the plume expansion of each thruster.

CHAPTER 4

FACILITY EFFECTS AND SINGLE THRUSTER CHARACTERIZATION

The preceding chapter yields a solid understanding of the background pressure map within a vacuum chamber that contains an expanding Hall thruster plume. Furthermore, it develops a technique to predict the background pressure anywhere in the vacuum chamber for a given Hall thruster flow rate and pumping speed. This foundation supports the investigation of backpressure-induced facility effects on Hall thruster performance and plume properties.

The aim of this chapter is to present the knowledge gained from the facility effects study. The first section of this chapter presents the results collected at each operating pressure. In addition, the measured performance and plume characteristics of the P5-A and P5-B Hall thrusters yield a solid baseline to compare cluster interaction effects against in Chapter 5. The second portion of this chapter discusses the knowledge gained about facility effects on Hall thruster performance and plume characteristics.

Measurements of the performance and plume characteristics at multiple facility operating pressures show how facility effects evolve with backpressure. To carry out the facility effects investigation, the plume and performance characteristics of each thruster are characterized at facility pumping speeds of 70, 140, and 240 kl/s. The variation in pumping speed leads to a range of facility backpressure for each thruster operating

condition characterized. The trends that appear as a function of operating pressure shed light on facility effects and possible tools to correct for elevated backpressure.

4.1 Probe Data

Each of the monolithic thrusters is characterized at the operating conditions displayed in Tables 4-1 and 4-2. The diagnostics discussed in Chapter 2 measured plume characteristics and thruster performance over a range of backpressures from 3.5×10^{-6} Torr to 1.4×10^{-5} Torr. Figure 4-1 shows the one-meter arc on which data are collected, as well as the sign convention used. For clarity, only data collected from the P5-A operating at 300 and 500 V with anode flow rates of 5.25 mg/s and 10.46 mg/s are shown. Data taken at discharge voltages of 400 and 600 V at anode flow rates of 5.25 and 10.46 mg/s show similar trends to the data presented here. In addition, selective plots of data collected on the P5-B are included to show that the cluster elements are identical.

The following subsections show that the plume and performance characteristics of a Hall thruster are affected by the facility operating pressure. There are only two apparent ways in which the neutral background gas can interact with the Hall thruster. First, the neutral background gas can be entrained in the discharge channel; or second, ions originating from the discharge channel can collide with the neutral background gas downstream of the exit plane. The subsections attempt to explain how these two processes change the performance and plume characteristics of the thruster. In addition, the changes in plume characteristics are correlated to the changes in performance.

Pumps	Discharge Voltage (V)	Discharge Current (A)	Anode (mg/s)	Cathode (mg/s)	Inner Magnet Current (A)	Outer Magnet Current (A)	Vc-g (V)	Pressure (Torr-Xe)	Pressure (Pa-Xe)
2	300	5.34	5.25	0.92	2.56	1.43	-16.5	9.1E-06	1.2E-03
2	400	5.46	5.25	0.92	3.14	1.55	-15.4	9.1E-06	1.2E-03
2	500	5.80	5.25	0.92	3.98	1.57	-14.9	9.1E-06	1.2E-03
2	600	7.36	5.25	0.92	3.95	2.71	-14.6	9.1E-06	1.2E-03
2	300	10.24	10.46	0.92	3.06	1.82	-18.2	1.4E-05	1.8E-03
2	400	10.36	10.46	0.92	3.92	2.00	-17.9	1.4E-05	1.8E-03
2	500	10.60	10.46	0.92	4.28	3.00	-17.9	1.4E-05	1.8E-03
2	600	11.02	10.46	0.92	6.25	3.00	-18.6	1.4E-05	1.8E-03
4	300	5.10	5.25	0.92	2.56	1.43	-16.2	5.3E-06	7.1E-04
4	400	5.22	5.25	0.92	3.14	1.55	-16.0	5.3E-06	7.1E-04
4	500	5.38	5.25	0.92	3.98	1.57	-16.7	5.3E-06	7.1E-04
4	600	5.88	5.25	0.92	3.95	2.71	-15.0	5.3E-06	7.1E-04
4	300	9.68	10.46	0.92	3.06	1.82	-17.5	8.1E-06	1.1E-03
4	400	9.76	10.46	0.92	3.92	2.00	-17.3	8.1E-06	1.1E-03
4	500	9.94	10.46	0.92	4.28	3.00	-17.0	8.1E-06	1.1E-03
4	600	10.52	10.46	0.92	6.25	3.00	-17.3	8.1E-06	1.1E-03
7	300	4.92	5.25	0.92	2.56	1.43	-16.4	3.5E-06	4.6E-04
7	400	5.04	5.25	0.92	3.14	1.55	-16.0	3.5E-06	4.6E-04
7	500	5.34	5.25	0.92	3.98	1.57	-15.2	3.5E-06	4.6E-04
7	600	5.84	5.25	0.92	3.95	2.71	-14.0	3.5E-06	4.6E-04
7	300	9.46	10.46	0.92	3.06	1.82	-16.8	5.3E-06	7.1E-04
7	400	9.56	10.46	0.92	3.92	2.00	-16.7	5.3E-06	7.1E-04
7	500	9.74	10.46	0.92	4.28	3.00	-16.5	5.3E-06	7.1E-04
7	600	10.44	10.46	0.92	6.25	3.00	-17.8	5.3E-06	7.1E-04

Table 4-1: P5-A Operating conditions

Pumps	Discharge Voltage (V)	Discharge Current (A)	Anode (mg/s)	Cathode (mg/s)	Inner Magnet Current (A)	Outer Magnet Current (A)	Vc-g (V)	Pressure (Torr-Xe)	Pressure (Pa-Xe)
2	300	5.42	5.25	0.92	2.56	1.43	-17.6	9.2E-06	1.2E-03
2	400	5.48	5.25	0.92	3.14	1.55	-17.6	9.2E-06	1.2E-03
2	500	5.74	5.25	0.92	3.98	1.57	-18.4	9.2E-06	1.2E-03
2	600	6.64	5.25	0.92	3.95	2.71	-17.4	9.2E-06	1.2E-03
2	300	10.52	10.46	0.92	3.06	1.82	-20.0	1.5E-05	2.0E-03
2	400	10.80	10.46	0.92	3.92	2.00	-20.6	1.5E-05	2.0E-03
2	500	10.64	10.46	0.92	4.28	3.00	-20.7	1.5E-05	2.0E-03
2	600	11.02	10.46	0.92	6.25	3.00	-21.1	1.5E-05	2.0E-03
4	300	5.06	5.25	0.92	2.56	1.43	-17.4	5.3E-06	7.1E-04
4	400	5.02	5.25	0.92	3.14	1.55	-18.7	5.3E-06	7.1E-04
4	500	5.20	5.25	0.92	3.98	1.57	-18.7	5.3E-06	7.1E-04
4	600	5.66	5.25	0.92	3.95	2.71	-17.5	5.3E-06	7.1E-04
4	300	9.66	10.46	0.92	3.06	1.82	-18.6	8.1E-06	1.1E-03
4	400	9.60	10.46	0.92	3.92	2.00	-19.4	8.1E-06	1.1E-03
4	500	9.68	10.46	0.92	4.28	3.00	-20.0	8.1E-06	1.1E-03
4	600	10.34	10.46	0.92	6.25	3.00	-20.1	8.1E-06	1.1E-03
7	300	4.98	5.25	0.92	2.56	1.43	-17.7	3.5E-06	4.6E-04
7	400	4.98	5.25	0.92	3.14	1.55	-18.2	3.5E-06	4.6E-04
7	500	5.12	5.25	0.92	3.98	1.57	-18.2	3.5E-06	4.6E-04
7	600	5.60	5.25	0.92	3.95	2.71	-17.2	3.5E-06	4.6E-04
7	300	9.44	10.46	0.92	3.06	1.82	-18.4	5.3E-06	7.1E-04
7	400	9.40	10.46	0.92	3.92	2.00	-19.0	5.3E-06	7.1E-04
7	500	9.50	10.46	0.92	4.28	3.00	-19.2	5.3E-06	7.1E-04
7	600	10.18	10.46	0.92	6.25	3.00	-20.0	5.3E-06	7.1E-04

Table 4-2: P5-B Operating conditions

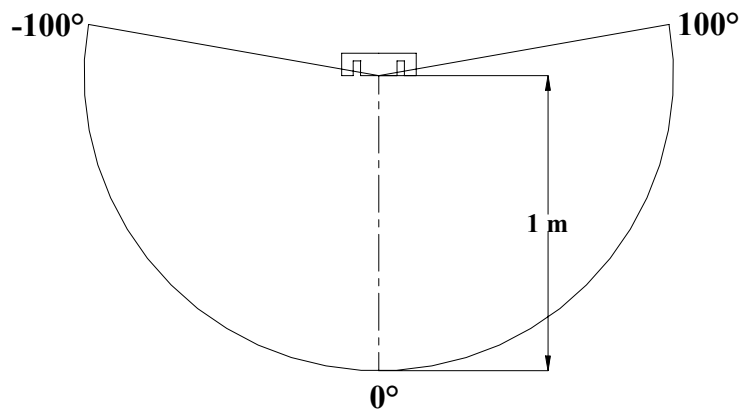


Figure 4-1: Diagram of the 1 m arc on which data are collected with respect to a single thruster. This diagram looks down on thruster with the thruster centerline parallel to the facility centerline.

4.1.1 Discharge Current Characteristics

Discharge current is a key parameter in Hall thruster operation. The discharge current oscillations of the monolithic thrusters are measured at each operating condition over the range of facility backpressure with a F.W. Bell IHA-25 Hall probe connected to a Tektronix TDS 3034B oscilloscope. The sampling frequency is 2.5 MHz. All discharge current measurements are made after the thrusters have operated for a minimum of one hour. During this time, water vapor desorbs from the ceramic channel, which results in steady, low-amplitude discharge current oscillations. Figures 4-2 through 4-5 present samples of the measured discharge current oscillation for each of the monolithic thrusters as a function of facility backpressure. Figure 4-3 presents the discharge current oscillation of P5-B, showing that the oscillation exhibits the same trend for both thrusters.

The discharge current characteristics indicate the stability of the plasma discharge. Fast Fourier transforms of the discharge current signals presented in Figures 4-2 through 4-5 show that the discharge is composed of oscillation frequencies of 0.85 to 10.4 kHz, which are characteristic of Hall thruster operation.⁴¹

The most apparent characteristic of the traces is the decrease in amplitude as facility backpressure decreases. For the 5.25 mg/s flow rates shown in Figures 4-2 and 4-3, the amplitude of the discharge current oscillations significantly decreases when the backpressure decreases from 9.2×10^{-6} Torr-Xe to 5.3×10^{-6} Torr-Xe. A further decrease in pressure to 3.5×10^{-6} Torr-Xe yields little change in amplitude.

Figures 4-4 and 4-5 show the discharge current oscillations at an anode flow rate of 10.46 mg/s. At the higher flow rate, the backpressure decreases from 1.4×10^{-5}

Torr-Xe to 5.3×10^{-6} Torr, but we do not see a significant change in the amplitude of the discharge current oscillations.

The ionization process within the discharge chamber drives the amplitude of the discharge current oscillations. The neutral background gas entrained into the discharge channel affects the ionization process, since the extra neutral gas is available for ionization. At low anode flow rates and high backpressures, the entrained neutral background gas is a higher fraction of the anode flow than at low backpressures. Thus, we see a significant decrease in the amplitude of the discharge current oscillations as backpressure decreases.

At the higher anode flow rate, the entrained neutral background gas is a small fraction of the anode flow at all backpressures. Thus, decreasing backpressure has little effect on the amplitude of the discharge current oscillations at high anode flow rates.

No attempt is made to correct the increase in discharge current oscillation amplitude with backpressure because the large discharge current oscillation amplitude is only measured at one operating pressure. The backpressure would need to be increased further to see if this trend holds at higher backpressures. Discharge current oscillations have been studied in greater detail by Choueiri.^{91,92}

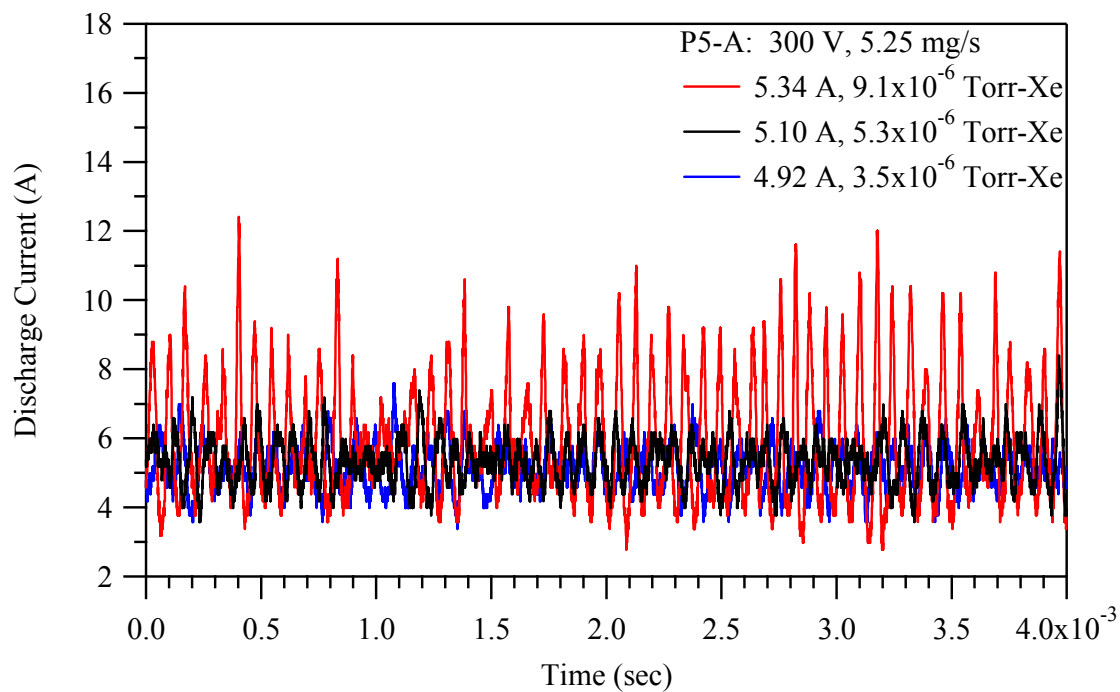


Figure 4-2: Discharge current characteristics of P5-A operating at 300 V, 5.25 mg/s as a function of backpressure.

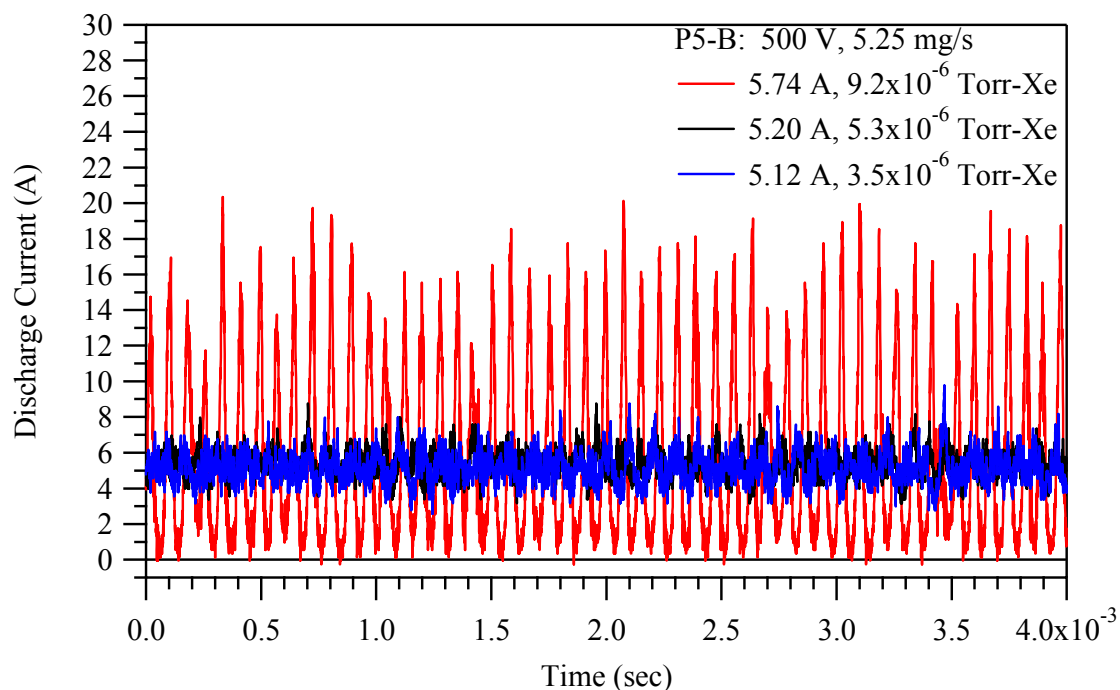


Figure 4-3: Discharge current characteristics of P5-B operating at 500 V, 5.25 mg/s as a function of backpressure.

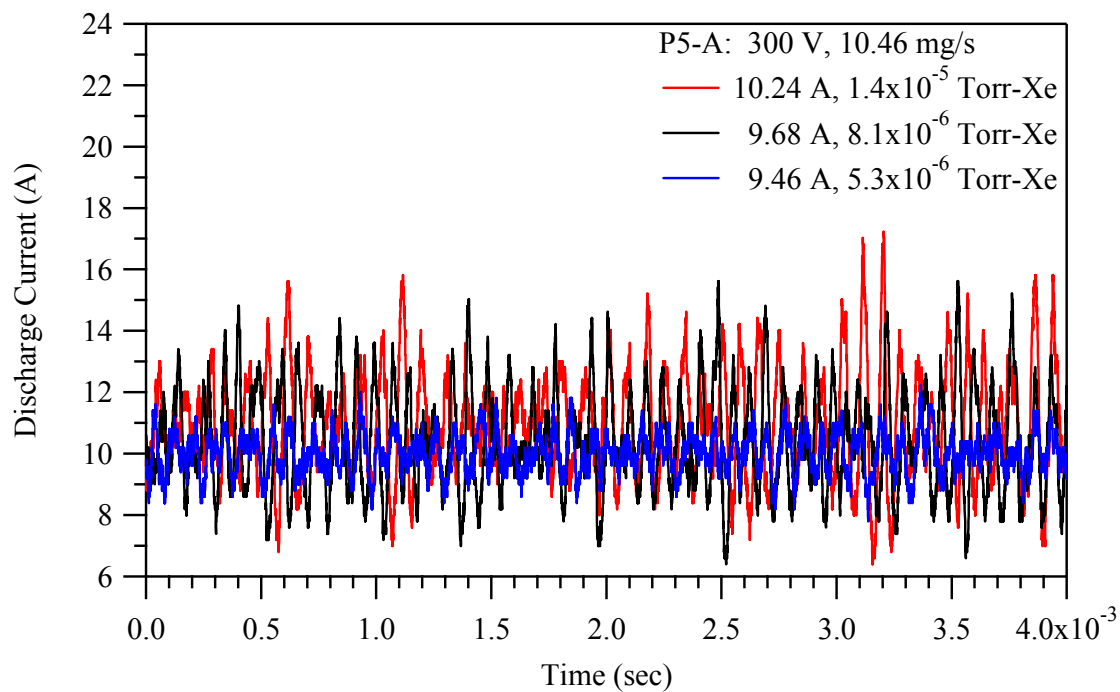


Figure 4-4: Discharge current characteristics of P5-A operating at 300 V, 10.46 mg/s as a function of backpressure.

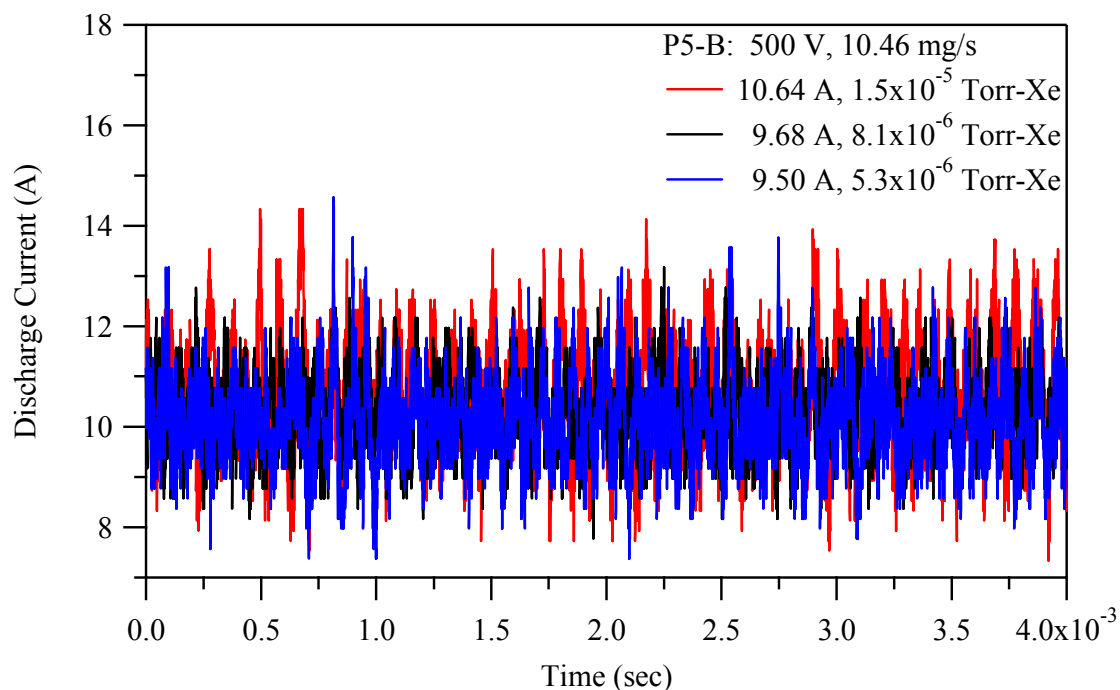


Figure 4-5: Discharge current characteristics of P5-B operating at 500 V, 10.46 mg/s as a function of backpressure.

4.1.2 Plasma Potential and Floating Potential

The plasma potential and floating potential in the P5-A and P5-B Hall thruster plumes is measured from -100° to $+100^\circ$ on the one-meter arc shown in Figure 4-1. The measurements are made in 5° increments from the thruster centerline to 50° . For angles greater than 50° , the measurements are made in 10° steps. Figures 4-8 through 4-12 present traces of the plasma potential and floating potential at each operating condition and pumping speed.

Figures 4-6 through Figure 4-10 show that the plasma potential and floating potential reach maxima on thruster centerline and smoothly decrease to minima at -100° . As the facility backpressure decreases, the plasma and floating potential decrease at all angles. The largest change in floating potential (~ 4 V) for the 5.25 mg/s anode flow rate occurs when the pressure drops from 9.1×10^{-6} Torr-Xe to 5.3×10^{-6} Torr-Xe. Little change in floating potential is observed when the pressure drops to 3.5×10^{-6} Torr-Xe. Figure 4-8 shows a 1.25 V decrease in the floating potential between -80° and -100° . Figure 4-10 shows approximately a 1.5 V decrease in the floating potential from -90° to -100° . The decrease in floating potential presented in both figures occurs at the lowest facility backpressure, which has the smallest number of CEX ions present in the plume. The decrease in the number of ions present reduces the local plasma potential.

A change in plasma potential directly affects the energy to which the beam ions are accelerated. The plasma potential traces show that as facility backpressure decreases, the plasma potential also decreases. A decrease in plasma potential results in an increase in thrust, efficiency, and specific impulse. The maximum change in plasma potential as a function of facility backpressure on thruster centerline is no more than 6 volts. The

increase in ion energy should lead to a slight (<1%) increase in thrust, but this is not supported by the measured performance, given the resolution of the thrust stand.

The floating potential is related directly to the ion density, electron number density, and electron temperature. These plasma parameters are discussed in the following sections.

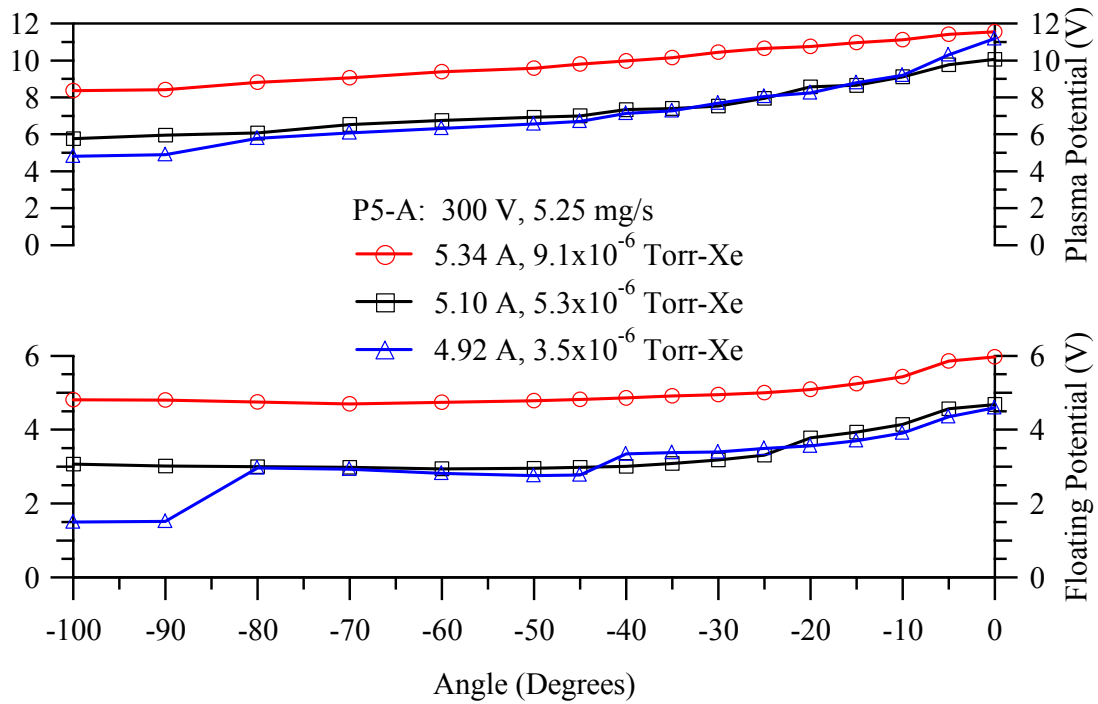


Figure 4-6: Traces of the P5-A floating potential and plasma potential as a function of angle at 300 V, 5.25 mg/s as a function of facility backpressure.

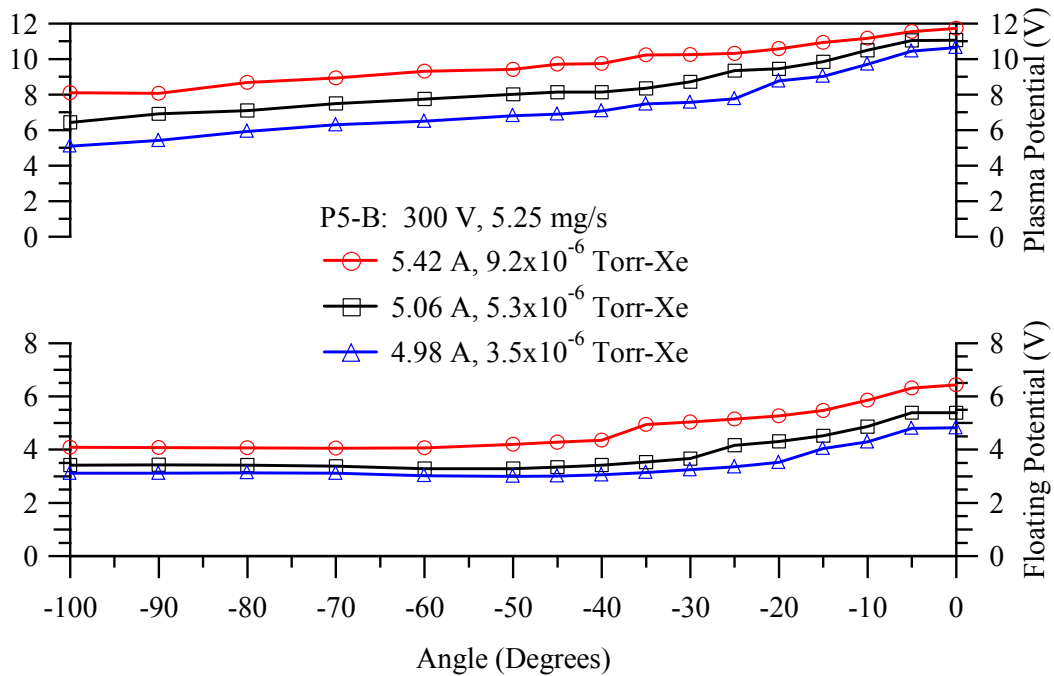


Figure 4-7: Traces of the P5-B floating potential and plasma potential as a function of angle at 300 V, 5.25 mg/s as a function of facility backpressure.

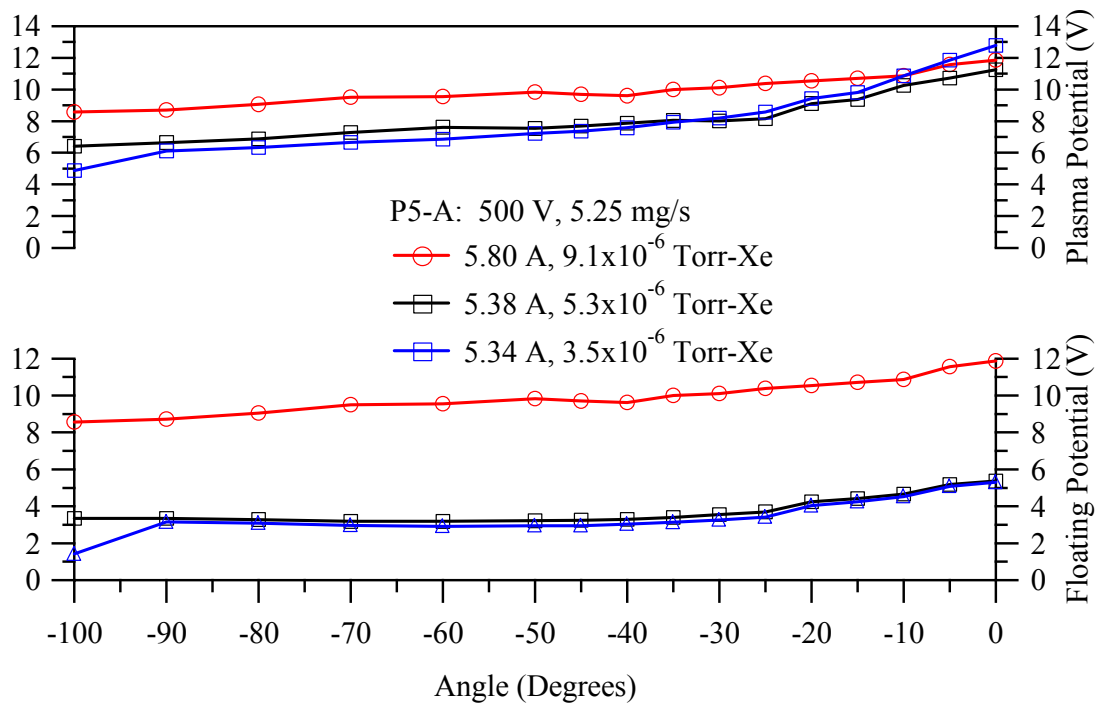


Figure 4-8: Traces of the P5-A floating potential and plasma potential as a function of angle at 500 V, 5.25 mg/s as a function of facility backpressure.

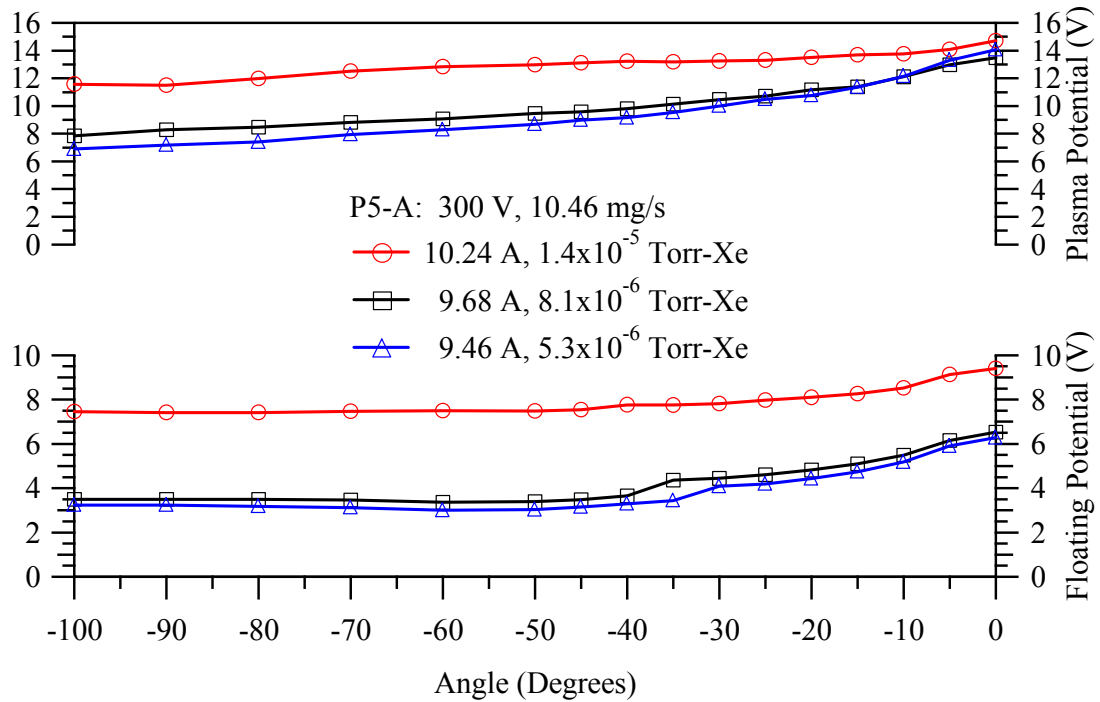


Figure 4-9: Traces of the P5-A floating potential and plasma potential as a function of angle at 300 V, 10.46 mg/s as a function of facility backpressure.

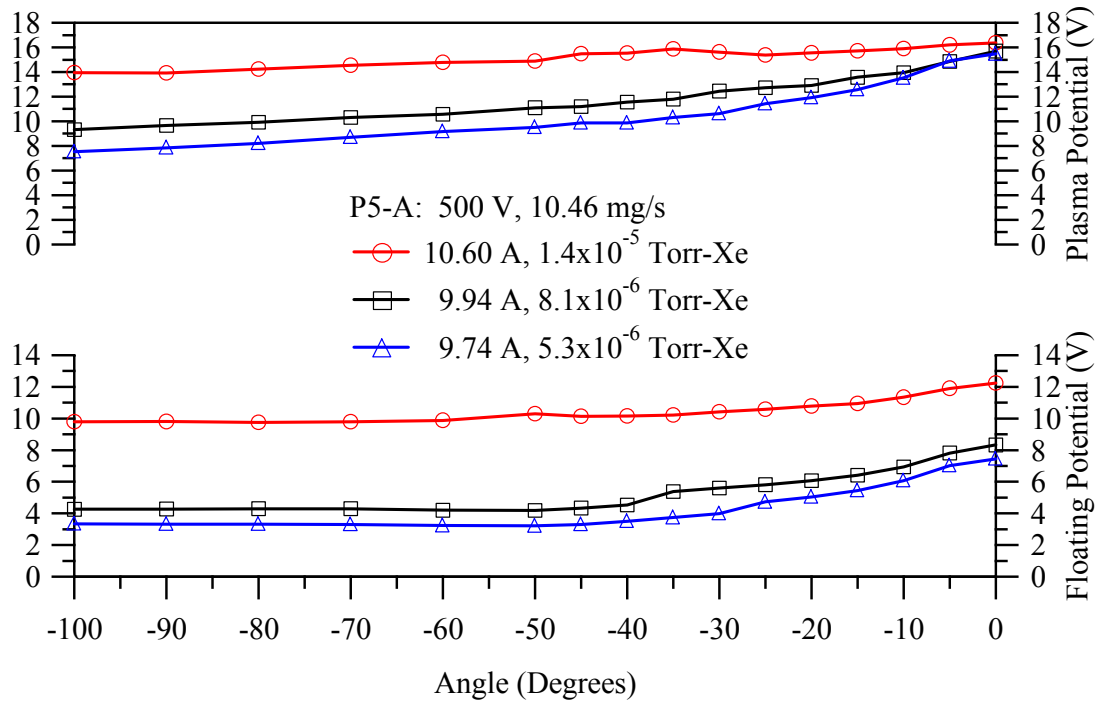


Figure 4-10: Traces of the P5-A floating potential and plasma potential as a function of angle at 500 V, 10.46 mg/s as a function of facility backpressure.

4.1.3 Electron Number Density and Electron Temperature

The electron number density and electron temperature 1 m downstream of the exit plane of the monolithic thruster plumes are measured from -90° to $+90^\circ$ on the one-meter arc shown in Figure 4-1. The measurement step size is 5° from the thruster centerline to 50° , and 10° for angles greater than 50° . After each measurement, the Langmuir probe is moved back to thruster centerline for 30 seconds to allow collisions with the 200+ eV ions to clean the probe. Figures 4-13 through 4-17 present traces of the electron number density and electron temperature for each operating condition and pumping speed. These data agree well with previous measurements of electron density and electron temperature in the original P5 thruster plume.⁵³

Figures 4-13 through 4-17 show that the electron number density and electron temperature reach maxima on thruster centerline and smoothly decrease to minima at -100° . The electron number density shows a plume core residing within a half-angle of approximately 20° . Figures 4-13 and 4-14 show that the P5-A and P5-B exhibit nearly identical electron number densities and electron temperatures for the same operating condition. Note, that the measurement of electron number density has an error of 50%.

The centerline electron number density traces at the 5.25 mg/s anode flow rate do not show a clear trend. Off centerline, there is a small decrease in electron number density as backpressure decreases. For a given operating condition, the profiles of electron number density at each pressure converge to a minimum value at -100° . This is because the plasma density is a function of discharge current, but the majority of the beam current is on thruster centerline. Therefore, at large angles the plasma consists primarily of low-density CEX ions; thus, the electron number density approaches zero as we move toward the wings of the plume.

At the 10.46 mg/s anode flow rate, the electron number density is greatest, as is the background pressure. The electron number density consistently decreases with decreasing backpressure. The increased discharge current associated with increasing backpressure results in an increased plasma density; this explains the correlation of electron number density with backpressure.

At the 5.25 mg/s anode flow rate, the electron temperature does not show a distinct trend on centerline. As the angle from centerline and the backpressure increase, the electron temperature for each also increases. The maximum difference between electron temperatures as a function of backpressure is 0.5 eV.

The trends in electron temperature are distinct at the 10.46 mg/s anode flow rates. On centerline at the 300 V operating point, the electron temperature at 5.3×10^{-6} Torr-Xe is 0.75 eV higher than at 1.4×10^{-5} Torr-Xe. This difference increases to 1 eV at the 500 V operating condition. The background gas ingested into the discharge channel increases the number of collisions that occur in the ionization and acceleration region. The collisions result in a decrease in electron temperature.

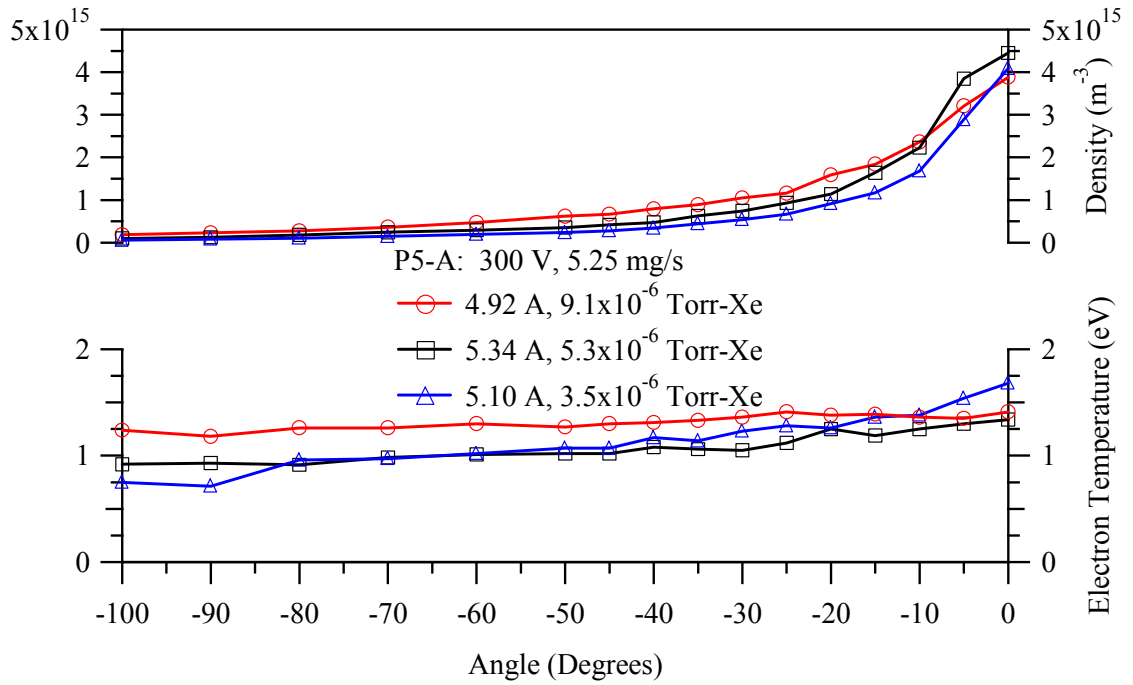


Figure 4-11: Traces of the P5-A electron temperature and electron number density as a function of angle at 300 V, 5.25 mg/s as a function of facility backpressure.

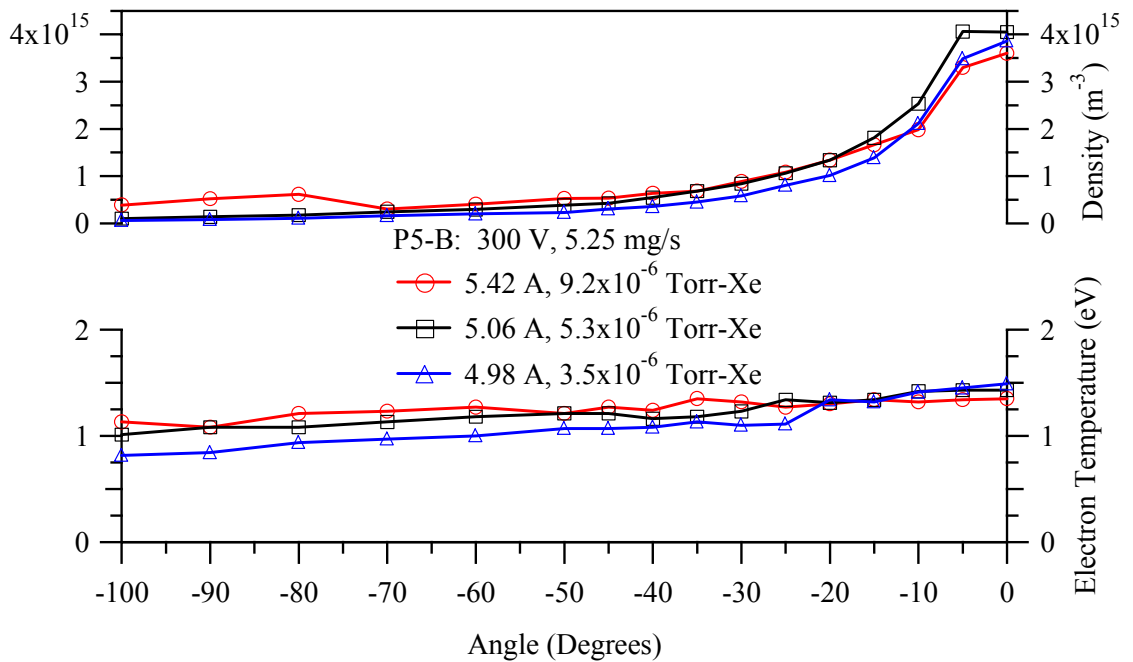


Figure 4-12: Traces of the P5-B electron temperature and electron number density as a function of angle at 300 V, 5.25 mg/s as a function of facility backpressure.

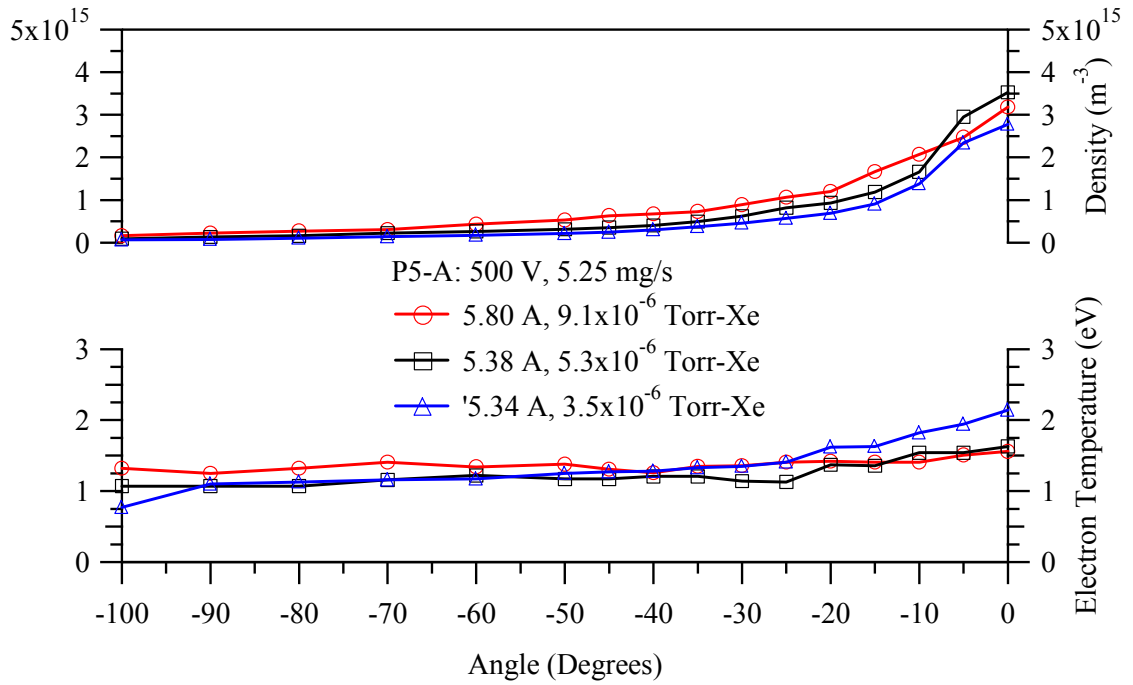


Figure 4-13: Traces of the P5-A electron temperature and electron number density as a function of angle at 500 V, 5.25 mg/s as a function of facility backpressure.

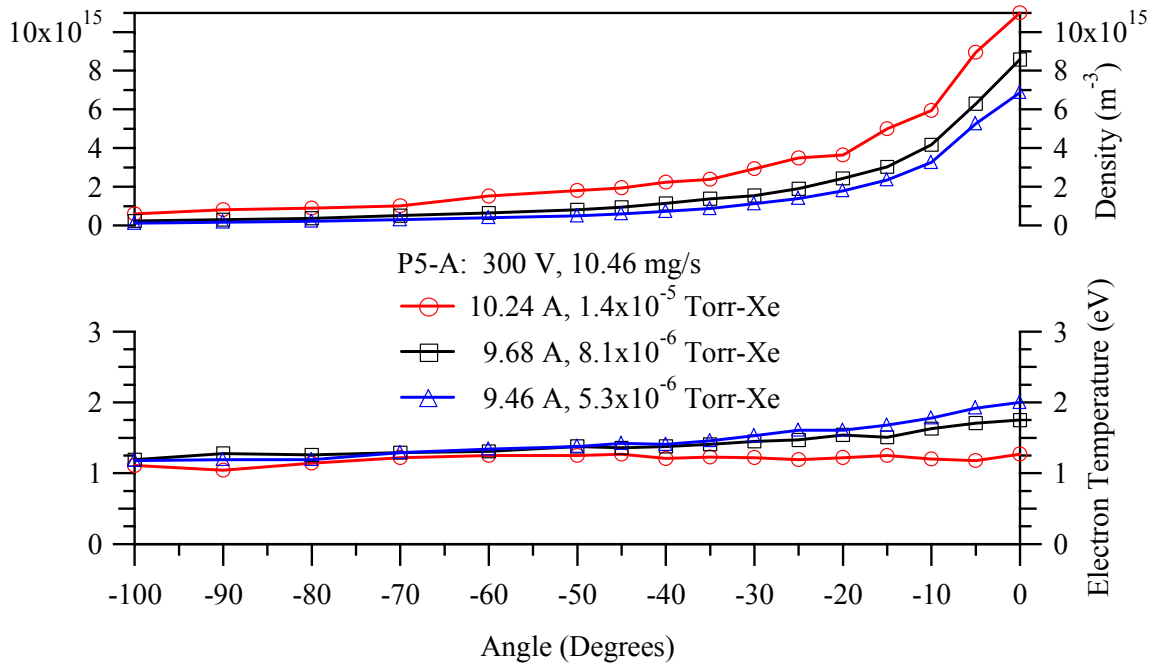


Figure 4-14: Traces of the P5-A electron temperature and electron number density as a function of angle at 300 V, 10.46 mg/s as a function of facility backpressure.

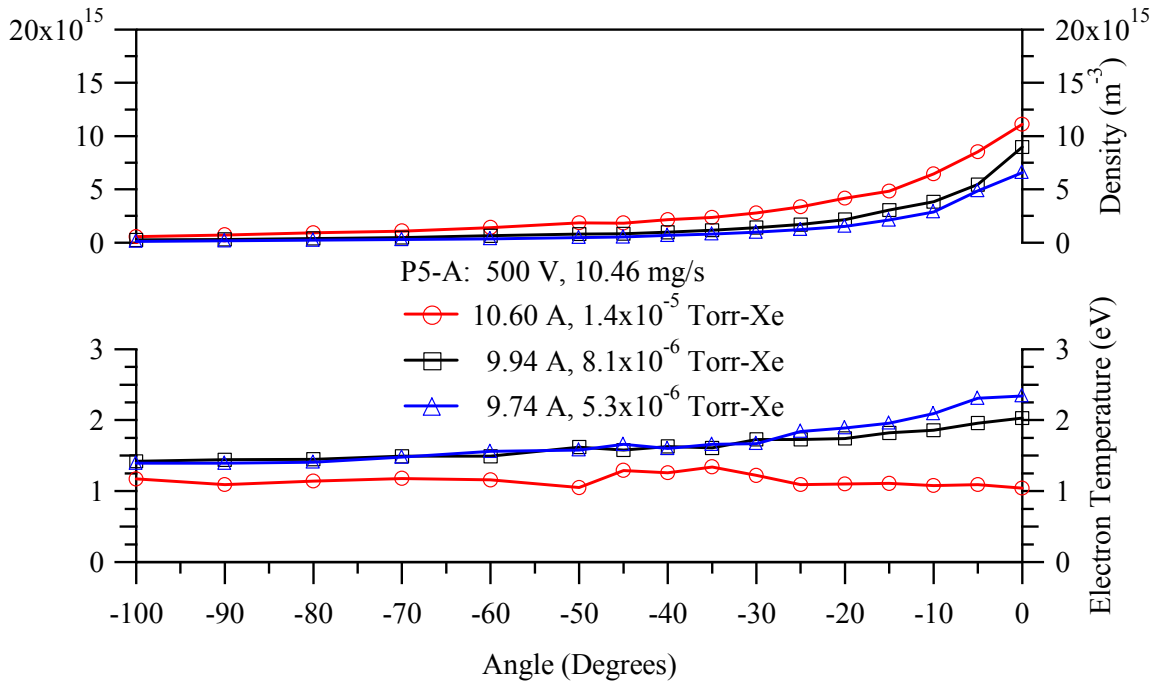


Figure 4-15: Traces of the P5-A electron temperature and electron number density as a function of angle at 500 V, 10.46 mg/s as a function of facility backpressure.

4.1.4 Ion Current Density

Faraday Probes A, B, C, D, and E measure the ion current density in the plume of the Hall thrusters P5-A and P5-B, which are operated over the range of 300 - 600 V at anode flow rates of 5.25 and 10.46 mg/s. The effect of facility background pressure is evaluated by varying the backpressures from 1.4×10^{-5} Torr-Xe to 3.2×10^{-6} Torr-Xe. The goal of the Faraday probe study is to develop a standardized method for measuring the ion current density, so that valid comparisons can be made between plume data taken in facilities with inherently different backpressures.

The measurements are taken on the one-meter arc shown in Figure 4-1 from -100° to +100° from thruster centerline in 1° increments. Figures 4-18 through 4-25

present traces of the ion current density as a function of angle from centerline for each operating condition and pumping speed.

The traces show a number of interesting characteristics. First, we notice the effect of facility backpressure on the traces. Figure 4-16 shows Probe A ion current density traces as a function of backpressure for the P5-A operating at the 5.25 mg/s anode flow rate. The ion current density in the wings of the plume increases with facility backpressure because of CEX ions. Figure 4-17 shows Probe A ion current density traces of the P5-A operating at 300 V, 10.46 mg/s. Previous studies confirm the increase in centerline ion current density at elevated backpressures at 10 mg/s anode flow rates.^{49, 67}

Randolph suggests that facility effects on plume measurements are negligible for background pressures below 1.0×10^{-5} Torr-Xe.³⁸ Figure 4-2 shows that at the 5.25 mg/s anode flow rate the amplitude of the discharge current oscillation continues to decrease at pressures below 1.0×10^{-5} Torr-Xe. Figure 4-16 shows that the ion current density traces measured at the 5.25 mg/s anode flow rate have distinct changes in the wings below 1.0×10^{-5} Torr-Xe. Figure 4-17 shows that the ion current density traces measured at the 10.46 mg/s anode flow rates not only change in the wings at backpressures below 1.0×10^{-5} Torr-Xe, but also on thruster centerline. Clearly, Randolph's suggested facility effects criterion is not accurate.

The increased ion current density on thruster centerline measured by Probe A is either caused by an increase in the number of CEX ions on centerline, or by an increase in the number of ions due to entrainment originating from the discharge channel. Ion current traces at the 5.25 mg/s anode flow rate operating condition do not show increased ion current density with facility backpressure on thruster centerline, even though the

thruster discharge current increases. Previous results of this study show that the entrained background gas flux is not large enough to account for the increase in thruster discharge current.⁹³ In addition, ion current traces at the 10.46 mg/s anode flow rate show a significant increase in the ion current density on thruster centerline with increasing backpressure; this increase is not accounted for by entrained background gas. Thus, the increased ion current density on thruster centerline may also be due to CEX ions. This possibility is discussed in more detail later in this section.

Figures 4-18 and 4-19 show ion current density traces of P5-A and P5-B collected with all 5 probes. The traces show that the ion current density profile of the Hall thruster plumes is nearly identical. Because all other parameters are identical, the small differences between the ion current density profiles of the probes are attributed to material selection and probe design. Probe B, which is magnetically filtered, yields ion current density traces that best match on-orbit ion current density measurements of the SPT-100.^{70, 94} It appears that the magnetic filter is adequate to filter CEX ions away from the collector surface. However, on-orbit there will still be a small percentage of CEX ions in the plume.

Figures 4-20 and 4-21 show ion current density traces measured with Probe B for 5.25 mg/s anode flow rates at 3 facility operating pressures. The traces are nearly identical at all backpressures, even though the discharge current increases with backpressure.

Figures 4-22 and 4-23 show traces of the ion current density measured with Probe B at an anode flow rate of 10.46 mg/s. The “noise” in the wing of Figure 4-22 at the 1.4×10^{-5} Torr-Xe operating pressure is due to large oscillations in the discharge

current because of the elevated backpressure. As noted above, Probe B filters the CEX ions in the plume wings. Presumably, Probe B filters CEX ions at all angles, but their effect is more obvious in the wings. Furthermore, the ion current density measured on the plume centerline is nearly identical for all backpressures. So, the change in ion current density off thruster centerline is due to CEX ions, not entrained background gas.

The Probe B traces lead to two conclusions. First, the magnetic filter prevents most of the CEX ions from reaching the collector surface of Probe B. Second, the increase in discharge current with increasing facility backpressure is caused by a greater number of electrons reaching the anode, and not by the entrained background gas contributing to the ion beam current. Because Probe B measures ion current density accurately at all backpressures investigated and agrees well with on-orbit data,⁹⁴ the other Faraday probes will not be considered in this discussion.

Another technique for evaluating Faraday probe performance is to compare the total ion beam current to the discharge current. The total ion beam current is calculated using the integration in Eqn. 4-1, where $i(\theta)$ is the measured ion current density distribution.⁴⁹ The integration assumes that the plume is axially symmetric

$$I_i \equiv 2\pi r^2 \int_0^{\pi/2} i(\theta) \sin \theta d\theta \quad \text{Eqn. 4-1}$$

In addition, the 90% half-angle divergence of the thruster plume can be calculated from the Probe B ion current density traces. Integration of the ion current density trace from thruster centerline to the 90% half-angle yields 90% of the total measured ion current. Table 4-3 shows the integrated ion beam current, the ratio of integrated ion beam current to discharge current, I_i/I_d , and the 90% divergence half-angle for the four operating

conditions presented. These values are determined by averaging the beam current and divergence angles calculated from first the positive and then the negative angles defined in Figure 4-1. The slight asymmetry of the beam profiles creates uncertainties in the integrated ion beam current and divergence half-angle calculations.

Thruster Condition	Pressure (Torr-Xe)	Integrated Ion Beam Current (A)	I_i/I_d (-)	90% Divergence Half-Angle
300 V, 5.25 mg/s	9.1×10^{-6}	2.82	0.51	42.5
	5.3×10^{-6}	3.21	0.60	43.5
	3.5×10^{-6}	3.40	0.64	44.5
500 V, 5.25 mg/s	9.1×10^{-6}	3.21	0.54	43.0
	5.3×10^{-6}	3.59	0.63	43.5
	3.5×10^{-6}	3.88	0.69	43.5
300 V, 10.46 mg/s	1.4×10^{-5}	4.52	0.42	39.5
	8.1×10^{-6}	6.16	0.59	42.0
	5.3×10^{-6}	6.30	0.63	43.5
500 V, 10.46 mg/s	1.4×10^{-5}	6.55	0.49	37.5
	8.1×10^{-6}	6.96	0.65	42.0
	5.3×10^{-6}	7.16	0.69	42.0

Table 4-3: Ion Beam current, ratio of discharge current to beam current, and 90% divergence half-angle for each backpressure.

The divergence half-angle remains nearly constant with backpressure. This is because the magnetic filter removes CEX ions from the centerline and wings of the thruster plume trace. Normally, nude Faraday probe traces show that the plume divergence half-angle increases with backpressure.⁶⁷

Notice that even though the discharge current increases with backpressure, the calculated ion beam current decreases with increasing backpressure. Thus, the increase

in discharge current due to enhanced electron mobility (caused by collisions with the neutral background gas) to the anode is far greater than the increase in discharge current due to entrained neutral background gas being ionized and added to the ion beam current. However, the thrust measurements decrease with decreasing facility backpressure, which does not agree with the increase in ion beam current with decreasing facility backpressure. Clearly, the Faraday probe does not fully capture how the backpressure changes the number of ions emanating from the thruster.

Furthermore, I_i/I_d increases with decreasing facility backpressure. At the lowest operating pressure with at 300 V, I_i/I_d is 63% and 64% for the 5.25 and 10.46 mg/s operating condition, respectively. At the 500 V operating conditions, I_i/I_d is 69%, which is close to the 74% reported by Kim and the 77% measured by Hofer in similar Hall thruster plumes. The 300 V operating conditions are not the nominal 5 kW operation condition of the P5. Thus, the low value of I_i/I_d for the 300 V operating conditions is not surprising.

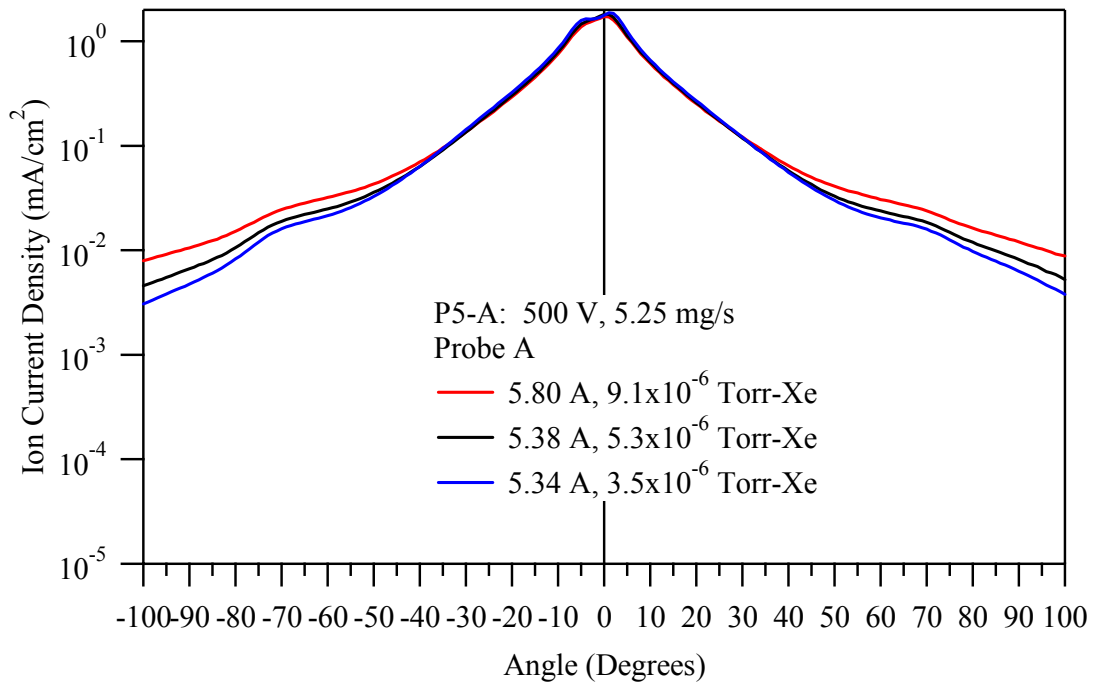


Figure 4-16: Ion current density versus position for Probe A at 3 backpressures. (P5-A: 300 V, 5.25 mg/s)

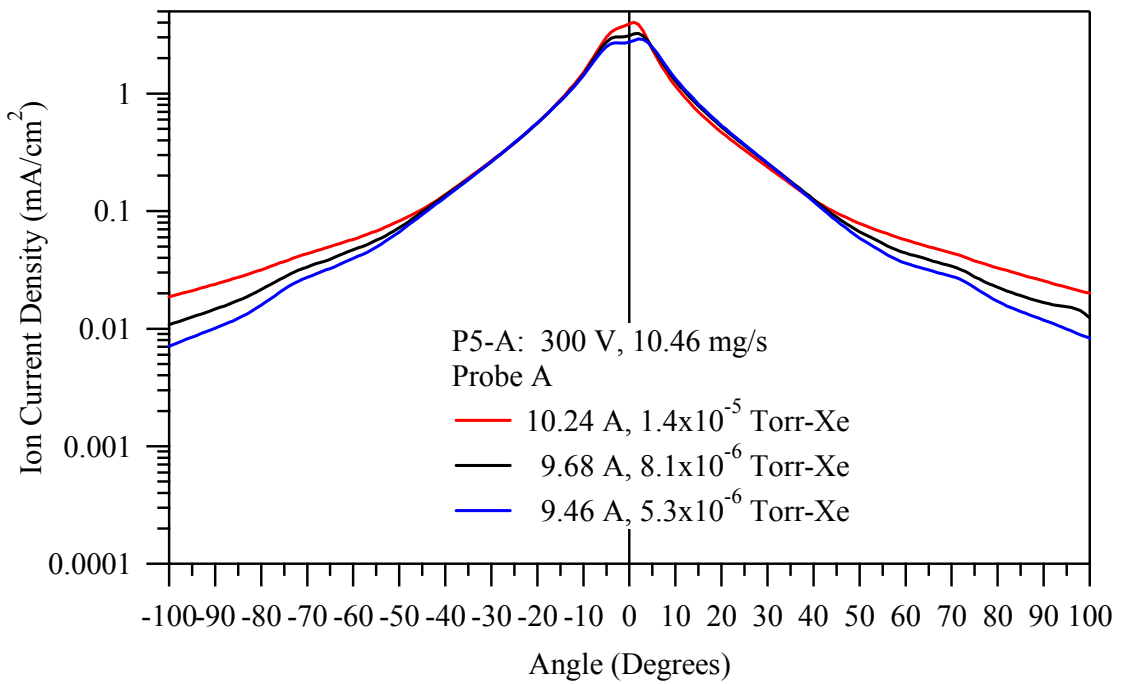


Figure 4-17: Ion current density versus position for Probe A at 3 backpressures. (P5-A: 500 V, 5.25 mg/s)

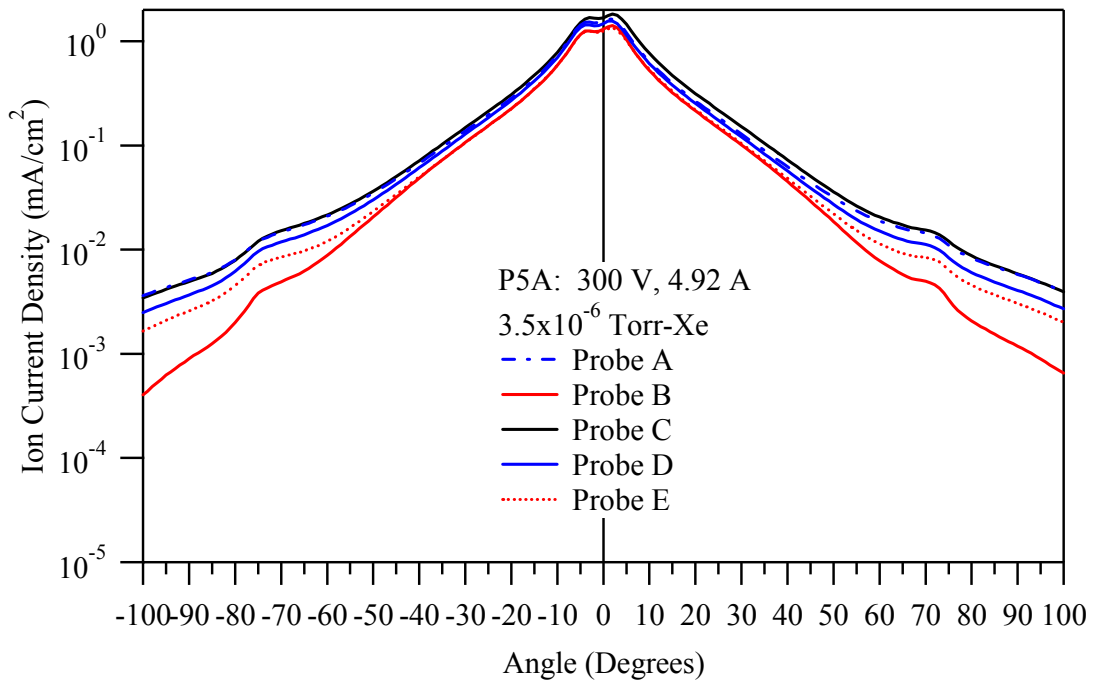


Figure 4-18: Ion current density versus position for 5 Faraday probe designs at a backpressure of 3.5×10^{-6} Torr-Xe. (P5-A: 300 V, 4.92 A).

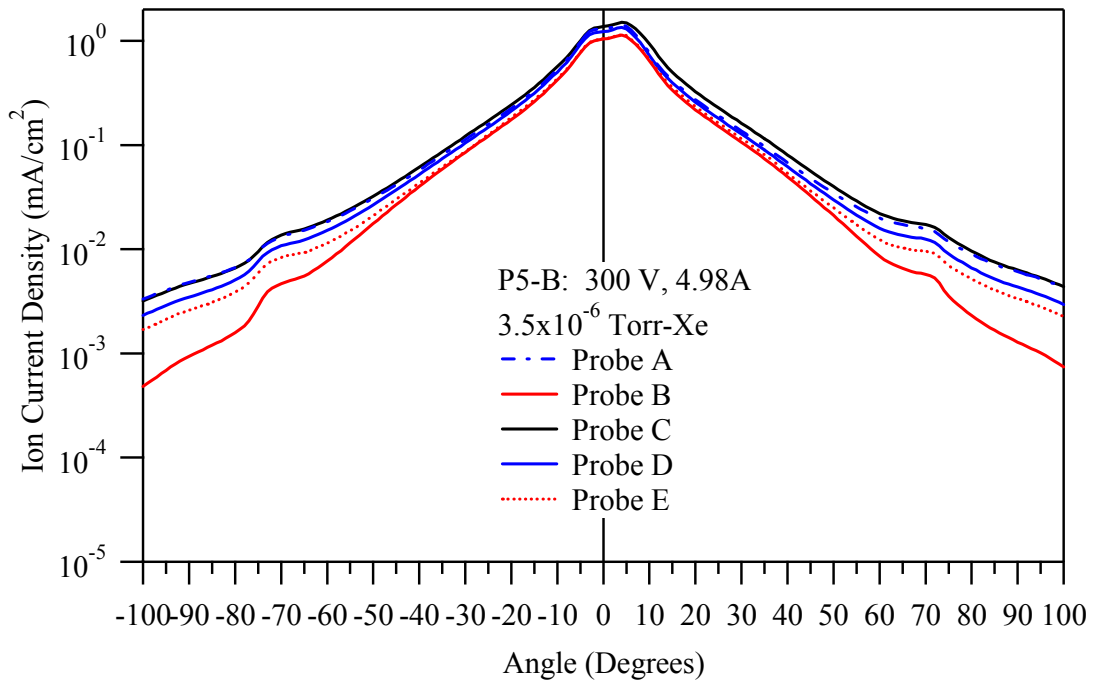


Figure 4-19: Ion current density versus position for 5 Faraday probes at a backpressure of 3.5×10^{-6} Torr-Xe. (P5-B: 300 V, 4.98 A)

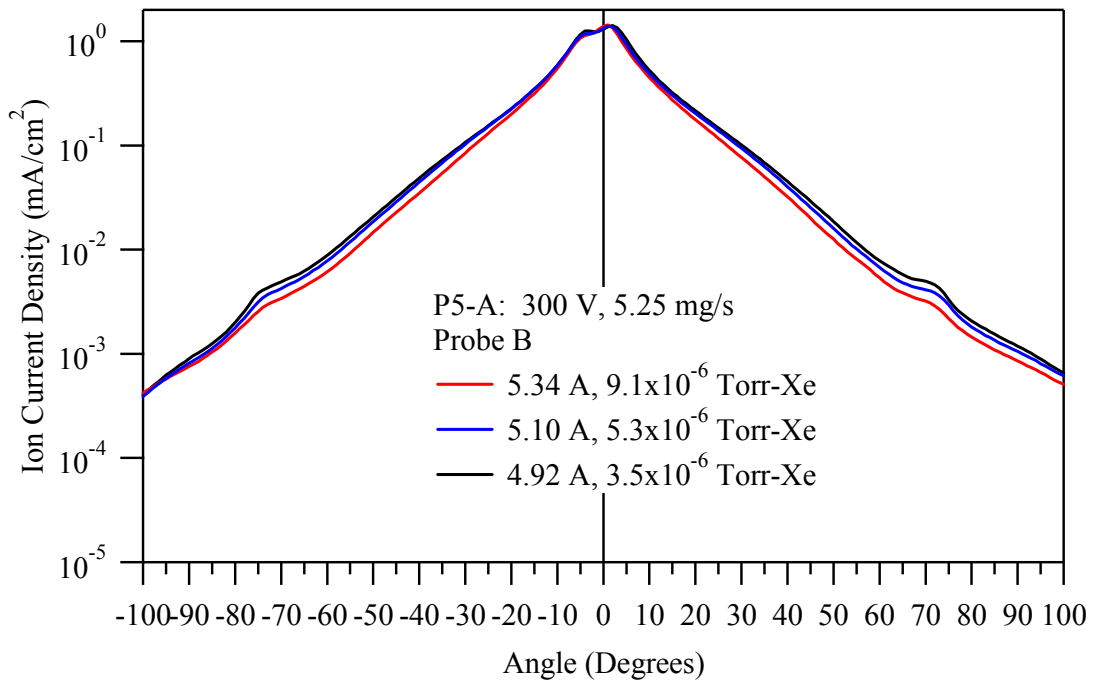


Figure 4-20: Ion current density versus position for Probe B at 3 backpressures. (P5-A: 300 V, 5.25 mg/s).

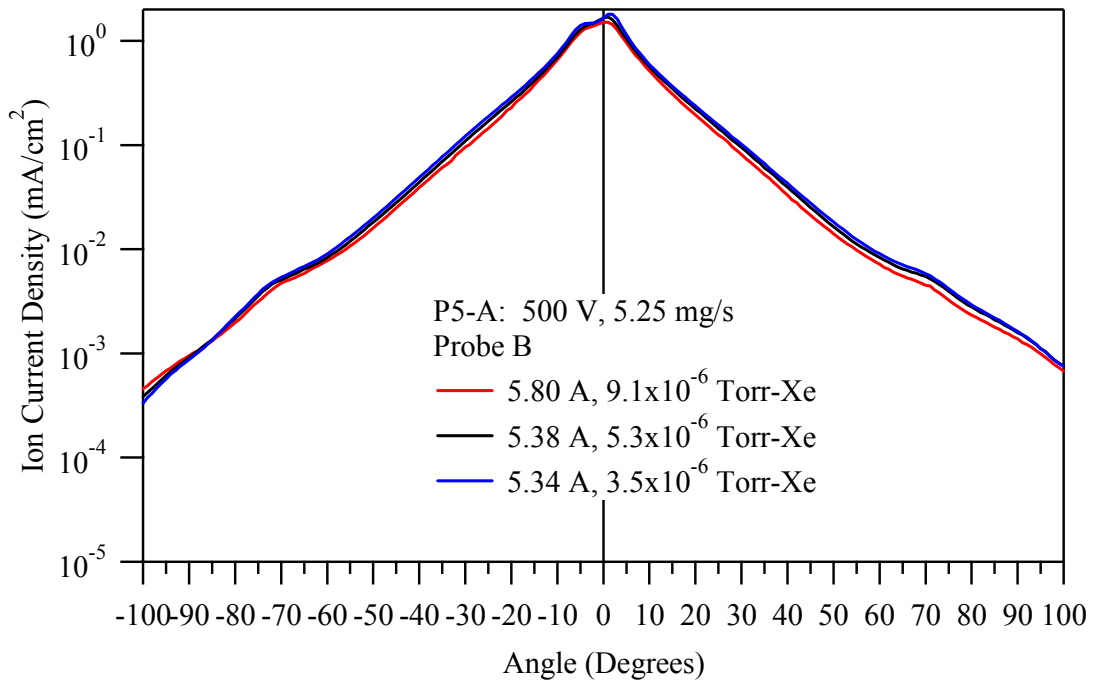


Figure 4-21: Ion current density versus position for Probe B at 3 backpressures. (P5-A: 500 V, 5.25 mg/s).

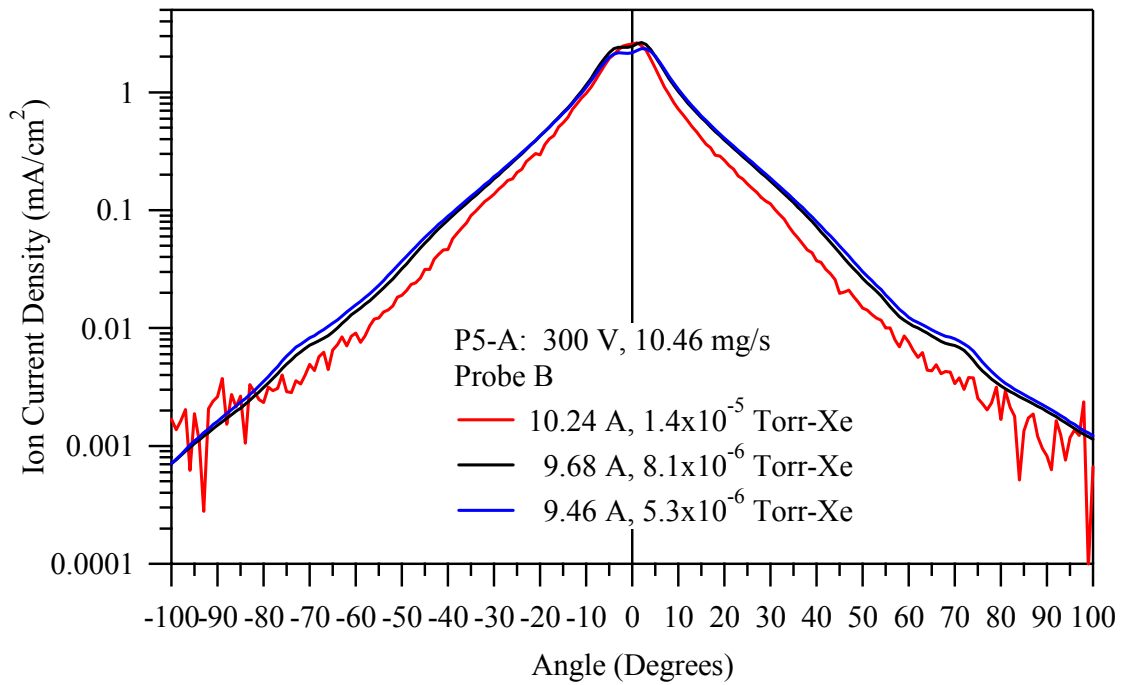


Figure 4-22: Ion current density versus position for Probe B at 3 backpressures (P5-A: 300 V, 10.46 mg/s)

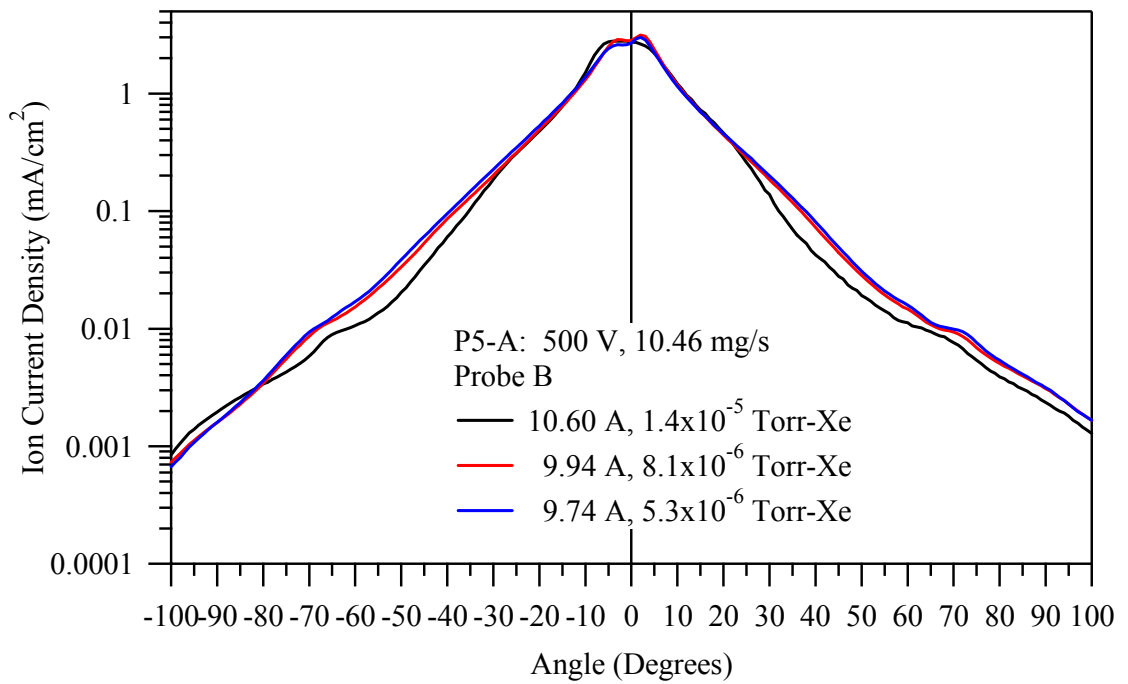


Figure 4-23: Ion current density versus position for Probe B at 3 backpressures. (P5-A: 500 V, 10.46 mg/s)

4.1.5 Ion Energy Spectra

The ion energy distribution functions of Hall thrusters P5-A and P5-B are measured 1 m downstream of the exit plane by the ESA and the RPA. The measurement step size is 5° from thruster centerline to an angle of 50° ; for angles greater than 50° the step size is 10° . At angular positions greater than 60° from centerline the signal-to-noise ratio is too low to discern the ion energy peaks. For all measurements the thruster is rotated about a vertical axis located at the intersection of the exit plane and the thruster centerline.

High anode flow rates result in a high plasma density inside the ESA probe. The ESA vents are designed to alleviate internal neutral density build-up, and the grounded foil should unobtrusively neutralize stray ions and collect the electrons. Nonetheless, elevated number density inside the ESA structure decreases the sheath thickness on the parallel plates to the point that the sheaths no longer merge between the plates. Furthermore, the sheaths do not merge across the trajectory slots milled in the center of each plate. Thus, the potential in the trajectory slot is lower than the applied potential. This causes the measured ion energy distributions to shift to higher voltages because the plates require a higher voltage to turn the ions.

In an attempt to reduce this shift, molybdenum foil is added to the deflection plates to decrease the width of the trajectory slots. This allows the plates to maintain a potential closer to the applied potential across the slot. The decrease in slot width results in a smaller voltage shift, but does not completely solve the problem.

At many of the high operating pressures it is not possible to measure a full ion energy distribution at a 10.46 mg/s anode flow rate with the ESA. The positively-biased

deflection plates collect enough electron current that the sourcemeter reaches the current compliance limit before the maximum potential can be applied to the deflection plate.

The RPA-measured ion energy distribution functions are used to correct the ESA ion energy distribution traces. Beal has shown that the RPA and ESA measure nearly identical ion energy distribution function (IEDF) peak energies for a given thruster operating point.⁵⁰ The correction method consists of shifting the ion energy distribution functions so that the peak ion energy matches that measured by the RPA for a given condition. All ESA data presented are corrected with this method.

Figures 4-24 and 4-25 present RPA traces of IEDFs in the P5-A and P5-B plume, respectively. The figures show that the ion energy distribution function peaks of the two thrusters are at nearly identical retarding voltages.

Figures 4-26 and 4-27 show ESA traces of the IEDFs as a function of angle. The traces are measured from the P5-A operating at 500 V and 5.12 A at a backpressure of 5.3×10^{-6} Torr-Xe. Notice that from centerline to an angle of -25° , the IEDF peaks at approximately 475 V. From -30° to -5° the IEDF peak decreases to nearly 465 V; for angles greater than -50° , the IEDF peak shifts back to 475 V. Also notice the low-energy ion tail on each of the traces. The ion energy distributions functions agree well with the original P5 data collected by Gulczinski.⁶⁹ In addition, Figure 4-27 shows that the decrease in signal-to-noise ratio limits the useable off-centerline traces to approximately -70° .

Figure 4-28 shows how facility backpressure affects the height-to-width ratio of the IEDF peak on the P5-A centerline for an operating condition of 300 V, 5.25 mg/s. As the backpressure increases, the height-to-width ratio decreases. King and Gulczinski

have shown that elastic and inelastic collisions within the plume increase the width of the IEDF.^{95, 69} The increase in width due to collisions agrees well with the increase in the centerline ion current density, which is also caused by CEX collisions. The broadening of the ion energy distribution function is nearly symmetric about the IEDF peak. Figure 4-29 shows the same trends for the 500 V, 5.25 mg/s anode flow rate on thruster centerline.

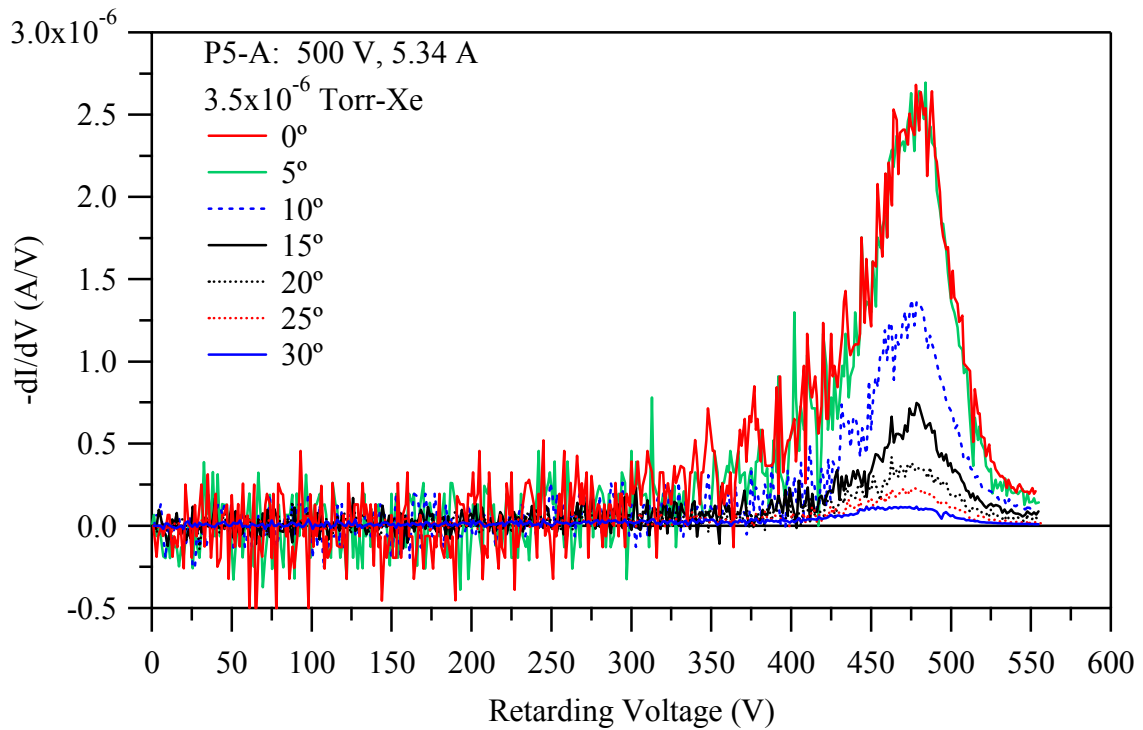


Figure 4-24: RPA traces of P5-A as a function of angle at an operating pressure of 3.5×10^{-6} Torr-Xe. (500 V, 5.34 A)

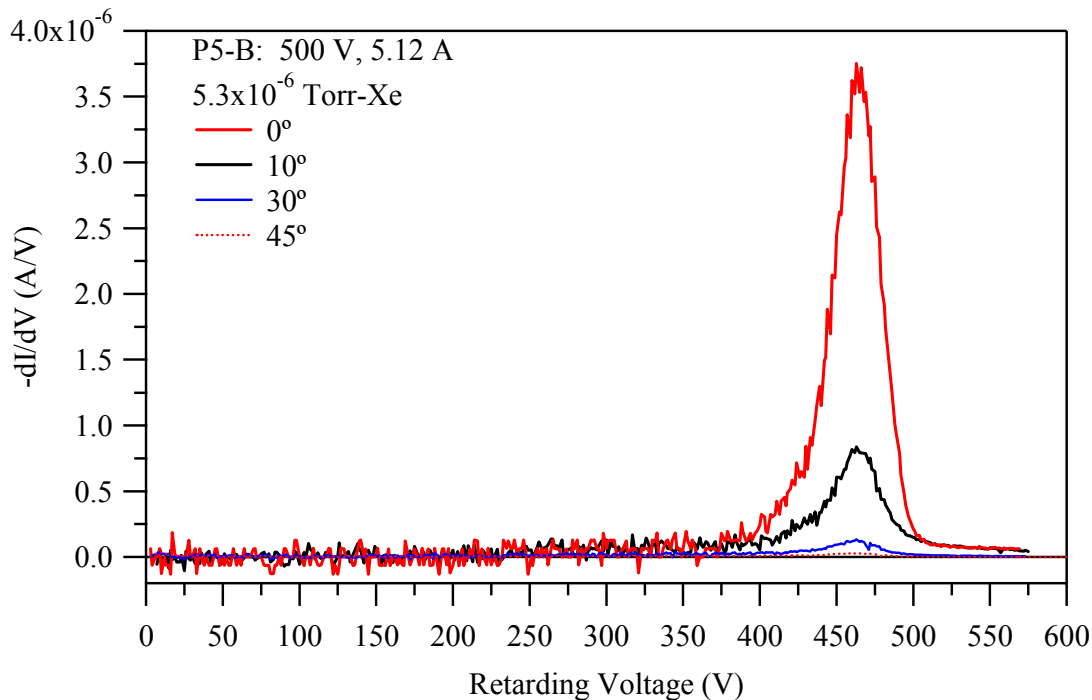


Figure 4-25: RPA traces of P5-B as a function of angle at an operating pressure of 5.3×10^{-6} Torr-Xe. (500 V, 5.12 A)

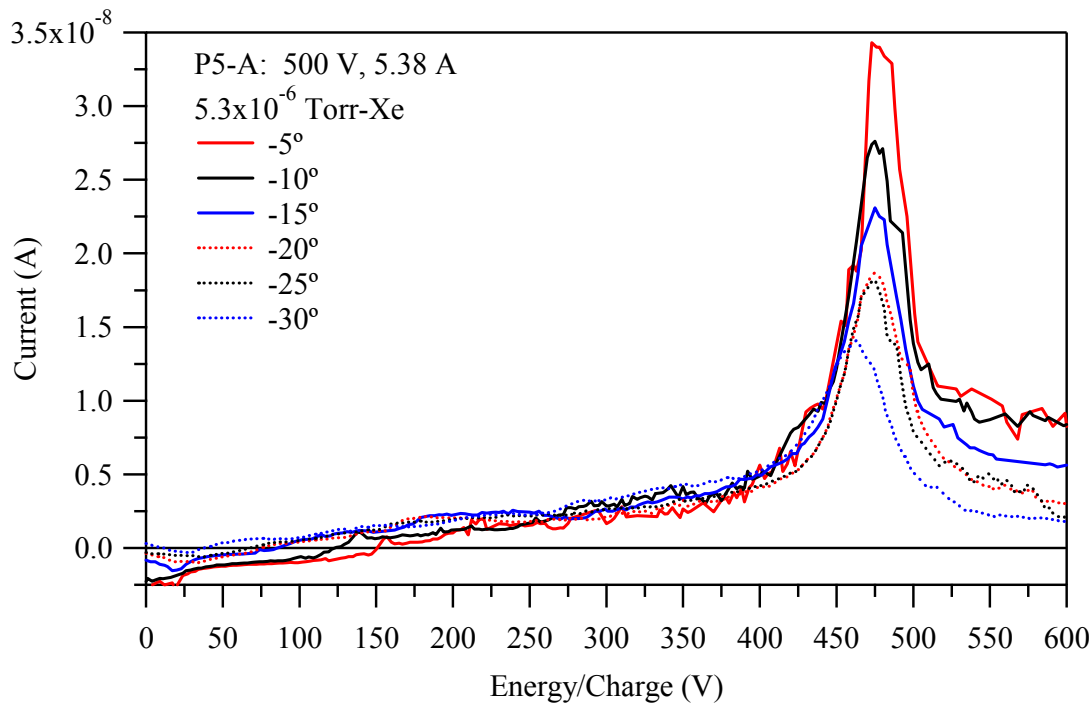


Figure 4-26: ESA traces of P5-A for angles of -5° to -30° at an operating pressure of 5.3×10^{-6} Torr-Xe. (500 V, 5.38 A)

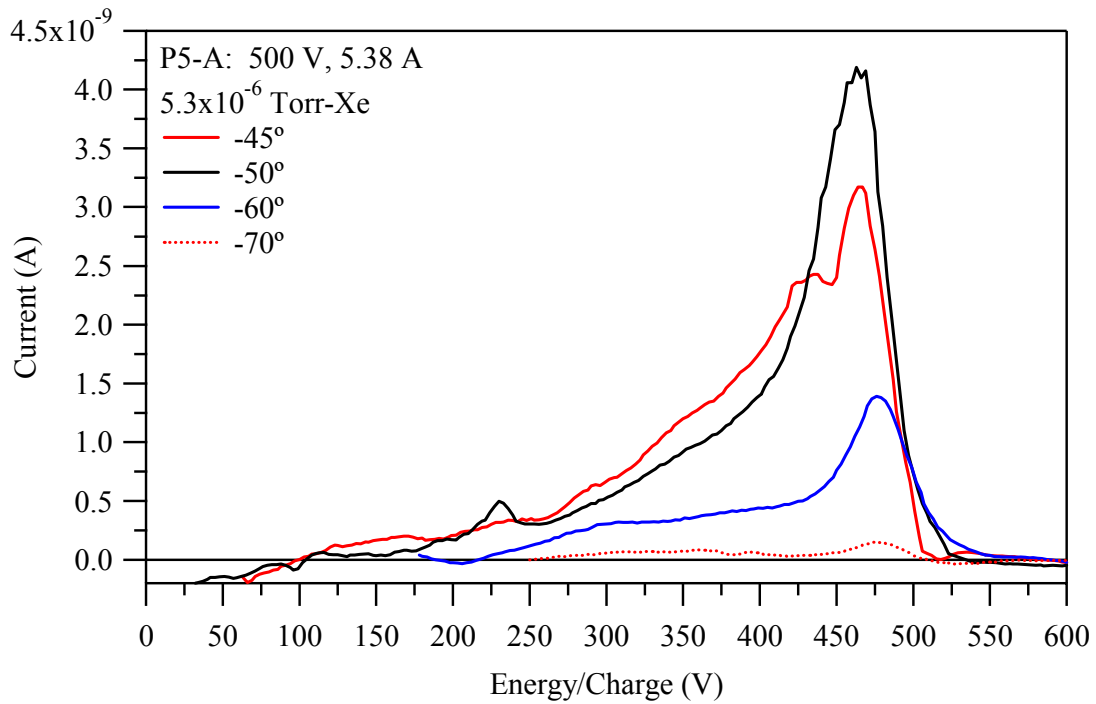


Figure 4-27: ESA traces of P5-A for angles of -45° to -70° at an operating pressure of 5.3×10^{-6} Torr-Xe. (500 V, 5.38 A)

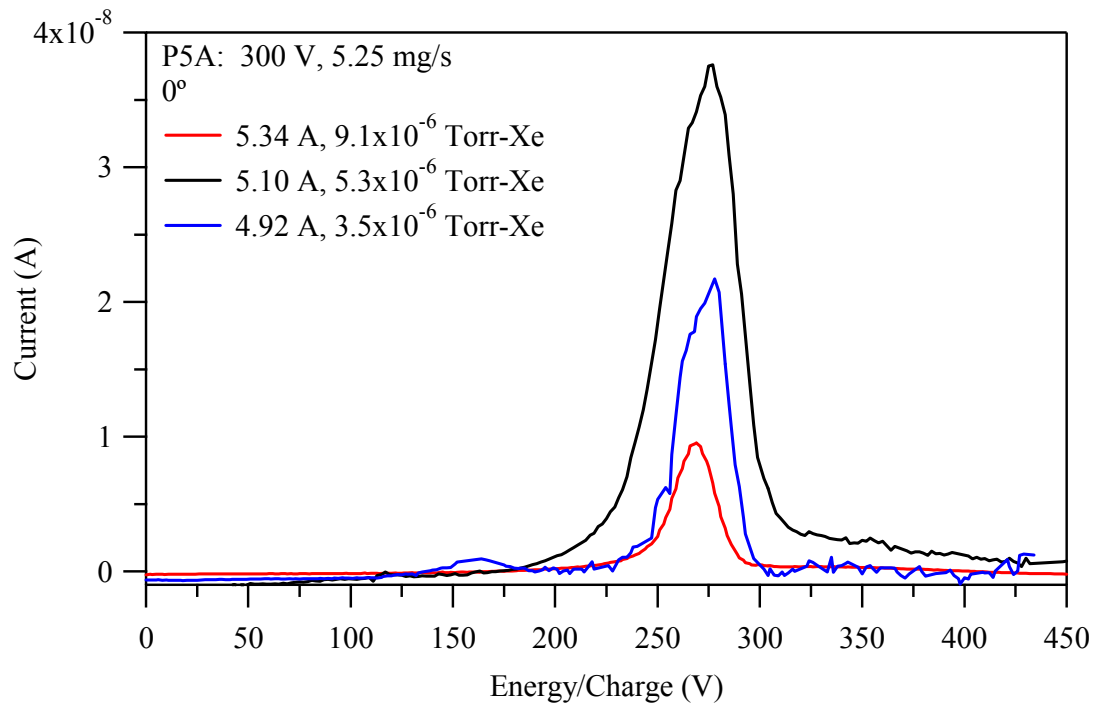


Figure 4-28: ESA traces of P5-A on centerline for 3 backpressures. (300 V, 5.25 mg/s)

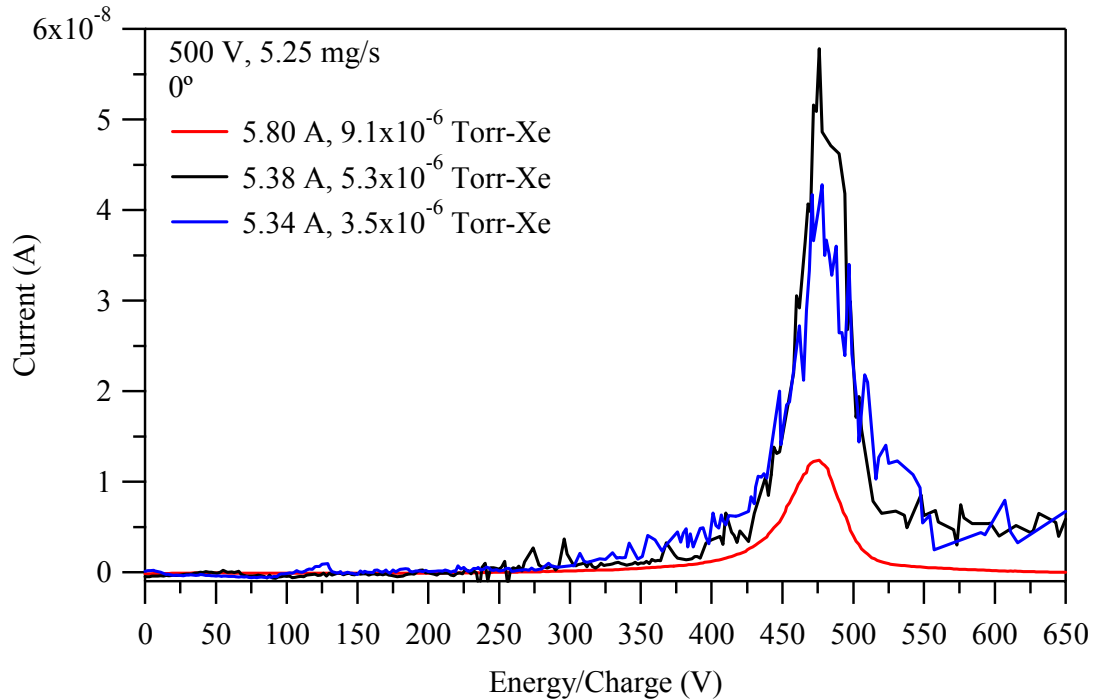


Figure 4-29: ESA traces of P5-A on centerline for 3 backpressures. (500 V, 5.25 mg/s)

4.1.6 Ion Species Fractions

The ion species fractions of Hall thrusters P5-A and P5-B are measured 1 m downstream of the exit plane with the ExB. The measurements are made in 5° increments from thruster centerline to 50° . For angles greater than 50° , the measurements are made in 10° steps. At angular positions greater than 60° from centerline, the signal-to-noise ratio is too low to discern the ion species peaks.

The ion species fractions are not measured at the higher operating pressures and anode flow rates. The high plasma density present at the ExB probe entrance elevates the plasma density inside the probe. At high plasma densities, the sheaths between the electrodes do not merge. Therefore, it is not possible for the electrostatic force to cancel the effect of the magnetic field, while allowing ions to reach the detector.

Figures 4-30 through 4-32 present ExB traces for several operating pressures and pumping speeds. These traces show how the P5-A plume species fractions change with angle from thruster centerline and facility backpressure.

The ExB probe traces of collector current versus probe voltage need explanation. A Faraday probe is used as the collector in the ExB probe. Thus, doubly-charged ions yield twice the current of an equivalent flux of singly-charged ions. Therefore, to convert the peak magnitudes to ion species fractions, divide the doubly charged peak by two and the triply-charged peak by three. Furthermore, the overlapping of the curves between adjacent species is so pronounced that the error in calculating the ion species fraction is very large; too large to be of use. Instead, we note the relative changes in species fraction as a function of angle from centerline and backpressure.

Figure 4-30 and 4-31 show traces of collector current versus probe voltage for the ExB probe for angles out to -35° from thruster centerline. There is a distinct drop in the percentage of doubly-charged ions produced as the probe moves off thruster centerline. For angles greater than 35° , the signal-to-noise ratio is too large to distinguish ion species peaks.

Figure 4-32 displays traces of collector current versus probe voltage on the centerline of the P5-A operating at 300 V, 5.25 mg/s as a function of pressure. There is a significant number of doubly-charged ions produced on thruster centerline at the uppermost pressure of 9.1×10^{-6} Torr-Xe. Decreasing facility backpressure decreases both the doubly-charged ion fraction and the magnitude of the entire profile. At the lowest operating pressure of 3.5×10^{-6} Torr-Xe, the doubly-charged ion peak is barely

distinguishable at a 180 V probe voltage. For this study, the ExB probe did not detect triply-ionized particles.

The ion species fractions on the centerline of the P5-A at an operating condition of 300 V, 5.25 mg/s are calculated for the 3 facility backpressures. The method uses the relative peak area, and corrects for the current gain created by multiply-charged species. The inherent error in this technique is approximately 30% and is discussed in Chapter 2. Table 4-4 shows the results of this analysis. The analysis shows that the doubly-charged ion species fraction is lowest at the highest pumping speed, which is an unexpected result. An increase in backpressure causes an increase in the number of CEX, inelastic, and elastic collisions that charged particles undergo on the way to the probe. These collisions change the energy-to-charge ratio and the trajectory of the ions. Therefore, fewer multiply-charged particles reach the probe collector. The results do not agree well with previous measurements of the P5 plume by Gulczinski show in Table 4-4.⁶⁹ Error bars of $\pm 30\%$ on the P5-A data do not overlap the original data collected for the P5. The error in the analysis technique and the elevated backpressure at the probe entrance yield little confidence in these ion species fraction results.

300 V, 5.25 mg/s				
Operating Pressure (Torr-Xe)	Discharge Current (A)	Xe⁺ (%)	Xe⁺⁺ (%)	Xe⁺⁺⁺ (%)
3.5x10 ⁻⁶	4.92	64	36	-
5.3x10 ⁻⁶	5.10	61	39	-
9.1x10 ⁻⁶	5.34	84	16	-
300 V, 5.3 A: Gulczinski				
5.5x10 ⁻⁶	5.3	92.5	6.8	0.7

Table 4-4: Ion species fraction on the centerline of P5-A for 3 facility backpressures (300 V, 5.25 mg/s) in comparison to ion species fractions measured by Gulczinski on the P5 operating at 300 V, 5.3 A.

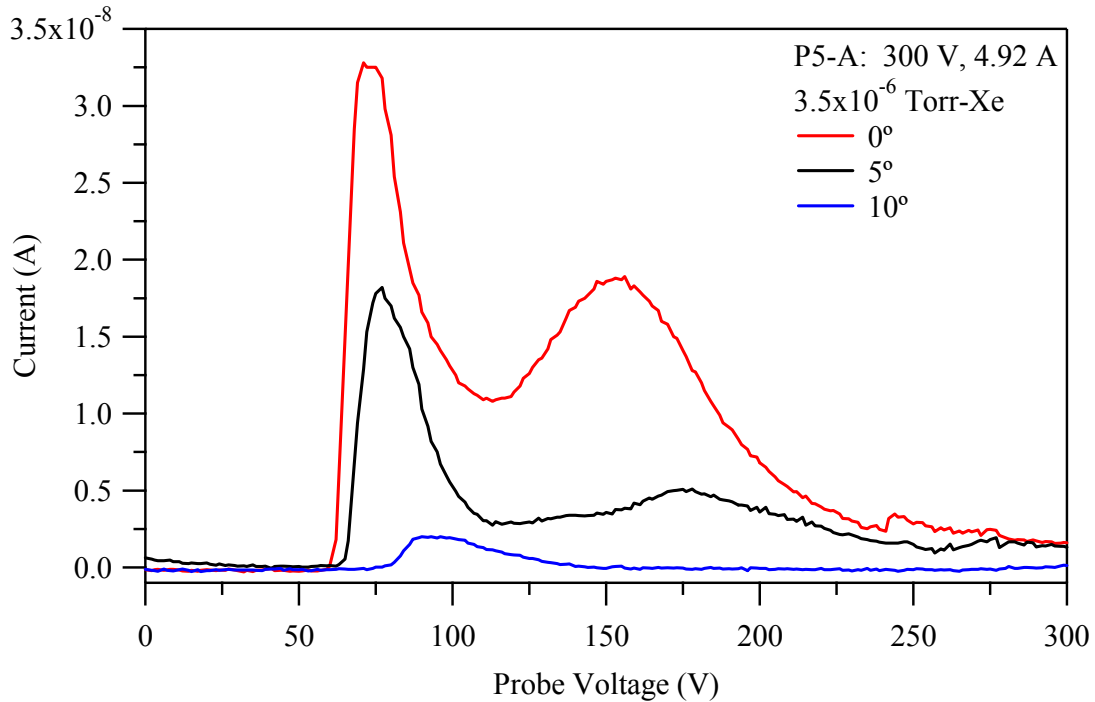


Figure 4-30: ExB traces of the P5-A operating at 300 V, 4.92 A at 0, 5, and 10° at a backpressure of 3.5×10^{-6} Torr-Xe. Note that the current is measured with a Faraday probe. Thus, the peak magnitudes cannot be directly related to the ion species without considering the amount of charge each species carries.

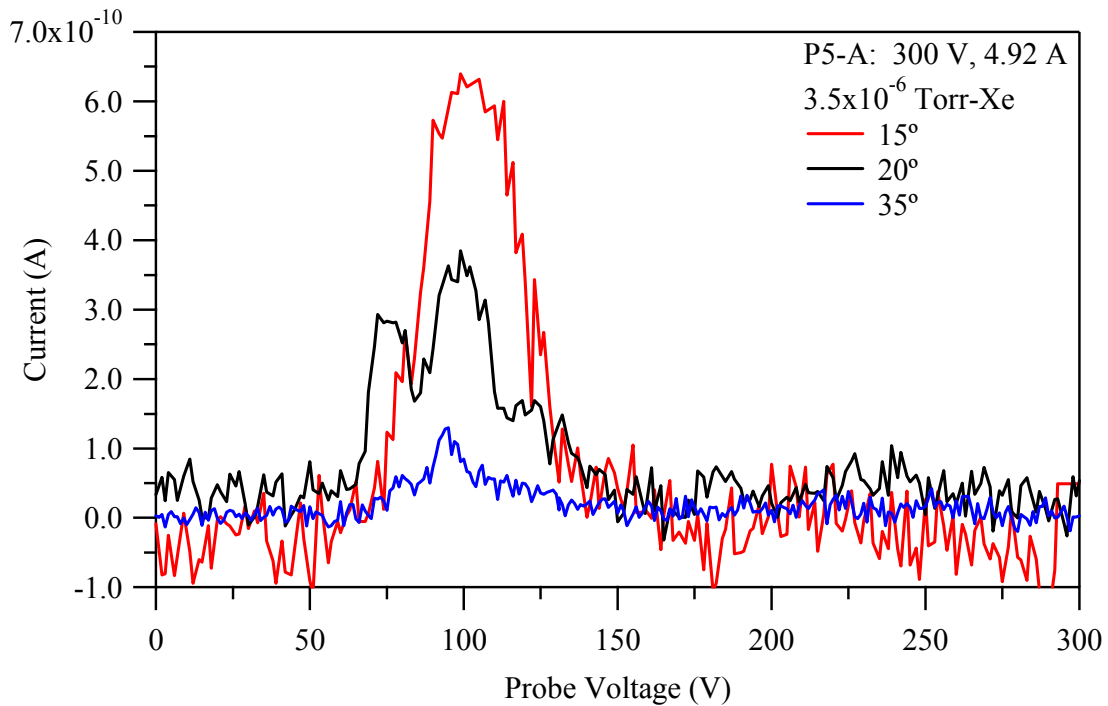


Figure 4-31: ExB traces of the P5-A operating at 300 V, 4.92 A at 15, 20, and 35° at a backpressure of 3.5×10^{-6} Torr-Xe. Note that the current is measured with a Faraday probe. Thus, the peak magnitudes cannot be directly related to the ion species without considering the amount of charge each species carries.

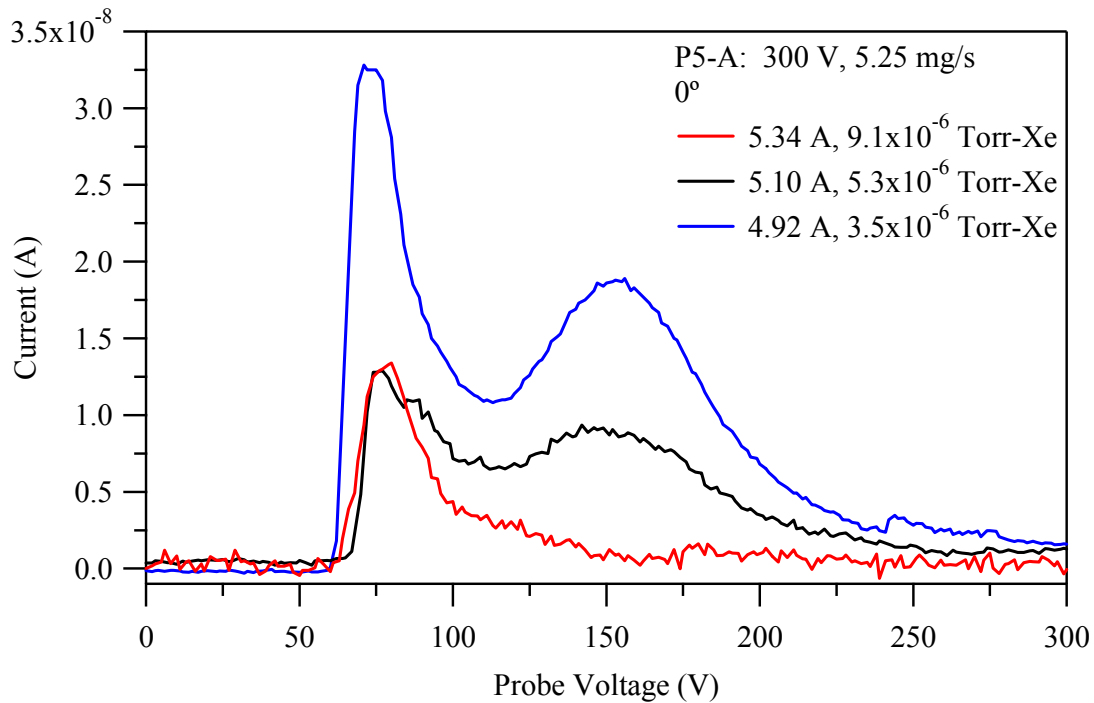


Figure 4-32: ExB traces of the P5-A operating at 300 V, 5.25 mg/s on thruster centerline at facility backpressures of 9.1×10^{-6} , 5.3×10^{-6} , and 3.5×10^{-6} Torr-Xe. Note that the current is measured with a Faraday probe. Thus, the peak magnitudes cannot be directly related to the ion species without considering the amount of charge each species carries.

4.1.7 Performance

The performance properties of Hall thrusters P5-A and P5-B are measured at three pumping speeds. Tables 4-1 and 4-2 show that the anode mass flow rate and magnet settings remain constant at each power setting for all three pumping speeds. The thrusters are mounted on the null-type inverted pendulum thrust stand located at station 1. As the facility backpressure increases, the thruster discharge current and thrust increase as more background xenon gas is ingested into the thruster discharge chamber. All performance parameters presented exclude the cathode mass flow and heater power.

Figures 4-33 and 4-34 present the measured thrust of the P5-A and P5-B, respectively, as a function of discharge voltage for anode flow rates of 5.25 mg/s and 10.46 mg/s. The thrust produced by each of the monolithic thrusters is nearly identical and increases with increasing backpressure, as expected. The agreement gives confidence in the similarity construction of the cluster elements. Figures 4-33 and 4-34 also show that the performances of the P5-A and P5-B are close to the original P5 Hall thruster within the error of the thrust measurement.^{53, 41} The similar performance implies that the thrusters are assembled similarly to the original P5 Hall thruster.⁵³

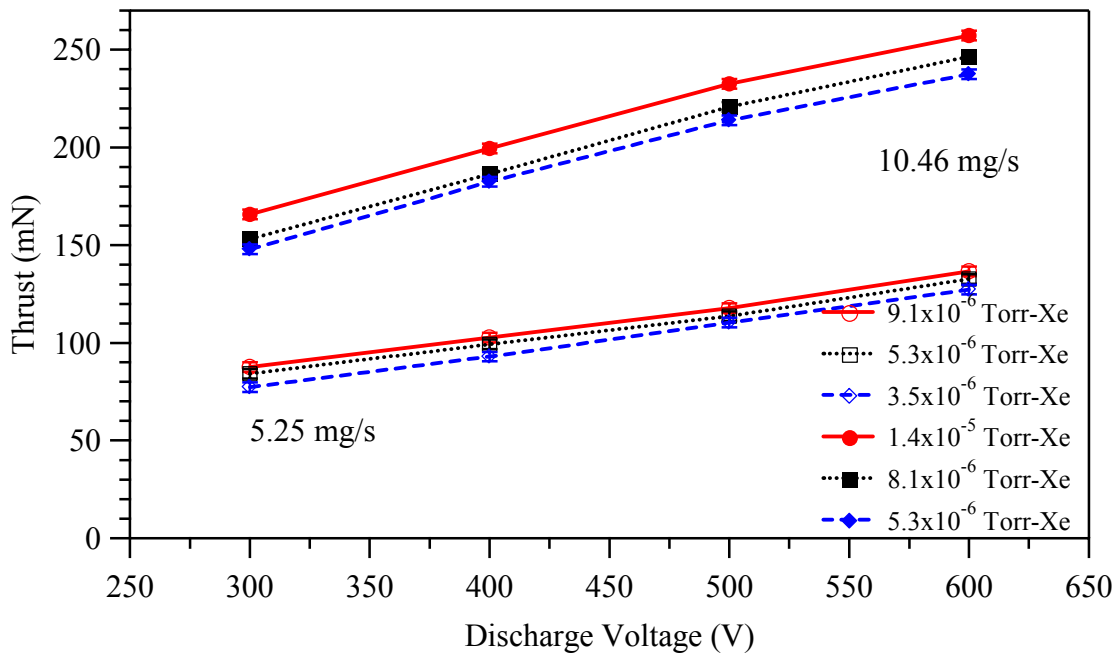


Figure 4-33: The P5-A thrust measurements at anode flow rates of 5.25 mg/s and 10.46 mg/s as a function of discharge voltage at nominal pumping speeds of 70 kl/s, 140 kl/s, and 240 kl/s.

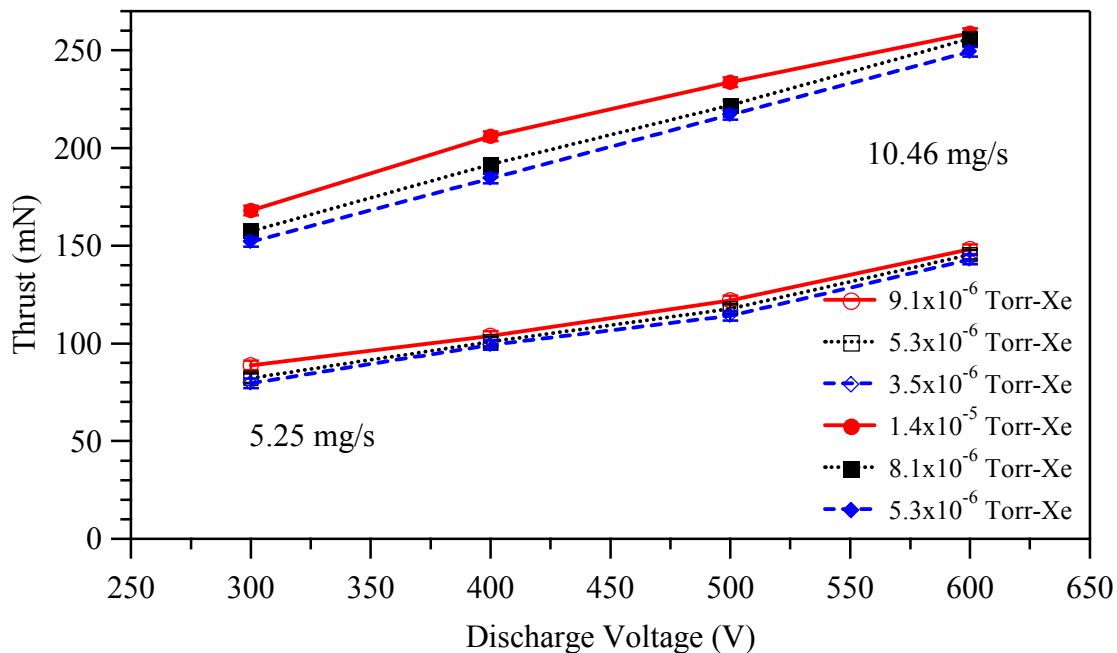


Figure 4-34: The P5-B thrust measurements at anode flow rates of 5.25 mg/s and 10.46 mg/s as a function of discharge voltage at nominal pumping speeds of 70 kl/s, 140 kl/s, and 240 kl/s.

Figure 4-35 presents the anode efficiency of the P5-A. Since the performance parameters of the P5-A and P5-B are similar, only the anode efficiency and specific impulse of the P5-A are shown. Figure 4-35 shows that, in general, the anode efficiency for a given flow rate increases with discharge voltage until a maximum is reached. Any further increase in voltage has little effect on the efficiency or causes it to decrease. Increasing the anode mass flow rate from 5.25 mg/s to 10.46 mg/s increases the maximum efficiency. At an anode flow rate of 5.25 mg/s with a backpressure of 9.1×10^{-6} Torr, the anode efficiency is a maximum at the 400 V discharge voltage. At this condition the ingested flow rate, (assuming effusion at a gas temperature of 300 K) is 0.8% of the injected anode flow, the highest ratio of injected flow to ingested flow. What appears to happen is that the increase in discharge current caused by background gas ingestion overwhelms the increase in thrust. Therefore, more power must be supplied to

the thruster, but the beam jet power does not increase as quickly. Unfortunately, the physical mechanisms that govern the interactions of ingested particles with the ionization and acceleration processes (which lead to the decrease in anode efficiency) are not understood.

Figure 4-36 presents the anode specific impulse of the P5-A. For each anode flow rate, the specific impulse increases continually with increasing discharge voltage. These observations agree well with the performance of the original UM/AFRL P5 Hall thruster and theory.^{53, 96}

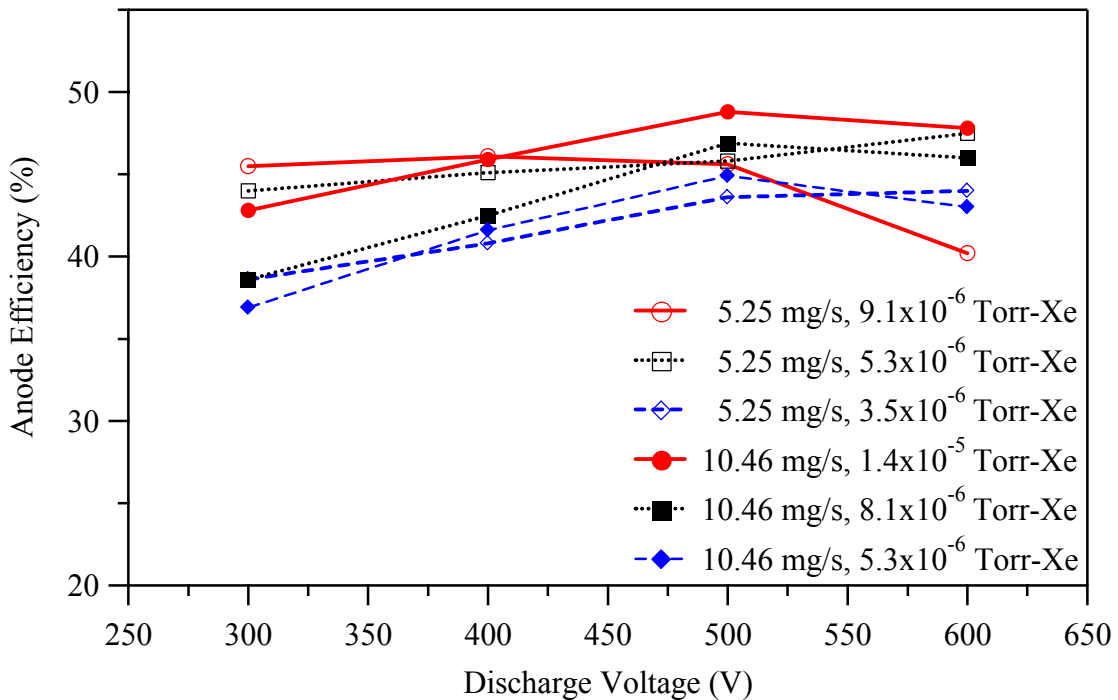


Figure 4-35: The P5-A anode efficiency versus discharge voltage.

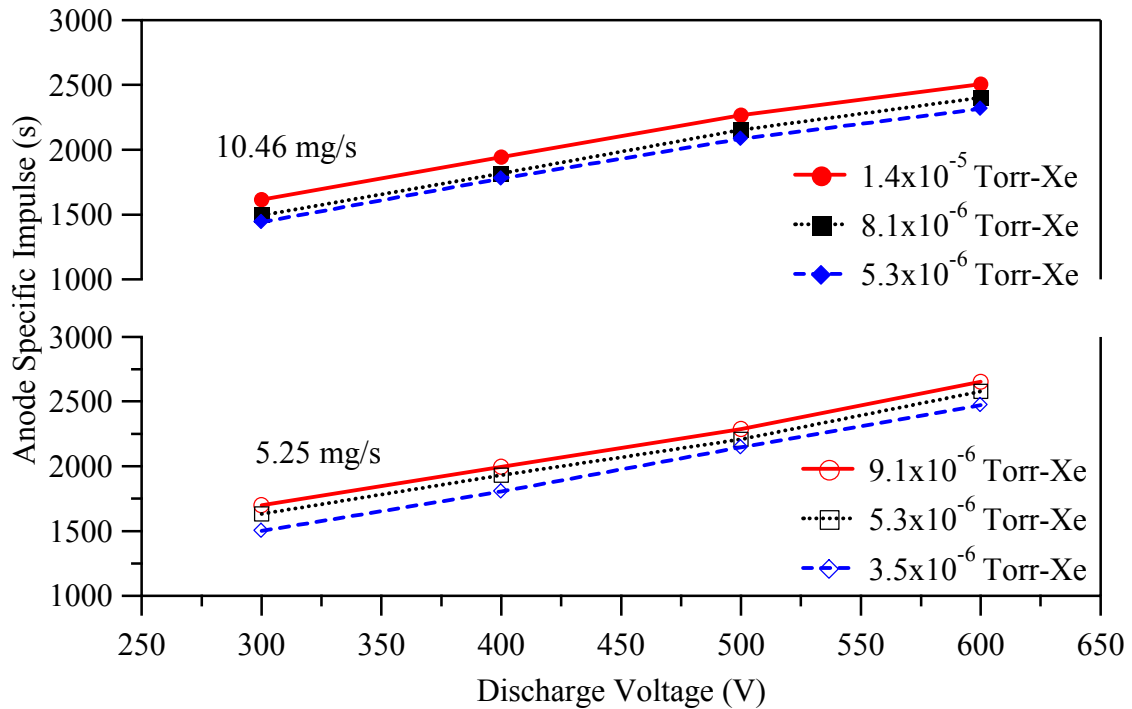


Figure 4-36: The P5-A anode specific impulse versus discharge voltage.

As shown in Figures 4-33 and 4-34, the performance of a Hall thruster is affected by the facility backpressure. The random flux of neutral particles is ingested into the discharge chamber. The ingested background gas increases the thrust, the discharge current, and the discharge current oscillation amplitude for a given operating condition. The ingested background particles are ionized in or near the discharge channel and accelerated downstream, artificially increasing the measured thrust. In addition, discharge current oscillations and electron collisions with the ingested neutrals enhance the electron mobility across the magnetic field. The increase in the number of electrons that reach the anode increases the discharge current at the expense of thrust. Several studies have attempted to explain the phenomena behind this behavior.^{36, 41} One approach that is routinely applied to correct performance data for ingested flow is to extrapolate thrust versus pressure data to zero background pressure.⁹⁷

Using thrust data collected across the P5 Hall thruster operating range at three operating pressures and two anode flow rates, we attempt to quantify the effects of the ingestion of neutral background gas at the Hall thruster exit plane. From this, we attempt to develop a tool to correct the performance of a Hall thruster operated at elevated facility backpressure. The approach towards correcting the thrust measured at elevated backpressures is to find the thrust increment provided by the ingested gas accelerated downstream.⁴⁹ For a known discharge channel open area, facility backpressure and wall temperature, we can use kinetic theory to calculate the mass flow rate of ingested background gas.³⁸ (Note that if the discharge extends significantly past the exit plane of the thruster, the effective area of the discharge is too small.) Next, assume that the Hall thruster has an ionization efficiency of 80% for neutral propellant leaving the anode.^{98, 3} The ionization probability of an ingested particle is 96% assuming an equal chance of ionization per pass through the ionization region because any particle that makes it through the ionization region on the way into the channel must travel through the ionization region a second time as it exits the channel. The particles are accelerated at the operating voltages measured by the ESA. The thrust increment created by ingested background neutrals is then calculated and used to correct measured thrust. The percent difference is calculated between the corrected thrust measured at 140 kl/s and the uncorrected thrust measured at 240 kl/s.

Figures 4-37 and 4-38 show the thrust percent differences for anode flow rates of 5.25 mg/s and 10.46 mg/s, respectively. The uncorrected data show that the thrust measurements taken at a pumping speed of 140 kl/s are as much as 8% greater than the thrust measurements taken at a pumping speed of 240 kl/s. The corrected data show that

the “random flux” correction method does not adequately account for the phenomena created by elevated backpressure.

To correct for the effect of ingested background gas on the performance of a Hall thruster, the composition of the plume must be considered at each backpressure pressure. Results presented earlier show that as the facility backpressure increases, electron temperature and electron number density increase 1 m downstream of the exit plane. The corresponding decrease in plasma potential (~ 6 V) yields a 2% increase in accelerating potential, which results in a 1 % increase in exit velocity, and thus thrust. This does not account for the increase in thrust with increasing backpressure. Measurements of the ion current density with Probe B show that the ion beam current decreases with increasing backpressure, which would lead to a decrease in thrust. However, the plume divergence half-angle is nearly constant for all backpressures at a given thruster operating condition. Results of the ESA measurements show that the ion energy distribution function increases in width as the backpressure increases. The amount of kinetic energy in the plasma plume may increase or decrease in magnitude depending on the ratio of trace height to width. Because the percentage of beam ions that reach the probe collector is significantly affected by backpressure, it is not possible to calculate the amount of energy in the plasma flow from the IEDF. As the backpressure increases, a greater number of multiply-charged ions may be created in the discharge chamber.³ The large error in the species fraction calculations does not inspire confidence in the ExB probe, or in results of their effect on the measured thrust.

It is not possible to point to a single distinct mechanism by which elevated facility backpressure increases measured thrust. The results of the performance and

plume characterization as a function of facility backpressure suggest that the overall change in thrust is the sum of several small changes in the plume characteristics, especially the plasma potential and IEDF.

$$\Phi = \frac{1}{4} n_b \left(\frac{8kT}{\pi m} \right)^{\frac{1}{2}} = \frac{P}{(2\pi mkT)^{\frac{1}{2}}} \quad \text{Eqn. 4-2}$$

$$\dot{m}_{en} = \Phi m A_{EXIT} = \frac{m^{\frac{1}{2}} A_{EXIT} P}{(2\pi k T_n)^{\frac{1}{2}}} \quad \text{Eqn. 4-3}$$

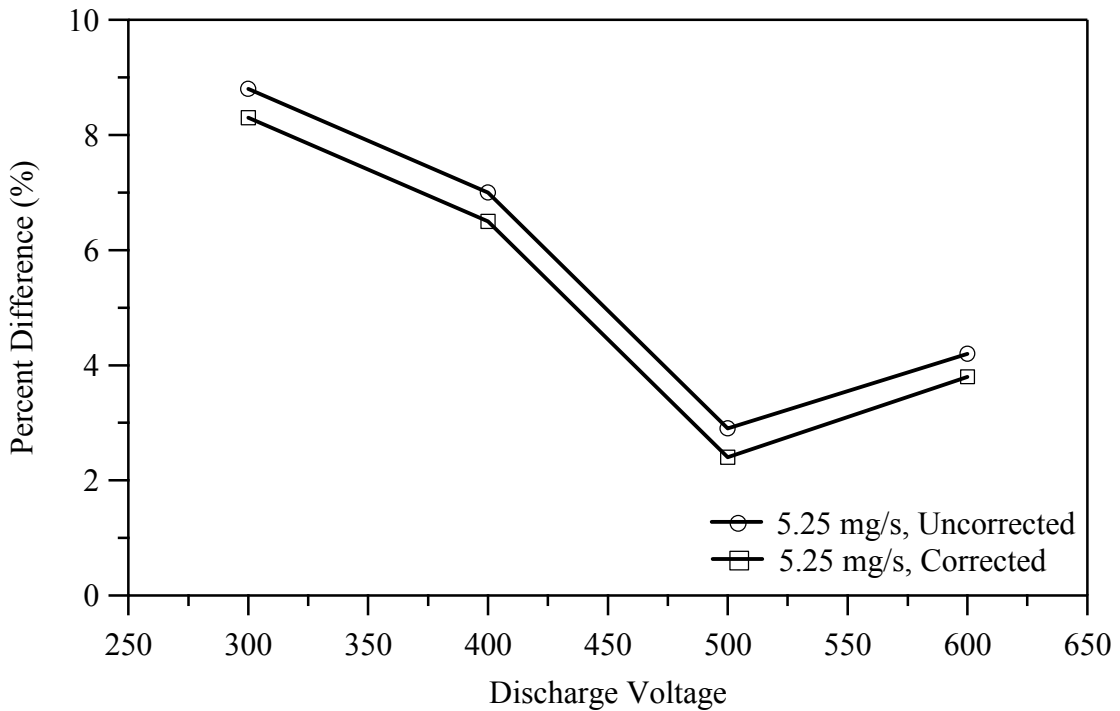


Figure 4-37: Percent difference in measured thrust of the P5-A at nominal pumping speeds of 140 kl/s and 240 kl/s for an anode flow rate of 5.25 mg/s.

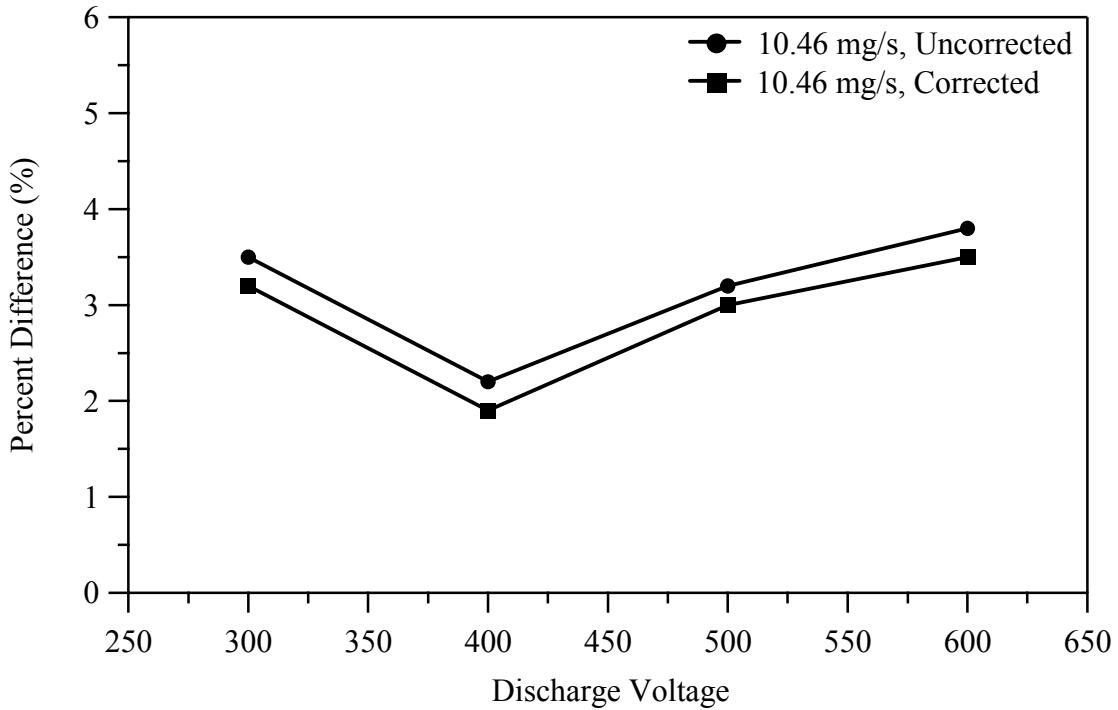


Figure 4-38: Percent difference in the measured thrust of the P5-A at nominal pumping speeds of 140 kl/s and 240 kl/s for an anode flow rate of 10.46 mg/s.

4.1.8 Facility Effects

The previous discussion thoroughly characterizes the effect of facility backpressure on the plume, performance, and operating characteristics of the thruster. The effects on the measured parameters are caused by background gas entrained into the discharge chamber of the thruster and collisions with the background gas as the beam particles travel downstream to the diagnostic. The changes in the plasma composition due to the entrainment of the facility background gas lead to an increase in the discharge current oscillations amplitude. At the higher-power operating conditions, discharge oscillations appear to increase the number of electrons that reach the anode. This may also be caused by an increase in the number of electron-neutral collisions created in the discharge chamber at higher backpressure, which enhances the electron mobility to the

anode. Because the increase in backpressure, discharge current, and discharge current oscillation amplitude occur at the same time, it is difficult to decipher what drives these changes other than increased neutral density.

Collisions downstream of the exit plane occur more frequently as the facility backpressure increases. The percentage of CEX ions in the plume increases with facility backpressure, and is most noticeable in the plume core and wings of the ion current density measurements. A magnetically-filtered Faraday probe effectively removes CEX ions from the ion current density measurements. In addition, the width of the ion energy distribution broadens with increasing backpressure. Unfortunately, the error in the calculation of the ion species fractions is too large to allow valid comparison of species fractions at different backpressures. Furthermore, the increase in beam ion collisions with the background gas leads to small changes in the floating potential, plasma potential, electron number density, and electron temperature. While the change in each of these parameters is small, the overall effect of increased facility backpressure leads to an increase in the thrust of the Hall thruster.

Because the increase in thrust with increasing backpressure appears to be due to the sum of these effects, a straightforward method to correct thrust for performance measurements is not yet clear. However, this investigation bounds the increase in thrust for a given increase in facility backpressure. To correct performance measurements taken at elevated backpressures, one must take into account the changes in the multiply-charged ion fraction, ion energy distribution, and plume divergence as the facility backpressure increases. I believe the most fruitful approach is to use these experimental data to validate a numerical model that simulates Hall thruster performance over a wide

range of pressures. The model can be calibrated with data collected at an arbitrary pressure for a given thrust, and then used to predict the on-orbit performance.

4.2 Conclusions

We now have a full characterization of the Hall thruster discharge current oscillations, electron temperature, electron number density, floating potential, plasma potential, ion current density, ion energy distribution, ion species fraction, and performance over a range of facility operating pressures above and below Randolph's suggested pressure of 1.0×10^{-5} Torr-Xe. The results show that Randolph's criterion for plume measurements does not hold.

This investigation verifies that the MFFP adequately filters out CEX ions in the wings of the plume. The current ESA and ExB diagnostic designs require adjustments if they are to accurately measure plume parameters at elevated facility backpressure in high-density plasma. The increase in thruster thrust with increasing facility backpressure is explained as the sum of incremental changes due to entrained gas, lower plasma potential, and broadening of the ion energy distribution function.

CHAPTER 5

CLUSTER CHARACTERIZATION

The previous chapter develops a baseline of the plume and performance characteristics of P5-A and P5-B at three facility backpressures. The results of that effort show that the plume and performance characteristics of the thrusters are nearly identical. This yields a thorough understanding of the monolithic thrusters, which is a solid foundation to start the investigation of high-power Hall thruster clustering.

The aim of this chapter is to investigate the effect of Hall thruster clustering on plume and performance characteristics. The study investigates how performance and plume characteristics of a single thruster are affected by an adjacent thruster element. In addition, the overall plume and performance parameters of the cluster are characterized. The results are used to determine the feasibility of high-power Hall thruster clustering.

To investigate the effect of Hall thruster clustering, the performance and plume characteristics of the cluster are characterized at three facility backpressures. The plume characteristics are measured at facility pumping speeds of 70, 140, and 240 kl/s. The plume measurements are performed two ways: first, with the axis of probe rotation centered on the P5-A exit plane; and second, centered on the cluster. The first configuration allows measurement of the effect of the adjacent thruster, while the second configurations allows for characterization of the overall cluster plume.

5.1 Probe Data

The plume and performance characteristics of the 2x1 cluster of UM/AFRL P5 Hall thrusters are characterized at the operating conditions displayed in Table 5-1. The measurements are performed with each of the diagnostics described in Chapter 2 over a range of backpressures from 5.4×10^{-6} Torr-Xe to 2.8×10^{-5} Torr-Xe. Figure 5-1 shows measurement Configuration 1, which centers the one-meter arc on which data are collected on P5-A. Figure 5-2 shows measurement Configuration 2, which centers the one-meter arc on which data are collected on the cluster centerline.

All of the measurements presented in this chapter are taken with a monolithic thruster centerline separation distance of 40 cm. Each of the monolithic elements is operated independently from its own cathode and power supplies. Only cluster data collected with both cluster elements operating at 300 and 500 V for anode flow rates of 5.25 and 10.46 mg/s are shown. The operation conditions of 400 and 600 V at anode flow rates of 5.25 and 10.46 mg/s show similar trends to the data presented.

The following subsections discuss the effect of facility backpressure on the measured plume and performance characteristics of the elements of the cluster. The overall plume and performance of the Hall thruster cluster as a function of backpressure are also discussed. In addition, the data are examined for signs of one thruster affecting the plume or performance characteristics of the adjacent thruster.

Pumps	Discharge Voltage (V)	P5A Discharge Current (A)	P5B Discharge Current (A)	Anode (mg/s)	Cathode (mg/s)	Inner Magnet Current (A)	Outer Magnet Current (A)	Pressure (Torr-Xe)	Pressure (Pa-Xe)
2	300	5.76	5.68	5.25	0.92	2.56	1.43	1.5E-05	2.0E-03
2	400	6.94	6.94	5.25	0.92	3.14	1.55	1.5E-05	2.0E-03
2	500	8.26	8.38	5.25	0.92	3.98	1.57	1.5E-05	2.0E-03
2	300	11.08	10.90	10.46	0.92	3.06	1.82	2.8E-05	3.7E-03
2	400	14.54	11.06	10.46	0.92	3.92	2.00	2.8E-05	3.7E-03
4	300	5.24	5.22	5.25	0.92	2.56	1.43	8.6E-06	1.1E-03
4	400	5.34	5.34	5.25	0.92	3.14	1.55	8.6E-06	1.1E-03
4	500	5.42	5.40	5.25	0.92	3.98	1.57	8.6E-06	1.1E-03
4	300	10.32	10.34	10.46	0.92	3.06	1.82	1.3E-05	1.7E-03
4	400	10.48	10.48	10.46	0.92	3.92	2.00	1.3E-05	1.7E-03
7	300	5.14	4.96	5.25	0.92	2.56	1.43	5.4E-06	7.2E-04
7	400	5.26	5.06	5.25	0.92	3.14	1.55	5.4E-06	7.2E-04
7	500	5.36	5.24	5.25	0.92	3.98	1.57	5.4E-06	7.2E-04
7	300	10.14	10.02	10.46	0.92	3.06	1.82	8.9E-06	1.2E-03
7	400	10.26	10.14	10.46	0.92	3.92	2.00	8.9E-06	1.2E-03
7	500	12.92	11.32	10.46	0.92	4.28	3.00	8.9E-06	1.2E-03

Table 5-1: Cluster operating conditions

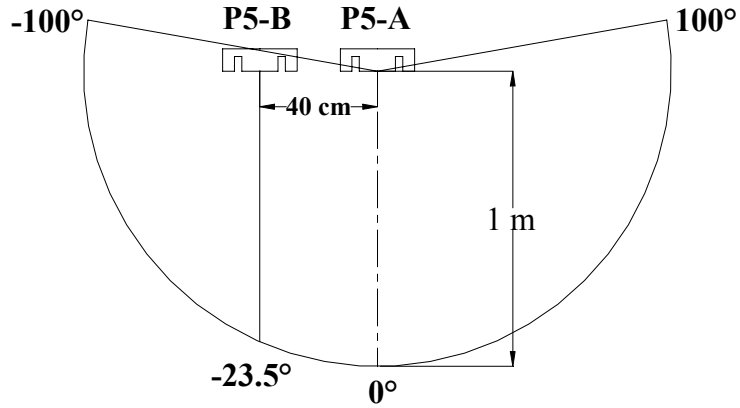


Figure 5-1: Configuration 1: Diagram of the cluster with the 1 m arc of data collection centered on P5-A.

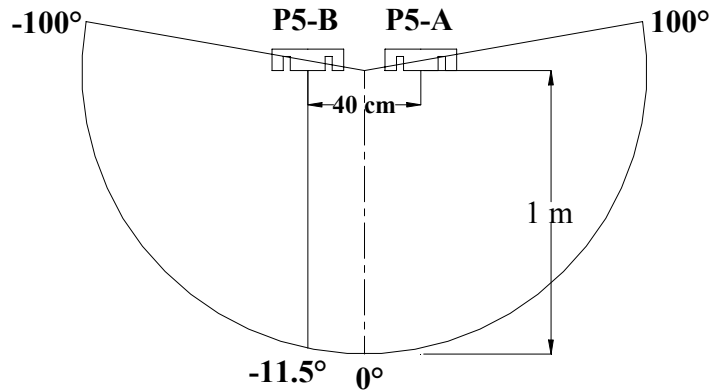


Figure 5-2: Configuration 2: Diagram of the cluster with the 1 m arc of data collection centered on the cluster.

5.1.1 Discharge Current Characteristics

The discharge current oscillations of the cluster elements are measured to determine if the cluster configuration causes the thrusters to couple in some way. The discharge current oscillations of each of the cluster elements are measured over the range of facility backpressures and operating conditions by separate F.W. Bell IHA-25 Hall probes connected to a single Tektronix TDS 3034B oscilloscope. As with the monolithic characterization, the discharge current measurements are made after the thrusters have operated for a minimum of one hour, so thermal equilibrium is reached.

Figures 5-3 through 5-5 present samples of the measured discharge current oscillations of each of the monolithic thrusters as a function of facility backpressure. Figures 5-3 and 5-4 show that the discharge current oscillations of P5-A and P5-B in the cluster configuration are nearly the same as when each engine operates alone. Fast Fourier transforms of the clustered monolithic thruster discharge current oscillations show that the discharge is composed of oscillation frequencies of 0.85 to 10.4 kHz, which are characteristic of Hall thruster operation.⁴¹ The phases of the discharge current oscillations show no sign of coupling between the two thrusters. In addition, discharge

current amplitude for each appears to be completely independent. Figure 5-5 shows P5-A discharge current oscillations for the thruster operating in the clustered and monolithic configuration at nearly equal facility backpressures. Notice that the amplitude of the discharge current oscillations is approximately the same when the monolithic thruster and cluster are operated at nearly the same facility backpressure.

Figure 4-2 shows nominal discharge current oscillations of the P5-A operating at 300 V, 4.92 A at an operating pressure of 3.5×10^{-6} Torr-Xe. The amplitude of the oscillations is approximately 17% of the average discharge current. Figure 5-3 shows the cluster element discharge currents with the P5-A operating at 300 V, 5.14 A and the P5-B operating at 300 V, 4.96 A at an operating pressure of 5.4×10^{-6} Torr-Xe. The cluster operates well at this condition, but the discharge current oscillation amplitude of the P5-A has increased to 22% of the average discharge current by the increase in facility backpressure. The amplitude of the P5-B is approximately 14% of the average discharge current. The difference between the P5-A and P5-B oscillation amplitudes may be caused by varying component material properties and assembly tolerances typical of hand-built thrusters, cathodes, and discharge filters.

Figure 5-4 shows the cluster discharge current oscillations with the P5-A operating at 300 V, 5.76 A and the P5-B operating at 300 V, 5.68 A at an operating pressure of 2.8×10^{-5} Torr-Xe. The discharge currents have increased from the values measured at the 5.3×10^{-6} Torr-Xe operating pressure. Furthermore, the amplitudes of the discharge oscillations have increased to approximately 37% of the discharge current for both the P5-A and P5-B.

The above analysis shows that the clustered thruster oscillation amplitudes increase with facility backpressure, and that each discharge current oscillation seems to be unaffected by the adjacent Hall thruster. Therefore, clustering Hall thrusters on a spacecraft should require no changes to existing Hall thruster power processing units.

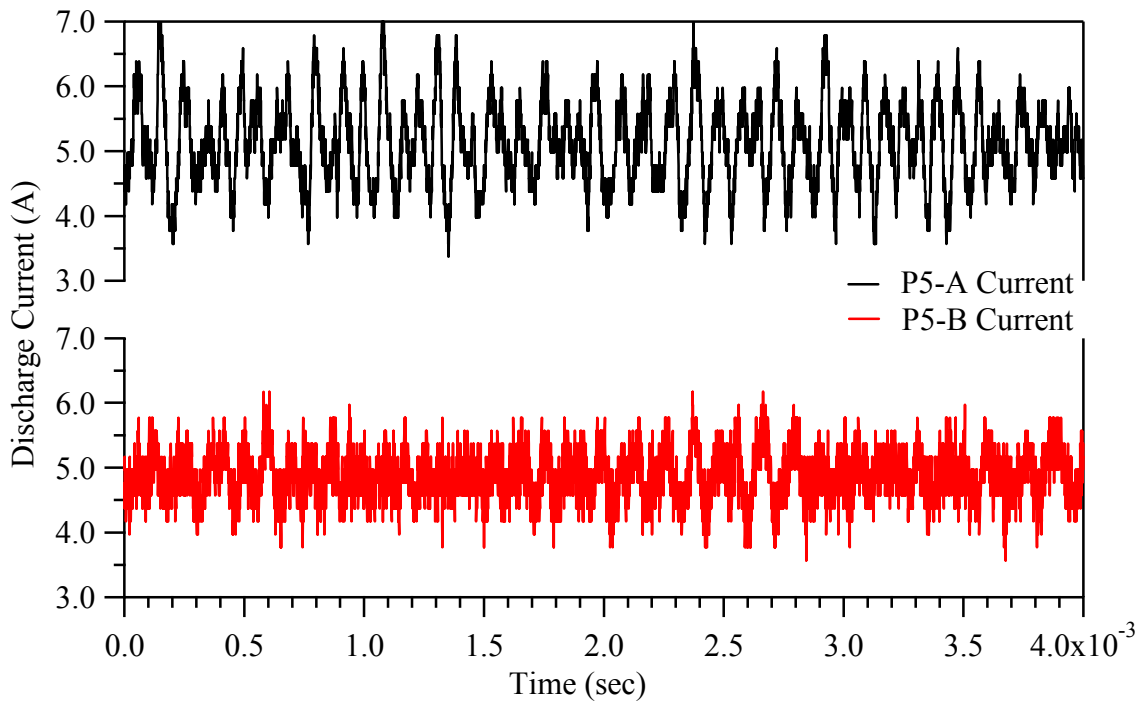


Figure 5-3: Cluster discharge current with the P5-A operating at 300 V, 5.14 A and the P5-B operating at 300 V, 4.96 A. The measurements are taken at a nominal pumping speed of 240 kl/s: 7.2×10^{-4} Pa (5.4×10^{-6} Torr).

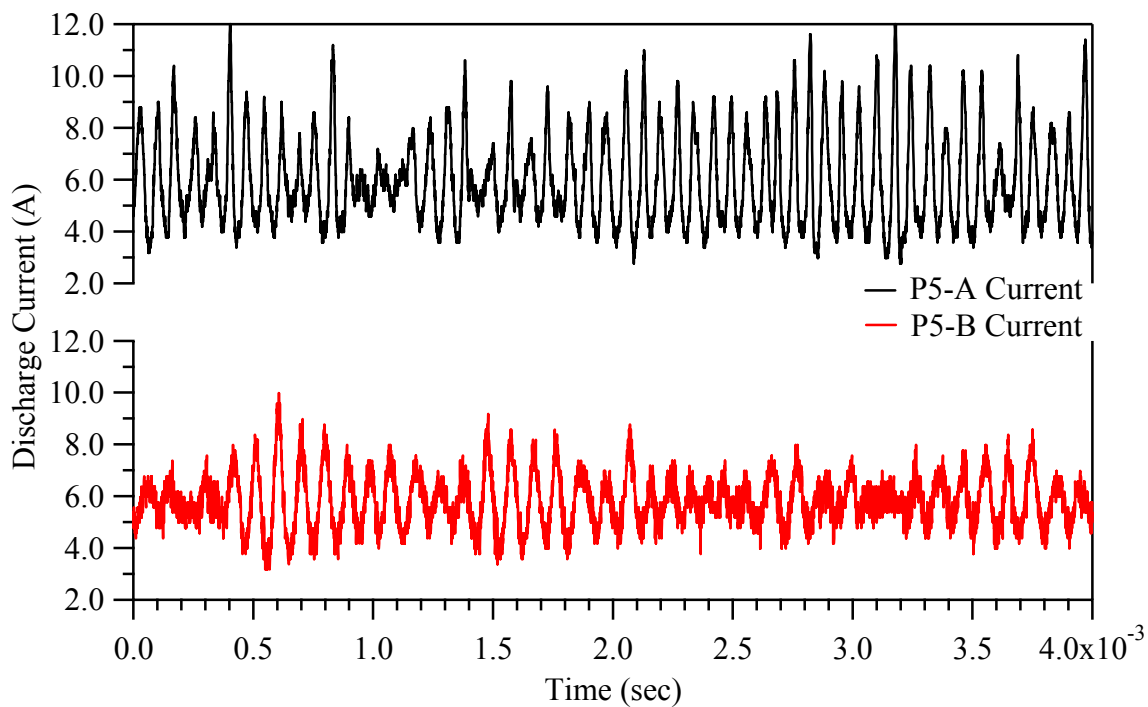


Figure 5-4: Cluster discharge current with the P5-A operating at 300 V, 5.76 A and the P5-B operating at 300 V, 5.68 A. The measurements are taken at a nominal pumping speed of 70 kl/s: 3.7×10^{-3} Pa (2.8×10^{-5} Torr).

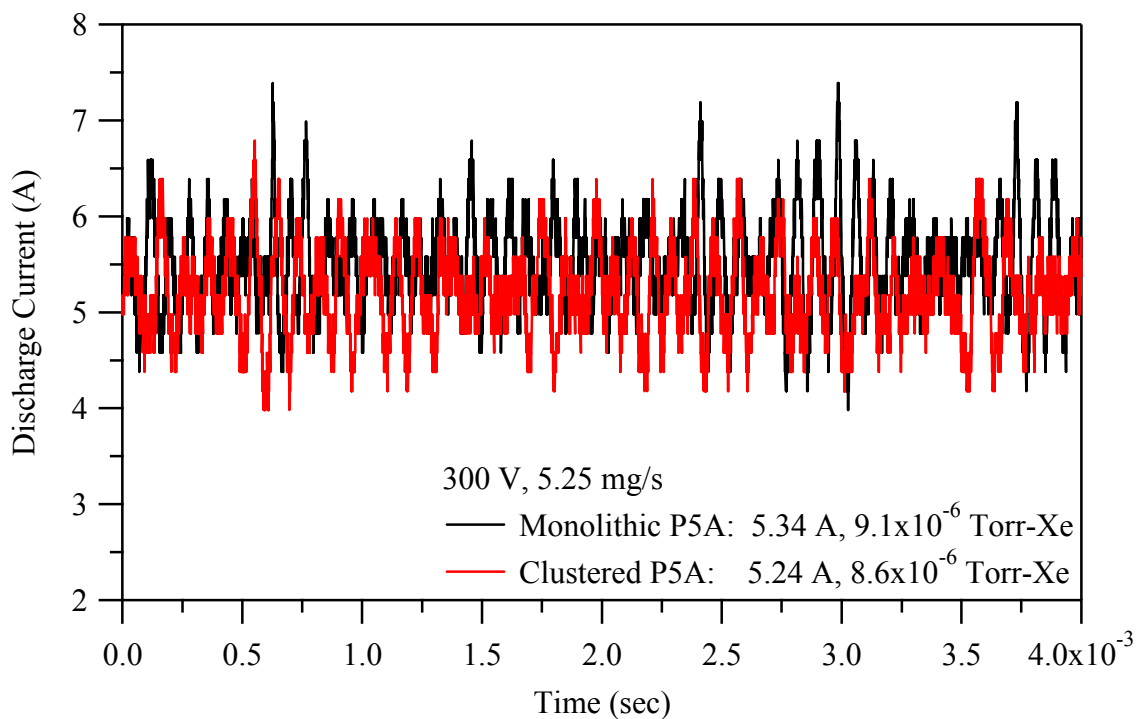


Figure 5-5: Discharge current of the monolithic P5-A (300 V, 5.34 A) at a backpressure of 9.1×10^{-6} Torr-Xe and the clustered P5-A (300 V, 5.24 A) at a backpressure of 8.6×10^{-6} Torr-Xe.

5.1.2 Plasma Potential and Floating Potential

The plasma potential and floating potential in the plumes of the P5-A and P5-B Hall thrusters are measured from -100° to $+100^\circ$ on the one-meter arc shown in Figures 5-1 and 5-2. The measurement step size is 5° from thruster centerline to an angle of 50° and 10° for angles greater than 50° . Figures 5-6 through 5-9 present traces of the plasma potential and floating potential measured in Configuration 1 at each operating condition and pumping speed. Figures 5-10 through 5-12 present traces of the plasma potential and floating potential measured in Configuration 2. Several of the figures presenting the Configuration 1 data include a P5-A trace collected at a nominal pumping speed of 70 kl/s. These data are included for a nearly equal-backpressure comparison with cluster data collected at a nominal pumping speed of 140 kl/s.

The plume characteristics in Configuration 1 (see Figures 5-6 through 5-9) show how a monolithic thruster is affected by an adjacent thruster, since the measurements are taken in the same configuration in which the monolithic thrusters are characterized. Note that the traces of floating potential and plasma potential show a peak on centerline (corresponding to the plume of P5-A) and a peak at approximately -25° (corresponding to the centerline of P5-B). The distinct peaks located at the angular positions of 0° and -25° (see Figure 5-1) verify that the plumes do not coalesce into a single structure.

The monolithic P5-A traces added to Figures 5-6 and 5-8 show that the floating potential of the plume has a similar shape as a function of angle for both the monolithic and cluster configurations. However, as the backpressure in the chamber increases, the magnitude of the floating potential in the cluster configuration is approximately 2 volts lower than that of the monolithic thruster. The figures also show that an increase in facility backpressure causes an increase in floating potential at all angles.

The traces of the plasma potential for Configuration 1 show different trends. The plasma potential of the monolithic P5-A plume is very similar to that of the cluster at nearly equal backpressures. On the centerline of P5-A there is little to no change in plasma potential with backpressure. However, for angular locations near the centerline of P5-B, the plasma potential increases with decreasing facility backpressure. This may be caused by a greater absolute number of beam ions impacting the Langmuir probe as the backpressure decreases. For large angles from P5-A centerline an increase in facility backpressure causes an increase in plasma potential. This is because as backpressure increases, the number of CEX ions at angles off centerline increases, which results in an increase in the plasma potential.

The results of Configuration 2 are presented in Figures 5-10 through 5-12. Configuration 2 shows how the overall plume of the cluster looks. Note that each trace shows distinct peaks at approximately $\pm 10^\circ$ from thruster centerline. These peaks correspond to the angular location of the monolithic thruster centerlines shown in Figure 5-2. These peaks show the symmetry of the cluster plumes, which means that the plume of the monolithic thrusters has not merged into one plume; also the location of the peaks shows that neither thruster appears to deflect or attract the plume of its neighbor. The cluster traces show that as the facility backpressure increases the floating potential increases at all angles. Figure 5-12 shows that the greatest increase in floating potential is approximately 4 volts and occurs at the 10.46 mg/s anode flow rate. The change in floating potential for both Configuration 1 and 2 is related to the electron temperature and electron number density, which are discussed in the next section.

The traces of plasma potential in Configuration 2 show clear trends. In the wings of the Configuration 2 traces, the plasma potential increases with increasing facility backpressure, which is identical to the plasma potential Configuration 1. For angles of $\pm 20^\circ$ and greater from thruster centerline, the plasma potential decreases with increasing facility backpressure. In addition, the peaks corresponding to the monolithic thrusters increase with decreasing backpressure. This trend is caused by an increase in the absolute number of high-energy beam ions that reach the Langmuir probe as the facility backpressure decreases.

The measurements of floating potential and plasma potential in the cluster plume for Configurations 1 and 2 show that backpressure-induced facility effects on plume properties are complex. The results show different trends as a function of backpressure for different locations in the cluster plume. Fortunately, the changes in magnitude are negligible when compared to the Hall thruster discharge voltages. Changes in floating potential and plasma potential do not appear to affect the overall cluster performance and should present no more challenge than monolithic thrusters for integration onto spacecraft.

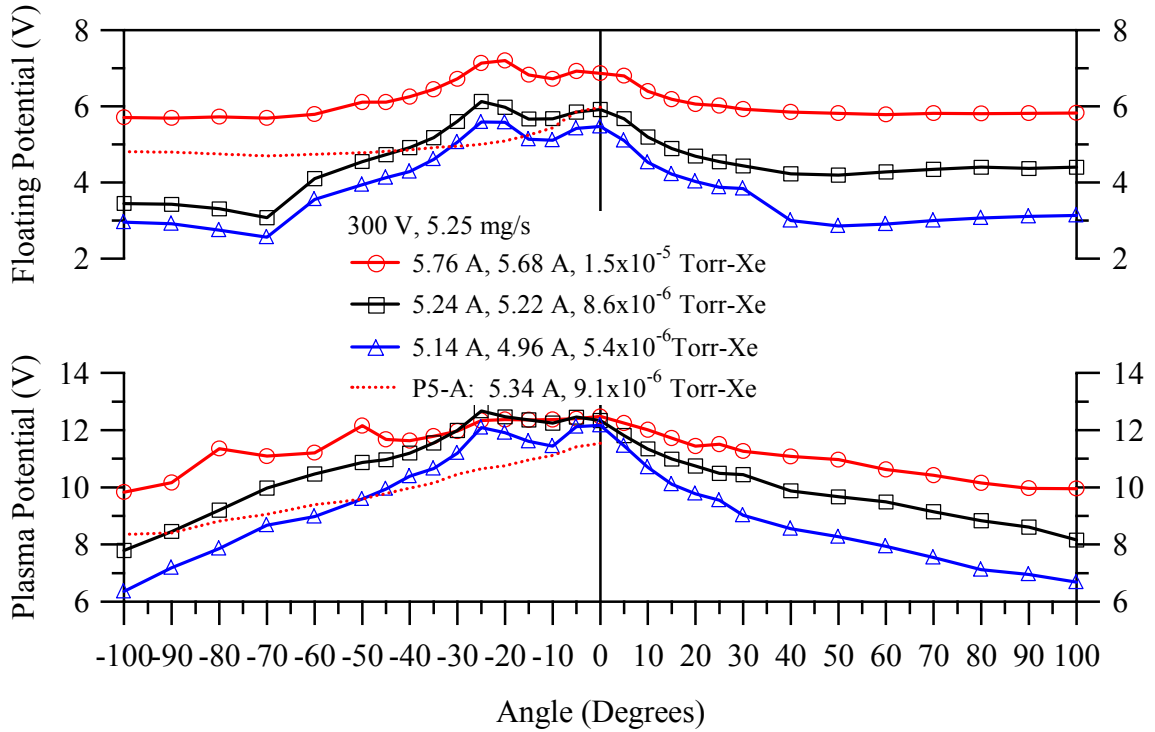


Figure 5-6: Traces of the floating potential and plasma potential as a function of angle in Configuration 1. The cluster operating condition is 300 V, 5.25 mg/s at 3 backpressures.

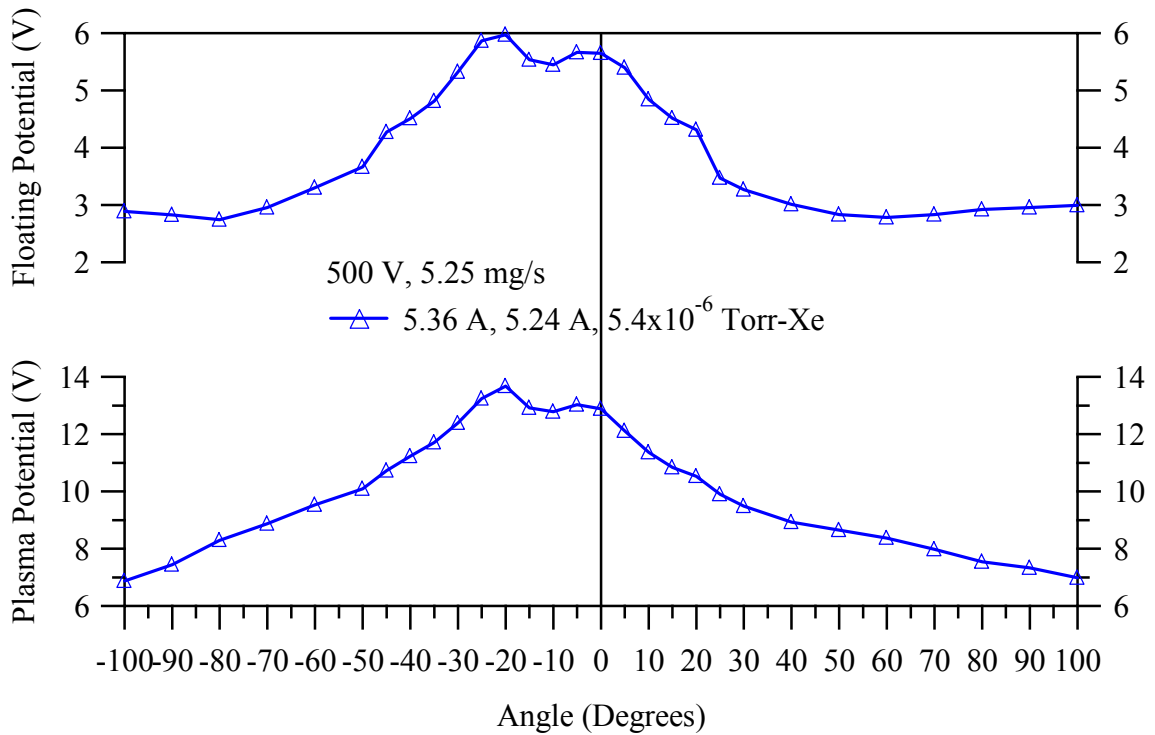


Figure 5-7: Traces of the floating potential and plasma potential as a function of angle in Configuration 1. The cluster operating condition is 500 V, 5.25 mg/s at a backpressure of 5.4×10^{-6} Torr-Xe.

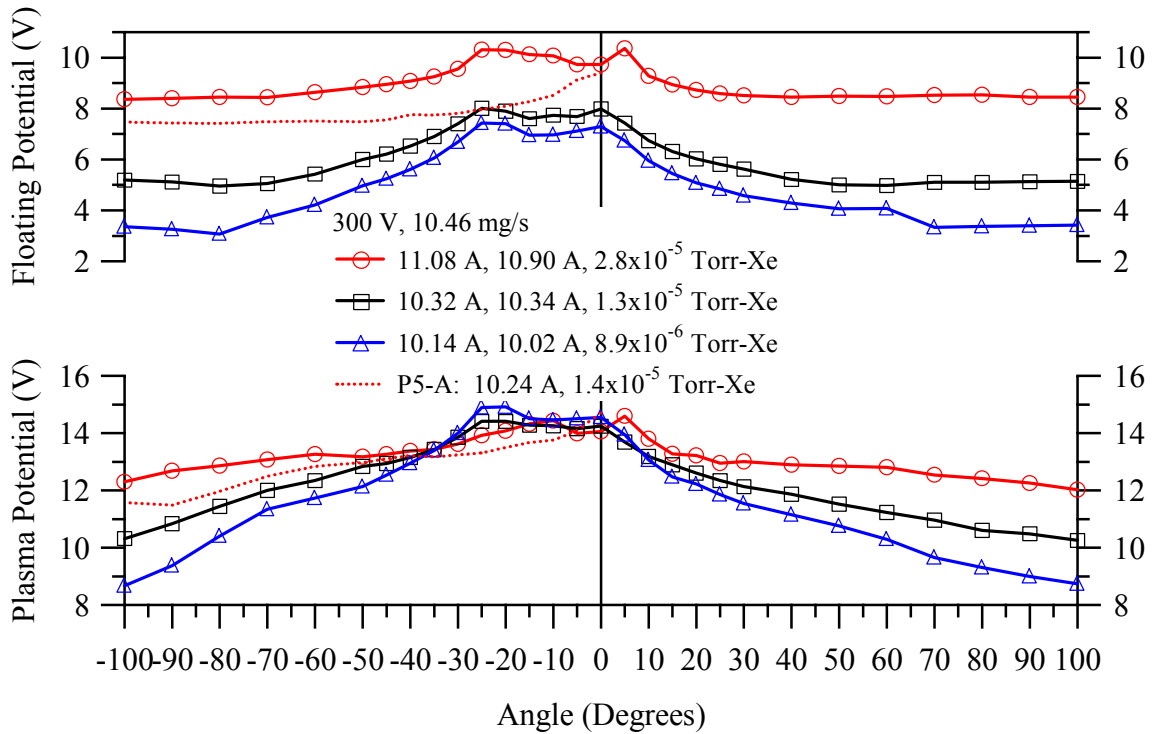


Figure 5-8: Traces of floating potential and plasma potential as a function of angle in Configuration 1. The cluster operating condition is 300 V, 10.46 mg/s at 3 backpressures.

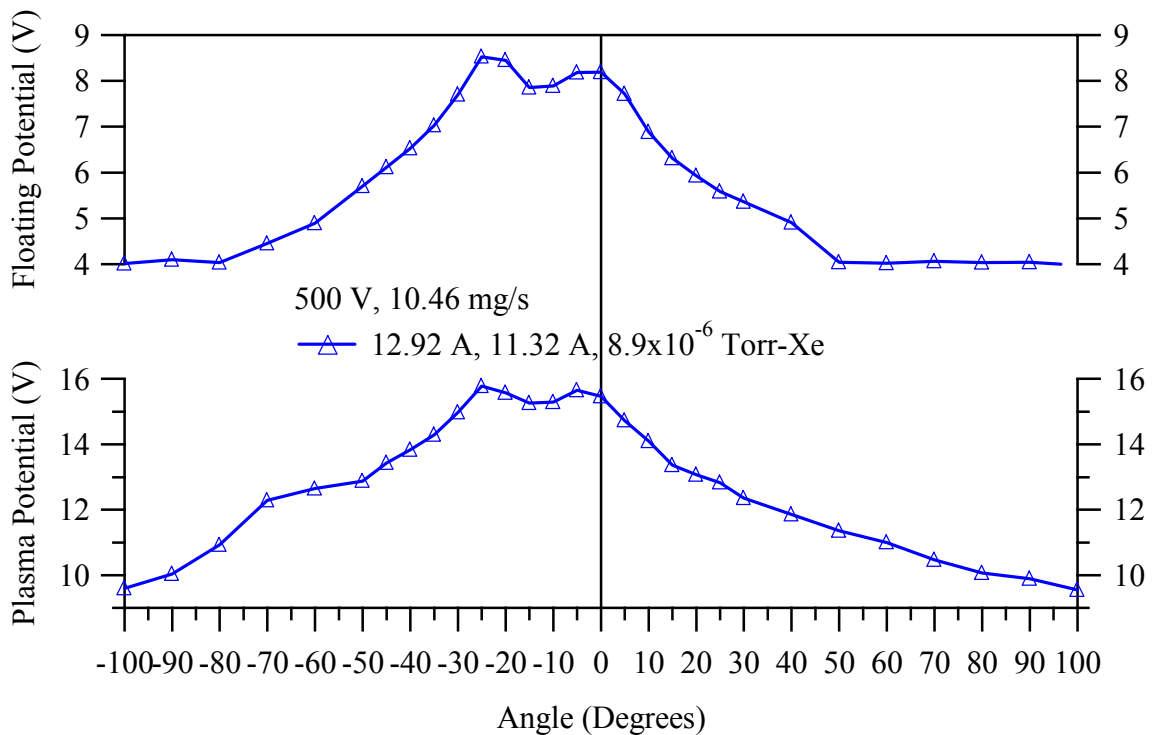


Figure 5-9: Traces of the floating potential and plasma potential as a function of angle in Configuration 1. The cluster operating condition is 500 V, 10.46 mg/s at a backpressure of 8.9×10^{-6} Torr-Xe.

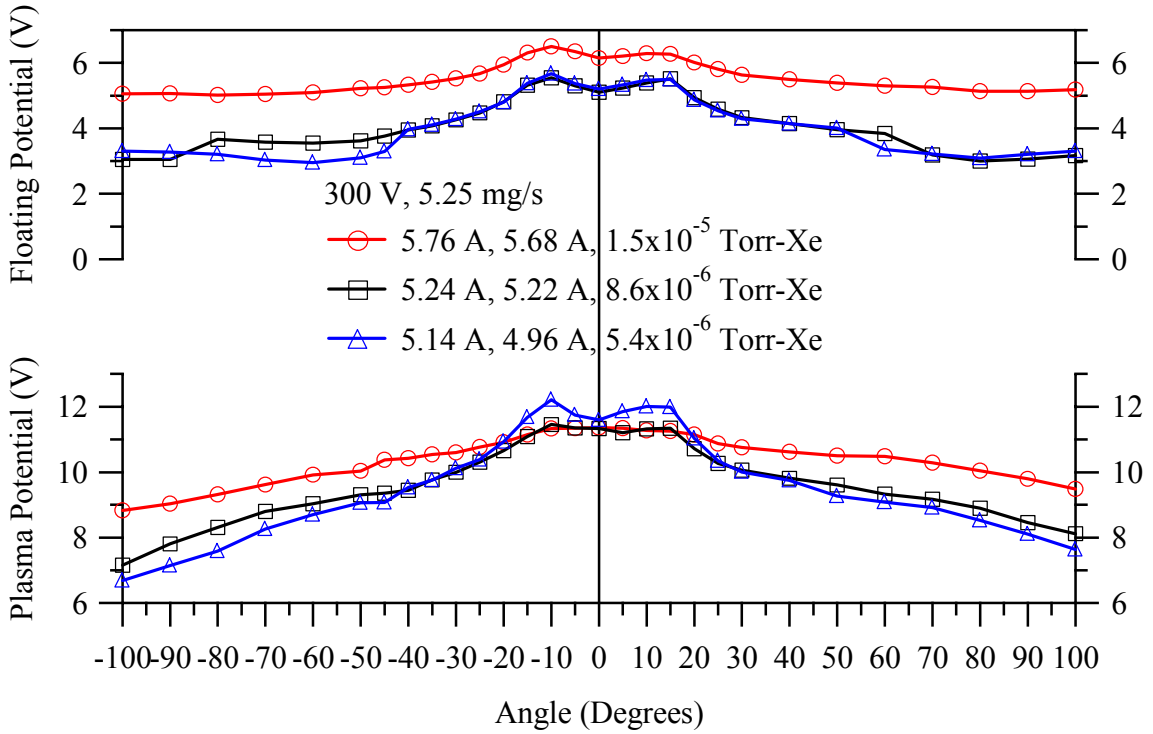


Figure 5-10: Traces of the floating potential and plasma potential as a function of angle in Configuration 2. The cluster operating condition is 300 V, 10.46 mg/s at 3 backpressures.

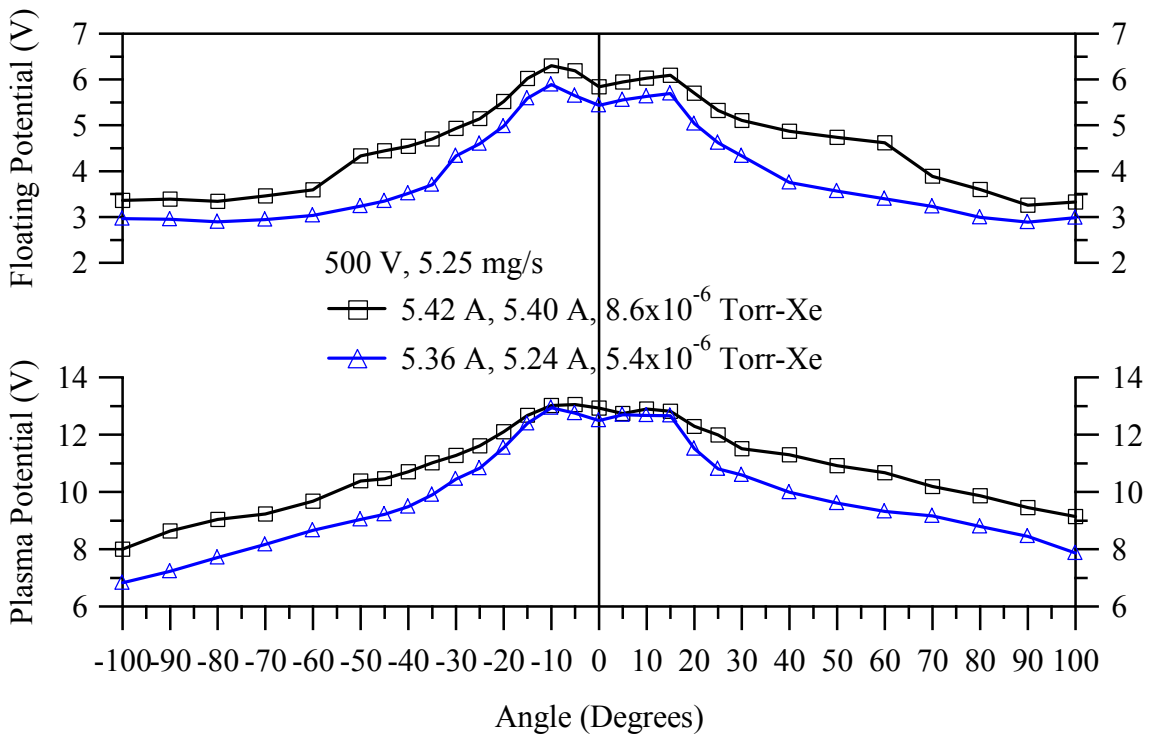


Figure 5-11: Traces of the floating potential and plasma potential as a function of angle in Configuration 2. The cluster operating condition is 500 V, 5.25 mg/s at 2 backpressures.

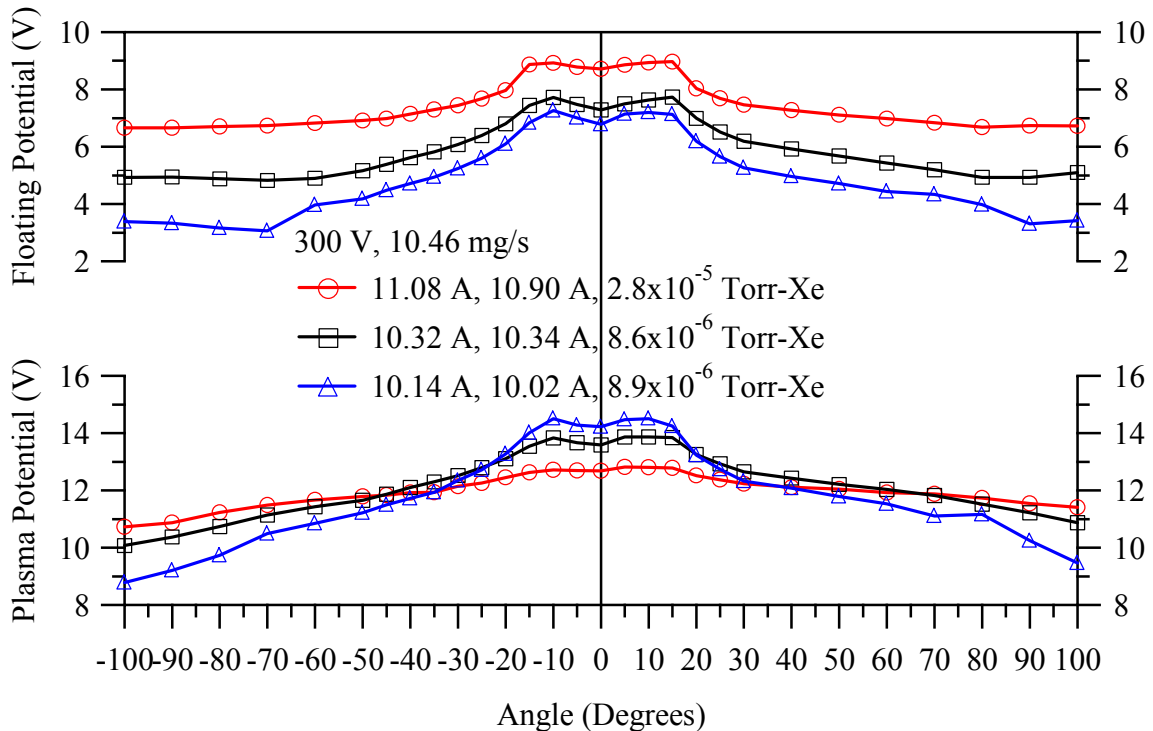


Figure 5-12: Traces of the floating potential and plasma potential as a function of angle in Configuration 2. The cluster operating condition is 300 V, 10.46 mg/s at 3 backpressures.

5.1.3 Electron Number Density and Electron Temperature

The electron number density and electron temperature of the P5 Hall thruster cluster is measured with a Langmuir probe from -100° to $+100^\circ$ on the one-meter arc shown in Figures 5-1 and 5-2. The measurement step size is 5° from thruster centerline to an angle of 50° . For angles greater than 50° the measurement step size is 10° . After each measurement, the Langmuir probe is moved back to thruster centerline for 30 seconds so that collisions with the 200+ eV ions can clean the probe. Figures 5-13 through 5-16 present traces of the electron number density and electron temperature measured in Configuration 1 at each operating condition and pumping speed. Figures 5-17 through 5-19 present traces of the electron number density and electron temperature measured in Configuration 2 at each operating condition and pumping speed. Several of

the figures that present the Configuration 1 data include a trace of the P5-A collected at a nominal pumping speed of 70 kl/s. These data are included for nearly equal-backpressure comparison with the cluster data collected at a nominal pumping speed of 140 kl/s.

Figures 5-13 through 5-16 present the results of Configuration 1. The electron number density and electron temperature traces show a peak on centerline that corresponds to the centerline of the plume of P5-A. In addition, there is a second peak between -25° and -15° that corresponds to the centerline of P5-B. The distinct peaks located at the angular positions of the individual thrusters verify that the plumes remain separate as they expand into the vacuum facility. The peaks also show that plume interaction does not attract or deflect the adjacent plume.

The monolithic P5-A trace added to Figure 5-15 shows that the electron number density of the plume is nearly identical to the electron number densities measured in the P5-A plume operating in the cluster configuration, within in the 50% error of the measurement. Monolithic P5-A electron temperature traces show similar agreement with the P5-A cluster measurements.

The electron number density traces measured in Configuration 1 show that on centerline, the number density increases with increasing backpressure. The same trend is apparent at the angular location corresponding to the P5-B. As the angle from thruster centerline increases, the electron number density at each backpressure decreases and apparently converges to a single background value. This is the same behavior shown in Chapter 4 for the monolithic thruster investigation.

The electron temperature traces measured in Configuration 1 show little change in magnitude as the angle from thruster centerline increases. Only the 500 V operating

conditions presented in Figures 5-14 and 5-16 show distinct peaks in the electron temperature that correspond to the centerline of the monolithic thrusters. This is because the higher discharge voltage creates higher electron energies that migrate downstream. However, the electron temperature decreases with increasing facility backpressure. Measurements of the electron energy distribution function are needed to understand how the background particles decrease the electron temperature.

Figures 5-17 through 5-19 present the results of configuration 2. The electron number density measurements in Configuration 2 show distinct peaks at angles of $\pm 10^\circ$. These peaks correspond to the centerlines of the monolithic thrusters. Once again, on centerline the electron number density increases with increasing backpressure. As the angle from thruster centerline increases, the electron number density appears to converge to a single value for all facility backpressures. As the angle from centerline increases, the present density will approach zero, which explains the decay in the electron number density with increasing angle from centerline.

Figures 5-13 and 5-14 show an approximately 50% increase in the electron number density from the centerline of the monolithic P5-A to the centerline of the P5-A operating in the cluster configuration. The radial configuration used to measure the electron number density does not allow the straightforward creation of a prediction method for the electron number density of a cluster. Previously, Beal has shown that the electron number density in a cluster is equal to the sum of the contribution of the individual thrusters.⁵⁰

Configuration 2 shows that the electron temperature is nearly constant with angle. Furthermore, peaks in the electron temperature are only distinguishable at the 500

V operating conditions. As discussed previously, the electron temperature appears to depend strongly on the discharge voltage and weakly on the backpressure. Comparison with the monolithic thruster measurements shows that the electron temperature is not affected by the adjacent thruster.

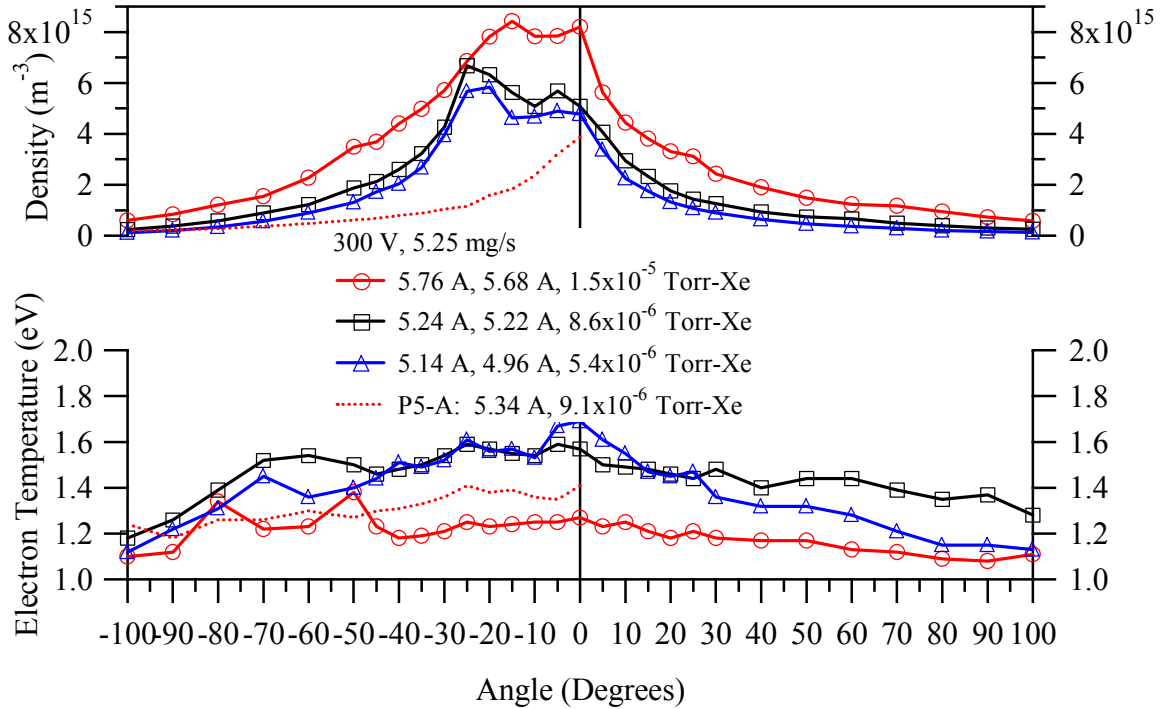


Figure 5-13: Traces of the electron number density and temperature as a function of angle in Configuration 1. The cluster operating condition is 300 V, 5.25 mg/s at 3 backpressures.

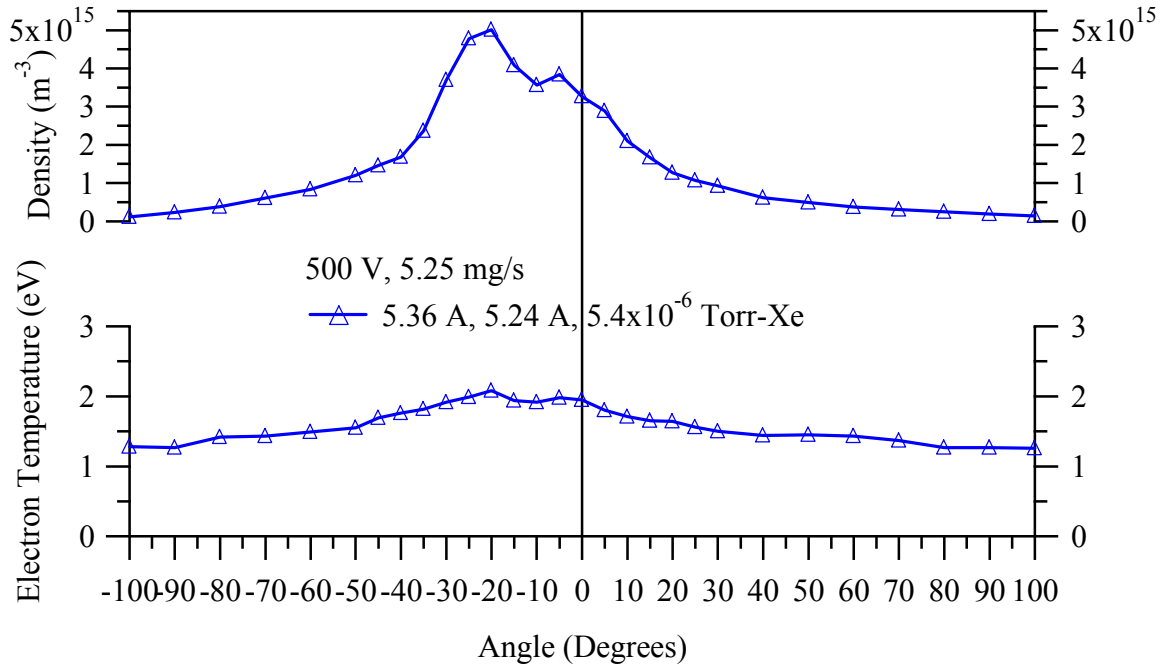


Figure 5-14: Traces of the electron number density and temperature as a function of angle in Configuration 1. The cluster operating condition is 500 V, 5.25 mg/s at 5.4×10^{-6} Torr-Xe.

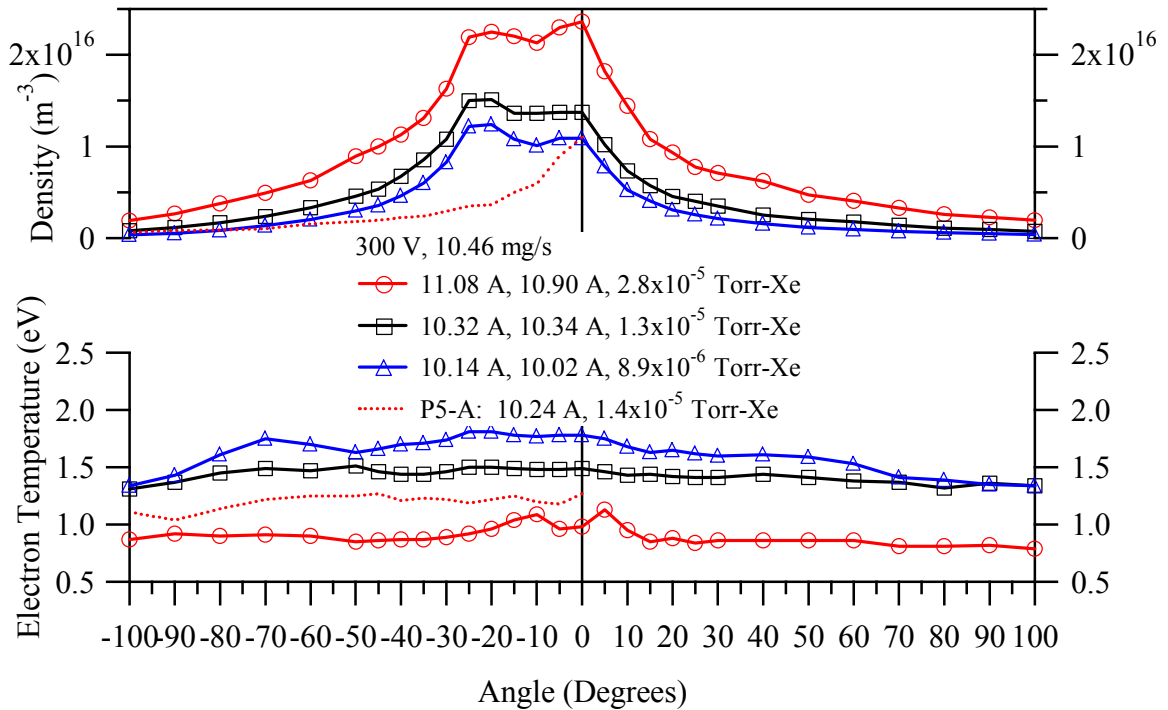


Figure 5-15: Traces of the electron number density and temperature as a function of angle in Configuration 1. The cluster operating condition is 300 V, 10.46 mg/s at 5.4×10^{-6} Torr-Xe.

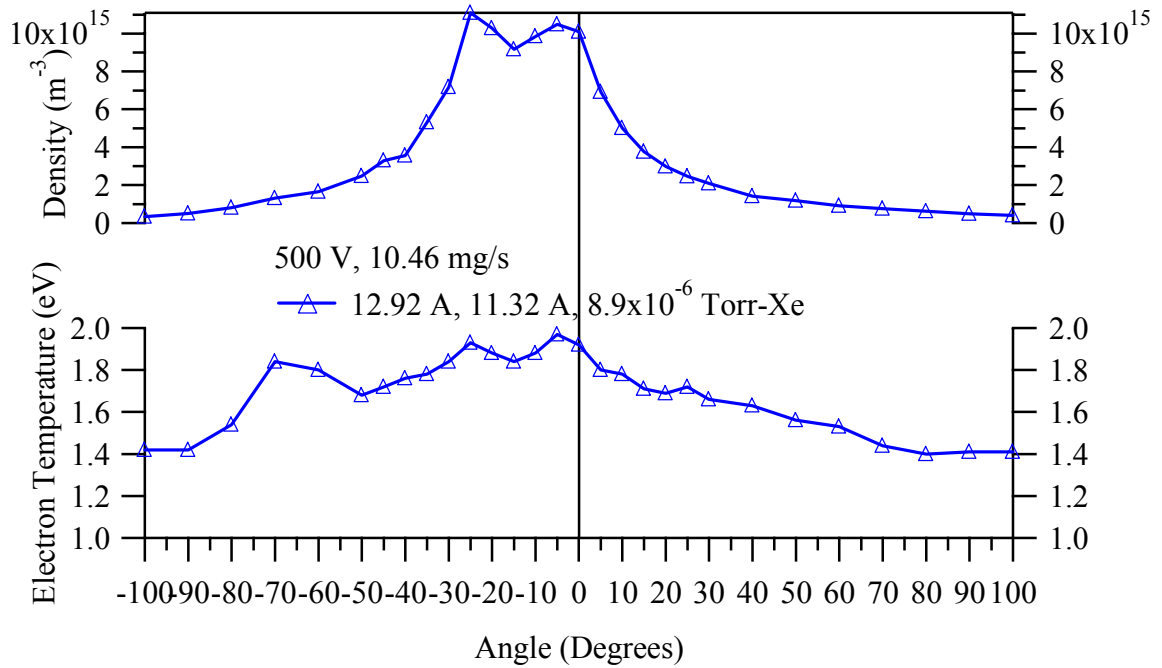


Figure 5-16: Traces of the electron number density and temperature as a function of angle in Configuration 1. The cluster operating condition is 500 V, 10.46 mg/s at 8.9×10^{-6} Torr-Xe.

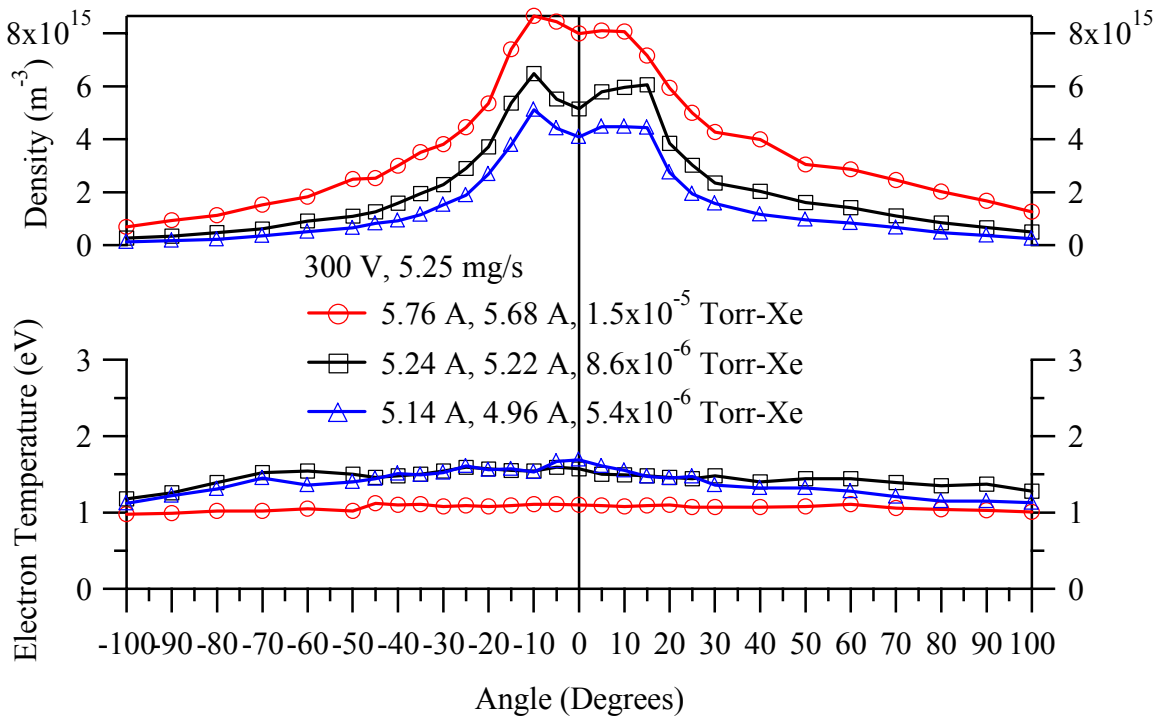


Figure 5-17: Traces of the electron number density and temperature as a function of angle in Configuration 2. The cluster operating condition is 300 V, 5.25 mg/s at 3 operating pressures.

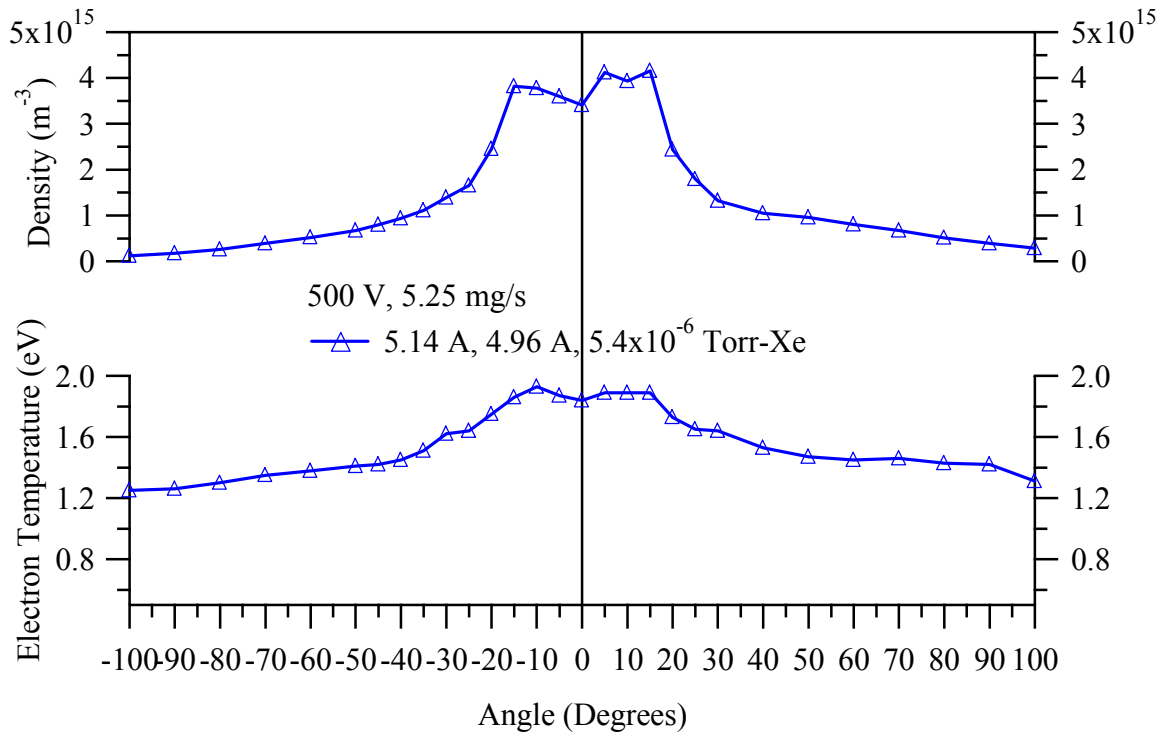


Figure 5-18: Traces of the electron number density and temperature as a function of angle in Configuration 2. The cluster operating condition is 500 V, 5.25 mg/s at 5.4×10^{-6} Torr-Xe.

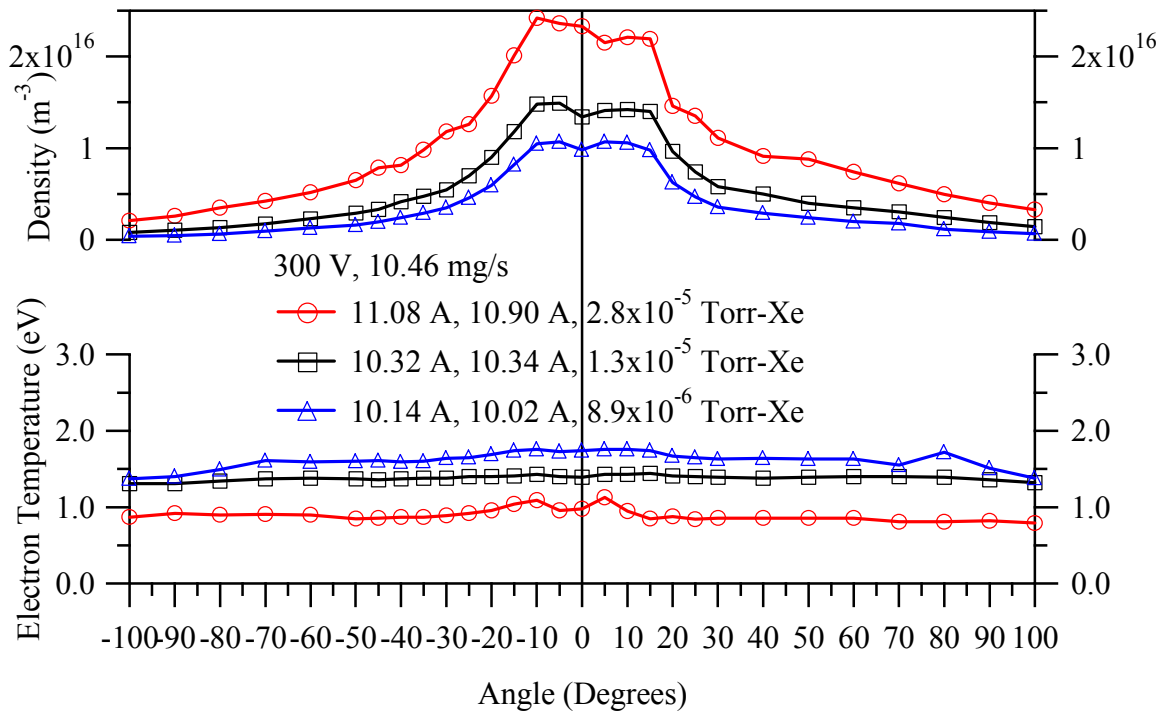


Figure 5-19: Traces of the electron number density and temperature as a function of angle in Configuration 2. The cluster operating condition is 300 V, 10.46 mg/s at 3 operating pressures.

5.1.4 Ion Current Density

Faraday Probes A through E are located one meter from the exit plane of the P5-A or the cluster as shown in Figures 5-1 and 5-2. The effect of facility background pressure is evaluated by varying the backpressures from 3.2×10^{-6} Torr-Xe to 1.4×10^{-5} Torr-Xe. The goals of this study are to investigate the effect of the adjacent thruster element on the ion current density in the plume of the thruster, to measure the shape of the ion current density trace downstream of the cluster, and to further evaluate the effect of facility backpressure on the ion current density. Figures 5-20 through 5-27 present the ion current density traces measured in the cluster plume for Configurations 1 and 2.

The ion current density is measured in Configurations 1 and 2. Because the plume of the cluster is not axially symmetric, it is not possible to calculate the integrated ion beam current or the plume divergence half-angle with data collected in this arrangement. Instead, the measured ion current density traces are qualitative measures of the shape of the cluster plume. The ion current density profiles also provide insight into the attraction or deflection of the ions in the adjacent plume. Configuration 1 allows investigation of the effect of the adjacent Hall thruster on the plume of P5-A. As is shown for the cluster electron number density measurements, Configurations 1 and 2 do not allow the creation of a method to predict the ion current density.

Figure 5-20 shows traces of the ion current density measured with all 5 Faraday probes at the lowest cluster facility backpressure of 8.9×10^{-6} Torr-Xe. Each probe measures a different value for the ion current density, even though it is immersed in the same plasma. The difference between the probes becomes more apparent as the angle from centerline increases and the plume contains a greater percentage of CEX ions. The facility backpressure study in Chapter 4 shows that Probe B does the best job of

measuring the ion current density at all facility backpressures. However, when measuring the plume of the cluster in Configuration 1, the small acceptance angle of the magnetic filter prevents the beam ions emanating from P5-B from reaching the collector. Thus, to measure the true shape of the ion current density profile of the cluster configuration the nude Probe A is used.

Figure 5-21 shows the ion current density profiles measured with all 5 Faraday probes in Configuration 2. With the axis of rotation centered on the cluster, the shape of the current density profiles is nearly identical for each Faraday probe. The traces differ in magnitude because each probe filters a different percentage of the CEX ions away from the probe collector. Thus, Probe A is used to measure the ion current density profiles of the cluster at all operation conditions.

Figures 5-22 through 5-24 present the ion current density traces of the cluster plume in Configuration 1 measured at the 140 kl/s nominal pumping speed. Traces of the monolithic ion current density are included in each of the figures measured at the identical discharge and flow rate, but at a nominal pumping speed of 70 kl/s so that a constant-pressure comparison can be made. The results show that within the error of the thruster alignment and the repeatability of the ion beam current, the P5-A monolithic thruster traces for angles of 0° to 100° are nearly identical to the cluster traces for all operating conditions. Several of the traces even duplicate the asymmetry of the P5-A ion current density profiles. The results show that the ion current density profile on the side of the monolithic thruster farthest from the adjacent thruster is not affected by the adjacent thruster. For the side of the monolithic thruster plume that touches the adjacent thruster, there appears to be no change in the ion current density profile out to

approximately 10° . It is possible that between the thrusters, the ion current density is the linear superposition of the individual plumes.

Figures 5-25 through 5-27 present traces of the ion current density profile of the cluster measured by Probe A in Configuration 2 at all the operating conditions for 3 backpressures. The results show that at the 5.25 mg/s anode flow rate, there is almost no difference in the magnitude of the ion current density on centerline. However, at large angles, the ion current density differences increase with increasing backpressure because of the increased fraction of CEX ions. For the 10.46 mg/s flow rate presented in Figure 5-26, there is a small increase in ion current density with increasing backpressure in the wings of the plume and near the cluster centerline. The increased ion current density on cluster centerline is the same trend shown by the monolithic 10.46 mg/s anode flow current density. The increase in the ion current density in the wings of the plume with increasing backpressure is caused by the increasing number of CEX ions due to increasing facility backpressure.

The ion current density traces measured in Configurations 1 and 2 display peaks at the angular locations corresponding to the individual thrusters. In addition, the monolithic thruster current density traces imposed on the Configuration 1 traces show excellent agreement with the P5-A operating in cluster Configuration 1. Because the peaks of the ion current density profiles do not move when operating in the cluster configuration, the beam ions of the monolithic thruster are not measurably deflected by the adjacent Hall thruster.

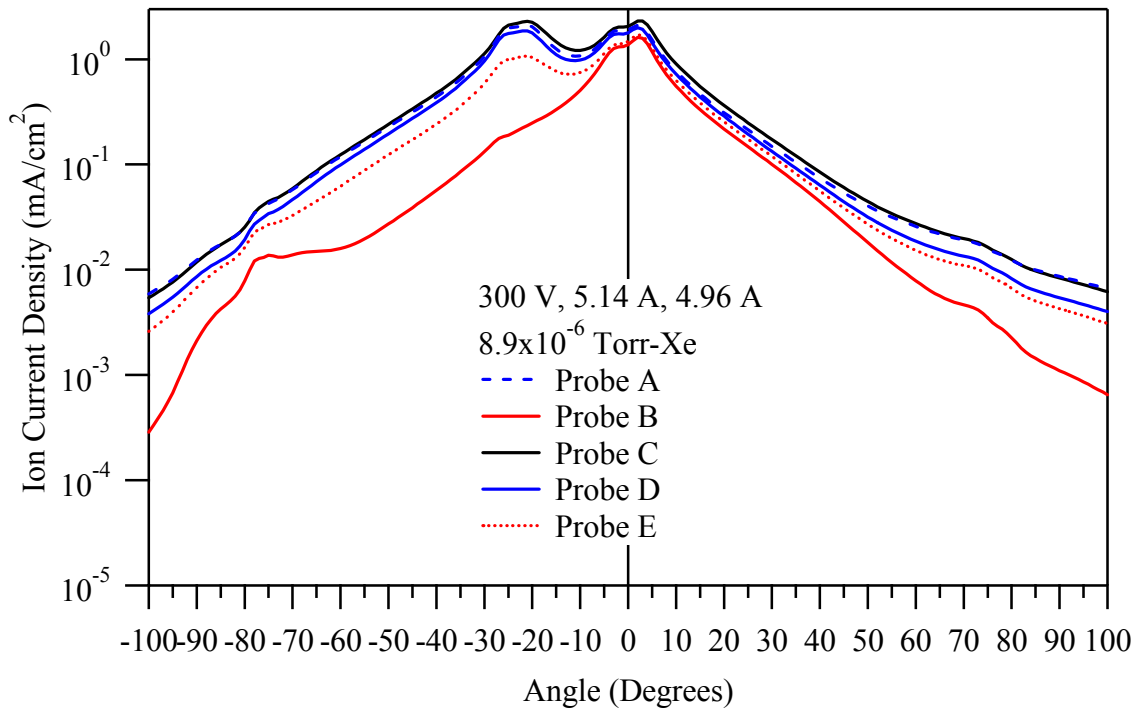


Figure 5-20: The cluster ion current density as a function of angle in Configuration 1. The cluster operating condition is 300 V, 5.25 mg/s at a backpressure of 8.9×10^{-6} Torr-Xe.

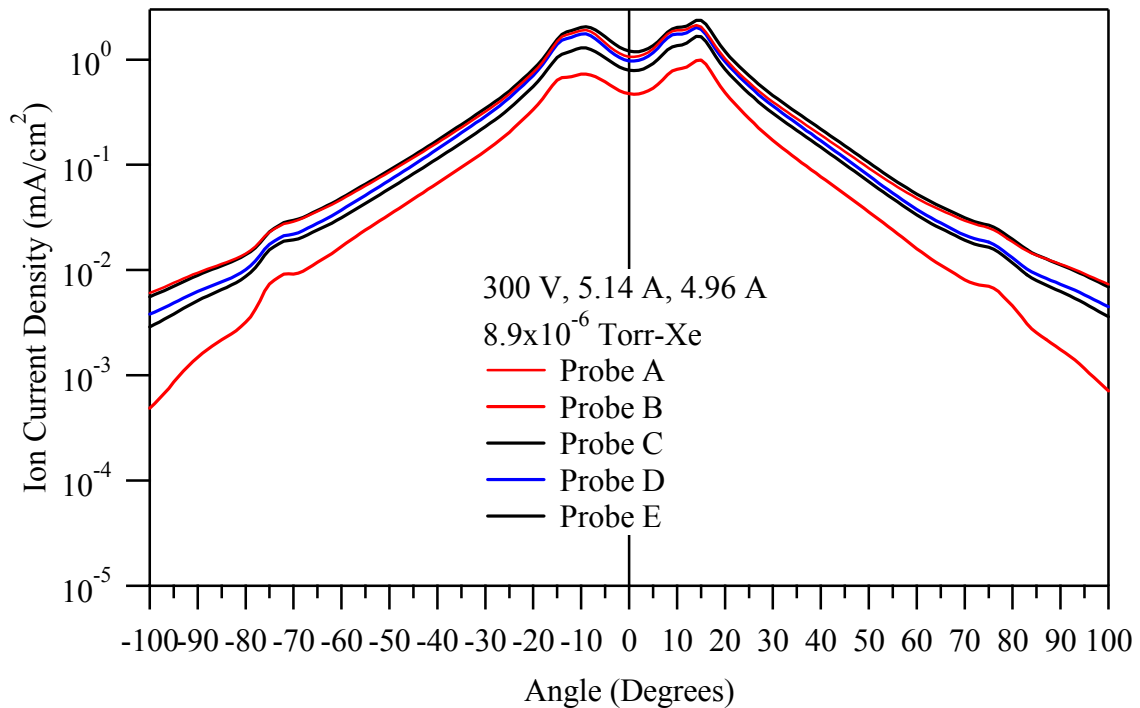


Figure 5-21: The cluster ion current density as a function of angle in Configuration 2. The cluster operating condition is 300 V, 5.14 A at a backpressure of 8.9×10^{-6} Torr-Xe.

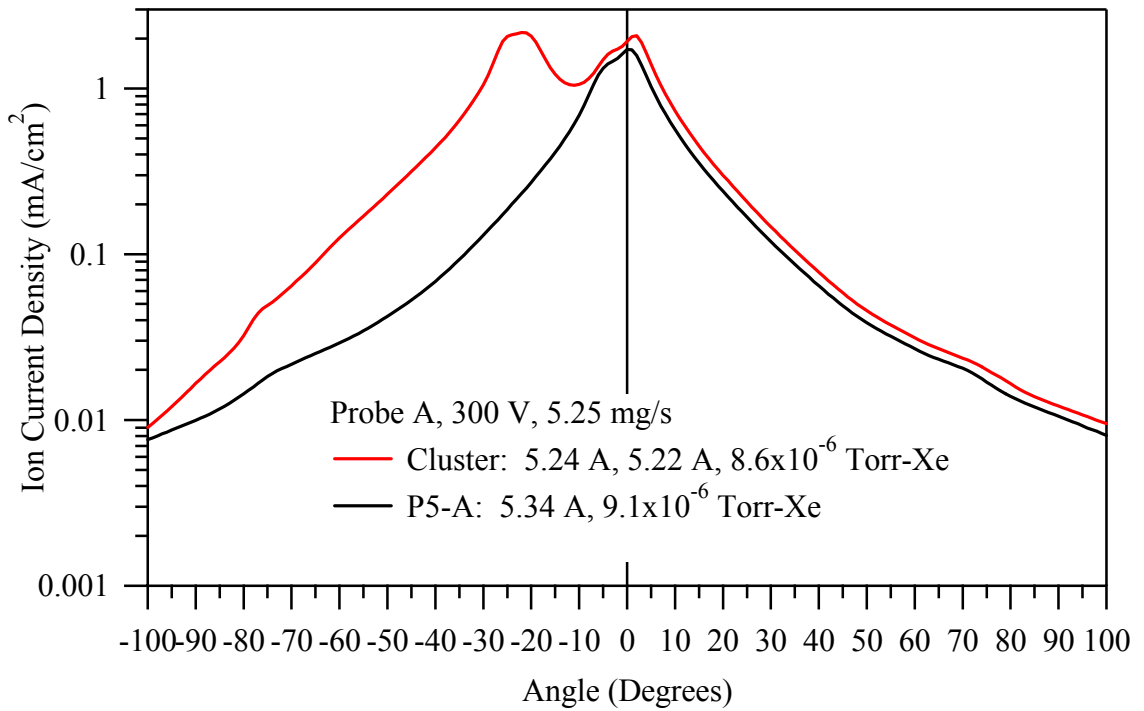


Figure 5-22: The cluster ion current density as a function of angle in Configuration 1. The monolithic thruster and cluster operating condition is 300 V, 5.25 mg/s.

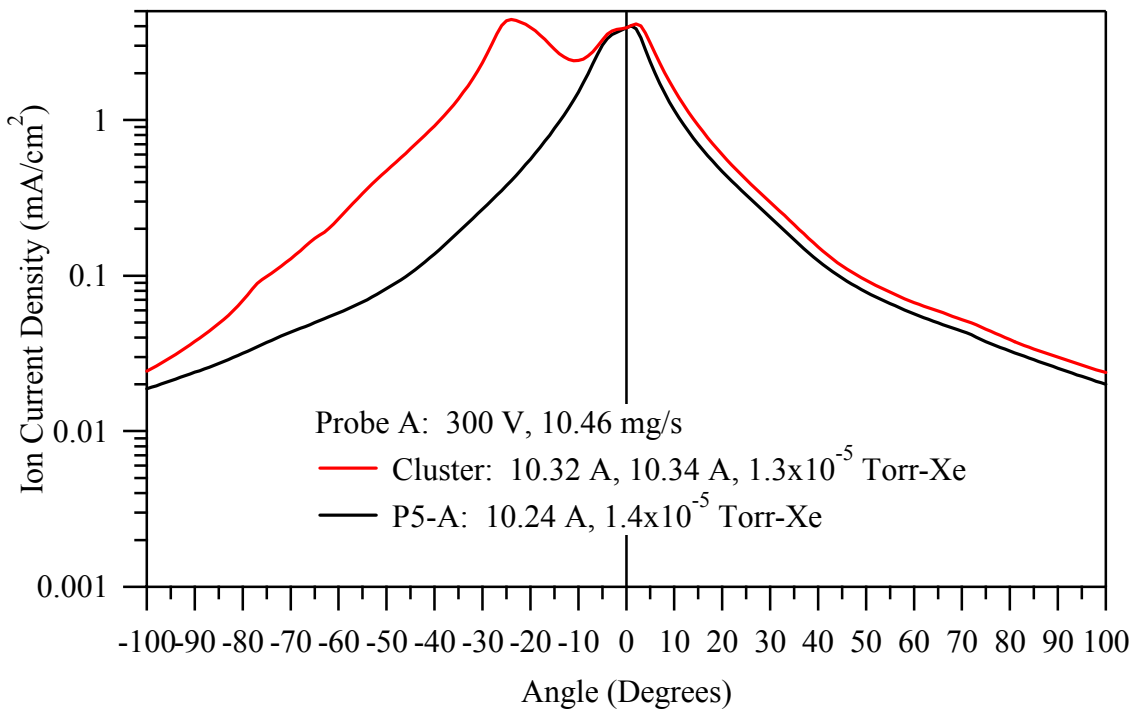


Figure 5-23: The cluster ion current density as a function of angle in Configuration 1. The cluster and monolithic thruster operating condition is 300 V, 10.46 mg/s.

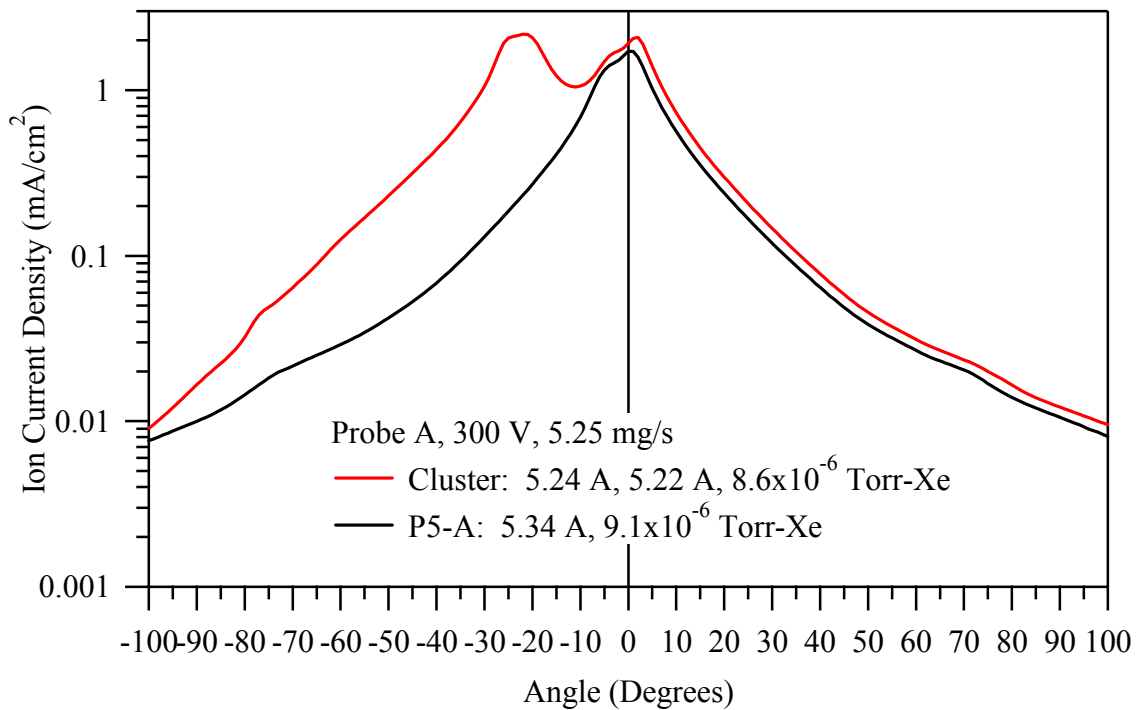


Figure 5-24: The cluster ion current density as a function of angle in Configuration 1. The cluster and monolithic thruster operating condition is 500 V, 5.25 mg/s.

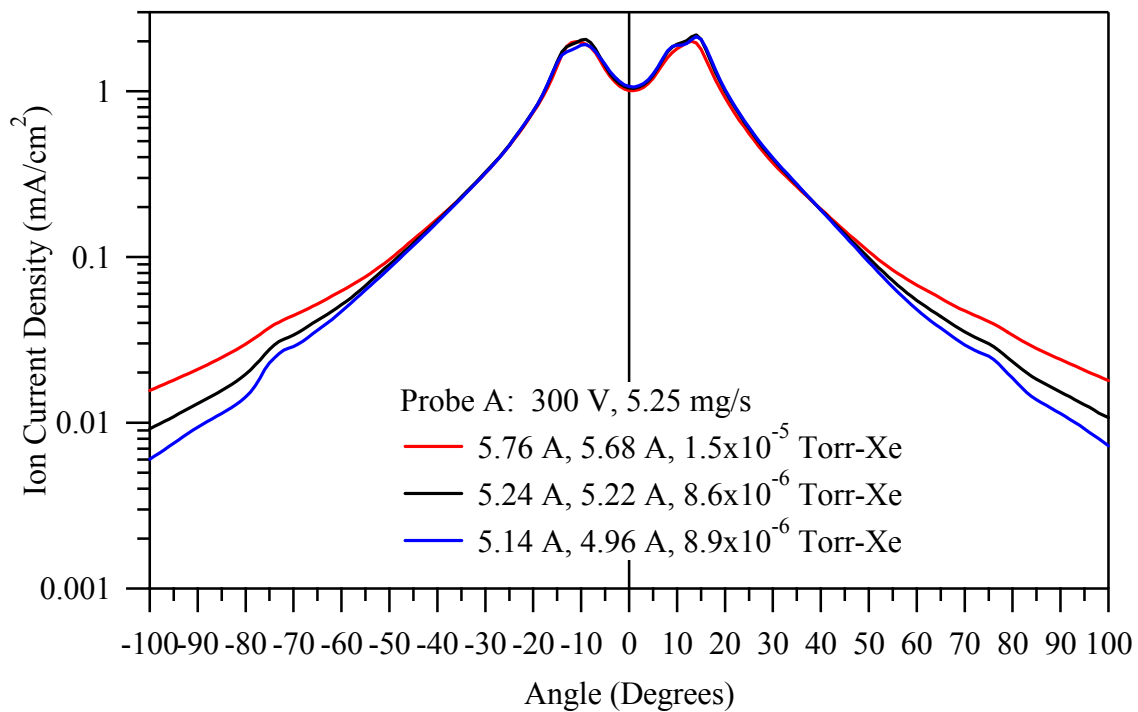


Figure 5-25: The cluster ion current density as a function of angle in Configuration 2. The cluster operating condition is 300 V, 5.25 mg/s at 3 backpressures.

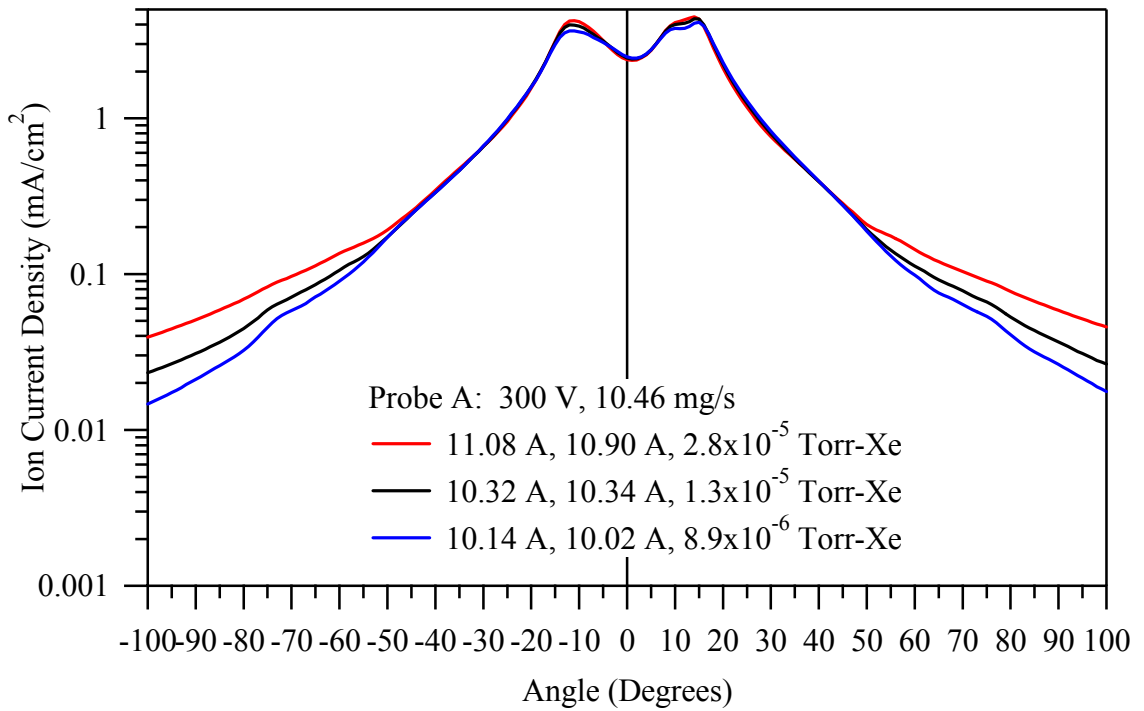


Figure 5-26: The cluster ion current density as a function of angle in Configuration 2. The cluster operating condition is 300 V, 10.46 mg/s at 3 backpressures.

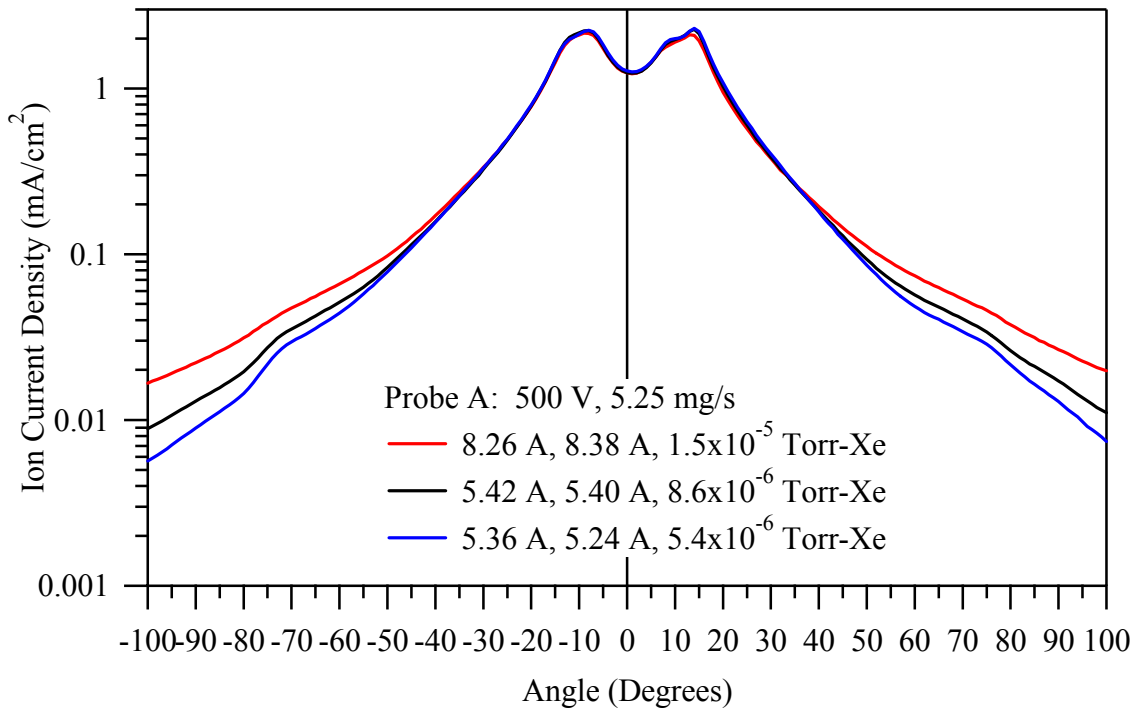


Figure 5-27: The cluster ion current density as a function of angle in Configuration 2. The cluster operating condition is 500 V, 5.25 mg/s at 3 backpressures.

5.1.5 Ion Energy Spectra

In the cluster configuration, the plasma density inside the ESA at 1 and 1.5 m downstream of the thruster exit planes is too high to collect usable ion energy per charge distributions. The plasma density at the ESA entrance is too high, and the high plasma density inside the ESA provides a large number of electrons for the positively-biased deflection plates to collect. Thus, the sourcemeter used to bias the plates reaches the current compliance limit before the ion energy distribution is fully characterized. This plasma density limitation is discussed in more detail in Chapter 4.

The RPA measures the ion energy distribution per charge in the plume of the cluster. Due to the physical limitations of the positioning tables, measurements of the ion energy per charge distributions are only collected for Configuration 2. The ion energy distributions of the clusters are measured from -90° to $+90^\circ$ on the one-meter arc shown in Figure 5-2. The measurements are made in 5° increments from thruster centerline to 50° . For angles greater than 50° , the measurements are made in 10° steps. For the RPA measurements, the cluster is rotated and the RPA remains stationary.

Because the RPA is not aligned on one of the point ion sources of the cluster, the results measure only the ion energy distribution of ions that have trajectories several degrees off the thruster centerline. Thus, the results are only qualitative in nature, and comparisons with the monolith thruster are difficult to make. The cylindrical RPA has an acceptance cone half-angle of approximately 25° . Therefore, the viewing angle of the RPA is wide enough to collect ions originating from both thrusters at the angular position of 0° .

The cluster spacing is 40 cm between the centerlines. Thus, the centerlines of the monolithic thruster are located 11.3° off the RPA centerline. Because the RPA has a

wide acceptance angle, ions entering the RPA need not have trajectories parallel to its centerline. However, nothing stops them from having parallel trajectories, and the grid transmission is much higher that way. Only the axial component of the velocity is measured by the diagnostic. The inlet angle of the ions in Configuration 2 never exceeds 11.3° , and the resulting error cosine is less than 3%. The ion energy distribution per unit charge varies with cluster rotation angle. At 0° , the distribution receives contributions from P5-A and P5B. At an angle of 11.3° , the distribution is dominated by the plume of P5-B because the plume of P5-A is approximately 22° off the centerline of the RPA.

Figures 5-28 through 5-30 present the ion energy per charge distributions for cluster operation at 300 V with an anode flow rate of 10.46 mg/s. Figures 5-31 and 5-32 present ion energy per charge distributions on the centerline of the cluster for two facility backpressures.

Figure 5-28 shows that the ion energy distribution peaks increase from 274 V at 0° to a maximum of 284 V at approximately 10° , which corresponds to the alignment of the single monolithic thruster with the RPA centerline. For angles greater than 10° , the peak of the ion energy distribution decreases continually to a minimum of 228 V at approximately 45° . For angles greater than 45° , the ion energy distribution shows that an increasing percentage of the plume is dominated by CEX ions. At 90° from cluster centerline, the CEX population is dominant, with the ion energy per charge distribution peaking at approximately 29 V. Notice that for angles of 80° and 90° the traces are much smoother than those for angles of less than 80° . This suggests that discharge current oscillations cause the noise, since CEX ions should be less sensitive to discharge current.

These measurements do not show the multiple peak structure observed by Beal.⁵⁰ Clearly, collision processes occur, since the CEX ions are detected at large angles off the cluster centerline. The elevated backpressure due to cluster operation may prevent the RPA from detecting the results of other types of collision.

Figures 5-31 and 5-32 present the ion energy distribution per charge on the cluster centerline for operating conditions of 500 V, 5.25 mg/s and 300 V, 10.46 mg/s at two different backpressures. The peaks of the distributions agree well with the earlier discussion. There is no noticeable change in the location of the ion energy distribution peak for changes in the facility operating pressure.

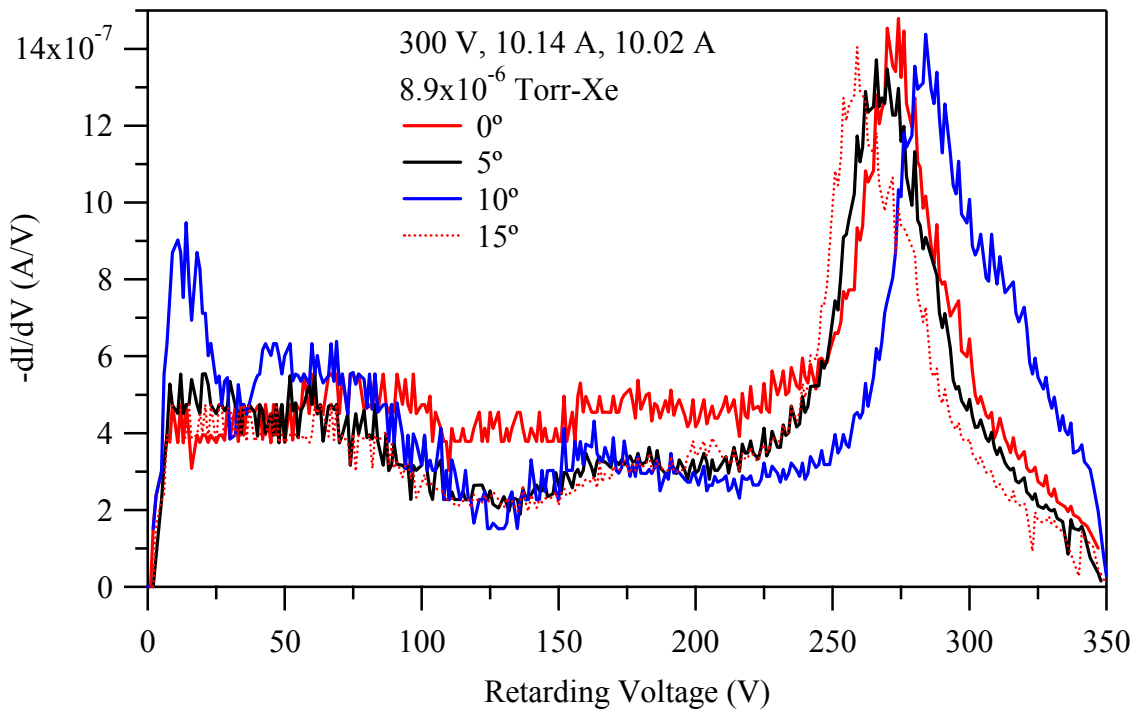


Figure 5-28: RPA traces of the cluster in Configuration 2 for backpressures of 8.9×10^{-6} Torr-Xe with the cluster elements operating at 300 V, 10.46 mg/s. (0° to 15°)

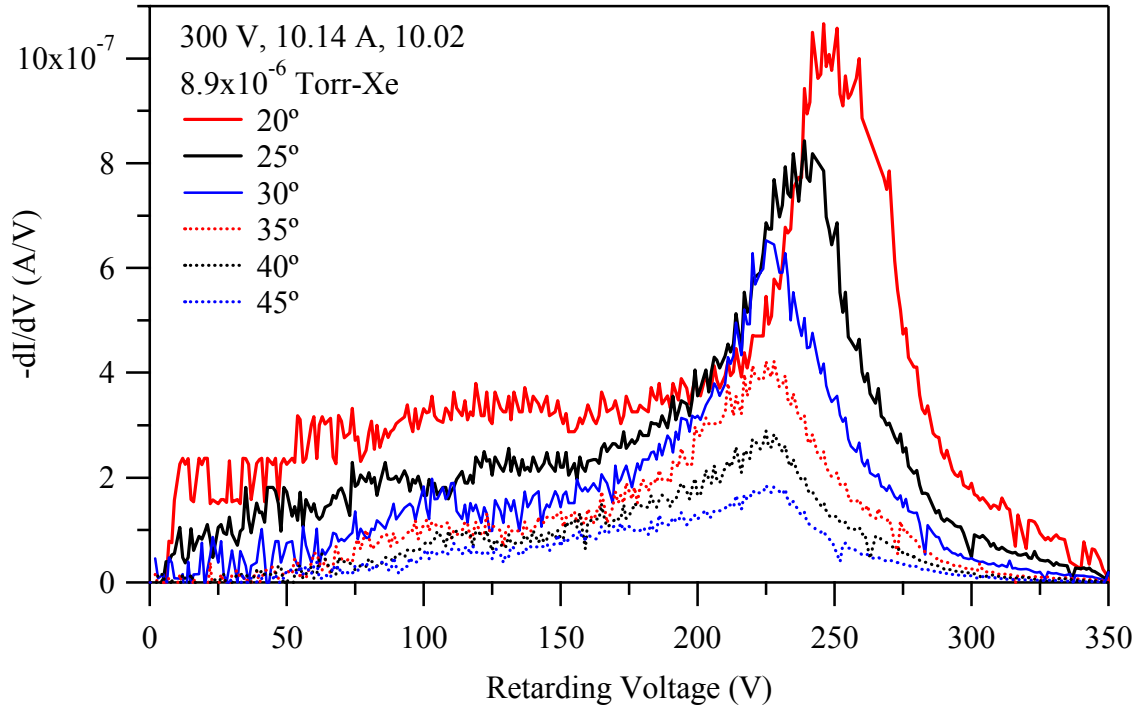


Figure 5-29: RPA traces of the cluster in Configuration 2 for backpressures of 8.9×10^{-6} Torr-Xe with the cluster elements operating at 300 V, 10.46 mg/s. (20° to 45°)

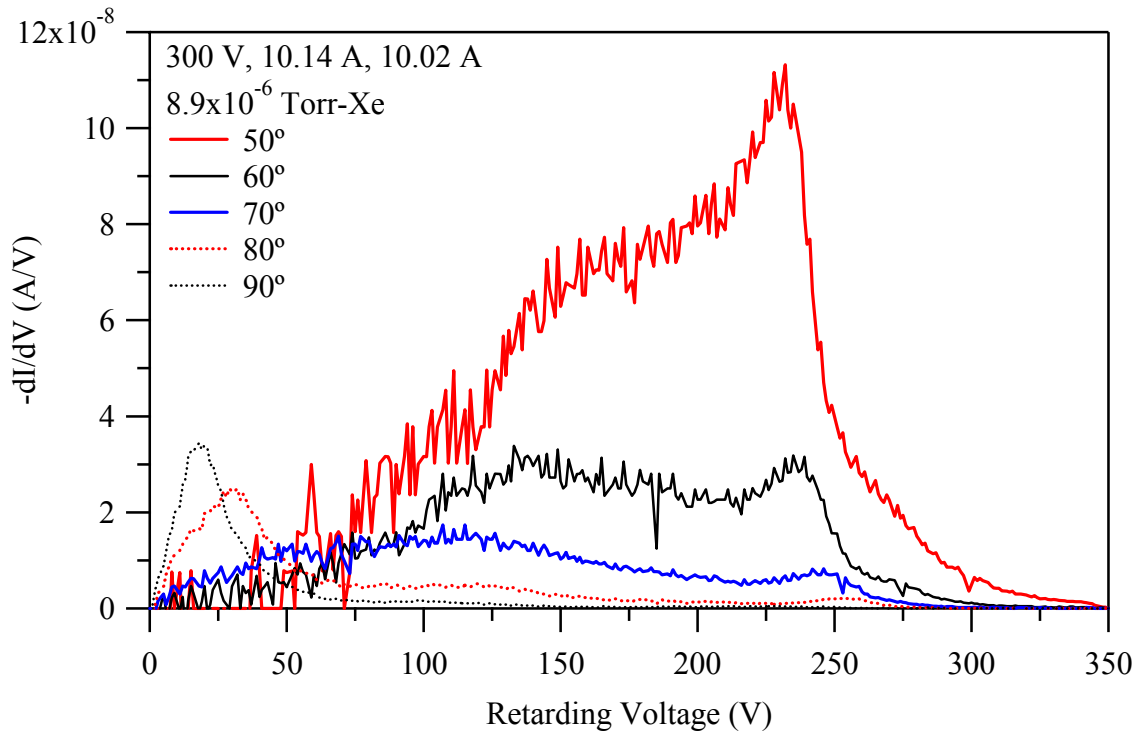


Figure 5-30: RPA traces of the cluster in Configuration 2 for backpressures of 8.9×10^{-6} Torr-Xe with the cluster elements operating at 300 V, 10.46 mg/s. (50° to 90°)

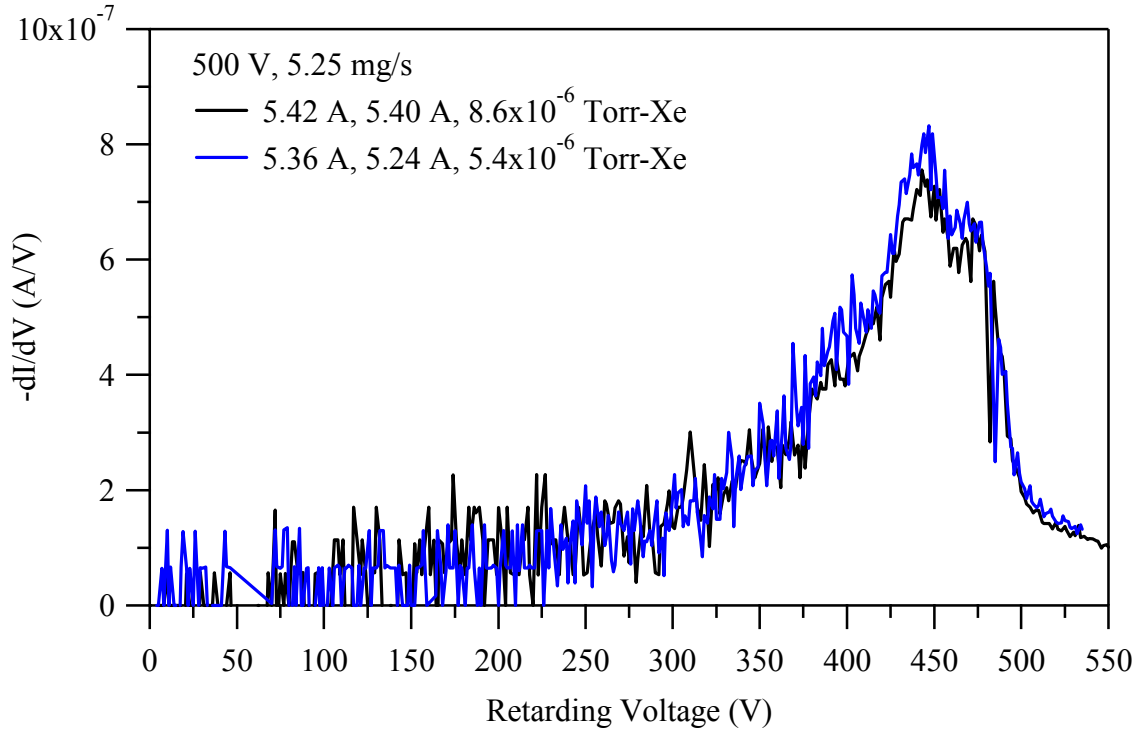


Figure 5-31: RPA traces of the cluster in Configuration 2 for backpressures of 8.6×10^{-6} Torr-Xe and 5.4×10^{-6} Torr-Xe with the cluster elements operating at 500 V, 5.25 mg/s.

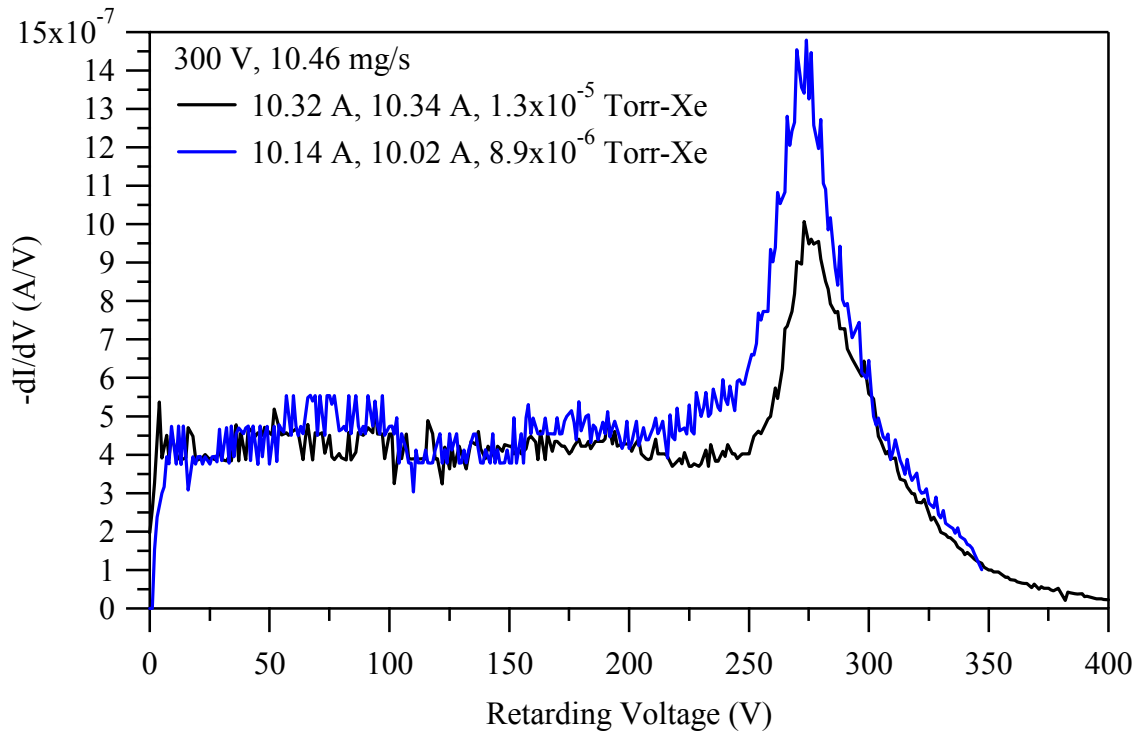


Figure 5-32: RPA traces of the cluster in Configuration 2 for backpressures of 1.3×10^{-5} Torr-Xe and 8.9×10^{-6} Torr-Xe with the cluster elements operating at 300 V, 10.46 mg/s.

5.1.6 Ion Species Fractions

The ExB probe is used to measure the ion species fractions in the cluster plume. Due to the physical limitations of the positioning tables, measurements of the ion species fractions are only collected for Configuration 2. The ion species fractions of the cluster are measured from -90° to $+90^\circ$ on the one-meter arc shown in Figure 5-2. The measurement resolution is 5° from thruster centerline to an angle of 50° . For angles greater than 50° , the measurement resolution is 10° . By approximately 30° , the signal-to-noise ratio from the probe is too low to discern peaks from the traces. In the cluster configuration, the plasma density inside the ExB probe 1 m downstream of the thruster exit planes is too high to detect multiply-charged ions in the plume. The facility backpressure at the 70 kl/s condition is too high to collect any usable ExB probe traces. For the same reason, traces of the 500 V, 10.46 mg/s operating condition are not recorded at the 140 kl/s pumping speed.

Because the ExB probe is not aligned on one of the cluster element centerlines, the measured ion species fractions are based on the axial component of the IEDF entering the probe. As with the ion energy per charge distribution, quantitative comparison of the ExB traces cannot be made, but the relative values may shed light on cluster interaction. Figures 5-33 through 5-37 show traces of the ion species fraction measured over the range of angles and facility backpressures.

Figure 5-33 shows how the ExB traces change with angle from plume centerline. Because of the geometric configuration, the magnitude of the peak of the traces increases from 0° to a maximum at 10° that corresponds to the centerline of the P5-A thruster. As the angle from thruster centerline increases further, the magnitude of the peak continually decreases until peaks are no longer discernable at 40° off centerline.

Notice that for all angles, multiply-charged ions are not detected. This does not mean that they are not present, it only means that the ExB probe cannot detect them at this facility backpressure and probe alignment.

Figures 5-34 and 5-35 present ExB traces collected at 300 V at an anode flow rate of 5.25 mg/s for backpressures of 5.4×10^{-6} and 8.6×10^{-6} Torr-Xe, respectively. Figures 5-36 and 5-37 present ExB traces collected at 500 V at an anode flow rate of 5.25 mg/ for backpressures of 8.6×10^{-6} and 8.9×10^{-6} Torr-Xe, respectively. For both operating voltages, an increase in facility backpressure increases both the width and the magnitude of the portion of the traces that contain the singly-charged particle peak. The increase in the width on the peak is due to an increase in collisions with the facility background gas.

The traces show a structure similar to those of the monolithic thrusters. Beal observes similar results for the low-power cluster. The only difference between the monolithic P5 data and the P5 cluster data is that the singly-ionized particles from the cluster are detected at a lower probe voltage. This is because the ExB probe is aligned on the cluster centerline and not the centerline of one of the monolithic thrusters. Thus, only the axial component is measured by the diagnostic.

As noted in Chapter 2, the ExB probe is a velocity filter. It is unable to detect changes in the charge state that occur downstream of the cluster. The agreement between the shape of the monolithic thruster and cluster traces only verifies that clustering does not affect the ionization and acceleration processes of the individual thrusters.

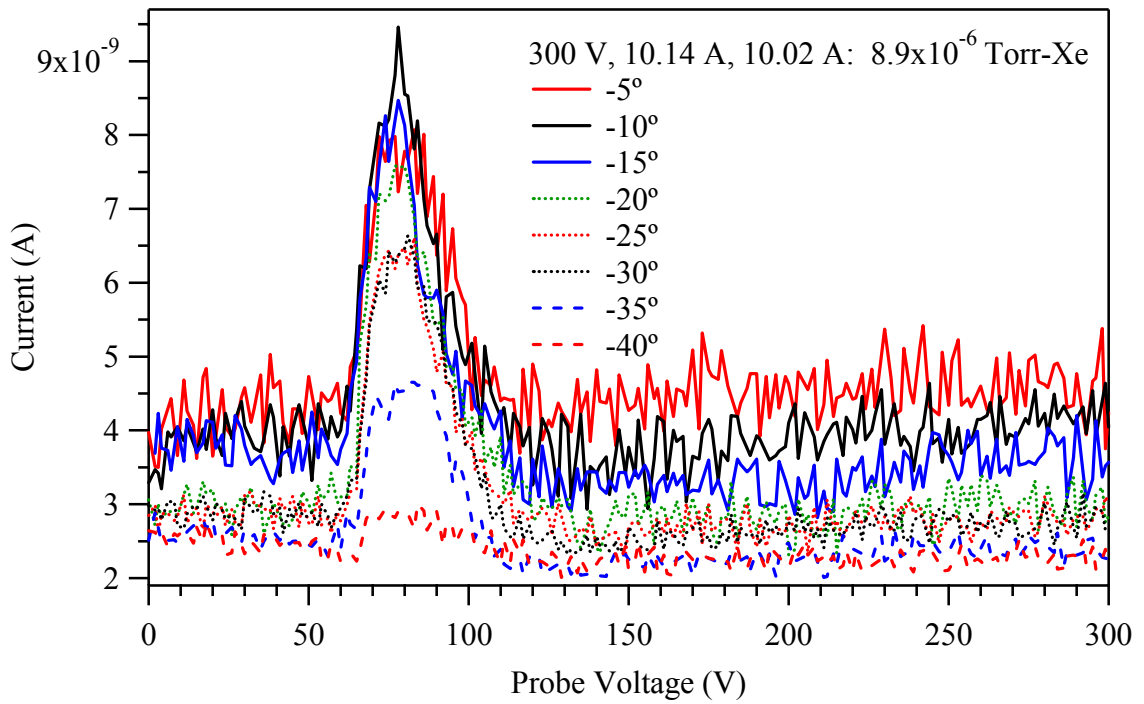


Figure 5-33: ExB traces of the cluster in Configuration 2 for backpressures of 8.9×10^{-6} Torr-Xe and with the cluster elements operating at 300 V, 10.46 mg/s.

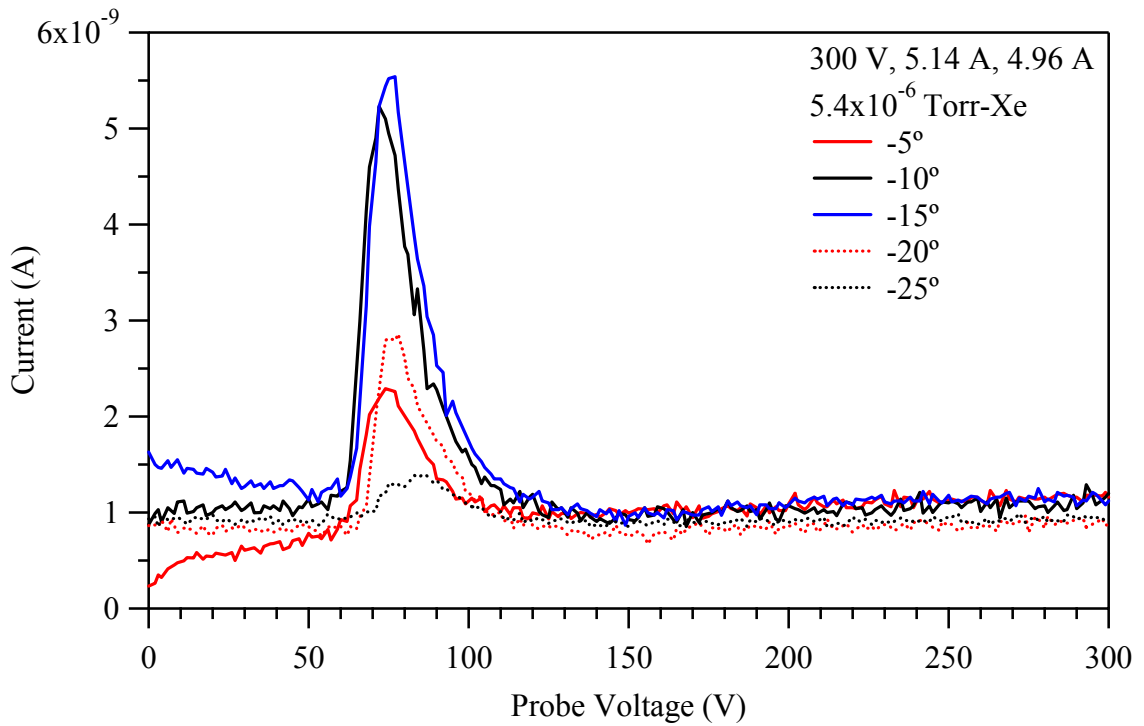


Figure 5-34: ExB traces of the cluster in Configuration 2 for backpressures of 5.4×10^{-6} Torr-Xe with the cluster elements operating at 300 V, 5.25 mg/s.

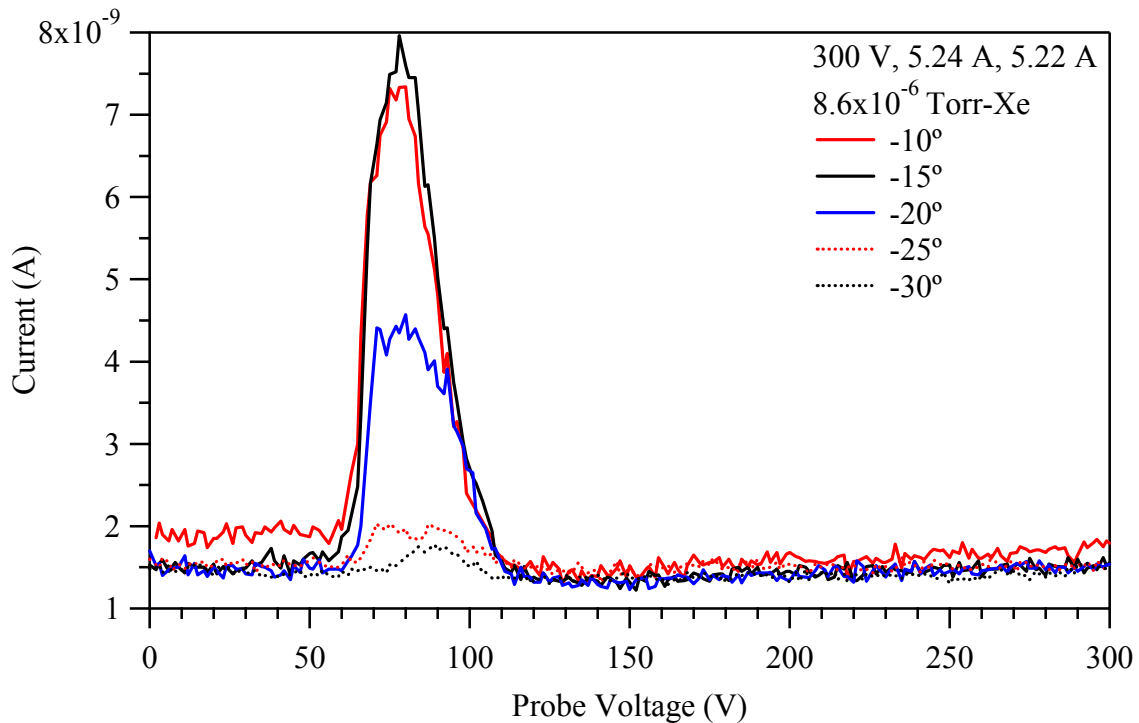


Figure 5-35: ExB traces of the cluster in Configuration 2 for backpressures of 8.6×10^{-6} Torr-Xe with the cluster elements operating at 300 V, 5.25 mg/s.

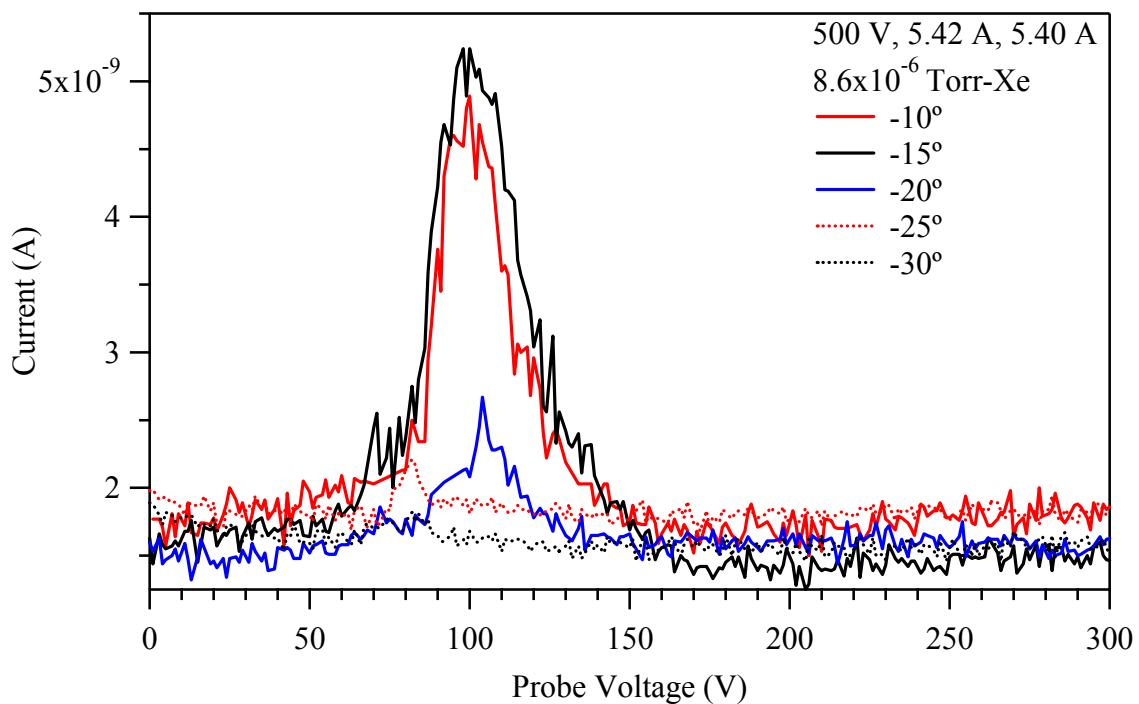


Figure 5-36: ExB traces of the cluster in Configuration 2 for backpressures of 8.6×10^{-6} Torr-Xe and with the cluster elements operating at 500 V, 5.25 mg/s.

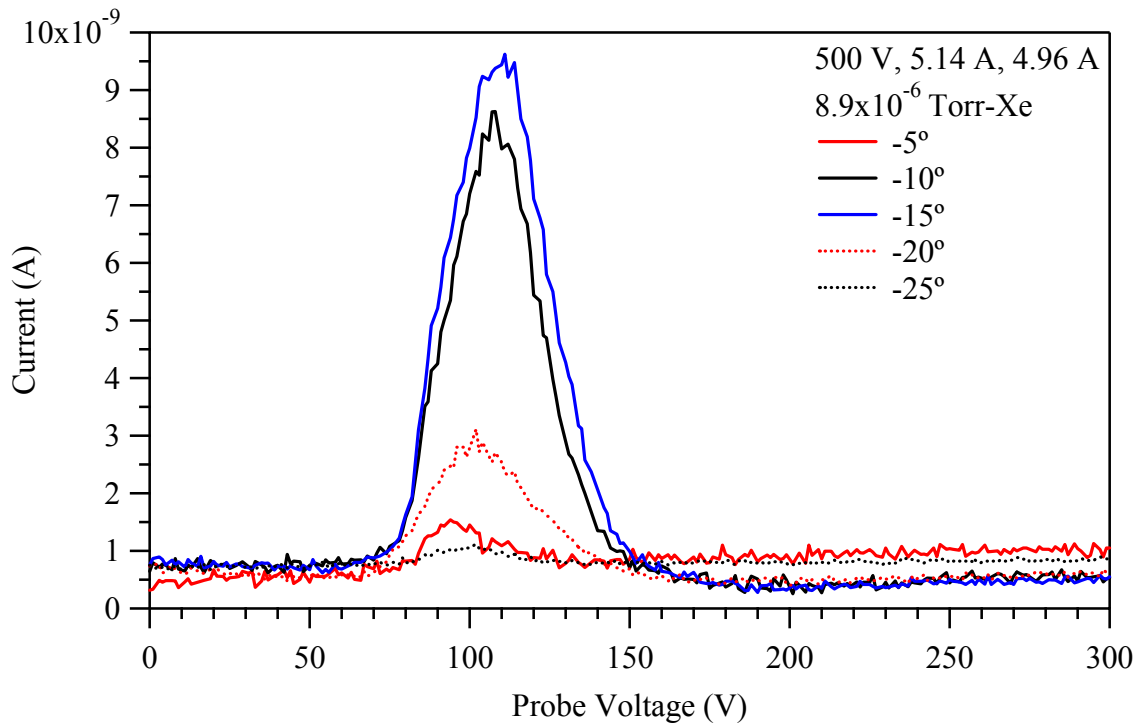


Figure 5-37: ExB traces of the cluster in Configuration 2 for backpressures of 8.9×10^{-6} Torr-Xe and with the cluster elements operating at 500 V, 5.25 mg/s.

5.1.7 Performance

Figure 5-38 shows the measured performance of the P5 cluster at all the conditions listed in Table 5-1. Figure 5-38 shows that thrust of the cluster increases as the facility backpressure increases. As with the monolithic thruster, this is due to the ingestion of neutral background gas into the discharge chambers. These data are discussed in more detail in the next section.

It is not possible to measure the performance of the cluster at the highest facility operating pressures and discharge voltages. This may be caused by the elevated facility backpressure in the immediate vicinity of the exit plane of each thruster. As the facility backpressure increases and background gas is ingested into the discharge chamber, the discharge current and the amplitude of the discharge current oscillations increase. At the

highest facility operating pressures, the discharge current instability becomes more severe as the discharge voltage is increased for constant backpressure. The amplitude of the discharge current oscillations increases as the backpressure increases until there is a disruption in the discharge. In addition, as the thruster approaches the discharge voltage disruption condition, portions of the inner channel begin to glow orange. It appears that the ingested background gas and consequent discharge oscillations enhance the thermal load on the boron nitride channel walls.

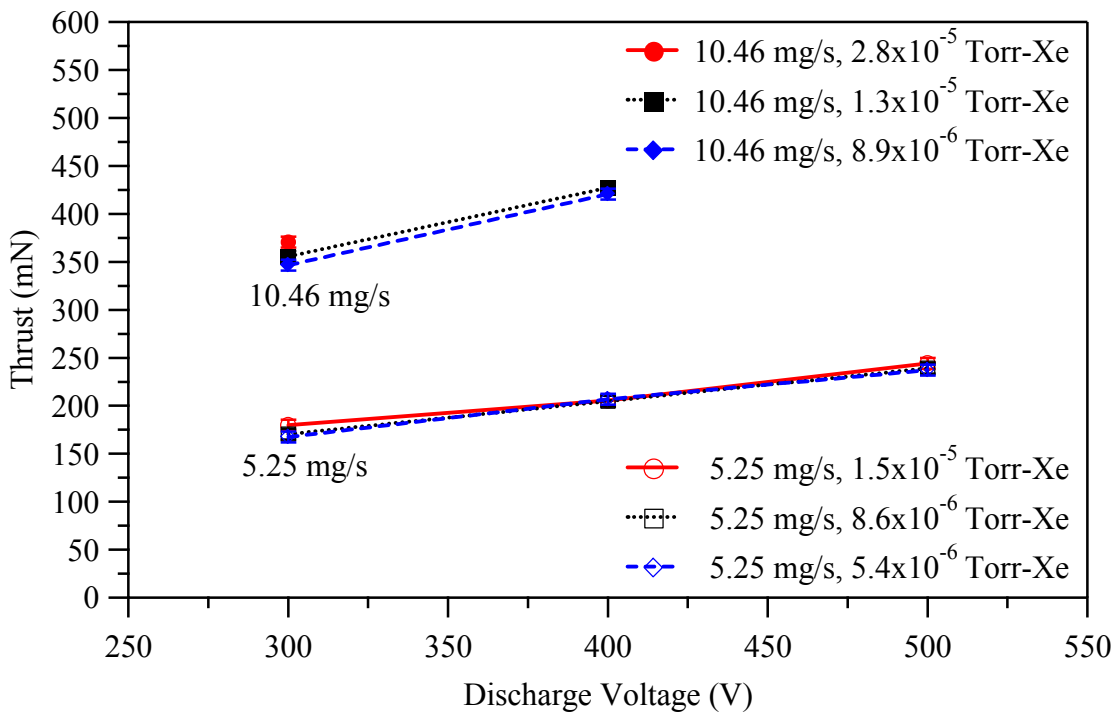


Figure 5-38: Cluster thrust measurements at anode flow rates of 5.25 mg/s and 10.46 mg/s as a function of discharge voltage at nominal pumping speeds of 70, 140, and 240 kl/s.

To use a cluster of Hall thrusters to create a high-power electric propulsion system, it is imperative to understand how the thrust of each engine contributes to that of the cluster. Figures 5-39 and 5-40 compare the sum of the thrust of the P5-A and P5-B to

the thrust of the cluster. All of the cluster thrust measurements are greater than the addition of the two monolithic thrusters for the same pumping speed. This is because the cluster introduces twice the mass flow rate of propellant into the facility, nearly doubling the backpressure in comparison to the same operating condition for a single thruster. Therefore, the thrust augmentation due to background gas ingestion, broadening of the ion energy distribution, and the decrease in the downstream plasma potential is greater for each element of the cluster than for the monolithic test case. Thus, the cluster thrust measurements are greater than the addition of the two monolithic thrust measurements. In addition, the cluster shows a much larger enhancement in thrust with increasing facility backpressure than is seen with the monolithic thruster. The thrust of the cluster may also be enhanced by plume interaction. Beal found that the electric field in the plume of an adjacent thruster is capable of turning CEX ions and accelerating them axially downstream.⁶⁹ The focusing of ions leads to a decrease in the plume divergence angle and thus an increase in thrust.

Figure 5-41 shows the thrust percent difference between measured cluster thrust and the sum of the measured thrusts of the monolithic thrusters for the flow rates of 5.25 and 10.46 mg/s at the three pumping speeds. The thrust percent difference is calculated by subtracting the sum of the thrust of the P5-A and P5-B from the thrust of the cluster and then dividing by the sum of the thrust of the P5-A and P5-B. The thrust percent difference changes little as the discharge voltage increases. The percent difference in thrust for the 10.46 mg/s anode flow rate varies from 11% to 16%, where the monolithic operating pressure varies from 5.3×10^{-6} Torr-Xe to 1.4×10^{-5} Torr-Xe and the cluster operating pressure varies from 8.9×10^{-6} Torr-Xe to 2.8×10^{-5} Torr-Xe. This is greater than

the percent difference in thrust for the 5.25 mg/s anode flow rate, which varies from 0% to 6%, where the monolithic operating pressure varies from 3.5×10^{-6} Torr-Xe to 9.1×10^{-6} Torr-Xe and the cluster operating pressure varies from 5.4×10^{-6} Torr-Xe to 1.5×10^{-5} Torr-Xe. These differences exist because the facility backpressure is greatest at the 10.46 mg/s anode flow rate; thus, the thrust augmentation due to facility effects is greatest at that flow rate. For a given flow rate, the thrust percent difference increases as the operating pressure decreases. This is primarily because the thrust of either the P5-A or P5-B operated alone decreases with backpressure faster than the thrust of the cluster decreases with pressure. This may be caused by the adjacent thruster ingesting the un-ionized neutral propellant of the adjacent thruster, which would cause an augmentation in thrust greater than that provided by ingestion of the background gas. It may also be caused by an increase in the width of the IEDF of each thruster because of elevated backpressure. Unfortunately, measurements of the IEDF are not collected in cluster Configuration 1 to verify this. Furthermore, Figure 5-8 shows that for the 300 V, 10.46 mg/s cluster operating condition the plasma potential increases by no more than 6 V with increasing facility backpressure. The increase in plasma potential leads to a decrease in thrust, not the increase measured.

A plot of cluster anode efficiency as a function of voltage is shown in Figure 5-42. In all but one case, the cluster anode efficiency increases with discharge voltage for a given anode flow rate. However, at an anode flow rate of 5.25 mg/s with an operating pressure of 1.5×10^{-5} Torr, the cluster anode efficiency decreases with increasing discharge voltage. The same behavior is seen in Figure 4-35 for the P5-A. The ingested flow rate, (as calculated by kinetic theory) is only 1.3% of the injected

anode flow at this condition. This condition has the highest ratio of injected flow to ingested flow of all the cluster measurements. As is shown in Chapter 4 for the monolithic thruster, the increase in discharge current overwhelms the increase in thrust. Thus, the ratio of supplied power to beam jet power decreases, as shown by the data presented in Table 5-1. This results in decreasing anode efficiency as the cluster discharge voltage increases.

The cluster anode efficiency is greatest at the 10.46 mg/s anode flow rate, which follows the same trend seen in the monolithic anode efficiency. The anode efficiency increases with facility backpressure because background gas ingestion artificially increases the thrust at a rate that is greater than the increase in power supplied to the thruster. This trend is also apparent in the monolithic thruster efficiency.

Figure 5-43 shows the cluster specific impulse. The cluster specific impulse increases continually with increasing discharge voltage. The same trend is observed in the specific impulse of the monolithic thrusters. The cluster specific impulse appears to increase slightly with anode flow rate for the measured points. This is opposite of the trend seen with the monolithic thrusters. The specific impulse is a function of the ion exit velocity which is determined by the discharge voltage. The cluster specific impulse appears to increase with facility backpressure for a constant discharge voltage. This is because background gas ingestion increases the thrust, but the ingested flow is not accounted for in the calculation of the anode specific impulse.

The differences in facility operating pressure make it difficult to compare the performance of the monolithic thruster and the cluster at the same thruster operating condition. As shown in Table 4-1, the chamber operating pressure with the monolithic

thruster operating in the facility at a nominal pumping speed of 70 kl/s is approximately the same as the operating pressure with the cluster operating in the facility at a nominal pumping speed of 140 kl/s. Thus, comparisons between monolithic and cluster data at these conditions may be independent of facility operating pressure.

Figures 5-44 through 5-46 show the thrust, specific impulse, and anode efficiency of the monolithic thruster operating in the facility at a nominal pumping speed of 70 kl/s and the cluster operating at a nominal pumping speed of 140 kl/s. As indicated in each figure, the operating pressure of the monolithic thruster and the cluster is approximately the same for anode flow rates of 5.25 mg/s and 10.46 mg/s. Figure 5-44 shows that at the 5.25 mg/s flow rate, the sum of the thrust of the monolithic thrusters is approximately equal to the thrust of the cluster. However, at the 10.46 mg/s flow rate, the cluster thrust is greater than that of the monolithic thrusters. The thrust of the cluster may be greater than the sum of the thrust of the monolithic thrusters because each cluster element elevates the operating pressure in the immediate vicinity of the adjacent thruster. The elevated operating pressure also affects the cluster specific impulse and anode efficiency at the 10.46 mg/s anode flow rate.

Figure 5-45 shows that, at the 5.25 mg/s anode flow rate, the specific impulse of the cluster is approximately the same as that of the monolithic thruster. However, at the 10.46 mg/s flow rate, the specific impulse of the cluster is approximately 250 seconds greater than that of the monolithic thruster. As discussed above, the increase in cluster specific impulse is caused by artificial inflation of the calculated specific impulse by ingested background gas.

Figure 5-46 shows that, at the 5.25 mg/s anode flow rate, the anode efficiency of the cluster is approximately the same as that of the monolithic thruster, within the error of the measurement. At the 10.46 mg/s anode flow rate, the cluster anode efficiency is higher than the anode efficiency of the monolithic thruster. As explained above, the ingestion of background gas from the adjacent thruster may lead to an augmentation of the jet power of the beam that is not strongly correlated to facility backpressure.

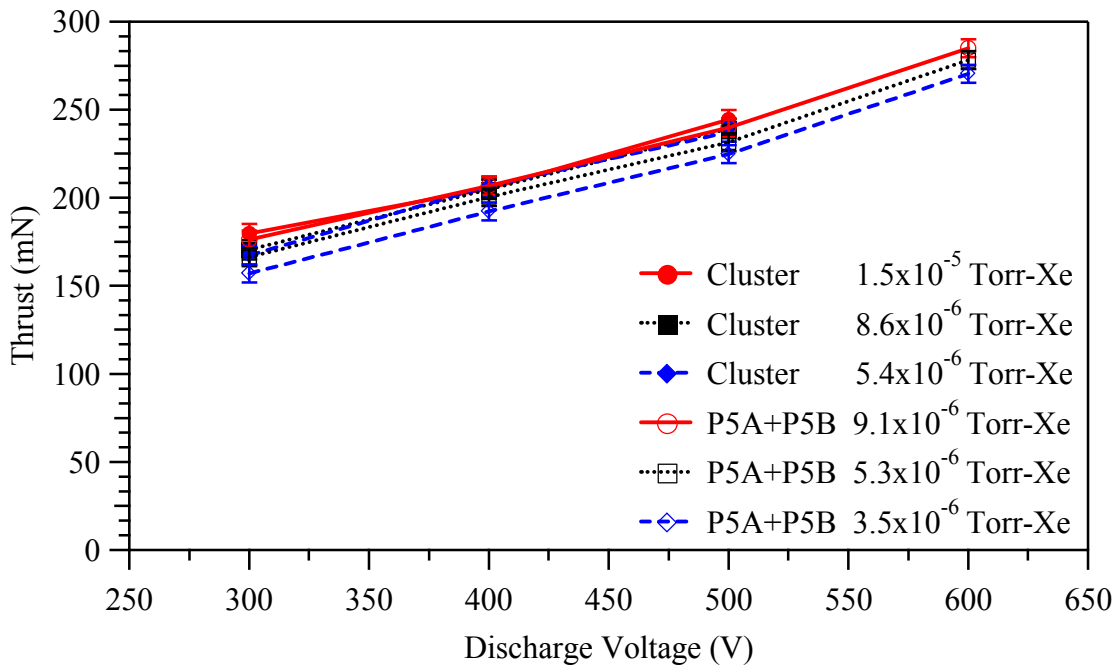


Figure 5-39: Cluster thrust measurements in comparison to the addition of the monolithic thrust for an anode flow rate of 5.25 mg/s at nominal pumping speeds of 70, 140, and 240 kl/s.

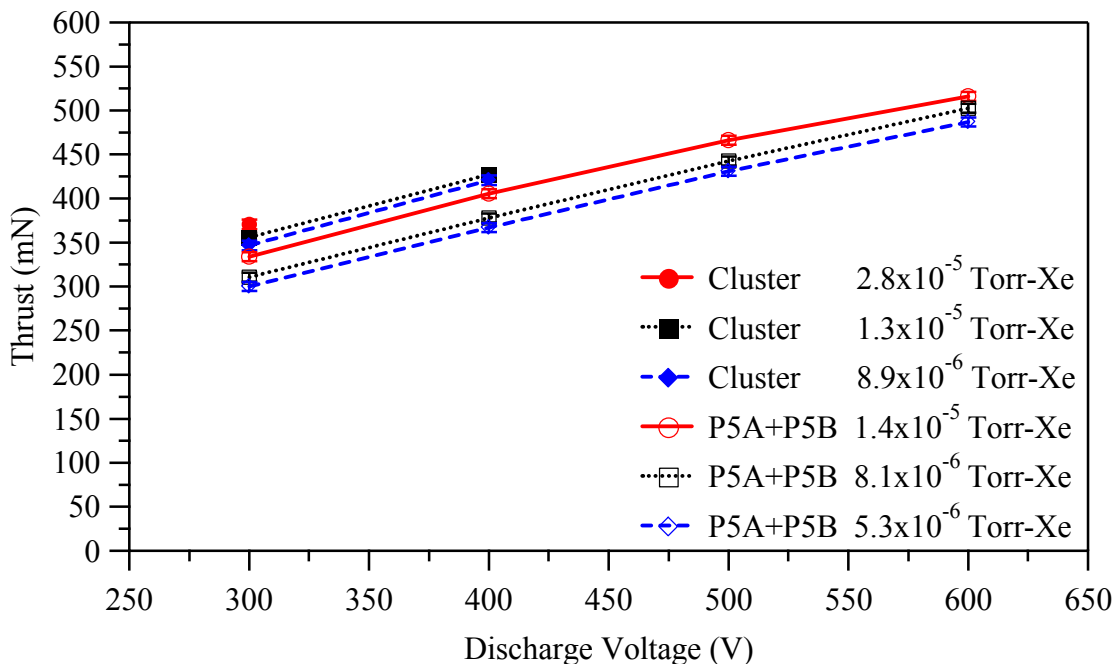


Figure 5-40: Cluster thrust measurements in comparison to the addition of the monolithic thrust at an anode flow rate of 10.46 mg/s at nominal pumping speeds of 70, 140, and 240 kl/s.

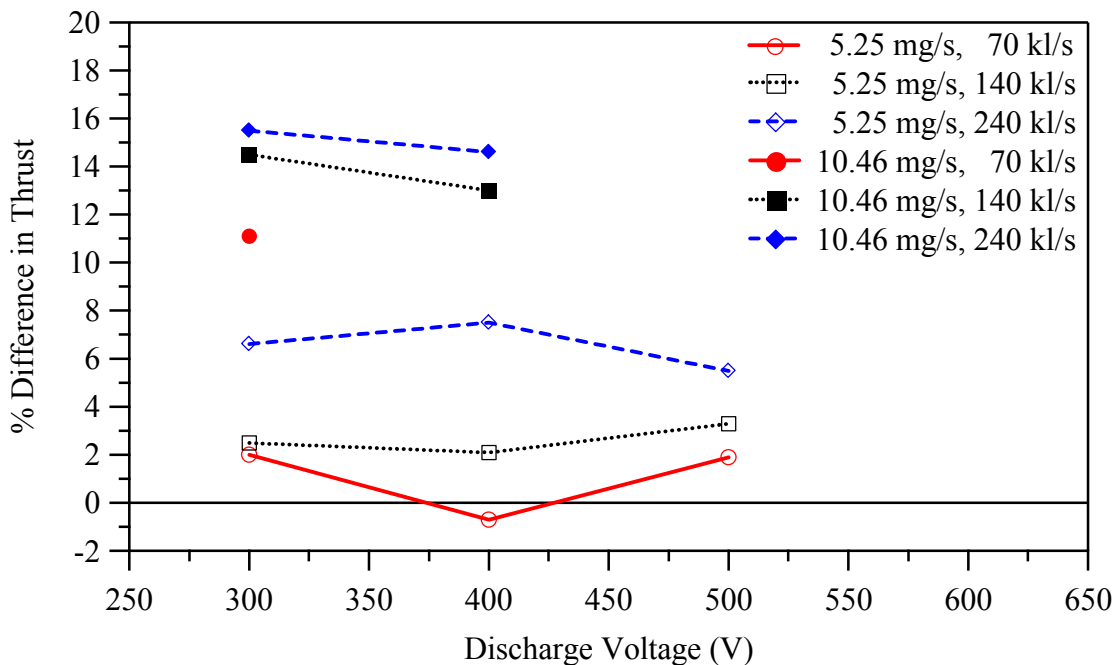


Figure 5-41: Percent difference between measured cluster thrust and the addition of the measured monolithic thrust at anode flow rates of 5.25 mg/s and 10.46 mg/s at nominal pumping speeds of 70, 140, and 240 kl/s.

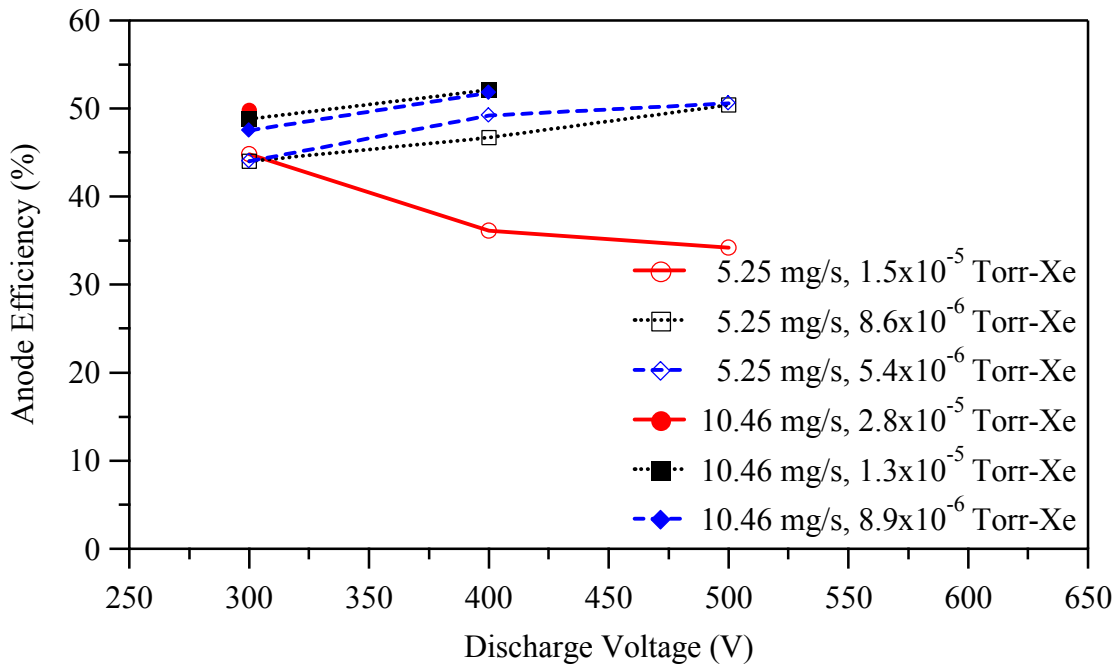


Figure 5-42: Cluster anode efficiency versus discharge voltage at nominal pumping speeds of 70, 140, and 240 kl/s.

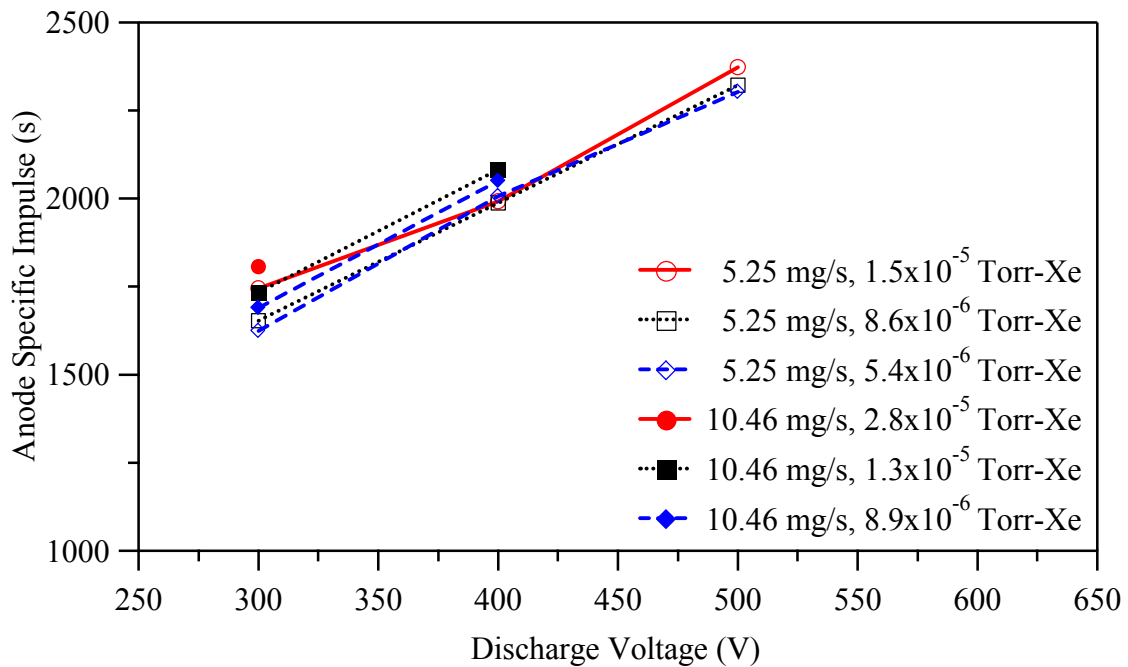


Figure 5-43: Cluster anode specific impulse versus discharge voltage at nominal pumping speeds of 70 kl/s, 140 kl/s, and 240 kl/s.

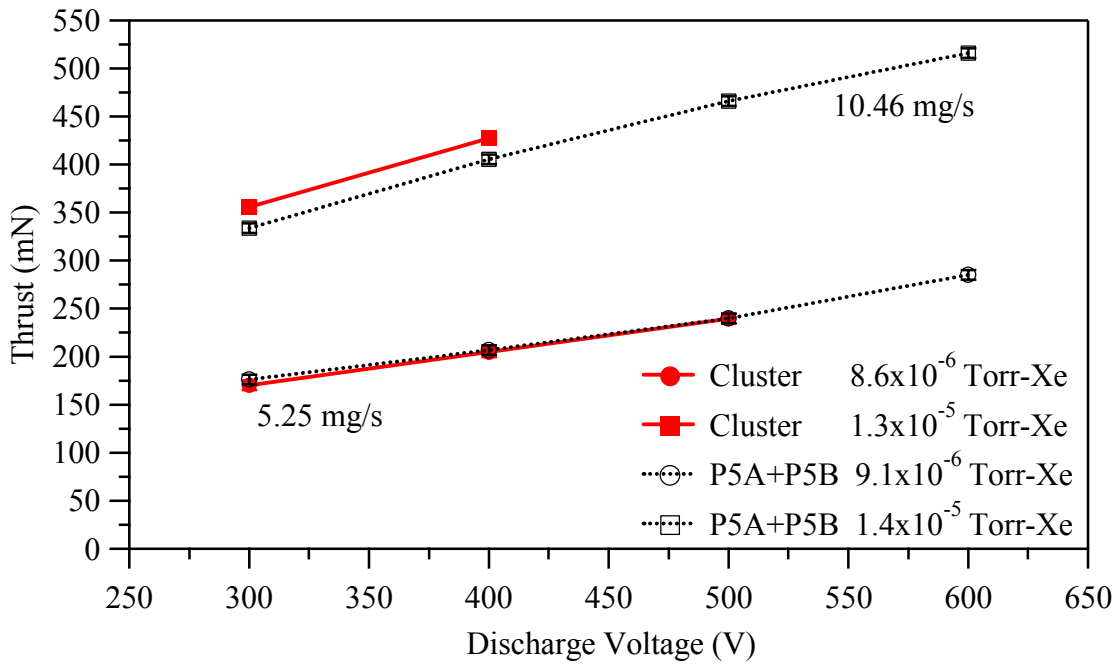


Figure 5-44: Thrust versus discharge voltage for the sum of the P5-A and P5-B at a nominal pumping speed of 70 kl/s, and the thrust of the cluster at nominal pumping speed of 140 kl/s.

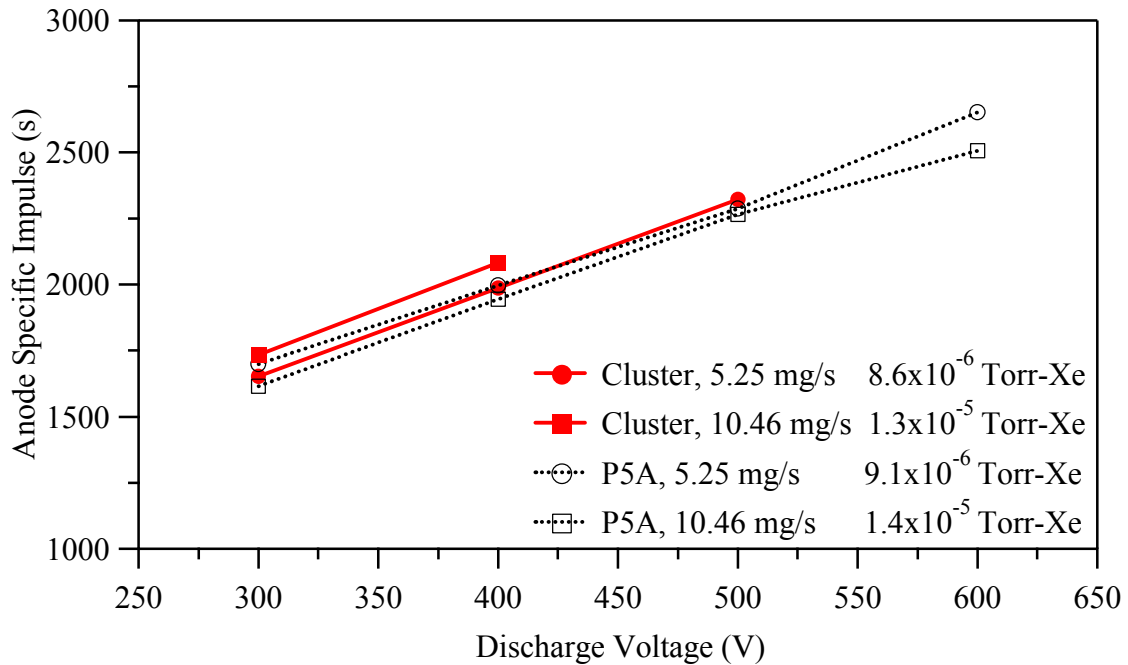


Figure 5-45: Specific impulse versus discharge voltage for the sum of the P5-A at a nominal pumping speed of 70 kl/s and the cluster at a nominal pumping speed of 140 kl/s.

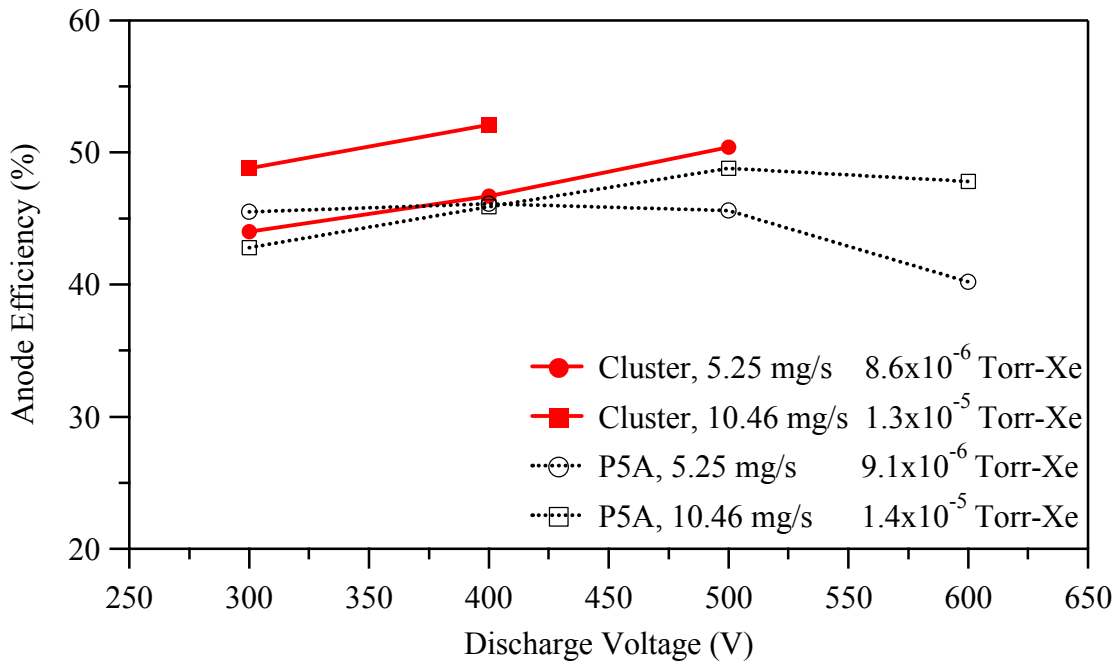


Figure 5-46: Anode efficiency versus discharge voltage for the sum of the P5-A at a nominal pumping speed of 70 kl/s, and the cluster at a nominal pumping speed of 140 kl/s.

Analysis of the monolithic thrust measurements shows that as the facility backpressure increases, more background gas is ingested into the discharge chamber, increasing the discharge current and thrust. The percent difference in thrust between the sum of the thrust of the monolithic thrusters and the thrust of the cluster for the 10.46 mg/s anode flow rate varies from 11% to 16% as the operating pressure varies from 5.3×10^{-6} Torr-Xe to 2.8×10^{-5} Torr-Xe. This is greater than the percent difference in thrust for the 5.25 mg/s anode flow rate, which varies from 0% to 6% as the operating pressure varies from 3.5×10^{-6} Torr-Xe to 1.5×10^{-5} Torr-Xe. The difference in thrust between the two flow rates is caused by the ingestion of background gas; thus, the difference in thrust between the cluster and the sum of the monolithic thrusters increases as the operating pressure decreases.

The efficiency of the cluster shows the same trends as the monolithic thruster. The efficiency values of the cluster are slightly greater than those of the monolithic thruster. The difference appears to be caused by the ingested background gas. The specific impulse of the cluster increases with discharge voltage. However, the specific impulse increases with facility backpressure, which was not seen with the monolithic thruster. This is possibly due to the fact that the calculation of specific impulse does not take the ingested background gas into account.

Comparison of the performance characteristics of the cluster and the monolithic thruster at conditions of nearly equal operating pressure shows that, for the 5.25 mg/s anode flow rate, the cluster thrust is simply the sum of the thrust of the two monolithic thrusters. In addition, the anode efficiency and specific impulse are approximately equal to that of the monolithic thruster. However, these trends do not hold at the 10.46 mg/s anode flow rate for conditions of equal operating pressure, because each cluster element elevates the operating pressure in the immediate vicinity of the adjacent thruster and the effects of ingestion are apparent. The cluster pressure map presented in Chapter 3 could not verify an increase in the operating pressure immediately downstream of the cluster because the spatial resolution is not small enough and the measurements are not collected closer than 0.5 m from the exit plane.

5.1.8 Predicting Cluster Performance and Plume Characteristics

The cluster spacing criterion (based on the inner channel magnetic field) appears to be adequate for performance measurements. Further verification of the criterion requires measurement of the cluster performance for different separation

distances. It may also be possible to move the elements of the cluster closer together without adversely affecting their performance.

Comparison of the results of monolithic thruster and cluster measurements show that at the 5.25 mg/s anode flow rate, the cluster thrust is simply the linear addition of the thrust of the 2 cluster elements. At the 10.46 mg/s anode flow rate, linear addition of the thruster elements does not correctly predict cluster thrust.

Beal has presented techniques to predict the plasma density, electron temperature, and plasma potential in the plume of a 2x2 cluster of 200 W Hall thrusters.⁵⁰ Unfortunately, the physical differences between the measurement configurations does not allow verification of Beal's prediction techniques for a high-power cluster. One of the most critical issues of Hall thruster integration is ensuring that the beam does not impinge on any of the spacecraft surfaces. The ion current density measurements show that the outer half of the cluster plume is nearly identical to its plume when operated alone. Thus, no increase in thruster element plume divergence angle is expected when operating in the cluster configuration. This investigation shows the changes in the floating potential, plasma potential, electron number density, and electron temperature are small in comparison to the error in the measurements and the magnitude of the values. In addition, the measurements of ion energy distribution per unit charge do not detect energetic ions in the plume of the cluster at angles greater than those measured with the monolithic thruster. Furthermore, ion species traces do not show a large number of multiply-charged ions at any location in the plume. The alignment problems in Configuration 2 make it difficult to compare the results of the ESA and ExB probes to those of the monolithic thruster.

5.2 Conclusions

This investigation thoroughly characterizes the effect of clustering on plume characteristics. In addition, the extent to which a monolithic thruster's performance and plume are affected by an adjacent thruster is characterized. At an anode flow rate of 5.25 mg/s, the thrust is equal to the sum of the thrust of the monolithic thrusters. Using this method for the 10.46 mg/s anode flow rate results in a less than 5% underprediction of the cluster thrust.

Simultaneously, the investigation characterizes the effect of backpressure on the cluster and monolithic thruster elements at pressures higher than those possible with the monolithic thruster. The backpressure effects still appear to gradually increase with increasing backpressure. The overall knowledge gained by each portion of the investigation shows that use of a high-power Hall thruster cluster should not be an issue using the current design rules for integrating monolithic Hall thrusters onto spacecraft.

CHAPTER 6 CATHODE SHARING

The previous chapter discusses how clustering affects the plume and performance characteristics of a cluster element. It also presents measurements of the overall cluster plume and performance characteristics. All of the measurements are taken with a thruster centerline distance of 40 cm, which is determined by the spacing criterion presented earlier.

This chapter aims to investigate three variables of Hall thruster clustering: thruster centerline spacing, cathode sharing, and cathode displacement from the nominal position on the thruster. In addition, the ability to restart a thruster from a displaced cathode is verified.

This study attempts to define the limits of cathode sharing by increasing the separation distance between the two cluster elements with various cathode configurations while monitoring the operation of each cluster element. Once the limits of operation are found within the physical constraints of the positioning system, the performance of one of the elements is measured as the cathode is displaced from its nominal position on the thruster.

6.1 Plume data as a function of cluster spacing

The plume parameters are not characterized as a function of cluster centerline spacing because the test matrix size is prohibitive. Instead, the thruster discharge current

and cathode-to-ground voltage, V_{cg} are monitored as a function of cluster centerline separation distance. These measurements are performed at operating conditions of 300 and 500 V at anode flow rates of 5.25 and 10.46 mg/s. A nominal pumping speed of 240 kl/s yields operating pressures most representative of those on-orbit. In addition, the thruster spacing criterion developed in Chapter 5 is tested by operating the cluster over a range of centerline separation distances. For all experiments the thrusters use independent mass flow controllers.

6.2 Cluster Displacement Results

The next four subsections present the results of the cluster cathode sharing and cluster displacement investigations. Each subsection presents the physical configuration used and the results of the parameters measured. An explanation of the results is given in the discussion.

Jumps in the steady state operation of the thrusters are caused by elevated facility backpressure due to the cluster anode flow rates. The jumps were observed in the previous cluster investigation, in which the cluster has a 40 cm thruster centerline spacing. The differences are not caused by operating the thruster in the cluster configuration unless noted. The jumps cause discontinuities in the discharge current and the cathode-to-ground potential.

When operating at the same discharge voltage and anode flow rate, the cluster elements have different discharge currents and cathode-to-ground potentials. The difference in the magnitude of the discharge currents is due primarily to the manufacturing and assembly tolerances. The difference in magnitude of the V_{cg} is due

only to the difference in the hand assembly of the cathodes. Figure 6-1 shows a diagram of the circuit used for the shared cathode configuration.

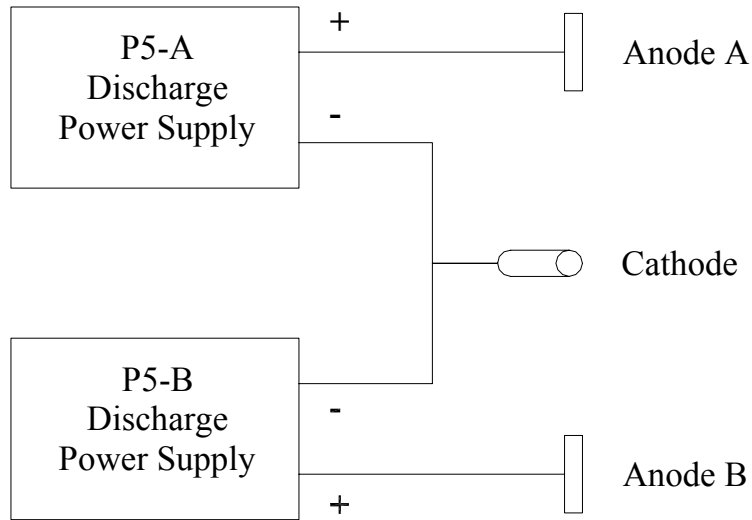


Figure 6-1: Diagram of the shared cathode circuit.

The data show several important features about clustering that are critical for spacecraft design. The following sections will discuss the features of interest for each configuration.

6.2.1 Separate Cathodes

Figure 6-2 shows a diagram of the cathodes mounted on the separate thrusters. Initial thruster centerline separation is 40 cm. This results in a minimum separation distance between the Hall thruster magnet poles of 10 mm. The poles are not allowed to touch to avoid any unforeseen complications with the electrical circuits.

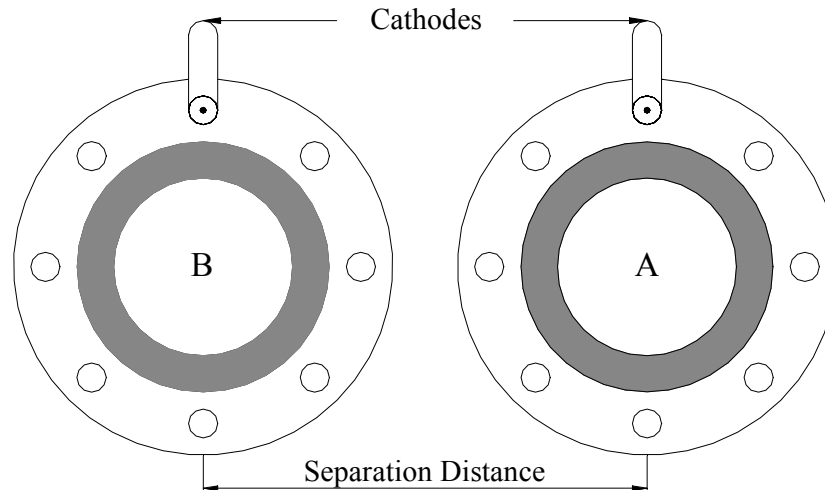


Figure 6-2: Diagram of the separate cathodes on the cluster.

For this experiment, P5-A and P5-B are operated through electrically independent circuits from their own cathodes and power supplies. The cluster elements are operated with their cathodes mounted at the 12 o'clock position. The effect of thruster separation distance is investigated by varying the separation distance between the thrusters and monitoring the discharge current and cathode-to-ground voltage. The initial thruster separation distance is 305 mm and the measurements are taken in 40 mm increments out to a maximum separation distance of 1405 mm. Figures 6-3 and 6-4 present the discharge current as a function of separation distance for the 5.25 mg/s and 10.46 mg/s operation conditions, respectively. Figures 6-4 and 6-5 present the cathode to ground voltage for the 5.25 and 10.46 mg/s operating conditions, respectively.

Figures 6-3 and 6-4 show that the discharge current remains nearly constant with increasing distance between the cluster element centerlines. Figure 6-4 shows that the discharge current is not steady at the 500 V, 10.46 mg/s operation condition. The variation in the discharge current is a result of the elevated facility backpressure not the separation distance. Figure 6-5 shows that the cathode-to-ground voltage is constant with

separation for all 5.25 mg/s anode flow rate conditions. Figure 6-6 shows that at the 300 V, 10.46 mg/s operating condition the cathode to ground voltage is nearly constant. However, the cathode-to-ground voltage varies with the unsteady discharge current at 500 V, 10.46 mg/s.

In addition, the effect of entrainment is investigated. While P5-A and P5-B are operating independently, one of the thrusters and its cathode are turned off. The anode and cathode flow through the adjacent thruster is not turned off. The discharge current and cathode-to-ground voltage are then monitored over the same range of separation distances. Both the discharge current and cathode to ground voltage remain constant for all separation distances for cold and hot flow through the adjacent thruster. The measurements show that the discharge current is not a function of the distance between the thruster centerlines. Thus, for this condition it appears that the monolithic elements are not ingesting propellant from the adjacent thruster.

These results differ from the results presented in Chapter 5 for the 10.46 mg/s anode flow rate. The major difference is that the cathode sharing measurements are performed at Station 2 (see Figure 2-4), while the cluster thruster measurements are performed at Station 1. The pressure field may be remarkably different in these two locations, thus leading to different facility background pressure effects.

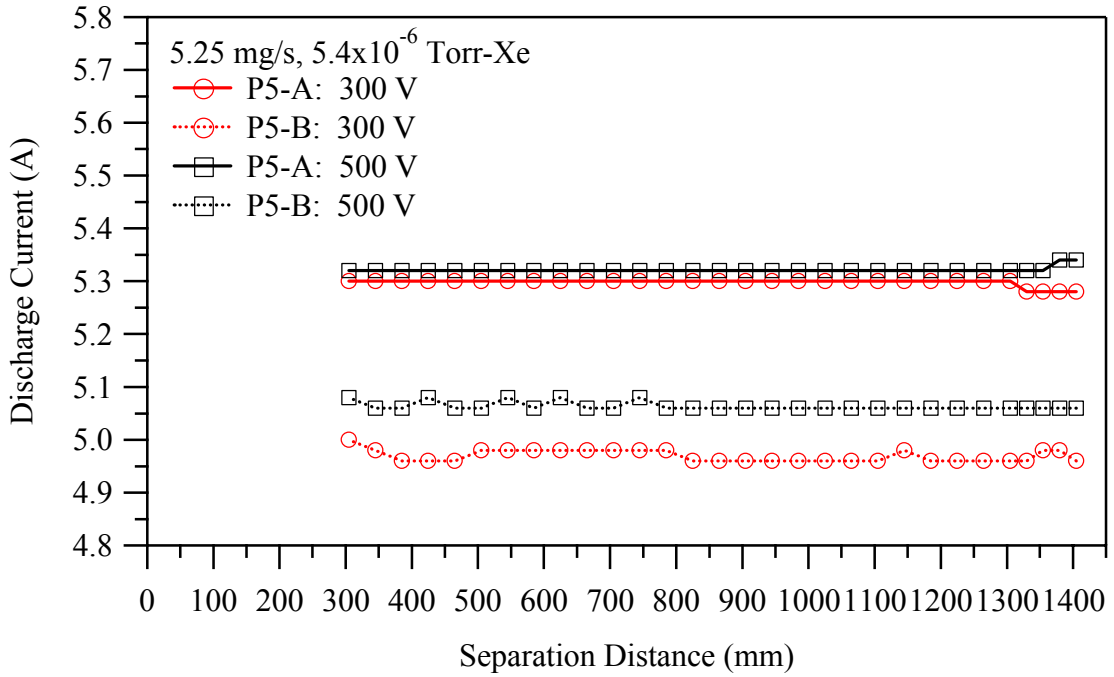


Figure 6-3: Discharge current as a function of thruster centerline distance for anode flow rates of 5.25 mg/s at a backpressure of 5.4×10^{-6} Torr-Xe.

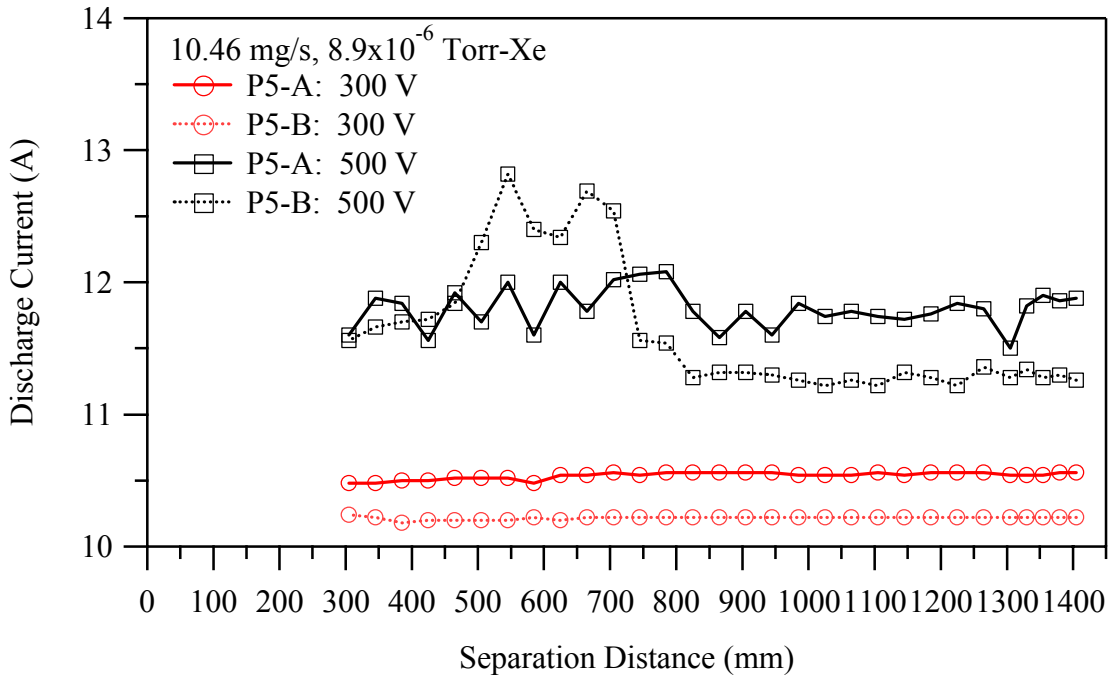


Figure 6-4: Discharge current as a function of thruster centerline distance for anode flow rates of 10.46 mg/s at a backpressure of 8.9×10^{-6} Torr-Xe.

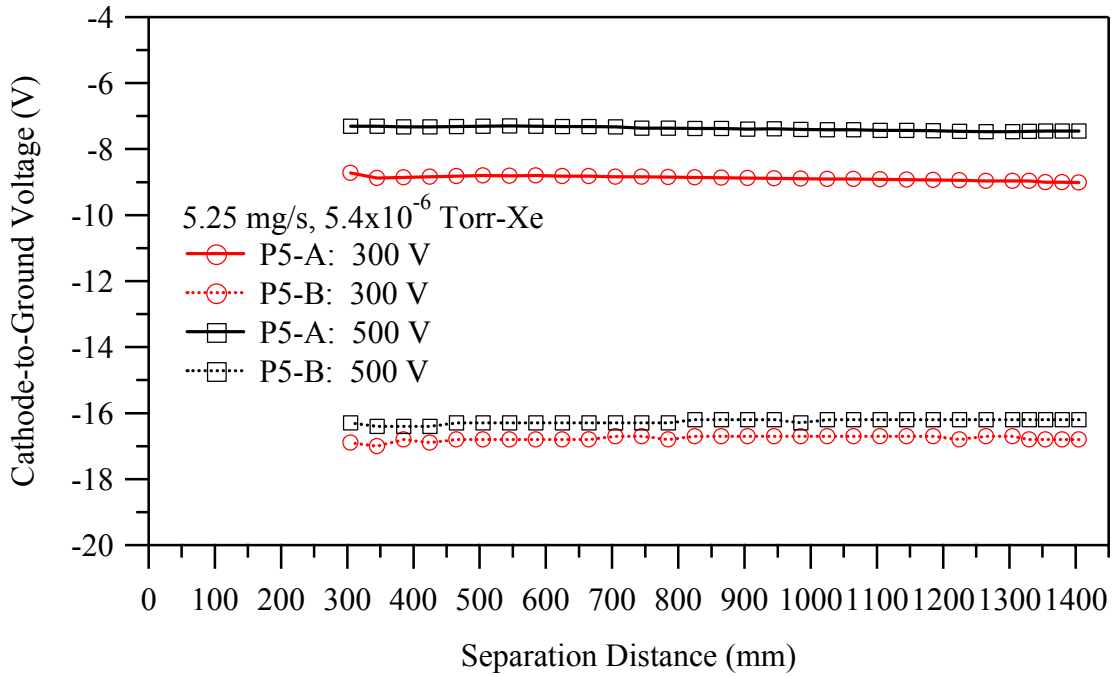


Figure 6-5: Cathode-to-ground voltage as a function of thruster centerline distance for an anode flow rate of 5.25 mg/s at a backpressure of 5.4×10^{-6} Torr-Xe.

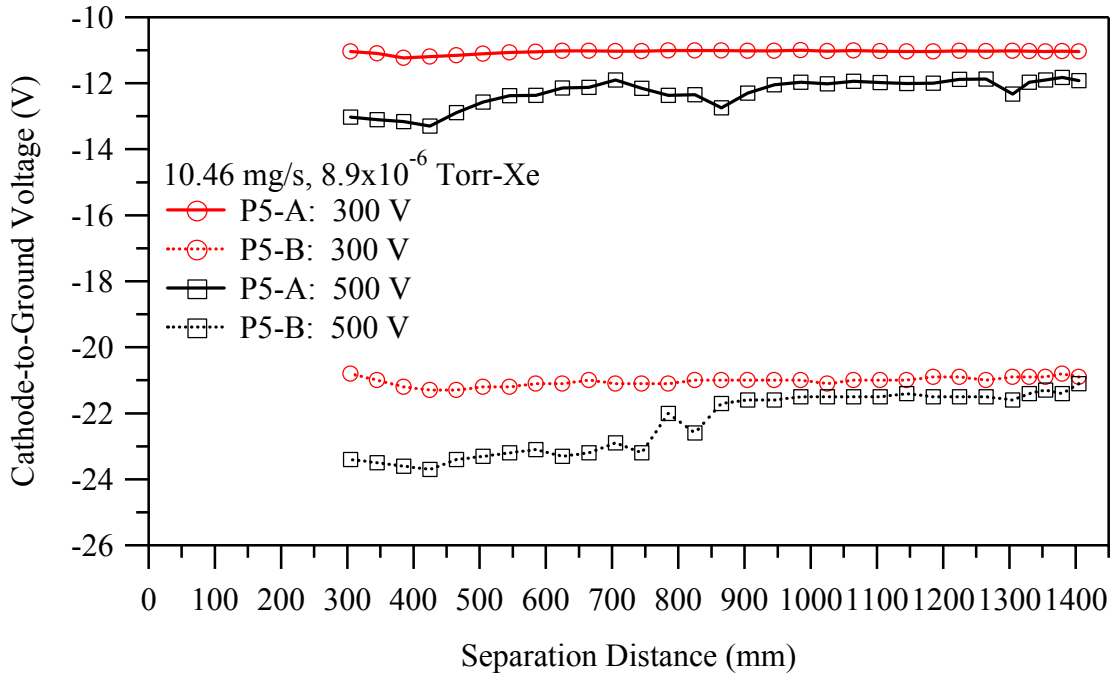


Figure 6-6: Cathode-to-ground voltage as a function of thruster centerline distance for an anode flow rate of 10.46 mg/s at a backpressure of 8.9×10^{-6} Torr-Xe.

6.2.2 Sharing the Cathode of an Adjacent Thruster

The effect of a cluster of thrusters sharing a single cathode mounted above one of the thrusters is investigated. For this experiment, P5-A and P5-B first operate sharing cathode A, and then sharing cathode B. Figure 6-2 shows a diagram of the adjacent thrusters and the position of their cathodes. No gas flows through the cathode of the non-operating cathode. Figure 6-1 shows the electrical circuit through which the cathodes are shared.

The effect of thruster separation distance is investigated by varying the separation distance between the thrusters and monitoring the discharge current and cathode to ground voltage of each thruster. The initial thruster separation distance is 305 mm and the measurements are taken in 40 mm increments out to a maximum separation distance of 1785 mm. Figures 6-7 and 6-8 present the discharge current as a function of separation distance sharing cathode A for the 5.25 mg/s and 10.46 mg/s operation conditions, respectively. Figures 6-9 and 6-10 present the cathode-to-ground voltage as a function of separation distance when sharing cathode A for the 5.25 mg/s and 10.46 mg/s operation conditions, respectively.

The cathode sharing investigation is then repeated with both thrusters sharing cathode B. Figures 6-11 and 6-12 presents the discharge current as a function of separation distance when sharing cathode B for the 5.25 mg/s and 10.46 mg/s operation conditions, respectively. Figures 6-13 and 6-14 presents the cathode-to-ground voltage as a function of separation distance when sharing cathode B for the 5.25 mg/s and 10.46 mg/s operation conditions, respectively.

Figures 6-7 through 6-10 present the discharge current and cathode-to-ground voltage with both thrusters sharing Cathode A. Figures 6-11 through 6-14 present the

discharge current and cathode-to-ground voltage with the thrusters sharing Cathode B. Sharing cathode A or cathode B does not change the characteristics of the discharge current or the cathode-to-ground voltage curves. The discharge current and cathode-to-ground voltage remain nearly constant for the 5.25 mg/s anode flow rates. The 10.46 mg/s anode flow rates result in elevated backpressures, which increase the number of electron-neutral collisions in the discharge channel. As discussed in Chapter 4, the collisions enhance the electron mobility to the anode, which leads to changes in the discharge current. Overall, the results show that no deleterious effects are caused by a cluster sharing the cathode mounted on one of the thrusters.

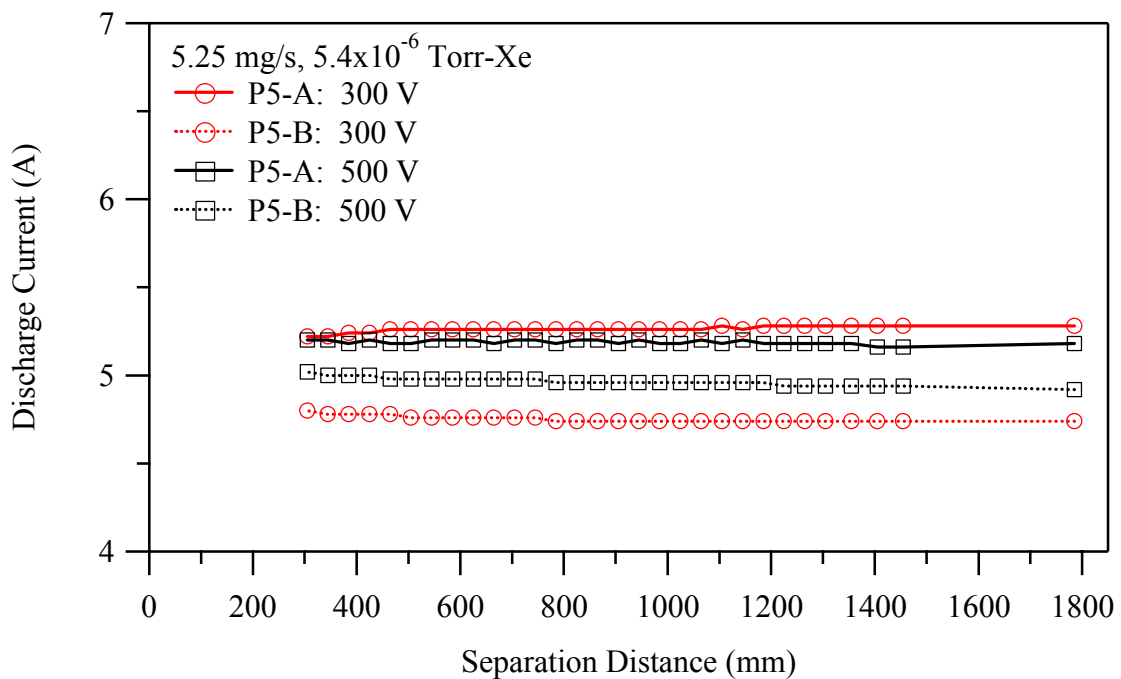


Figure 6-7: Sharing Cathode A - Discharge current as a function of thruster centerline distance 5.25 mg/s at a backpressure of 5.4×10^{-6} Torr-Xe

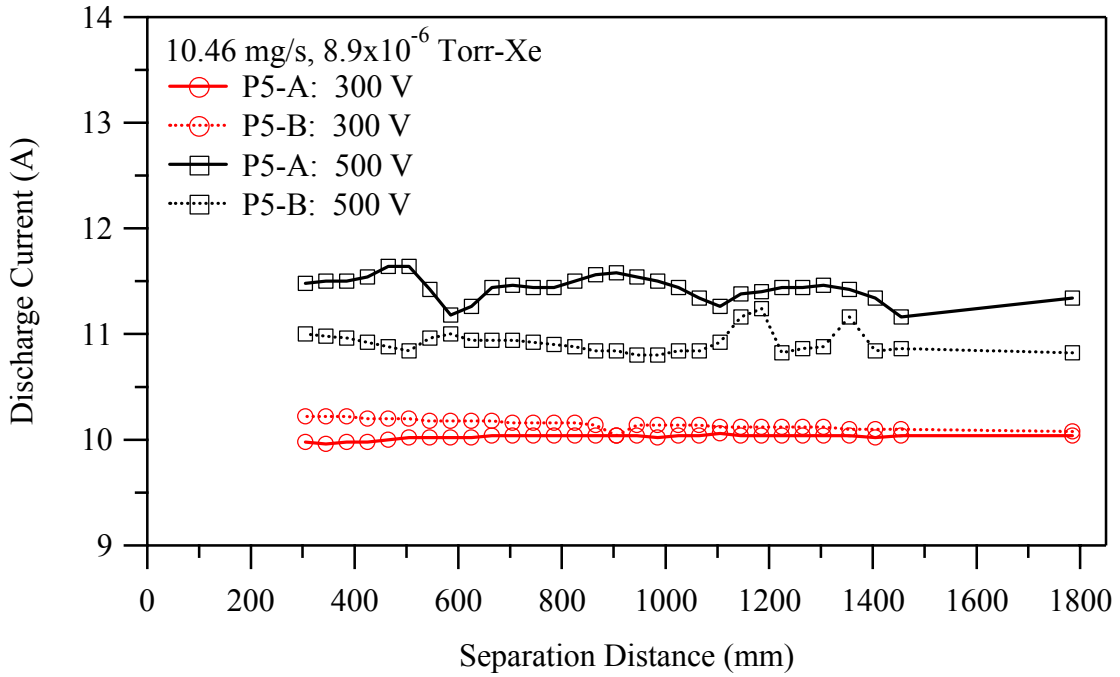


Figure 6-8: Sharing Cathode A - Discharge current as a function of thruster centerline distance 10.46 mg/s at a backpressure of 8.9×10^{-6} Torr-Xe.

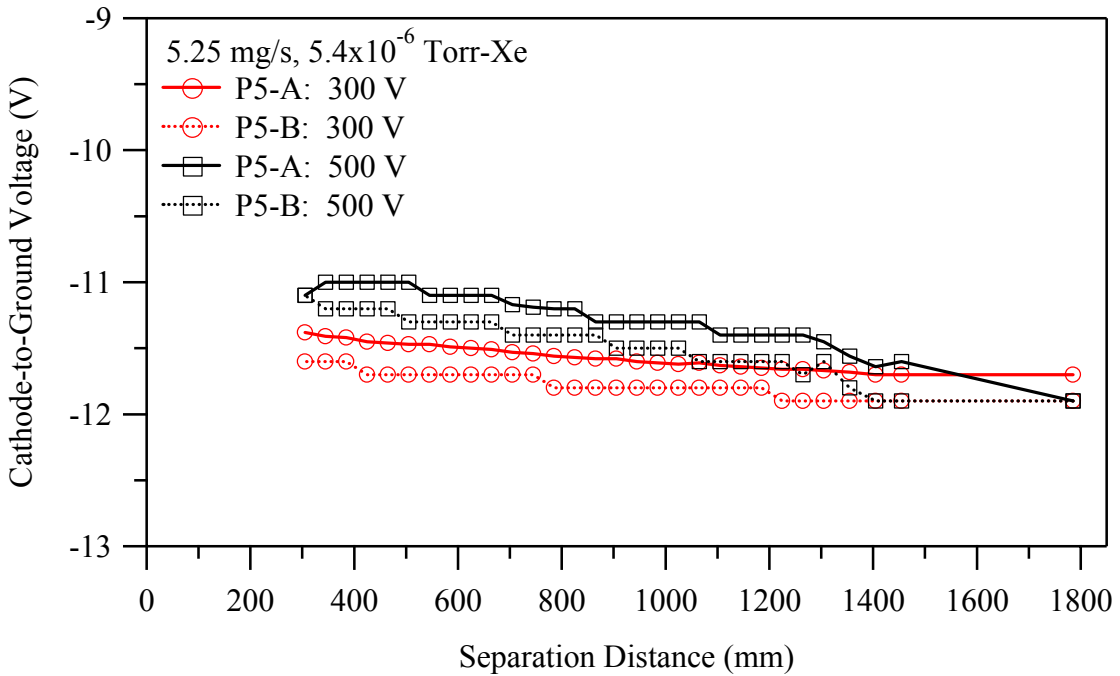


Figure 6-9 Sharing Cathode A – Cathode-to-ground voltage as a function of thruster centerline distance 5.25 mg/s at a backpressure of 5.4×10^{-6} Torr-Xe.

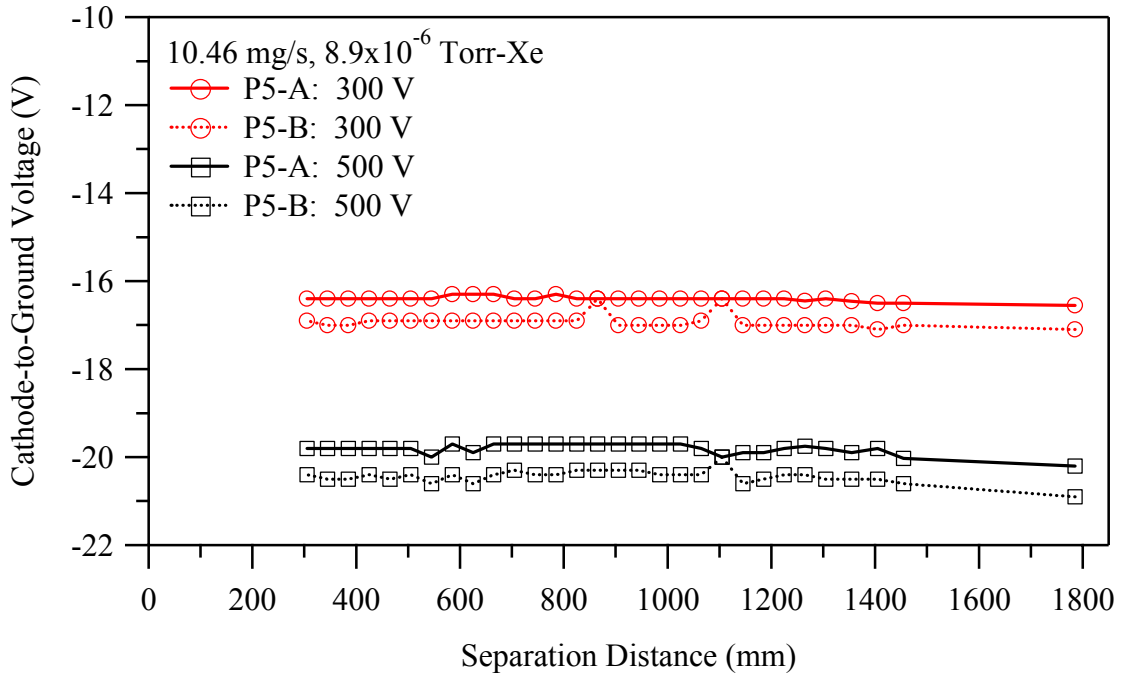


Figure 6-10: Sharing Cathode A - Cathode-to-ground voltage as a function of thruster centerline distance 10.46 mg/s at a backpressure of 8.9×10^{-6} Torr-Xe.

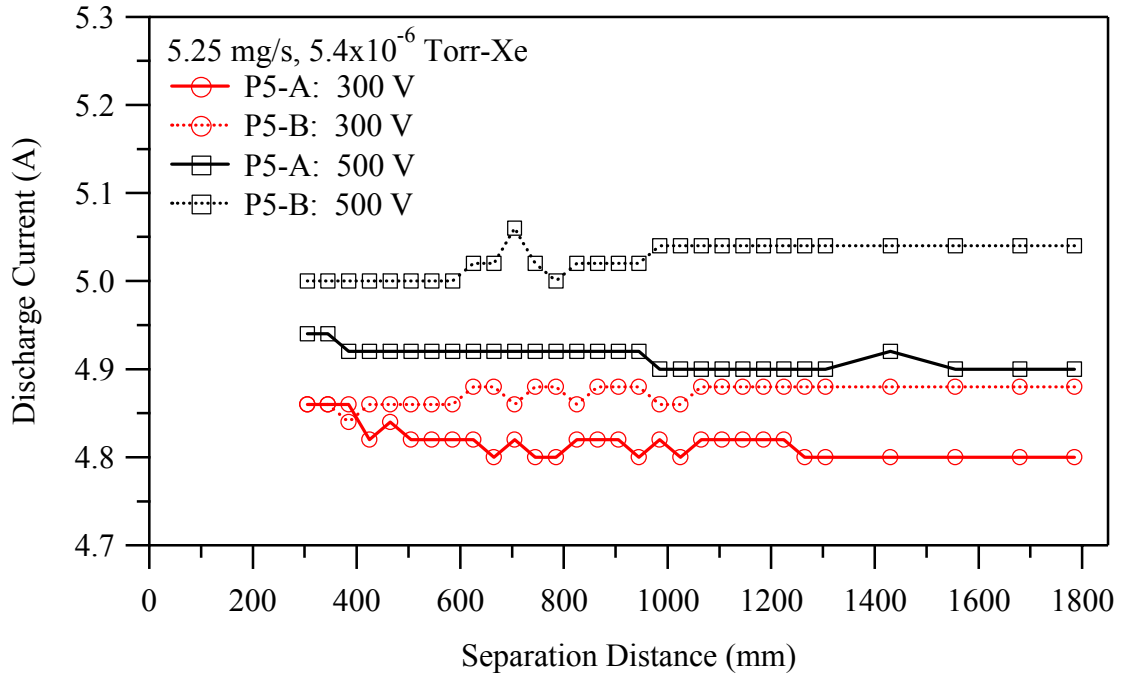


Figure 6-11: Sharing Cathode B - Discharge current as a function of thruster centerline distance 5.25 mg/s at a backpressure of 5.4×10^{-6} Torr-Xe

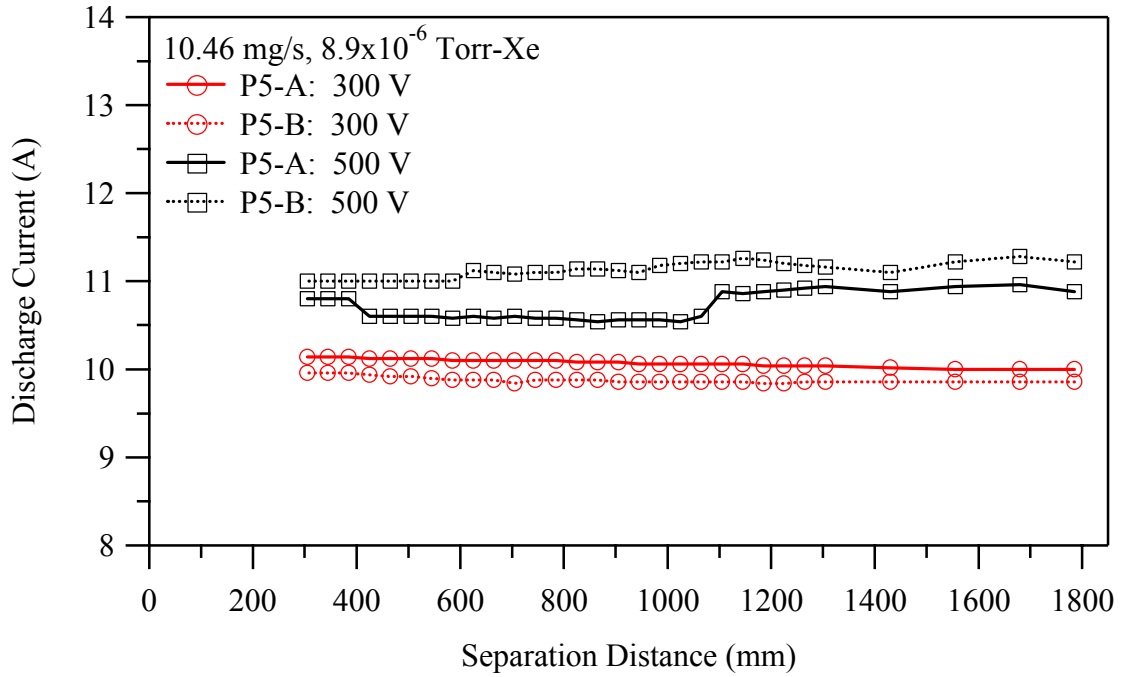


Figure 6-12: Sharing Cathode B - Discharge current as a function of thruster centerline distance 10.46 mg/s at a backpressure of 8.9×10^{-6} Torr-Xe

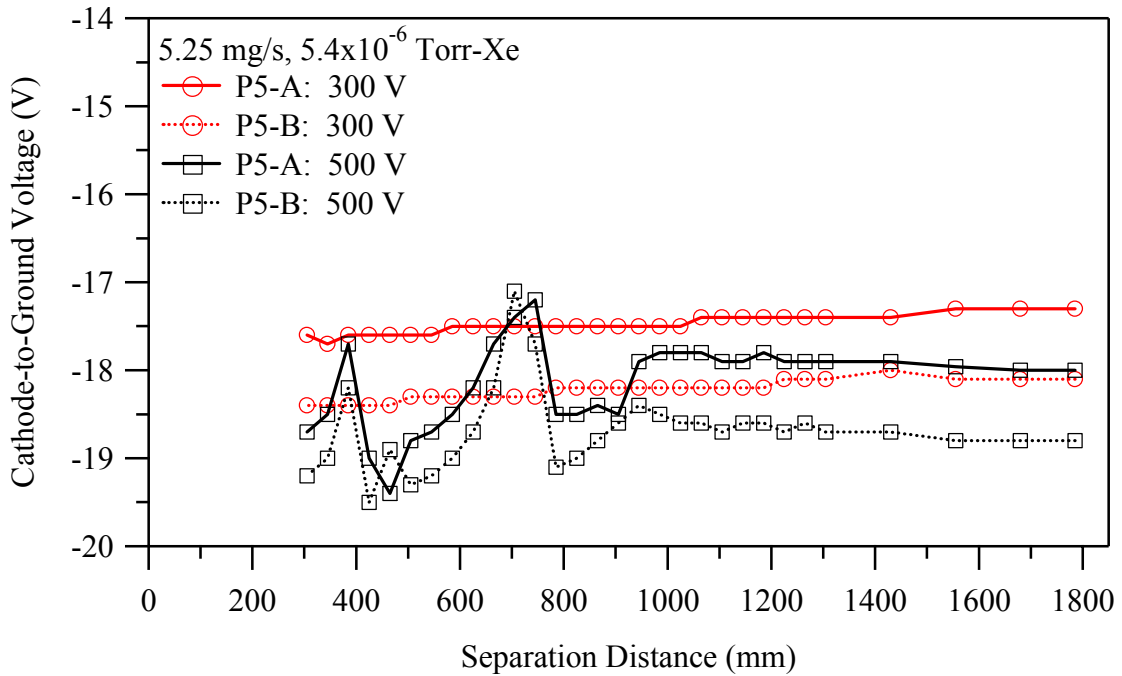


Figure 6-13: Sharing Cathode B - Cathode-to-ground voltage as a function of thruster centerline distance 5.25 mg/s at a backpressure of 5.4×10^{-6} Torr-Xe

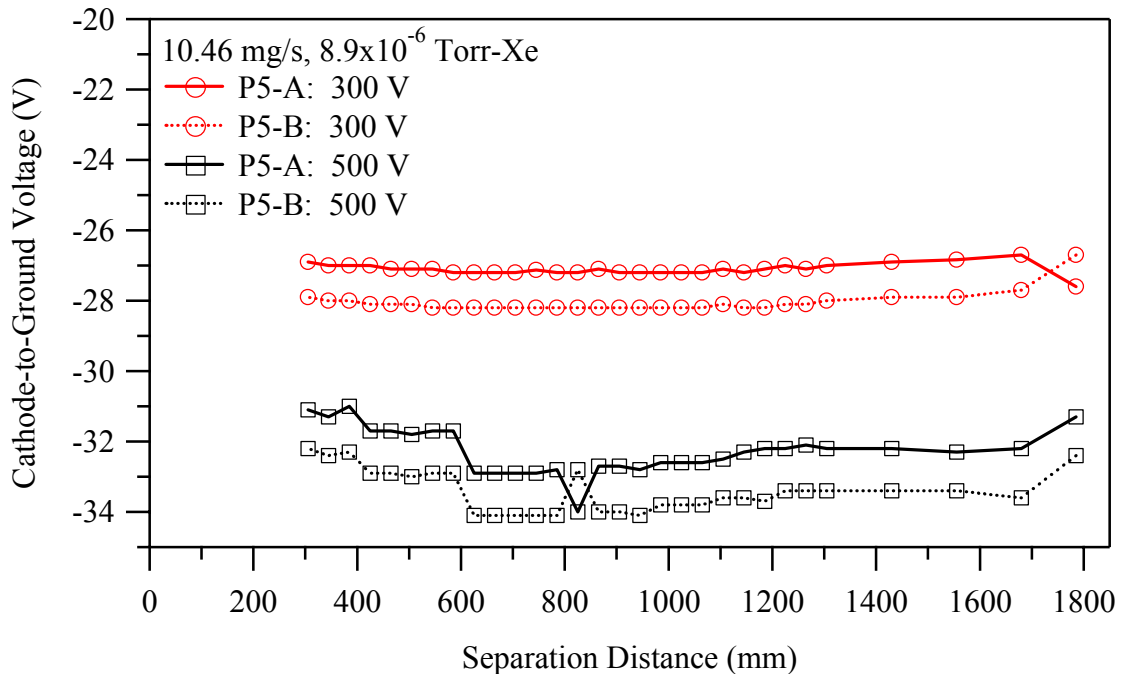


Figure 6-14: Sharing Cathode B - Cathode-to-ground voltage as a function of thruster centerline distance 10.46 mg/s at a backpressure of 8.9×10^{-6} Torr-Xe

6.2.3 Sharing a Centered Cathode

This portion of the experiment investigates the operation of P5-A and P5-B while sharing a centered cathode. Figure 6-1 shows the electrical cathode sharing circuit and Figure 6-15 shows a diagram of the physical configuration. For this experiment, P5-A and P5-B are operated from the centered cathode. The effect of cluster centerline separation distance is investigated by varying the separation distance between the thrusters and monitoring the discharge current and cathode-to-ground voltage. The initial thruster centerline separation distance is 390 mm and the measurements are taken in 50 mm increments out to a maximum separation distance of 1970 mm. Figures 6-16 and 6-17 present the discharge current as a function of separation distance while sharing cathode B for the 5.25 mg/s and 10.46 mg/s operation conditions, respectively. Figures 6-18 and 6-19 present the cathode-to-ground voltage as a function of separation distance

while sharing cathode B for the 5.25 mg/s and 10.46 mg/s operation conditions, respectively.

Figures 6-16 and 6-17 show that the discharge current is nearly constant as a function of centerline separation distance for the configuration in which the cluster shares a center cathode. There is a slight variation in the discharge current at a 10.46 mg/s anode flow rate due to the elevated facility backpressure. Figures 6-18 and 6-19 show that as the distance from the centered cathode increases, the magnitude of the cathode-to-ground voltage also increases until the separation distance between the cathode and each thruster element is 700 mm. Since the setup is bilaterally symmetric, the thruster centerline spacing is thus 1400 mm. The reason behind the change in cathode coupling voltage with separation distance is that the cathode is no longer immersed in the magnetic field of one of the thrusters. The lack of magnetic field strength weakens the coupling between the cathode and the Hall thruster, causing the magnitude of the cathode-to-ground voltage to increase by approximately 8 V. Fortunately, it appears that the cathode-to-ground voltage plateaus between 24 and 28 V below ground. The increase in cathode-to-ground voltage magnitude will reduce the exit velocity of the beam ions, but the difference is negligible in comparison to the discharge voltage (4% for 300 V, 2.4% for 500 V).

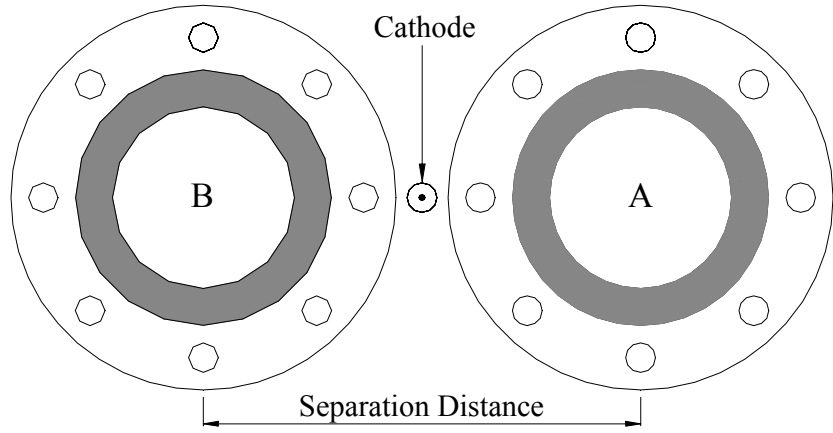


Figure 6-15: Diagram of cluster sharing a single cathode.

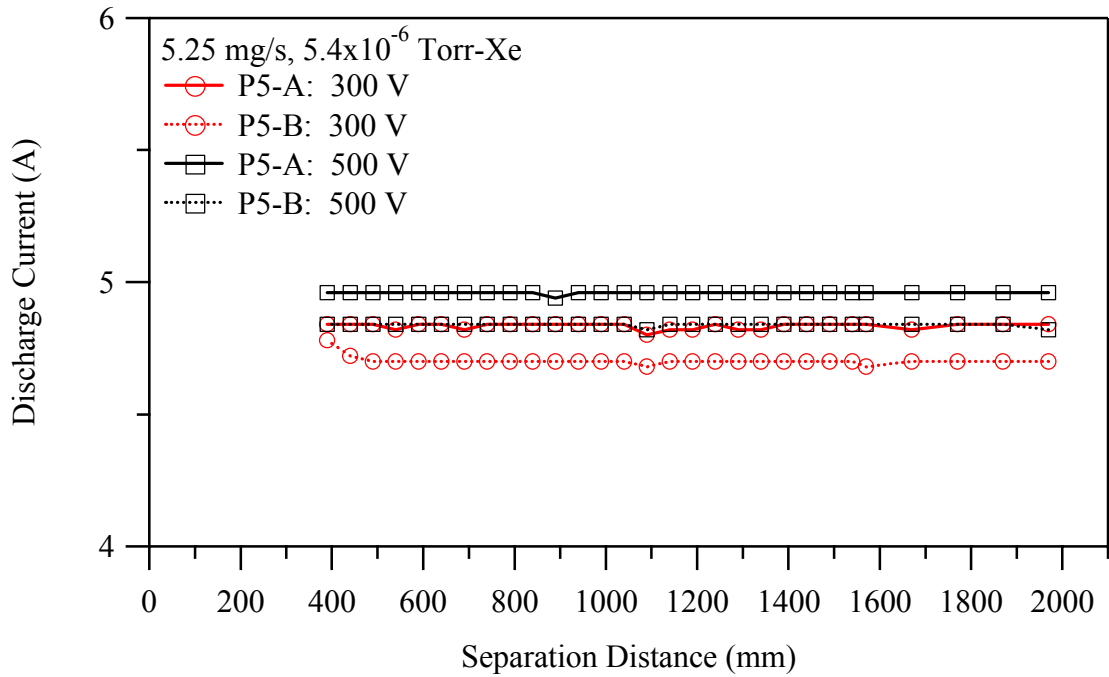


Figure 6-16: Sharing a Centered Cathode - Discharge current as a function of thruster centerline distance at an anode flow rate of 5.25 mg/s at a backpressure of 5.4×10^{-6} Torr-Xe.

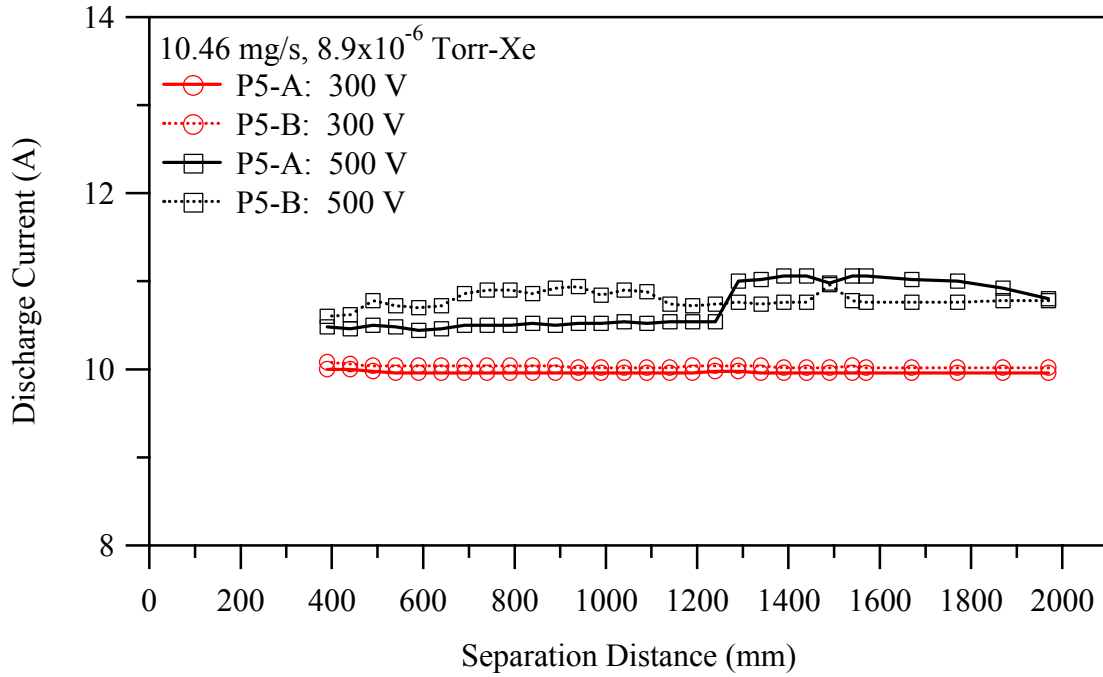


Figure 6-17: Sharing a Centered Cathode - Discharge current as a function of thruster centerline distance at an anode flow rate of 10.46 mg/s.

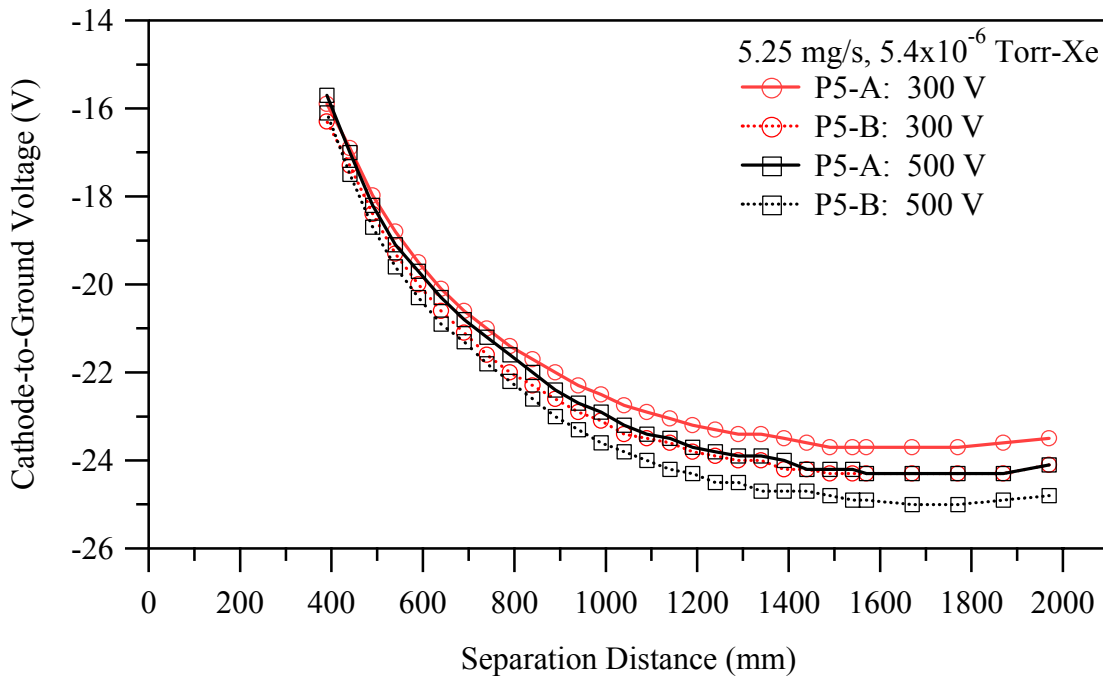


Figure 6-18: Sharing a Centered Cathode - Cathode-to-ground voltage as a function of thruster centerline distance at an anode flow rate of 5.25 mg/s.

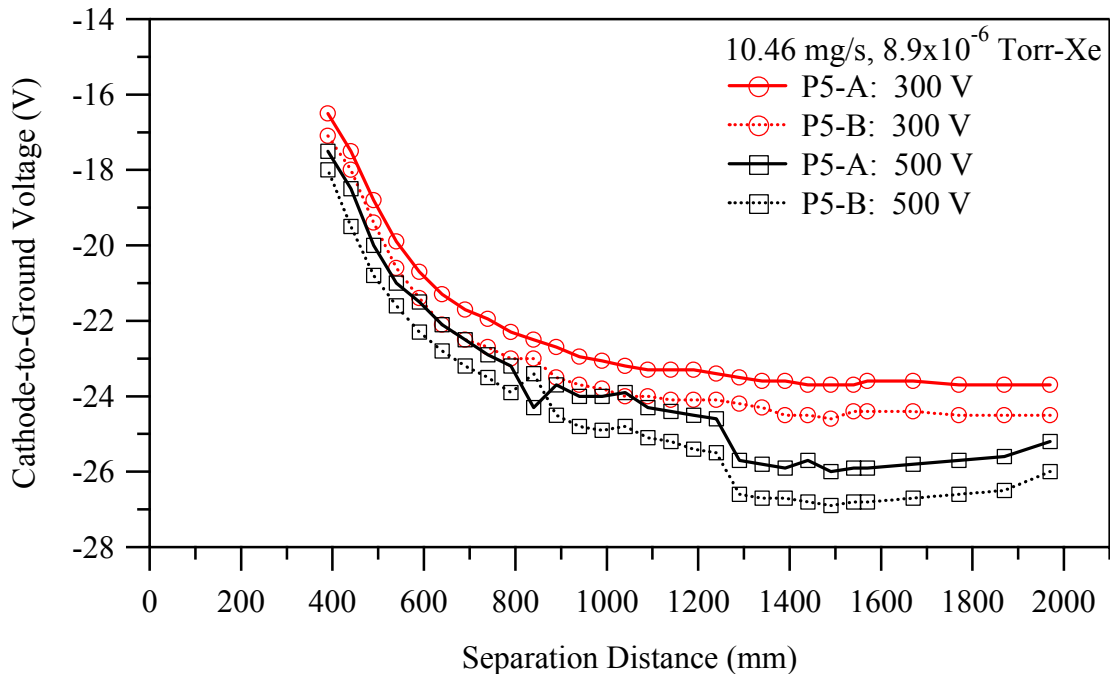


Figure 6-19: Sharing a Centered Cathode - Cathode-to-ground voltage as a function of thruster centerline distance at an anode flow rate of 10.46 mg/s.

6.2.4 Operation from a displaced Cathode

For this experiment, P5-B is operated alone from its own cathode. The effect of cathode separation distance is investigated by varying the distance between the cathode and thruster centerline distance. Figure 6-20 shows a diagram of the cathode displacement from the thruster setup. The cathode centerline is initially 20 cm from the thruster centerline. The axial table moves the cathode to a distance of 1.1 m from the thruster centerline. The thrust, discharge current, and cathode-to-ground voltage are measured in 10 cm increments at each of the 4 operating conditions.

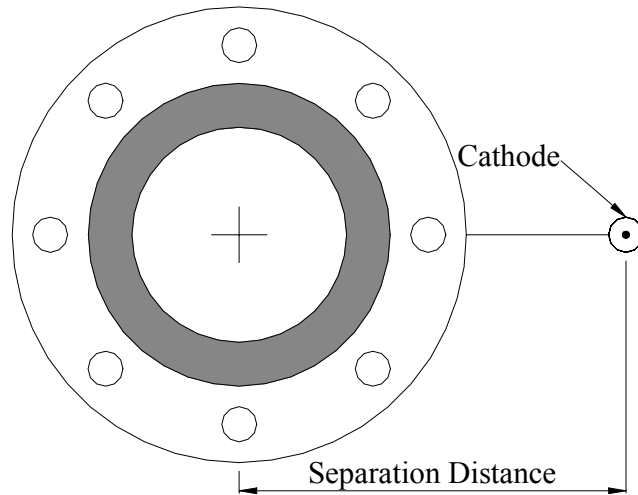


Figure 6-20: Diagram of the cathode displacement setup.

Figures 6-21 through 6-24 present the results of the cathode displacement investigation. Figure 6-21 shows traces of the thruster discharge current and the cathode-to-ground voltage as a function of the separation distance between the thruster and cathode centerlines. Figure 6-22 shows traces of the cathode to ground voltage as a function of the separation distance between the thruster and cathode centerlines. Figures 6-23 and 6-24 show traces of the thrust as a function of the separation distance between the thruster and cathode centerlines.

Figure 6-21 shows that the discharge current remains constant as a function of cathode displacement distance for all operating conditions. Figure 6-22 shows that cathode-to-ground voltage increases in magnitude as the cathode is displaced from the thruster. The magnitude of cathode to ground voltage for each operating condition asymptotes to its maximum value at a cathode separation distance of approximately 700 mm. As with the cluster sharing the centered cathode, this behavior is caused by the cathode losing the coupling effect of the magnetic field.

In addition, Figures 6-23 and 6-24 show that the thrust for each condition does not change as the cathode is displaced from the thruster centerline. There is some drift in the thrust measurements over the range of cathode displacement. This is because the translating axial table causes a deflection in the chamber floor grating to which the thrust stand is attached. The resulting thrust stand tilt, along with the vibration caused by the stepper motor rotation, creates a systematic error in the thrust measurements. Nonetheless, the drift in the thrust measurements is nearly within typical error bounds for the thrust stand. Thus, cathode displacement from the thruster does not appear to cause a change in the thrust produced by the Hall thruster.

It is clear that a Hall thruster operates efficiently from a cathode that is displaced from its usual position on the thruster. However, in order to position cathodes on spacecraft that are significantly displaced from the thruster centerline the thruster must start with the cathode in the displaced position. This study verifies that the P5 Hall thruster can be reliably restarted at the 300 V, 5.25 mg/s operating condition at an operating pressure of 3.5×10^{-6} Torr-Xe with a cathode displaced up to 1.1 m away from the thruster centerline.

The only difference between the displaced cathode start procedure and a normal Hall thruster start procedure is when the magnets are turned on. The first step in the displaced cathode starting procedure is to run the cathode on the keeper. Next, set the anode mass flow rate to the amount required for the operating condition. Then set the anode discharge voltage to that of the operating condition. The plasma breaks down in less than 2 seconds from the time that the anode voltage is reached. Finally, dial the magnets supplies up to the required coil currents for the given operating condition.

The size of the axial positioning table limits the cathode centerline to thruster centerline separation distance to 1.3 m. It may be possible to start and operate the thruster at greater cathode separation distances. The data show no trends that would prevent further separation.

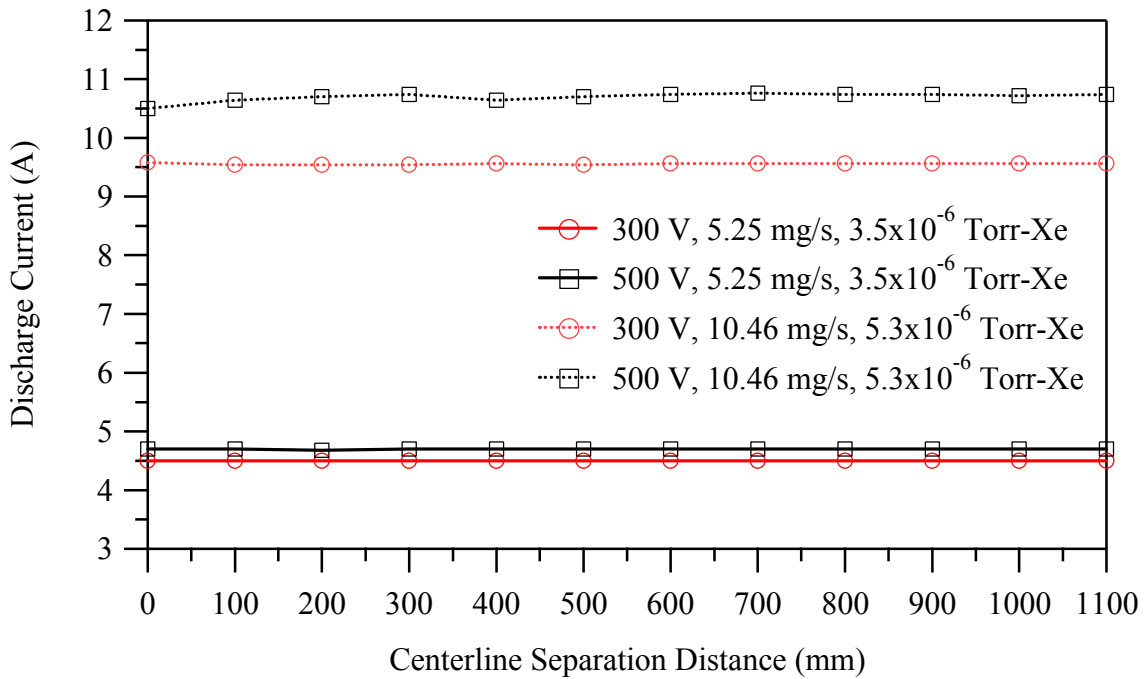


Figure 6-21: Discharge current versus thruster-to-centerline separation distance for a nominal pumping speed of 240 kl/s.

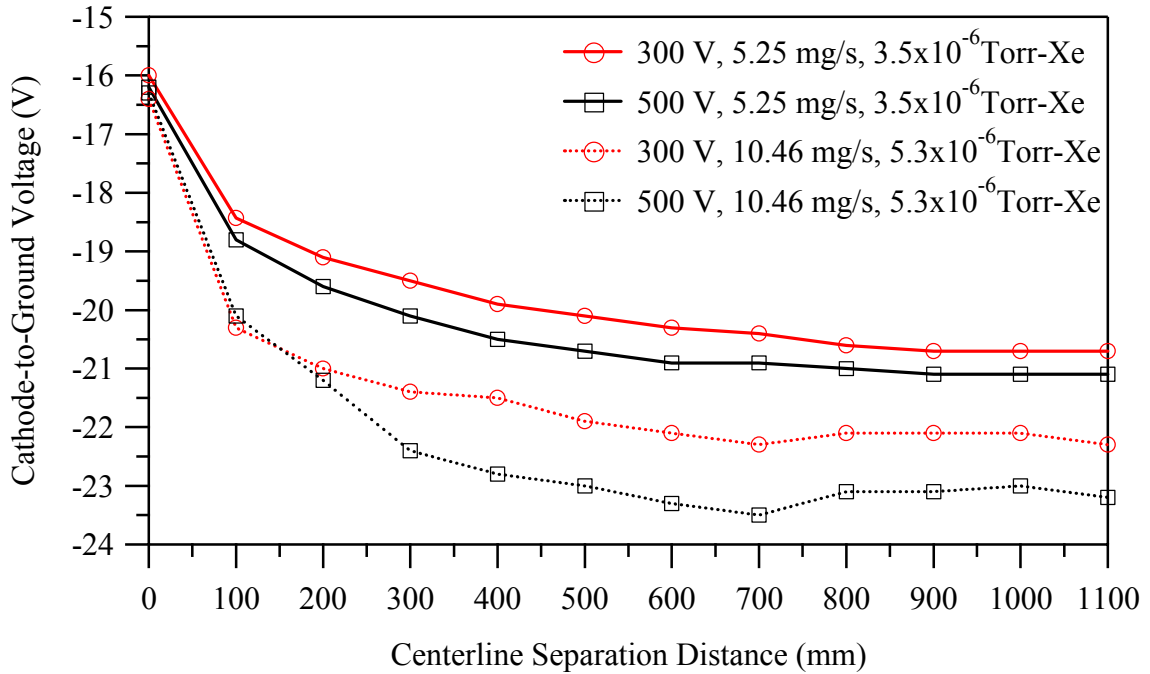


Figure 6-22: Cathode-to-ground floating voltage versus thruster-to-centerline separation distance for a nominal pumping speed of 240 kl/s.

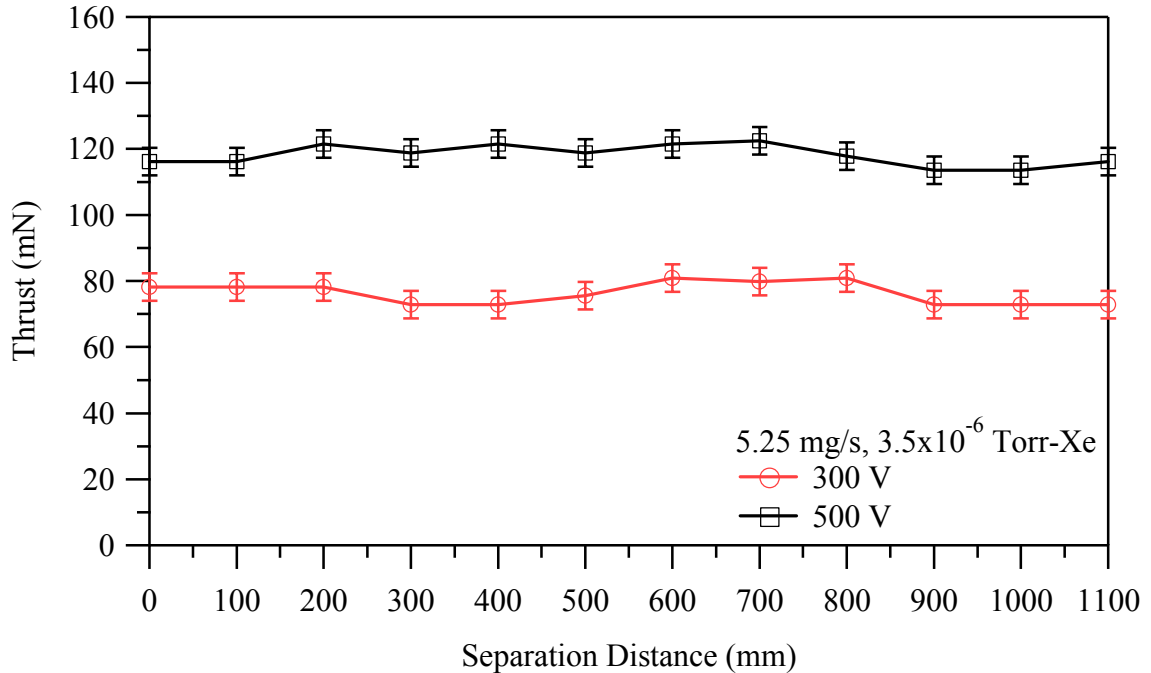


Figure 6-23: Thrust versus thruster-to-centerline separation distance for the 5.25 mg/s anode flow rate at a nominal pumping speed of 240 kl/s.

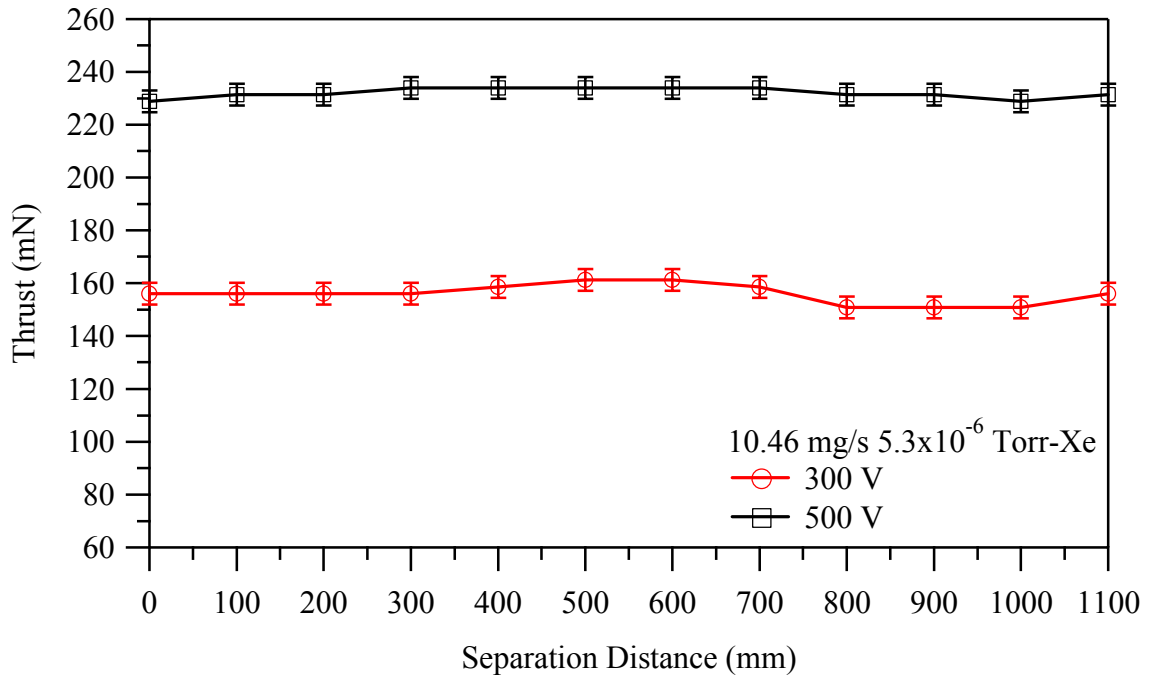


Figure 6-24: Thrust versus thruster-to-centerline separation distance for the 10.46 mg/s anode flow rate at a nominal pumping speed of 240 kl/s.

6.3 Conclusions

The study characterizes the operation of clustered thrusters for various separation distances and cathode sharing configurations. This investigation establishes that the gas of one thruster element is not ingested into the adjacent thruster at station 2 of the LVTF. It also shows that varying the separation distance between the thruster centerlines from 0.3 m (with the poles nearly touching) to 1.405 m causes no negative effects on the performance of the individual thrusters. The cathode sharing study shows that the cluster elements can operate in several cathode sharing configurations at thruster centerline separation distances up to 1.97 m. The only change in thruster performance occurs when the cathode is not immersed in the magnetic field of one of the thrusters. As the cathode leaves the magnet field, the magnitude of the cathode-to-ground voltage

increases by approximately 8 V; the cathode-to-ground voltage stabilizes for cathode to thruster centerline distances of 700 mm and greater. In addition, reliable restarts for cathode to thruster centerline distances of 1.3 m are verified. This knowledge opens the design envelope of EP-propelled spacecraft, and allows propulsion system redundancy by placing cathodes in convenient locations.

CHAPTER 7 CONCLUSIONS

This dissertation contains a large amount of data gathered in an effort to overcome the limitations of current vacuum facilities. The plume and performance characteristics of a monolithic thruster are measured over a wide range of pressures to facilitate the development of techniques for overcoming facility effects. Hall thruster clustering, another approach to developing high-power EP systems without deleterious facility effects, is investigated over the same range of operating conditions permitting the development of cluster performance and plume prediction tools, as well as establishing the feasibility of cathode sharing. This chapter summarizes the results of these efforts and suggests future areas of activity for understanding facility effects.

7.1 Calibration of a Vacuum Facility with a Numerical Tool

The pressure map experiment demonstrates that the measured pressure fields in a vacuum facility due to cold flow and hot flow from the Hall thruster anode and cathode are equivalent. This simplifies the determination of pressure in a vacuum facility containing a Hall thruster plume, and gives us the ability to calibrate a vacuum facility in terms of pressure.

The measured facility operating pressure at several cold flow rates is used to calibrate a Direct Simulation Monte Carlo model of the operating facility.⁸³ The numerical model can then make accurate predictions of the vacuum facility backpressure

for a given propellant flow rate. The numerical model includes facility geometry and pumping surface location. Simulations of the facility using the numerical model show the optimal location on the facility of an ionization gauge to monitor operating pressure. The simulation results also show any differences between the wall-mounted ionization gauge and the actual backpressure to which the plume expands. Thus, from a measurement of the pressure on the facility wall, the true operating pressure at the centerline of the facility can be determined.

In addition, the cluster plume pressure map verifies that the pressure map technique accurately measures the background pressure at very high facility backpressures. The pressure map also shows that the plume expansion of each thruster is not affected by the adjacent thruster.

7.2 Corrections for Facility Effects

The monolithic Hall thruster investigation thoroughly characterizes the effect of facility backpressure on the plume, performance, and operating characteristics of the thruster. The microscopic changes in the plasma due to the entrainment of the facility background gas lead to an increase in the magnitude of the discharge current oscillations. At the higher power operating conditions, the discharge oscillations appear to increase the electron current reaching the anode. This may be due to an increase in the number of electron-neutral collisions, which enhances the electron mobility to the anode.

Collisional processes downstream of the exit plane increase as the facility backpressure increases. The percentage of CEX ions in the plume increases with facility backpressure and is most noticeable in the plume of the ion current density measurements. A magnetically-filtered Faraday probe effectively removes the CEX ions

from the ion current density measurements. The width of the ion energy distribution per unit charge and the species fraction broaden with increasing backpressure. Due to the elevated pressures present at the ExB probe entrance during P5 operation, it is not possible to accurately measure the percentage of multiply-charged particles in the thruster plume. The existing ESA and ExB diagnostic designs require adjustments if they are to accurately measure plume parameters at elevated facility backpressure in high-density plasma.

The increase in beam ion collisions with the background gas lead to small changes in the floating potential, plasma potential, electron number density, and electron temperature. While the change in each of these parameters is small, the overall effect of increased facility backpressure leads to an increase in the thrust of the Hall thruster.

Because the increase in thrust with increasing backpressure appears to be the sum of each of these effects, a straightforward method to correct thrust is not clear. However, this investigation bounds the increase in thrust for a given increase in facility backpressure. To correct performance measurements taken at elevated backpressures, one must take into account the changes in the percentage of multiply-charged ions, the ion energy distribution, and the plume divergence as the facility backpressure increases. The author believes the most fruitful approach is to use these experimental data to validate a numerical model which simulates Hall thruster performance over a wide range of pressures. The model can be calibrated with data collected at an arbitrary pressure for a given thrust, and then used to predict the on-orbit performance.

This work shows that Randolph's ingestion explanation does not adequately account for the elevated discharge current measured at elevated facility backpressures.

The Hall thruster discharge current oscillations, electron temperature, electron number density, floating potential, plasma potential, ion current density, ion energy distribution, ion species fraction, and performance over a range of facility operating pressures above and below Randolph's suggested pressure of 1.0×10^{-5} Torr-Xe has been fully characterized. The results show that Randolph's criterion for plume measurements does not hold. The variation of the facility backpressure did not lead to a clear technique to correct the performance of the Hall thruster operating at elevated backpressure.

7.3 Prediction of Cluster Performance

The effect of clustering on plume performance is characterized as a function of backpressure. Furthermore, the extent to which a monolithic thruster's performance and plume are affected by an adjacent thruster are also characterized. The thrust is equal to the sum of the thrust of the monolithic thrusters at the 5.25 mg/s anode flow rate. The sum of the thrust of the monolithic thrusters results in an under prediction of 5% of the cluster thrust for the 10.46 mg/s anode flow rate.

The large flow rate present during the cluster investigations allows characterization of the effect of backpressure on the monolithic thruster elements at pressures higher than those possible with the monolithic thruster. The backpressure effects still appear to gradually increase with increasing backpressure. The investigation shows that specifying a high-power Hall thruster cluster should not cause integration problems using the current design rules for integrating monolithic Hall thrusters onto spacecraft.

The cluster spacing criterion based on magnetic field in the inner channel appears to be adequate for performance measurements. Further verification of the

criterion requires measurement of the cluster performance for different separation distances. It may also be possible to move the elements of the cluster closer together without adversely affecting their performance.

One of the most critical components of Hall thruster integration is ensuring that the beam does not impinge on any of the spacecraft surfaces. The ion current density measurements show that the outer half of the cluster plume is nearly identical to its plume when operated alone. Thus, no increase in thruster element plume divergence angle is expected when operating in the cluster configuration. This investigation shows the changes in the floating potential, plasma potential, electron number density, and electron temperature are small in comparison to the error in the measurements and the magnitude of the values.

In addition, the measurements of ion energy per unit charge distribution do not detect energetic ions in the plume of the cluster at angles greater than those measured with the monolithic thruster. Furthermore, ion species traces do not show a large number of multiply-charged ions at any location in the plume. The alignment problems posed by Configuration 2 make it difficult to compare the results of the ESA and ExB probe to those of the monolithic thruster. A structure should be created to allow the diagnostics to characterize the plume in Configuration 1. Unfortunately, the physical location of these measurements does not allow us to verify Beal's prediction techniques.

7.4 Cathode Sharing

To further understand the feasibility of clustering Hall thrusters on spacecraft, a study of thruster centerline spacing and cathode-to-thruster separation distance is performed. The study characterizes the operation of cluster thrusters for various

separation distances and cathode sharing configurations. This investigation has established that the gas of one thruster element is not ingested into the adjacent thruster at Station 2 of the LVTF. It also shows that varying the separation distance between the thruster centerlines from 0.3 m (with the poles nearly touching) to 1.405 m causes no negative effects on the performance of the individual thrusters.

Cluster elements can operate in several cathode sharing configurations over a range of thruster centerline separation distances up to 1.97 m. When the cathode is not immersed in the magnet field of one of the thrusters, the magnitude of the cathode-to-ground increases by approximately 8 V. The increase stabilizes for cathode-to-thruster centerline distances of 700 mm and greater. Furthermore, reliable restarts are verified for cathode-to-thruster centerline distances of 1.3 m. This knowledge is of great importance to spacecraft designers implementing electric propulsion systems.

7.5 Facility Design

The results of this work shed light on future facility designs that can reduce facility effects without a significant increase above current facility pumping speeds. The results of Chapter 5 show that changing the separation distance between the thruster centerlines over from 0.3 to 2.0 m caused no change in the discharge current of the thrusters. This means that un-ionized propellant emanating from each thruster is not ingested by the adjacent thruster. Instead, the gas undergoes a free molecular expansion into the chamber.

On-orbit, no particle that leaves the thruster ever returns. Thus, the vacuum facility must duplicate this fact as closely as possible to reduce facility effects. The plume of a Hall thruster is composed of 3 distinct populations: beam ions, CEX ions, and

un-ionized neutral propellant. We must consider each of these components when designing our pumping scheme to make optimum use of the facility pumping speed. Approximately 10% of the pumping surfaces should be placed in a concentric pattern around the thruster to evacuate the un-ionized propellant and CEX ions in the immediate vicinity of the thruster. The remaining 90% of the pumping speed should be positioned downstream of the thruster in protective-cryogenic halo baffles. The halo baffles serve as a thermal barrier for the cryosurfaces and scatter beam ions toward the pumping surface. This split location pumping scheme duplicates the on-orbit environment – any particle that leaves the thruster never returns. This creates a significant reduction in facility effects without an enormous increasing in pumping speed.

7.6 Suggestions for Future Work

This dissertation has investigated many of the fundamental issues of facility effects on Hall thruster performance and plume characteristics. In addition, the feasibility of high-power Hall thruster clustering has been addressed. While many of the fundamental questions have been answered, several new questions have been developed. The questions that stem from each of the investigation areas are discussed below as well as suggested approaches.

7.6.1 Validation of Numerical Tool

The cluster pressure map data provide an excellent test case to validate a 3-dimensional numerical model of a Hall thruster expansion into a vacuum chamber. Currently, Boyd is developing this type of model and these data should be compared to

the model results. The results of the model would allow us to investigate the possibility of neutral propellant ingestion from one cluster element into the adjacent element.

7.6.2 Faraday Probe Design Recommendations

The following suggestions should be considered when selecting a Faraday probe design. The collector should be spray-coated with tungsten to reduce secondary electron emission. The guard ring of the probe should be designed and positioned to ensure a flat, uniform sheath over the collector surface. The CEX and elastically scattered ions present at angles greater than 40° from thruster centerline must be actively filtered away from the Faraday probe collector surface to reduce the effect of facility backpressure on the measurements. Placing a magnetically-filter in front of the nude Faraday probe performs this function well.

7.6.3 Energy Spectra and Species Fractions measurements in the Cluster Plume

Measurements of the ion energy distribution and species fractions were measured in cluster Configuration 2. These measurements did not allow us to make a direct comparison of plume properties with the monolithic Hall thruster operating alone. A structure should be created to allow measurements of the energy spectra and species fractions in Configuration 1. These data would allow us to determine if the ion energy distribution function and ion species fractions are affected by the adjacent thruster plume.

7.6.4 Validation of Cluster Performance Predictions

The cluster performance prediction technique must be validated for higher power Hall thrusters. The next level of cluster investigation should be performed with a cluster of large (~ 10 kW) Hall thrusters. To insure that the facility pressure effects are

negligible, the study should be performed in Vacuum Facility 5 at NASA GRC. A systematic increase in cluster power and validation of the prediction methods at those powers will insure that cluster technology will be at the level of maturity required to fulfill the Project Prometheus propulsion requirements.

Chapter 4 presented an argument that states that the increase in discharge current amplitude and discharge current with backpressure is caused by an increase in the number of electron-neutral collisions in the discharge chamber. These collisions then enhance the electron mobility to the anode. To validate this argument, further work should be done to compare the classical diffusion to the Bohm diffusion.

7.6.5 Cluster Spacing

Cluster spacing should be further studied with a commercially available 2D cluster of Hall thrusters to verify that the behavior is independent of thruster design and power. The cluster elements should be small (< 1 kW) so that the experiments can be performed at operating pressure lower than those encountered during the P5 cluster experiments.

REFERENCES

1. Morozov, Stationary Plasma Thruster (SPT) Development Steps and Future Perspectives, IEPC-93-101, 23rd International Electric Propulsion Conference, Seattle, WA, Sept. 13-16, 1993.
2. Sovey, J. S., Rawlin, V. K., Patterson, M. J., A Synopsis of Ion Propulsion Development Projects in the United States: SERT I to Deep Space I, AIAA-99-2270, 35th Joint Propulsion Conference and Exhibit, Los Angeles, CA, June 20-24, 1999.
3. Zhurin, V. V., Kaufman, H. R., Robinson, R. S., Physics of Closed Drift Thrusters, *Plasma Sources Science and Technology*, Vol. 8, No. R1-R20.
4. Oleson, S. R., Electric Propulsion Technology Development for the Jupiter Icy Moons Orbiter Project, AIAA-2004-3449, 40th Joint Propulsion Conference and Exhibit, Fort Lauderdale, FL, July 11-14, 2004.
5. Manzella, D. H., Penko, P. F., De Witt, K. J., Keith Jr., T. G., Test-Cell Pressure Effects on the Performance of Resistojets, *Journal of Propulsion and Power*, Vol. 7, No. 2, pp. 269-274.
6. Pivrotto, K., Deininger, Brophy, The Design and Operating Characteristics of a 30 kW Thermal Arcjet Engine for Space Propulsion, AIAA-86-1508, Joint Propulsion Conference, 1986.
7. Haag, T. W., Recent Testing of 30 kW Hydrogen Arcjet Thrusters, AIAA-93-1902, 29th Joint Propulsion Conference and Exhibit, Monterey, CA, June 28 - July 1, 1993.
8. Smith, Y., Armbruster, Roberts, Lichtin, Beck, Flight Qualification of a 1.8 kW Hydrazine Arcjet System, IEPC-93-007, 23rd International Electric Propulsion Conference, Seattle, WA, Sept. 13-16, 1993.
9. Goodfellow, K., Polk, J. E., Design and Development of a 3 to 10 kW Ammonia Arcjet, IEPC-93-078, 23rd International Electric Propulsion Conference, Seattle, WA, Sept. 13-16, 1993.
10. Boyd, I. D., Beattie J. R., Cappelli, M., Chamber Effects on Plume Expansion for a Low-Power Hydrogen Arcjet, IEPC-93-126, 23rd International Electric Propulsion Conference, Seattle, WA, Sept. 13-16, 1993.
11. Jahn, R. G., *Physics of Electric Propulsion*, McGraw-Hill Book Company, 1968.
12. LaPointe, M. R., Mikellides, P. G., High Power MPD Thruster Development at the NASA Glenn Research Center, AIAA-2001-3499, CR-2001-211114, 37th Joint Propulsion Conference and Exhibit, Salt Lake City, UT, July 8-11, 2001.

13. Mikellides, P., Pulsed Inductive Thruster (PIT) Modeling and Validation Using the MACH2 Code, IEPC-2003-0135, 28th International Electric Propulsion Conference, Toulouse, France, Mar. 17-21, 2003.
14. Vondra, T., Flight Qualified Pulsed electric Thruster for Satellite Control, *Journal of Spacecraft and Rockets*, Vol. 11, No. 9, pp. 613.
15. Gulczinski III, F. S., Spores, R. A., Stuhlberger, J., In-Space Propulsion, AIAA-2003-2588, International Air and Space Symposium and Exposition: The Next 100 Y, Dayton, OH, July 14-17, 2003.
16. Ziemer, J., Gallimore, A. D., Sub-Micronewton Thrust Measurements of Indium Field Emission Thrusters, IEPC-03-0247, 28th International Electric Propulsion Conference, Toulouse, France, Mar. 17-21, 2003.
17. Pote, B., Hruby, V., Tedrake, R., Performance of a Multi-Kilowatt Non-Circular Discharge Hall Thruster, AIAA-2000-3249, 36th Joint Propulsion Conference & Exhibit, Huntsville, AL, July 16-19, 2000.
18. Hargus, W. J., Cappelli, M., Development of a Linear Hall Thruster, AIAA-98-3336, 34th Joint Propulsion Conference and Exhibit, Cleveland, OH, July 12-15, 1998.
19. Beal, B. E., Gallimore, A. D., Development of the Linear Gridless Ion Thruster, AIAA-2001-3649, 37th Joint Propulsion Conference, Salt Lake City, Utah, July 8-11, 2001.
20. Meezan, G., Cappelli, M., Linear Geometry Hall Thruster with Boron Nitride and Diamond Walls, IEPC-2001-39, 27th International Electric Propulsion Conference, Pasadena, CA, Oct. 15-19, 2001.
21. Morozov, Electric Propulsion Thrusters and Plasmadynamics, IEPC-95-05, 24th International Electric Propulsion Conference, Moscow, Russia, Sept., 1995.
22. Meyer, R. X., A Space-Charge-Sheath Electric Thruster, *AIAA Journal*, Vol. 5, No. 11, pp. 2507-9.
23. Hofer, R. R., Peterson, P. Y., Gallimore, A. D., A High Specific Impulse Two-Stage Hall Thruster with Plasma Lens Focusing, IEPC-01-036, 27th International Electric Propulsion Conference, Pasadena, CA, Oct. 15-19, 2001.
24. Sankovic, J. M., Hamley, J. A., Haag, T. W., Performance Evaluation of the Russian SPT-100 Thruster at NASA LeRC, IEPC-93-094, 23rd International Electric Propulsion Conference, Seattle, WA, Sept. 13-16, 1993.
25. Garner, C. E., Brophy, J. R., Polk, J. E., Pless, L. C., A 5,730-Hr Cyclic Endurance Test of The SPT-100, AIAA-95-2667, 31st Joint Propulsion Conference and Exhibit, San Diego, CA, July 10-12, 1995.

26. Hargus, W. J., Fife, J., Mason, L., Jankovsky, R. S., Haag, T. W., Pinero, Snyder, Preliminary Performance Results of the High Performance Hall System SPT-140, AIAA-2000-3250, 36th Joint Propulsion Conference and Exhibit, Huntsville, AL, July 17-19, 2000.
27. Fife, J. M., Hargus, W. Jr., Jaworske, D. A., Sarmiento, C. J., Mason, L., Jankovsky, R. S., Snyder, J. S., Malone, S., Haas, J. M., Gallimore, A. D., Spacecraft Interaction Test Results of the High Performance Hall System SPT-140, AIAA-2000-3521, 36th Joint Propulsion Conference and Exhibit, Huntsville, AL, July 17-19, 2000.
28. Pollard, J. E., Diamant, K. D., Khayms, V., Werthman, L., King, D. Q., de Grys, K. H., Ion Flux, Energy, and Charge-State Measurements for the BPT-4000 Hall Thruster, AIAA-2001-3351, 37th Joint Propulsion Conference, Salt Lake City, UT, July 8-11, 2001.
29. Mason, L. S., Jankovsky, R. S., Manzella, D. H., 1000 Hours of Testing on a 10 Kilowatt Hall Effect Thruster, AIAA-2001-3773, 37th Joint Propulsion Conference and Exhibit, Salt Lake City, UT, July 8-11, 2001.
30. Britt, N., McVey, J., Electric Propulsion Activities in U.S. Industries, AIAA-2002-3559, 38th Joint Propulsion Conference and Exhibit, Indianapolis, IN, July 7-10, 2002.
31. Jankovsky, R. S., Jacobson, D., Rawlin, V. K., NASA's Hall Thruster Program, AIAA-2001-3888, 37th Joint Propulsion Conference and Exhibit, Salt Lake City, UT, July 8-11, 2001.
32. Spanjers, G. G., Birkan, M., Lawrence, The USAF Electric Propulsion Research Program, AIAA-2000-3146, 36th Joint Propulsion Conference and Exhibit, Huntsville, AL, Jul. 17-19, 2000.
33. Beal, B. E., Gallimore, A. D., The Effects of Clustering Multiple Hall Thrusters on Plasma Plume Properties, AIAA-2003-5155, 39th Joint Propulsion Conference and Exhibit, Huntsville, AL, July 20-23, 2003.
34. "Project Prometheus," [on line catalog], <http://spacescience.nasa.gov/missions/prometheus.htm> [cited May 1]. pp.
35. King, L. B., Gallimore, A. D., Marrese, C. M., Transport-Property Measurements in the Plume of an SPT-100 Hall Thruster, *Journal of Propulsion and Power*, Vol. 14, No. 3, pp. 327-335.
36. Semenkin, A., Kim, V., Gorshkov, O., Jankovsky, R. S., Development of Electric Propulsion Standards - current status and further activity, IEPC-2001-070, 27th International Electric Propulsion Conference, Pasadena, CA, Oct. 15-19, 2001.

37. Hruby, V., Monheiser, J., Pote, B., Rostler, P., Kolencik, J., Freeman, C., Development of Low Power Hall Thrusters, AIAA-99-3534, 30th Plasmadynamics and Lasers Conference, Norfolk, VA, June 28 - July 1, 1999.
38. Randolph, T., Kim, V., Kaufman, H., Kozubsky, K., Zhurin, V. V., Day, M., Facility Effects on Stationary Plasma Thruster Testing, IEPC-93-093, 23rd International Electric Propulsion Conference, Seattle, WA, Sept. 13-16, 1993.
39. King, L. B., Gallimore, A. D., Ionic and Neutral Particle Transport Property Measurements in the Plume of an SPT-100, AIAA-96-2712, 32nd Joint Propulsion Conference, Lake Buena Vista, FL, July 1-3, 1996.
40. Boyd, I. D., Interactions Between Spacecraft and Thruster Plumes, *Journal of Spacecraft and Rockets*, Vol. 38, No. 3, pp. 380-387.
41. Hofer, R. R., Peterson, P. Y., Gallimore, A. D., Characterizing Vacuum Facility Backpressure Effects on the Performance of a Hall Thruster, IEPC-01-045, 27th International Electric Propulsion Conference, Pasadena, CA, Oct. 15-19, 2001.
42. Hofer, R. R., Walker, M. L. R., Gallimore, A. D., A Comparison of Nude and Collimated Faraday Probes for Use with Hall Thrusters, IEPC-01-20, 27th International Electric Propulsion Conference, Pasadena, CA, Oct. 15-19, 2001.
43. de Grys, K. H., Tilley, D. L., Aadland, R. S., BPT Hall Thruster Plume Characteristics, AIAA-99-2283, 35th Joint Propulsion Conference and Exhibit, Los Angeles, CA, June 20-24, 1999.
44. Pollard, J. E., Diamant, K. D., Hall Thruster Plume Shield Wake Structure, AIAA-2003-5018, 39th Joint Propulsion Conference, Huntsville, AL, July 20-23, 2003.
45. Walker, M. L. R., Gallimore, A. D., Cai, C., Boyd, I. D., Pressure Map of a Facility as a Function of Flow Rate to Study Facility Effects, AIAA-2002-3815, 38th Joint Propulsion Conference and Exhibit, Indianapolis, IN, July 7-10, 2002.
46. Beal, B. E., Gallimore, A. D., Hargus, W. Jr., Preliminary Plume characterization of a Low-Power Hall Thruster Cluster, AIAA-2002-4251, 38th Joint Propulsion Conference and Exhibit, Indianapolis, IN, July 7-10, 2002.
47. Beal, B. E., Gallimore, A. D., Energy Analysis of a Hall Thruster Cluster, IEPC-03-035, 28th International Electric Propulsion Conference, Toulouse, France, March 17-21, 2003.
48. Hargus, W. J., Reed, The Air Force Clustered Hall Thruster Program, AIAA-2002-3678, 38th Joint Propulsion Conference and Exhibit, Indianapolis, IN, Jul. 7-10, 2002.

49. Manzella, D. H., Sankovic, J. M., Hall Thruster Ion Beam Characterization, AIAA-95-2927, 31st Joint Propulsion Conference and Exhibit, San Diego, California, July 10-12, 1995.
50. Beal, B. E., *Clustering of Hall Effect Thrusters for High-Power Electric Propulsion Applications*, Ph.D. Dissertation, University of Michigan Department of Aerospace Engineering, 2003.
51. Zakharenkov, L. E., Semenkin, A. V., Urchenko, N. A., Tverdokhlebov, S. O., Garkusha, V. I., Bebedev, T. V., Podkolsin, S. N., Fife, J. M., Study of Multi Thruster Assembly Operation, IEPC-2003-0311, 28th International Electric Propulsion Conference, Toulouse, France, Mar. 17-21, 2003.
52. Teverdokhlebov, S. O., Semenkin, A. V., Baranov, V. I., Zakharenkov, L. E., Soldukihin, A. E., Consideration of Cluster Design Approach for High Power Hall Propulsion, AIAA-2003-0494, 41st Aerospace Sciences Meeting and Exhibit, Reno, Nevada, Jan. 6-9, 2003.
53. Haas, J. M., Gulczinski III, F. S., Gallimore, A. D., Spanjers, G. G., Spores, R. A., Performance Characteristics of a 5 kW Laboratory Hall Thruster, AIAA-98-3503, 34th Joint Propulsion Conference and Exhibit, Cleveland, OH, July 12-15, 1998.
54. Hofer, R. R., Gallimore, A. D., Recent Results from Internal and Very-Near-Field Plasma Diagnostics of a High Specific Impulse Hall Thruster, IEPC-2003-037, 28th International Electric Propulsion Conference, Toulouse, France, Mar. 17-21, 2003.
55. Dushman, S., *Scientific Foundations of Vacuum Technique*, Vol. 4, Wiley, New York, 1958.
56. Moore, J. H., Davis, C., C., Coplan, M., A., *Building Scientific Apparatus*, Westview Press, Boulder Colorado, 2003.
57. Varian, "Vacuum Measurement," *Vacuum Measurement Catalog* [on line catalog], URL: <http://www.varianinc.com/cgi-bin/nav?products/vacuum/measure/gauges&cid=JPLHPIHFO> [cited 15 April 2004]. 2003 Product Catalog pp. 46
58. Tilford, C. R., Sensitivity of hot cathode ionization gages, *Journal of Vacuum Science and Technology*, Vol. A3, No. 3, pp. 546-550.
59. Lafferty, J. M., *Vacuum Science Technology*, John Wiley & Sons, Inc., 1998.
60. Redhead, The measurement of vacuum pressures, *Journal of Vacuum Science and Technology*, Vol. A2, No. 2, pp.
61. Chung, P. M., Talbot, L., Touryan, K. J., Electric Probes in Stationary and Flowing Plasmas: Part 1. Collisionless and Transitional Probes Part 2. Continuum Probes, *AIAA Journal*, Vol. 12, No. 2, pp. 133-154.

62. Hershkowitz, N., *How Langmuir Probes Work*, in *Plasma Diagnostics*, M. J. Auciello, Flamm, D. L., Editor. 1980, Academic Press: Washington, DC. p. 113-183.
63. Schott, L., "*Electrical Probes*" in *Plasma Diagnostics*, in *Plasma Diagnostics*, e. b. W. Lochte-Holtgreven, Editor. 1995, American Institute of Physics: Woodbury, NY.
64. Hutchinson, I. H., *Principles of Plasma Diagnostics*, Cambridge University Press, New York, 1987.
65. Laframboise, J. G., *UTIAS Report No. 100*. 1966, University of Toronto.
66. Analytical, H., *Handbook of Plasma Diagnostics*. 2000, Hiden Analytical Limited.
67. Walker, M. L. R., Hofer, R. R., Gallimore, A. D., The Effects of Nude Faraday Probe Design and Vacuum Facility Backpressure on the Measured Ion Current density Profile of Hall Thruster Plumes, AIAA-2002-4253, 38th Joint Propulsion Conference and Exhibit, Indianapolis, IN, July 7-10, 2002.
68. Haas, J. M., *Low-Perturbation Interrogation of the Internal and Near-field Plasma Structure of a Hall Thruster using a High-Speed Probe Positioning System*, Ph.D. Dissertation, University of Michigan Aerospace Engineering, 2001.
69. Gulczinski, F. S., *Examination of the Structure and Evolution of Ion Energy Properties of a 5 kW Class Laboratory Hall Effect Thruster at Various Operational Conditions*, Ph.D. Dissertation, University of Michigan Aerospace Engineering, 1999.
70. Rovey, J. L., Walker, M. L. R., Gallimore, A. D., Peterson, P. Y., Evaluation of a Magnetically-Filtered Faraday Probe for measuring the ion current density profile of a Hall thruster, AIAA-2004-3948, 40th Joint Propulsion Conference, Fort Lauderdale, FL, July 11-14, 2004.
71. Kaminsky, M., *Atomic and Ionic Impact Phenomena on Metal Surfaces*, Springer-Verlag, New York, NY, 1965.
72. Varga, P., Winter, H., Determination of metastable fractions in noble-gas-ion beams, *Physical Review A*, Vol. 18, No. 6, pp. 2453-2458.
73. Gulczinski III, F. S., Gallimore, A. D., Near-Field Ion Energy and Species Measurements of a 5-kW Hall Thruster, *Journal of Propulsion and Power*, Vol. 17, No. 2, pp. 418-427.
74. ESA, *Field Emission Electric Propulsion. Industrial Development of Emitter Modules, Phase 1, Vol. 1, Final Report*.
75. Pollard, J. E., Lichtin, D., Janson, Cohen, H., Time-resolved mass and energy analysis by position-sensitive time-of-flight detection, *Review of Scientific Instruments*, Vol. 61, No. 10, pp. 3171-3180.

76. Pollard, J. E., Plume Angular, Energy, and Mass Spectral Measurements with T5 Ion Engine, AIAA-95-2920, Joint Propulsion Conference and Exhibit, 1995.
77. Hofer, R. R., Haas, J. M., Gallimore, A. D., Development of a 45-degree parallel-plate Electrostatic Energy Analyzer for Hall Thruster Plume Studies: Preliminary Data, IEPC-99-113, 26th International Electric Propulsion Conference, 1999.
78. King, L. B., Gallimore, A. D., Ion Energy Diagnostics in the Plume of an SPT-100 from Thrust Axis to Backflow Region, AIAA-98-3641, 34th Joint Propulsion Conference and Exhibit, Cleveland, OH, July 12-15, 1998.
79. Brown, S., *Basic Data of Plasma Physics*, McGraw-Hill Book Company, New York, 1959.
80. Hofer, R. R., Haas, J. M., Gallimore, A. D., Ion voltage diagnostics in the far-field plume of a high-specific impulse Hall thruster, AIAA-2003-4556, 39th Joint Propulsion Conference and Exhibit, Huntsville, AL, July 20-23, 2003.
81. Kim, S. W., *Experimental Investigations of Plasma Parameters and Species-Dependent Ion Energy Distribution in the Plasma Exhaust Plume of a Hall Thruster*, Ph.D. Dissertation, University of Michigan Department of Aerospace Engineering, 1999.
82. Hofer, R. R., Gallimore, A. D., Ion species fractions in the far-field plume of a high specific impulse Hall thruster, AIAA-2003-5001, 39th Joint Propulsion Conference and Exhibit, Huntsville, AL, July 20-23, 2003.
83. Van Gilder, D. B., Boyd, I. D., Keidar, M., Particle Simulations of a Hall Thruster Plume, *Journal of Spacecraft and Rockets*, Vol. 37, No. 1, pp.
84. Boyd, I. D., Computation of the Plume of an Anode-Layer Hall Thruster, *Journal of Propulsion and Power*, Vol. 16, No. 5, pp. 902-909.
85. Bird, G. A., *Molecular Gas Dynamics and the Direct Simulation of Gas Flows*, Vol. 42, Oxford Science Publications, 1994.
86. Birdsall, C. K., Langdon, A. B., *Plasma Physics Via Computer Simulation*, Adam Hilger, 1991.
87. Boyd, I. D., Van Gilder, D. B., Liu, X., Monte Carlo Simulation of Neutral Xenon flows in Electric Propulsion Devices, *Journal of Propulsion and Power*, Vol. 14, No. 6, pp. 1009-1015.
88. Ketsdever, A. D., Design Considerations for Cryogenic Pumping Arrays in Spacecraft-Thruster Interaction Facilities, *Journal of Spacecraft and Rockets*, Vol. 38, No. 3, pp. 400-410.

89. Garner, C., Polk, J. E., Brophy, J. R., Goodfellow, K., Methods for Cryopumping Xenon, AIAA-96-3206, 32nd Joint Propulsion Conference and Exhibit, Lake Buena Vista, FL, July 1-3, 1996.
90. Walker, M. L. R., Gallimore, A. D., Hot Flow Pressure Map of a Vacuum Facility as a Function of Flow Rate to Study Facility Effects, IEPC-03-0077, 28th International Electric Propulsion Conference, Toulouse, France, Mar. 17-21, 2003.
91. Choueiri, E. Y., Plasma oscillations in Hall thrusters, *Physics of Plasmas*, Vol. 8, No. 4, pp. 1411-1426.
92. Gascon, N., Cappelli, M. A., Plasma instabilities in the ionization regime of a Hall thruster, AIAA-2003-4857, 39th Joint Propulsion Conference and Exhibit, Huntsville, AL, July 20-23, 2003.
93. Walker, M. L. R., Gallimore, A. D., Performance Characteristics of a Cluster of 5 kW Laboratory Hall Thrusters, AIAA-2004-3767, 40th Joint Propulsion Conference, Fort Lauderdale, FL, July 11-14, 2004.
94. Manzella, D. H., Jankovsky, R. S., Elliott, Mikellides, Jongeward, Allen, Hall Thruster Plume Measurements On-Board the Russian Express Satellites, IEPC-2001-44, International Electric Propulsion Conference, Pasadena, CA, Oct. 15 - 19, 2001.
95. King, L. B., Gallimore, A. D., Ion-Energy Diagnostics in the Plasma Exhaust Plume of a Hall Thruster, *Journal of Propulsion and Power*, Vol. 16, No. 5, pp.
96. Kaufman, Theory of Ion Acceleration with closed Electron Drift, *Journal of Spacecraft and Rockets*, Vol. 21, No. 6, pp.
97. de Grys, K. H., Meckel, N., Callis, G., Greisen, D., Hoskins, A., King, D., Wilson, F., Werthman, L., Khayms, V., Development and Testing of a 4500 Watt Flight Type Hall Thruster and Cathode, IEPC-01-011, 27th International Electric Propulsion Center, Pasadena, CA, Oct. 15-19, 2001.
98. Hofer, R. R., Jankovsky, R. S., A Hall Thruster Performance Model Incorporating the Effects of a Multiply-Charged Plasma, AIAA-2001-3322, 37th Joint Propulsion Conference and Exhibit, Salt Lake City, UT, July 8-11, 2001.